Micro- and Milli-fluidic Systems for X-Ray Scattering Analysis of Crystallization Processes

Mark Alan Levenstein

Submitted in accordance with the requirements for the degree of
Doctor of Philosophy

The University of Leeds
School of Mechanical Engineering
School of Chemistry

March 2019

The candidate confirms that the work submitted is his own, except where work which has formed part of jointly-authored publications has been included. The contribution of the candidate and the other authors to this work has been explicitly indicated below. The candidate confirms that appropriate credit has been given within the thesis where reference has been made to the work of others.

The preliminary design and construction of the insert-based microfluidic device presented in Section 2.1.1 of “Chapter 2: Microfludics-Coupled X-ray Powder Diffraction” was initiated as a part of an earlier MSc program undertaken by the candidate: *Microfluidic Devices for Crystallization*, Mark A. Levenstein, MSc (Eng) by Research, University of Leeds, 2015. Improvements and modifications to the device were made as a part of the current PhD program, and all device characterization and X-ray analysis presented in this thesis was completed as a part of this new program.

“Chapter 3: Nucleant-Mediated Crystallization of Calcium Carbonate” and some elements from Section 2.1 and 2.3 of “Chapter 2: Microfludics-Coupled X-ray Powder Diffraction” are based on the paper: Droplet Microfluidics XRD Identifies Effective Nucleating Agents for Calcium Carbonate, Mark A. Levenstein, Clara Anduix-Canto, Yi-Yeoun Kim, Mark A. Holden, Carlos González Niño, David C. Green, Stephanie E. Foster, Alexander E. Kulak, Lata Govada, Naomi E. Chayen, Sarah J. Day, Chiu C. Tang, Britta Weinhausen, Manfred Burghammer, Nikil Kapur, and Fiona C. Meldrum *Advanced Functional Materials*, 2019, **29**, 1808172. All microfluidics experiments, DMC-XRD hardware and software development, and DMC-XRD data processing were done by the candidate under the supervision of Nikil Kapur and Fiona C. Meldrum. Additionally, the candidate planned and led all beamtimes where DMC-XRD data was collected. Clara Anduix-Canto cleaned the nucleants and preformed initial mineral nucleant trials in bulk conditions. Yi-Yeoun Kim synthesized the gold nanoparticles and conducted TEM. David C. Green synthesized the magnetite and calcite nanoparticles and conducted TEM. Alexander N. Kulak performed BET-BJH and SEM analysis. Clara Anduix-Canto, Yi-Yeoun Kim, Carlos González Niño, Stephanie E. Foster, Sarah J. Day, Chiu C. Tang, Britta Weinhausen, and Manfred Burghammer assisted with beamtimes. Mark A. Holden, Lata Govada, and Naomi E. Chayen assisted in discussing and interpreting the nucleant results.

Acknowledgements

There are so many people who have helped me reach this milestone, whether personally or professionally, or a little of both(!), and I will try my best to thank them all. To begin, I was fortunate to have not one, but two supervisors, each training me in different areas and allowing me to pool the resources and expertise of two different schools: Mechanical Engineering and Chemistry. My engineering supervisor, Prof. Nik Kapur, is the British MacGyver, and he too can build a flow system or a temperature controller with only a paper clip and some duct tape (…or was it a nitrile lab glove?). Nik taught me to use my creativity and engineering ingenuity to solve complex problems with simple solutions. I also appreciated his open door policy, and made use of it frequently when deadlines loomed – I hope I didn't abuse it, Nik! My chemistry supervisor, Prof. Fiona Meldrum, is a world class science communicator and visionary. I think she could look at the most diffuse set of scientific writing and pull out a great story – and I know this from personal experience because she has done it for me! If there is anything I hope to take from her, it is this incredible ability to get people excited about her research, and if I can become half the writer she is, I will be lucky. I thank you both for initiating such an interesting collaboration and welcoming me into your groups and country!

Although I am really an engineer, I have called the Meldrum Group in Chemistry West Block my home for the better part of the past 5 years during my MSc and PhD programs (and a 5-month undergraduate exchange in 2013). The two people who facilitate this group and truly make it a family are Dr. Yi-Yeoun Kim and Dr. Alex Kulak. Not only do they keep the lab running day to day, but they also provide a vibrant social life for the constant stream of new PhD students who arrive here "fresh off the boat". I think as a group we are spoiled having not only one, but two scientists as talented and knowledgeable as Yi-Yeoun and Alex, and I know it will take some adjustment for me to get used to not having their support. Thank you Yi-Yeoun and Alex for all of your help and also for your friendship over the years.

Next, I would like to thank every member of the Meldrum Group over the various stents that I've been here. Thank you Yi-Yeoun, Alex, Bram, Yun-Wei, Johannes, Luke, Tony, Ciara, Joe, Bart, Phill, Shunbo, Muling, Angela, Thembi, Mark H., David, Steph, Ouassef, Ilaria, Yifei, Tom D., Tom W., Shu, Jo, anyone I've left out, and most of all, thank you Clara Anduix Cantó! Clara, now Dr. Anduix, was the PhD student a year ahead of me who became my main collaborator within the group. She is the one who directly introduced me to the $CaCO_3$ nucleants and did the preliminary work that led to the results presented in Chapter 3 and the first publication from my PhD. Outside of

work, Clara is a great friend, who is unbelievably fun and deeply loyal. I will never forget our great conversations on the many forms of transport we took to and from beamtimes, good times (or bad times) in Spain, or fun nights in Leeds or at the synchrotron school. Leeds hasn't been the same this final year since you've been gone!

While I wasn't based in Mechanical Engineering day to day, I still received a lot of support from people over there. I would like to thank Graham Brown and Andy Pickering for machining and UV laser etching assistance, Tony Wiese for general lab support and IR camera help, Patrick Mason for additional IR camera assistance, and Fiona Slade and Judith Schneider for administrative assistance (somebody has to keep Nik on track!). Most of all, I would like to thank fellow PhD student, Carlos González Niño, who like Clara, became a vital collaborator and an even better friend. Carlos is a world class engineer who provided excellent technical support at my most important and productive beamtimes and helped with the fReactor experiments presented in Chapter 4. I truly enjoyed our semi-regular lunches and coffees, post beamtime beers, and extra-beamtime excursions into France and Switzerland. I am coming to visit you in Valladolid!

I would also like to thank my great external collaborators. Thank you to Dr. Karen Robertson (now of Nottingham), Prof. Chick Wilson, Lois Wayment, and (now Dr.) Pierre-Baptist Flandrin of the University of Bath for partnering with me on the KRAIC-D. These people are the real experts on UBA, FeTrz, and mesoscale synthesis, but I think with my knowledge of X-ray compatible flow systems and time-resolved PXRD processing we make a great team! Thank you also to Dr. Marcus Winter, Dr. Pierre LeMagueres, Dr. Jakub Wojciechowski, and Dr. Mathias Meyer of Rigaku Oxford Diffraction for inviting Karen and I to come and perform experiments on the Synergy-R at your application center in Wrocław, Poland. And finally, thank you to Cate O'Brien and Oleksandr (Sasha) O. Mykhaylyk of the University of Sheffield for letting us trial the Xeuss 2.0 SAXS/WAXS system. These final experiments on the Synergy-R and Xeuss were so important, and really demonstrate how much potential this type of flow-based X-ray analysis has for enabling new materials research.

I also appreciate the support I received from other members of Leeds University staff. First, thank you to Dr. Chris Pask who runs the X-ray Diffraction Suite within the School of Chemistry. Chris was very helpful with running powder samples and prepping for the experiments with Rigaku, and I truly benefited from our discussions regarding *in situ* X-ray diffraction instrumentation and methodology. I would also like to thank university fellows, Dr. Robert Menzel and Dr. Paolo Actis, who provided me with a great deal of encouragement throughout my PhD program. Being several years

ahead of me in the academic lifecycle, they were able to give me some really valuable advice, and I always came away from our conversations with more confidence than I had previously!

As a final acknowledgement to work-related assistance, I would like to thank everyone who was a part of one of my beamtime teams or who provided beamline support. Thanks to my first ever beamtime team of Fiona, Yi-Yeoun, and Tony. Since then, a number of additional people have joined in for one or more of these trips. Thank you to Joe, Shunbo, Steph, Carlos, Clara, and Nik ("The A-Team"; Fig. A). Thank you to the beamline scientists who've helped over the years including Dr. Stephen Thompson, Dr. Sarah Day, and Dr. Chui Tang from Diamond I11, Dr. Andy Smith, Dr. Tim Snow, and Dr. Nick Terrill from Diamond I22, and Dr. Michael Sztucki, Dr. Britta Weinhausen, and Dr. Manfred Burghammer from ESRF ID13. I especially want to thank Sarah and Chui for helping us in those early days when almost nothing worked, and Britta and Manfred who used their extensive prior microfluidics and X-ray experience to select scan settings that actually got DMC-XRD off the ground. Finally, I would like to thank Pierre Lloria, Peter van der Linden, and Diego Pontoni from the Partnership for Soft Condensed Matter (PSCM) of the ESRF for letting us use their wonderful lab facilities during ESRF beamtimes.

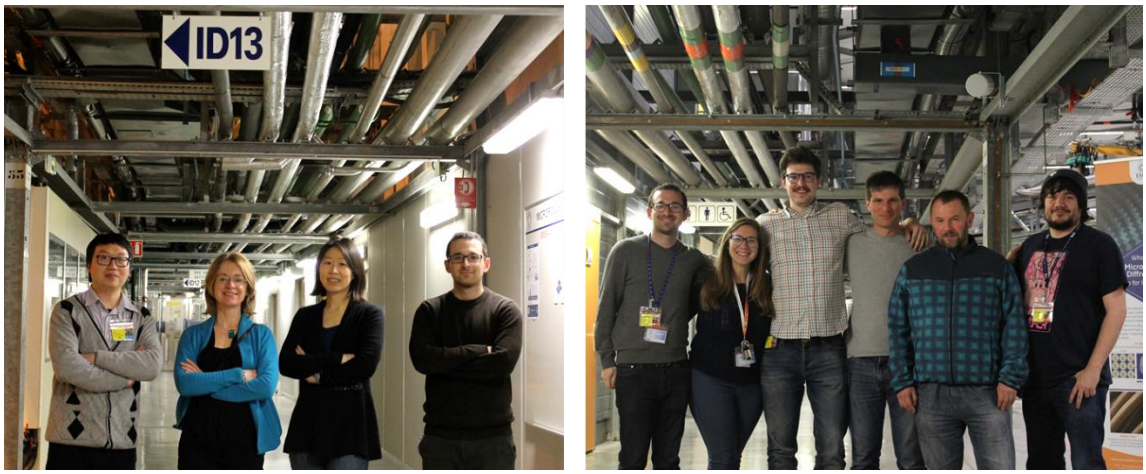

Fig. A: (left) First ESRF beamtime team, Nov. '15. From left to right, Shunbo, Fiona, Yi-Yeoun, and me. (right) Final ESRF beamtime team, Nov. '17. From left to right, me, Clara, Carlos, Nik, Manfred, and Joe.

There are also many people who have contributed to my personal life these 5 years. I would like to thank all "Los Bonicos" including Clara, Natalia, Alberto, Rosa, Jésus, Edu, Rodridgo, and Marina, and newer friends including Julio, Davide, Silvia, Vishnu, Michaël, Marine, and Rodrigo Argentino for providing me with a great social group in and around uni. Additionally, I would like to thank the people of Redeemer Church Leeds, and especially Chris and Naomi Bennigsen, Fraser and Chloe Malyk, Dan and Louise Logan, Lizzie Fry, Alex and Beth Passmore, Rachael Newton, and the

rest of the Wednesday City Group for providing great friendship and fellowship. Last, but not least, I want to thank my 4-year housemate, Fergus Mckie, for being such an amazing friend. We've had some great times over the years like in Wales, Bruges, Pitchfork Paris, the Lake District, or just at home after work watching Peep Show/Always Sunny/Seinfeld/the Office (U.S.)/etc., and I know it will be hard on both of us when the El Dude Brothers separate.

Finally, I'd like to thank my family for supporting me while I've been away. I know it has been difficult for all of us, but it makes it so much easier knowing you have a family that loves you back home and supports what you're doing. Thank you for raising me in such a caring environment, providing for all of my needs and even most of my wants, training me in the Word, disciplining me when I needed it, and always encouraging me in my studies! I love you Mom, Dad, David, Uncle Keith, BB & GG, and Grandma Shell, and I can't wait to be closer to home soon!

Abstract

X-ray diffraction is one of the oldest, most popular, and also most powerful techniques for the study of crystals, and microfluidic devices provide some of the cleanest and most controlled environments for crystal growth. However, it is extremely rare to see these two tools combined for the study of crystallization processes *in situ*. This is in part due to the difficulty of building X-ray "transparent" sample environments and the low performance of most diffractometers, which requires the use of specialized synchrotron radiation facilities for analysis. This thesis presents the development of X-ray compatible microfluidic and millifluidic devices and the required data collection and processing strategies to begin to address this deficiency in the study of crystal nucleation and growth.

After a thorough review of crystallization theory, microfluidic devices, and previous efforts at building flow systems for time-resolved X-ray scattering analysis, the initial results chapters are focused on the characterization and optimization of a versatile polymer insert-based microfluidic platform. A range of experiments in continuous and segmented flow were conducted with the device, and the effects of these different flow configurations on device performance and data collection are discussed. Well-segmented flow is shown to effectively isolate reactions from the channel walls, enabling crystallization to be studied as a function of the residence time of individual droplets along the microchannel in steady flow operation. Here termed, "Droplet Microfluidics-Coupled X-ray Diffraction" or DMC-XRD, this type of analysis allows the collection of serial powder diffraction patterns that reveal the average crystal structure present at each time-point along the flow. Then as a demonstration, this technique is utilized to help identify effective nucleating agents for calcium carbonate and quantitatively and qualitatively compare their efficiency.

The remainder of the thesis explores the possibility of conducting similar types of experiments at larger length-scales and with different X-ray sources. First, a mesoscale flow crystallizer is demonstrated to be suitable for the millifluidic equivalent of DMC-XRD. Next, the successful trial of a very different continuous stirred-tank reactor (CSTR)-type system for inline X-ray analysis is reported. Finally, this thesis presents a series of microfluidic and millifluidic experiments that were conducted with two different state-of-the-art commercial diffractometers. Preliminary results obtained with these systems suggest that there is enormous potential for performing flow-based X-ray analysis of crystallization processes in the home laboratory, as long as X-ray source optics and detectors are tuned to provide comparable beamsizes and exposure frame rates to those employed at the synchrotron.

Table of Contents

List of Tables

List of Figures

List of Abbreviations

ACC – Amorphous calcium carbonate

AFM – Atomic force microscopy

BG – Bioactive glass

CNP – Calcite nanoparticle

CNT – Classical Nucleation Theory

CPG – Controlled porous glass

Cryo-TEM – Cryogenic transmission electron microscopy

CSTR – Continuous stirred tank reactor

DMC-XRD – Droplet microfluidics-coupled X-ray diffraction

FeTrz – Iron triazole

FTIR – Fourier-transform infrared spectroscopy

IAP – Ion activity product

ID – Inner diameter

KRAIC – Kinetically regulated automated input crystallizer

K_{SP} – Solubility product

LC-TEM – Liquid cell transmission electron microscopy

NP – Nanoparticle

OD – Outer diameter

PDF – Pair distribution function

Pe – Péclet number

PXRD – Powder X-ray diffraction

Re – Reynolds number

ROI – Region of interest

RT – Residence time

RTD – Residence time distribution

SAM – Self-assembled monolayer

SANS – Small angle neutron scattering

SAXS – Small angle X-ray scattering

SEM – Scanning electron microscopy

SI – Saturation index

SX – Serial crystallography

TEM – Transmission electron microscopy

UBA – Urea-barbituric acid

WAXS – Wide angle X-ray scattering

XRD – X-ray diffraction

Chapter 1:
Introduction and Background

Crystallization processes have an indelible effect on the world around us. The mineralization of coral reefs, the stabilization of active pharmaceutical ingredients, the synthesis of the active components of solar cells, and the scaling of a common kitchen kettle are just a few examples of the varied ways crystallization processes regularly affect technology and the environment. A common feature of many of these processes is that they occur in solution. As will be discussed in detail later in the chapter, such a solution may become supersaturated with respect to a particular solid phase, causing one or a number of nucleation events to occur. While this can be predicted to a certain extent, the exact timing and location of this nucleation appears random. Additionally, it happens rapidly and on the nanometer-scale, and stabilized nuclei subsequently grow quickly across multiple length scales. These features make crystal nucleation and growth extremely difficult processes to study and why, after more than a century of investigation, they are still active fields of research.

Most studies of crystal growth and nucleation are either indirect, e.g. recording the number of crystals that form as a function of time with optical microscopy, or *ex situ*, e.g. collecting final products in dried powder form and performing Fourier-transform infrared spectroscopy (FTIR) or X-ray diffraction (XRD). The problem with both of these routes is that dynamic and mechanistic information is lost, or never captured in the first place. With the former, low sensitivity and/or resolution limits the amount of information which can be obtained, and the result is often only a statistical inference. With the latter, detailed information is only obtained from the final product, where even the very act of drying a sample could change its properties and hence, introduce uncertainty into the interpretation of a measurement. Therefore, it is in the best interest of materials scientists to develop high resolution *in situ* techniques which enable detailed and mechanistic data to be collected and interpreted with as little ambiguity as possible.

For crystallization processes that occur in solution, it is reasonable to assume that the elucidation, and ultimately, the control of heat and mass transport phenomena within a solution is the first step to making high-resolution and high-certainty measurements. This is precisely where microfluidics, and also millifluidics, find utility. These technologies enable sensitive manipulation of fluids, where the beneficial blend of physics that occurs at these length scales facilitates rapid mixing, minimizes unwanted convection, and permits unparalleled time-resolution of fluids in flow. Additionally, the small scale of micro- and milli-fluidic platforms means that they require minimal reagents, which is advantageous when dangerous or expensive chemicals are

required. This last property also minimizes the requisite path length of a probe (whether photon, electron, etc.) through a solution, lowering background noise from and beam attenuation by the solvent.

This thesis presents an investigation of micro- and milli-fluidic platforms for time-resolved X-ray scattering analysis of crystal growth at specialized synchrotron radiation facilities. The primary focus (covered in Chapters 2 and 3), is the development and utilization of a technique, referred to as Droplet Microfluidics-Coupled X-Ray Diffraction (DMC-XRD), whereby serial powder diffraction patterns can be compiled from individual diffraction events from a succession of flowing droplets containing crystals. Data obtained using this method is compared with data obtained from single-phase, or so called “continuous” flow (Chapter 2.3), and then the utility of the method is illustrated by presenting its usage for the study of crystal nucleation in the presence of insoluble particulate additives (Chapter 3). The generality of the method is then investigated by conducting analogous experiments at the millifluidic-scale (Chapter 4). The penultimate chapter presents initial experiments to determine the suitability of state-of-the-art laboratory-based X-ray sources for performing these measurements without the need for a synchrotron (Chapter 5), and then the final chapter concludes the thesis with a general outlook for the nascent field of flow-based X-ray scattering analysis of materials synthesis and its future.

1.1 Crystallization and Materials Synthesis

As the scientific topic at the heart of this work is crystallization, it is appropriate to begin with an introduction to the theory of crystal nucleation and growth and some general background of previous synthetic and analytical work done in the crystal growth and design community. The traditional frameworks for understanding the nucleation and growth of crystals from solution are Classical Nucleation Theory (CNT) and the Terrace-Ledge-Kink Model, respectively.[1] This first section will be focused on crystal nucleation, with a focus on CNT and various aspects of heterogeneous nucleation on surfaces.

1.1.1 Crystal Nucleation

Classical Theory and Homogeneous Nucleation

Nucleation from solution is thermodynamically motivated by the solubility of a particular material. Solubility is typically expressed as the number of moles per liter that can be dissolved in solution before precipitation and is the observable consequence of the free energy (ΔG) balance of the system. This is illustrated by the equation:

$$\Delta \boldsymbol{G_S} = \Delta \boldsymbol{G_L} - \Delta \boldsymbol{G_{AS}} \quad \textbf{(1)}$$

where ΔG_S is the free energy of the solution, ΔG_L is the free energy needed to break up a crystal lattice, and ΔG_{AS} is the free energy released through the formation of aqueous species.[2] Practically, this means the lower the free energy needed to disrupt lattice bonds and the greater the loss of free energy through the formation of aqueous species, the lower the free energy of a solution and the greater the solubility of a compound.

The concept of solubility (*s*) is even more useful when linked with the activities, or effective concentrations, of the species in solution. Consider an ionic solid at equilibrium with its ionic constituents in solution:

$$\boldsymbol{M_n X_m}(\boldsymbol{solid}) \rightleftharpoons \boldsymbol{n M^+}(\boldsymbol{aq}) + \boldsymbol{m X^-}(\boldsymbol{aq}) \quad \textbf{(2)}$$

where *M* is the cation, *X* is the anion, and *n* and *m* are the number of moles of *M* and *X*, respectively. The equilibrium activity of each ion in Eq. 2 is described by the equations:

$$\{\boldsymbol{M^+}\} = \boldsymbol{n} \cdot \boldsymbol{s};\ \{\boldsymbol{X^-}\} = \boldsymbol{m} \cdot \boldsymbol{s} \quad \textbf{(3)}$$

where the brackets denote the quantity represents the activity of the ion within.[2] These equilibrium activities are specific to the solubility value used in their calculation, which is important to note as different polymorphs (crystal structures with the same chemical formula) can have differing solubility. Taking these activities, one can then calculate the solubility product, K_{SP}, for a specific compound or structure:

$$\mathbf{K_{SP}} = \{\boldsymbol{M^+}\}^{\boldsymbol{n}} \cdot \{\boldsymbol{X^-}\}^{\boldsymbol{m}} \quad \textbf{(4)}$$

This parameter is key to understanding the thermodynamic driving force in a particular crystallization scenario. By comparing the K_{SP} value to the actual activity of ions in a real solution (the ion activity product or *IAP*), one can determine the likelihood of a particular solid to appear. This comparison is often reported in terms of the saturation index (SI):

$$\mathbf{SI} = \mathbf{log}\left(\frac{\boldsymbol{IAP}}{\mathbf{K_{SP}}}\right) \quad \textbf{(5)}$$

where for SI < 0, the solution is undersaturated, for SI = 0, the solution is saturated, and for SI > 0, the solution is supersaturated with respect to a particular phase.[3] The term “saturation index” is often freely interchanged with the word “supersaturation”, the latter being equal to IAP/K_{SP} without taking the logarithm.[2] In turn, both of these values are also proportional to the chemical potential difference of the solution, $\Delta\mu$, which can

also be used to describe nucleation from a thermodynamic perspective.[4] However, all of these terms describe the same phenomenon, principally that if the *IAP* in solution is greater than the K_{SP} of a solid (i.e. when SI > 0), precipitation of that solid phase will be thermodynamically favorable until the *IAP* drops to equal the K_{SP} (when SI = 0).

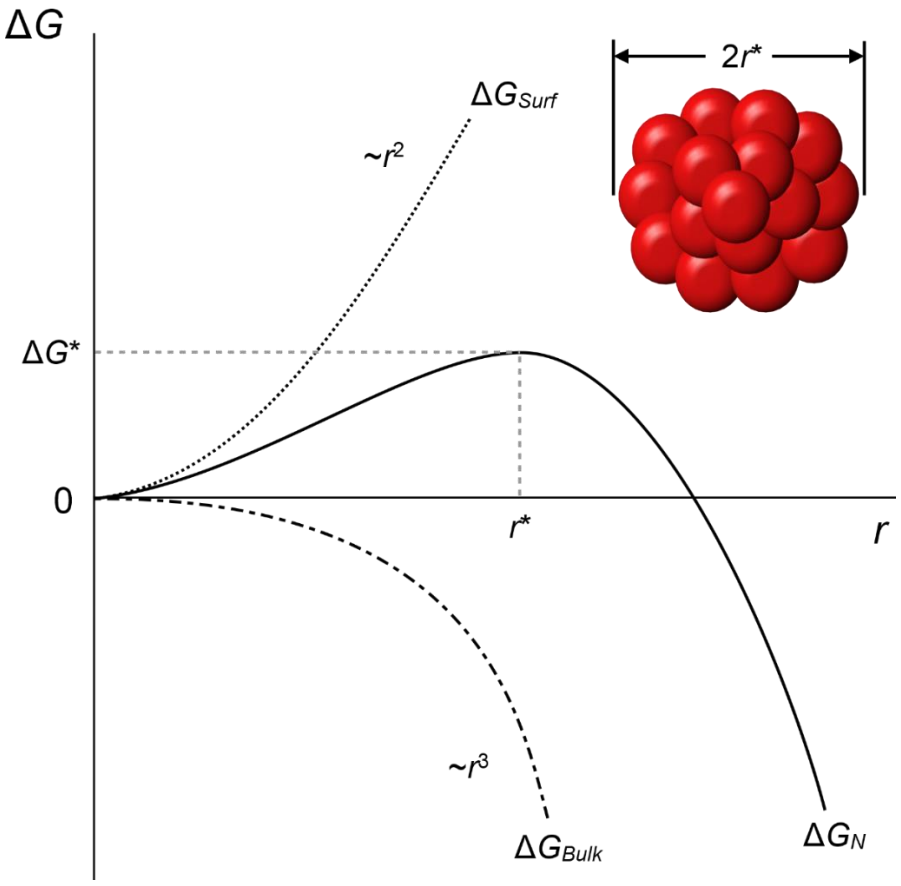

Figure 1: Plot of the free energy (ΔG) vs. nucleus radius (r). The free energy associated with the formation of a crystal nucleus (ΔG_N) comprises a surface (ΔG_{Surf}) and a bulk (ΔG_{Bulk}) term. ΔG_{Surf} scales proportional to r^2 and inhibits nucleus stabilization, whereas ΔG_{Bulk} scales proportional to r^3 and promotes stabilization. At a particular ΔG and r value, ΔG^* and r^*, the bulk and surface terms become equal, and any further growth results in a stable, growing crystal. The inset illustrates a critical nucleus with a diameter of $2r^*$. Adapted from ref[2] and ref[4].

In spite of this thermodynamic driving force, unaided nucleation is actually quite rare at low saturation indexes. This is due to the large kinetic barrier associated with the creation of a new solid-liquid interface – the crystal surface. The result is that homogenous nucleation, or nucleation in free solution, has a large activation energy that must be overcome.[2] This is illustrated in Figure 1, which displays the free energy required for a crystal nucleus to grow (ΔG_N). This curve comprises a positive surface term which inhibits nucleus stabilization (ΔG_{Surf}, dotted line), and a negative bulk term which promotes nucleation (ΔG_{Bulk}, dashed line). At small radii, the surface term is larger than the bulk term, meaning that these small nuclei are unstable. However, since surface area is proportional to r^2 and volume is proportional to r^3, the bulk term will

eventually overtake the surface term at a critical nucleus size, *r**. The free energy associated with this critical size, ΔG^*, is the activation energy required to generate a stable crystal.[2] Once a nucleus reaches this size, even an infinitesimal amount of surface growth will push the system out of equilibrium and enable the crystal to grow freely.[4]

Heterogeneous Nucleation

Crystals in many natural and synthetic scenarios alike will form via heterogeneous nucleation on a surface rather than wait for this barrier to bulk precipitation to be overcome. Nuclei can be more easily stabilized on a surface than in bulk since the interfacial area between the nucleus and the solution is decreased (i.e. lower ΔG_{Surf}). Consider the classical analogy for heterogeneous nucleation of the condensation of a liquid phase from a vapor (Fig. 2). According to CNT, the activation energy of forming a liquid droplet, ΔG^*, is proportional to the contact angle of the droplet with a surface, θ_L. When the activation energies of all cases are normalized, homogenous nucleation of a free droplet has a ΔG^* of 1, whereas heterogeneous nucleation of a sessile droplet with θ_L = 30° has a ΔG^* of 0.01 – a 100-fold decrease.[5] Further, in wedges or other high surface area non-planar features, the activation energy can drop to essentially zero. While a solid critical nucleus does not "wet" a surface in the same way as a liquid, this nevertheless illustrates the effect of varying degrees of surface interaction on promoting or stabilizing nucleation.

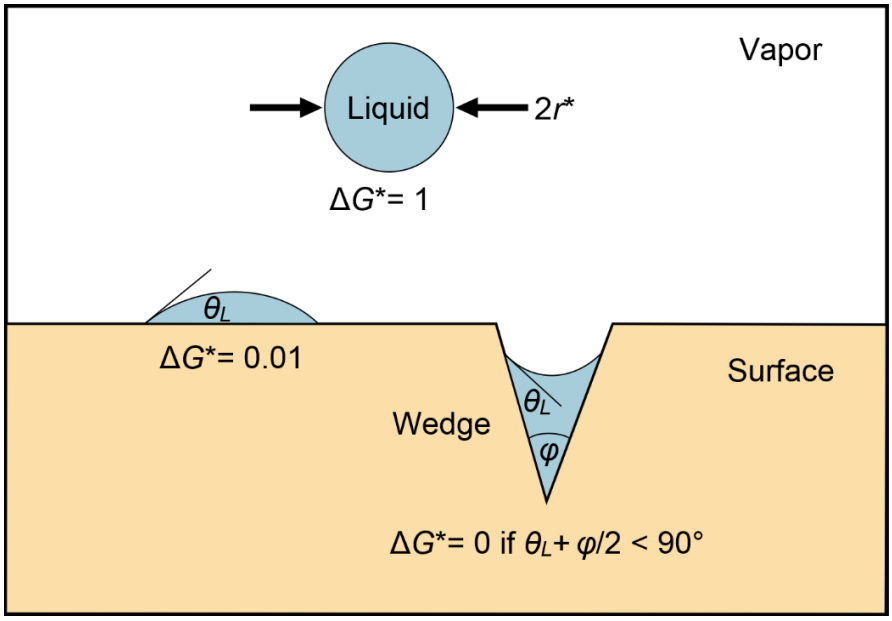

Figure 2: The vapor condensation analogy for heterogeneous nucleation. The degree of wetting of the liquid condensate and surface features have a significant effect on the activation energy of nucleation, ΔG^*. Adapted from ref[4] and ref.[5]

There has been a great deal of work investigating the mechanisms of heterogeneous nucleation, both due to its importance in many crystallization processes and also because of the possibility of one day being able to design surfaces to nucleate desired crystalline products. Indeed, the affinity of a crystal for a surface goes beyond simply minimizing the interfacial area, and there are many ways that a surface can interact with a forming nucleus and direct its growth. For simplicity, they will be grouped into three sets of effects. These are *(1)* surface chemistry,[6] *(2)* surface topography,[7] and *(3)* pore effects,[8] where it is possible – and even probable – for multiple types of effects to work synergistically. These are illustrated in Figure 3:

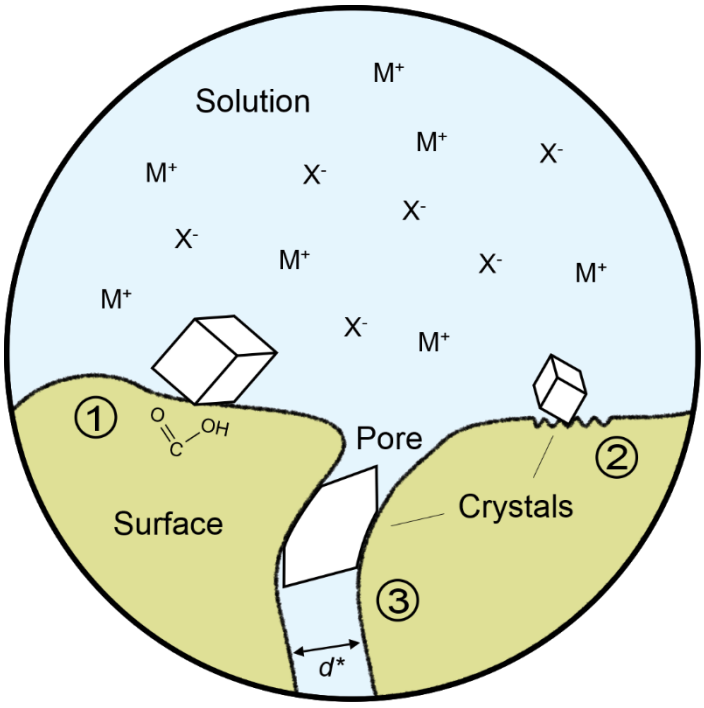

Figure 3: Examples of surface features (not to scale) which promote heterogeneous nucleation: *(1)* surface chemistry, *(2)* surface topography and *(3)* pore size-critical nucleus matching.

Surface Chemistry Effects

For the purpose of this thesis, surface chemistry effects are ones that promote or inhibit nucleation because of the presence and arrangement of specific atoms, molecules, or charges at a surface. Most of the chemical mechanisms by which surfaces can affect nucleation can be considered as some form of molecular recognition.[2] The simplest of these are electrostatic and polar interactions, whereby specific surface charge distributions can attract ions from solution. For example, soft tissues in calcium-containing biominerals have been shown to have a high density of anionic groups which can form weak bonds with Ca^{2+} ions (Fig. 3, feature 1).[2] Such bonding can increase the local supersaturation close to a surface or even stabilize a

particular arrangement of molecules if the charge distribution is arranged appropriately (i.e. there is stereochemical matching between the surface and the crystal lattice).

Additional recognition can occur if the surface itself is crystalline, as the similarity of the surface atomic lattice to the atomic lattice of the crystal overgrowth can affect nucleation. Specifically, the ΔG_{Surf} term decreases the closer these two lattices match, which can result in oriented, or epitaxial growth of the crystal with respect to the surface.[2] For example, Azienberg *et al*. combined surface charge distributions and epitaxial matching to pattern calcite crystal growth on a planar substrate.[6] By using microcontact printing to pattern a two-dimensional (2D) array of polar self-assembled monolayer (SAM) "islands" in a "sea" of non-polar methyl-terminated SAMs, the authors created localized regions of supersaturation over the polar regions while keeping the rest of the solution undersaturated. This confined crystal nucleation and growth to the polar regions alone, where the orientation of the crystals that formed was determined by the polar SAM utilized (COOH, SO_2OH, or OH) and the structure of the underlying substrate (Ag, Au, or Pd on top of Cr). An important implication of such specific molecular recognition is that it can select for a particular face/orientation of a crystal, or even select for a particular structure to crystallize if multiple polymorphs of the same chemical formula are supersaturated.[9]

Surface Topographical Effects

The second group of surface effects is topography, where certain physical micro- or nano-sized features of a surface promote nucleation (Fig. 3, feature 2). These could function in conjunction with surface chemistry effects or act alone. Recall the liquid condensation analogy from earlier in the section (Fig. 2), where the activation energy of nucleation was lowered with increased "wetting." This effect was amplified in the wedge, since small angles φ decrease the interfacial contact with the bulk phase even if the fluid contact angle with the surface (θ_L) is high.[10] This explains why nucleation in a surface feature could be favored kinetically. However, there are several ways topography can influence nucleation beyond simple kinetics.

One such way is by templating a particular crystal structure. For example, perhaps the geometry of a particular surface feature matches the shape of a crystal (e.g. the walls of a surface "pit" are parallel with particular crystal facets; Fig. 4).[11] Such an effect was demonstrated by Diao *et al.*, who studied aspirin crystallization on patterned polymer substrates with round, square and hexagonal pits of 15-120 nm size.[12] They found that round pits inhibited nucleation compared to a flat surface, square pits increased the nucleation rate by 3 times, and hexagonal pits resulted in a 10-fold increase. Additionally, multiple surface features could work in conjunction with each other to template a crystal. Such an effect was observed by van Blaaderen *et al*. who

patterned a substrate with a periodic arrangement of pits corresponding to a face-centered cubic (FCC) crystal structure.[13] They observed that colloidal crystals which formed on top of these substrates grew in an FCC arrangement matching the underlying surface structure.

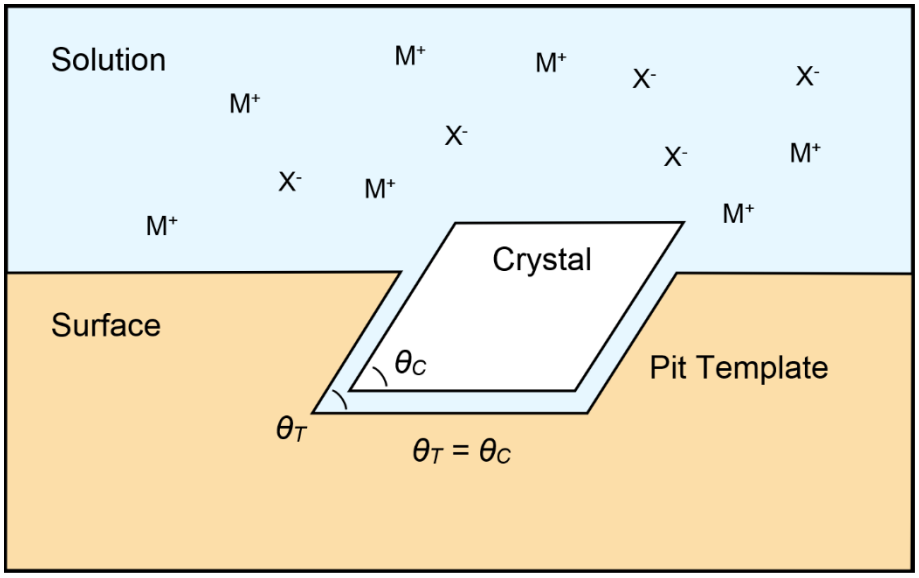

Figure 4: Example of surface pits templating a crystal structure based on a geometric match.

However, an ideal fit between a crystal and pit – as illustrated in Figure 4 – is quite rare. A more likely scenario is that some mismatch between the structure of the pit and of the crystal will introduce strain in the crystal lattice which could slow down growth. In fact, van Meel *et al*. modelled growth in such pits and found that pits with rough amorphous surfaces were better at nucleating crystals than crystalline pits since they resulted in less strained crystals.[14] These seemingly contradictory results demonstrate the complexity of topography-induced nucleation, and make it difficult to make generalizations about what features will promote nucleation in every situation.

A great deal of what is known about heterogeneous nucleation comes from the study of ice, as there are decades worth of scholarship on topics ranging from synthetic cloud seeding[15, 16] to the effect of atmospheric aerosols (e.g. natural dusts) on the weather patterns.[17-19] The most well-known material that nucleates ice is silver iodide (AgI), a fact that was first noted by Vonnegut in 1947.[20] This has historically been attributed to the structural similarity of the two materials resulting in epitaxial growth of ice. However, other materials with a similar structural match to ice have been shown to be poor ice nucleators, casting doubt on this purely surface chemistry-based interpretation.[21] Recent studies have focused on the ability of mineral dusts with more complex surface chemistries and topographies to nucleate ice at high temperatures. For instance, Kiselev *et al*. observed that oriented ice crystals form from small defects or cracks – so-called “active sites” – on potassium-rich alkali feldspar mineral

($KAlSi_3O_8$) fragments.[22] Using a combination of scanning electron microscopy (SEM) and molecular modelling, they suggested that high-energy (100) feldspar planes, which are exposed at these active sites, preferentially nucleate prismatic planes of hexagonal ice. This provides a good example of topography working in conjunction with surface chemistry to promote nucleation. In contrast, Whale *et al*. isolated the effect of topography by studying the ice nucleating efficiency of a range of alkali feldspars of different chemical composition and crystal structure.[7] They found that feldspars with similar composition and structure could have very different ice nucleating ability – the only difference between them being surface topography. More specifically, efficient feldspars contained K- and Na-rich regions delimited by grain boundaries, giving these feldspars a unique microtexture.

Pore-Stabilized Nucleation

The final group of surface effects is pore-based stabilization of crystal nuclei. A great deal of work has sought porous materials which can act as nucleating agents, or "nucleants", for protein crystals, as a major bottleneck in the structure determination of proteins is growing high quality protein crystals necessary for X-ray diffraction (XRD) analysis.[23] Empirical studies over the last two decades have identified a range of porous materials such as silicon,[24] bioactive glass,[8] carbon nanotubes,[25] gold,[26] molecularly imprinted polymers (MIPs),[27] and even hair,[28] which are effective at nucleating many proteins.

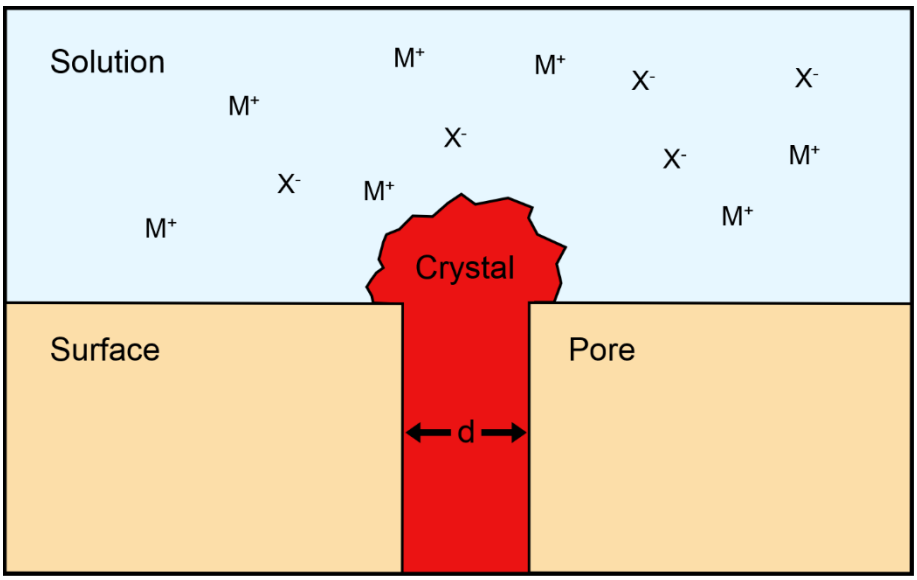

Figure 5: Crystal nucleation from a pore of diameter, *d*. The size of the pore must be optimized to both stabilize the critical nuclei within the pore and provide sufficient surface area for outgrowth. Adapted from ref.[29]

The underlying assumption behind these studies has been that nanometer-sized pores can serve as compartments which confine and stabilize the solute molecules

needed for crystal nucleation. Diao *et al*. demonstrated this effect by confining supersaturated solutions within polymer microgels of varying mesh size and found there was an optimal size which balanced solute-solute and solute-polymer interactions to stabilize a nucleus.[30] Meshes above the optimal size did not allow surface stabilized solute molecules to sufficiently interact with each other to form a nucleus, while meshes below the optimal size did not allow solute molecules to form large enough clusters to nucleate. Taking this a step further, Page and Sear developed a two-step model which predicts that there exists an optimal pore size for balancing the initial pore-based stabilization of the critical nucleus and nucleation out of the pore.[29] Their model shows that these two steps are in competition: critical nuclei can be more easily stabilized in smaller pores, but nucleation out of the pore will be inhibited if the pore size, *d*, does not provide a large enough interface with the solution to overcome the higher energy barrier that is present outside of the pore (Fig. 5). Based on their results, the optimal pore size for promoting nucleation is very close to the critical nucleus size.

While this sounds like a simple principle to follow for the selection or design of porous nucleants, in practice it is much more complicated. The critical nucleus size is dependent on the material and the solution supersaturation and is not always trivial to calculate.[31] Further, the above model only accounts for pore size and does not consider the pore shape, which is also important.[8] However, experimentally characterizing pore shape is difficult and only of limited use, as very little is known about the shape of critical nuclei. Therefore, since it is hard to predict the correct pore size and shape for a given crystallization scenario *a priori*, it has been suggested – and indeed demonstrated – that the best nucleants are highly disordered with a range of pore sizes and geometries.[8] If this range is sufficiently wide, it follows that a certain percentage of pores are bound to be the right shape and size to induce nucleation.

1.1.2 Crystal Growth

Classical Growth

Once a crystal phase has overcome the free energy barrier and nucleated, the next step is for it to grow. The classical model of crystal growth assumes that free ions or monomers in solution order themselves into an existing crystal lattice ion-by-ion (Fig. 6a).[32] The simplest mechanism by which this occurs is called “birth and spread”, where a new layer nucleates on an existing crystal face and spreads outwards until the previous layer is covered.[33] However, as was noted by Burton, Cabrera, and Frank (BCF) in the early 1950s, such a process is thermodynamically costly, and should proceed much slower than demonstrated experimentally.[34, 35] This is because the

nucleation and growth of a new layer on top of an atomically smooth crystal face has a high energy barrier.

To account for this discrepancy, BCF proposed a new model that took into account defects, called kink sites, which form at the steps between layers of flat crystal terraces (Fig. 6b).[34] Growth occurs at these steps, particularly at the kinks, since these locations minimize interfacial interaction of binding monomers with the solution. BCF also proposed that new layers can be added continuously through screw dislocations, which provide a practically endless number of kink sites, as opposed to the birth and spread mechanism alone, which requires costly terrace nucleation to create each new layer.[35] According to this theory, an imperfection in the crystal lattice results in a dislocation which propagates normal to the crystal surface.[34] This causes the growth front to continually spiral upwards around the dislocation – meaning that nucleation on a flat terrace is not required to generate new layers. While initially just a theory, early experiments reinforced this mechanism,[35] which was further confirmed by modern high resolution imaging techniques (Fig. 6c).[36]

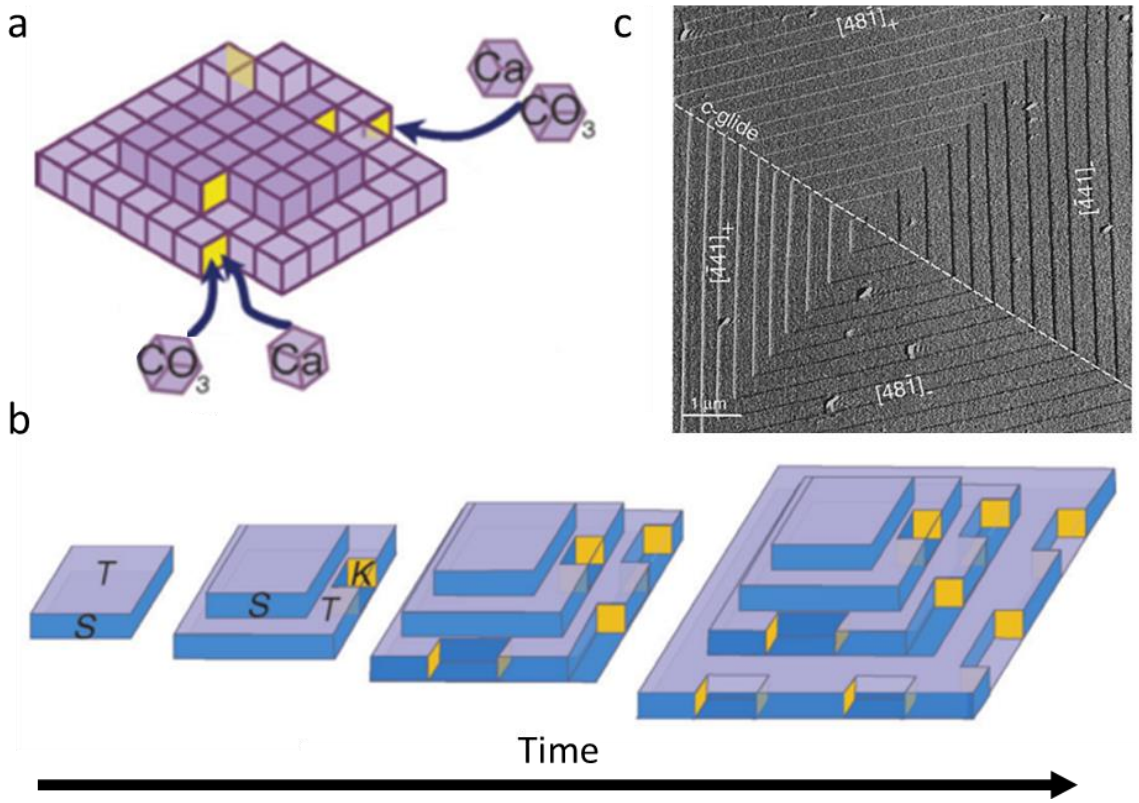

Figure 6: Ion-by-ion growth according to the BCF or Terrace-Ledge-Kink Model. (a) Ca^{2+} and CO_3^{2-} ions incorporating into a $CaCO_3$ crystal at kink sites. (b) Growth at a crystal face over time resulting in more steps (S), kinks (K) and ledges or terraces (T). (c) Atomic force microscope (AFM) image of a screw dislocation on a calcite [104] surface. Scale bar is 1 µm. (a) and (b) adapted from ref.[37] and (c) adapted from ref.[36]

Multistep Growth

While the BCF or Terrace-Ledge-Kink model can accurately describe ion-by-ion crystal growth, there are many growth pathways which do not follow this one-step classical route. In order to explain, let us quickly return to the topic of nucleation. As briefly mentioned earlier in the chapter, a particular compound can have more than one solid form or polymorph. Each polymorph has a unique solubility and also a unique energy landscape for nucleation and growth.[38] While less thermodynamically favored, more soluble polymorphs may nucleate first due to their lower activation energy. Then, following a process explained by Ostwald's Step Rule, these polymorphs may transform into increasingly stable structures until the lowest energy form is reached (Fig. 7).[39-41]

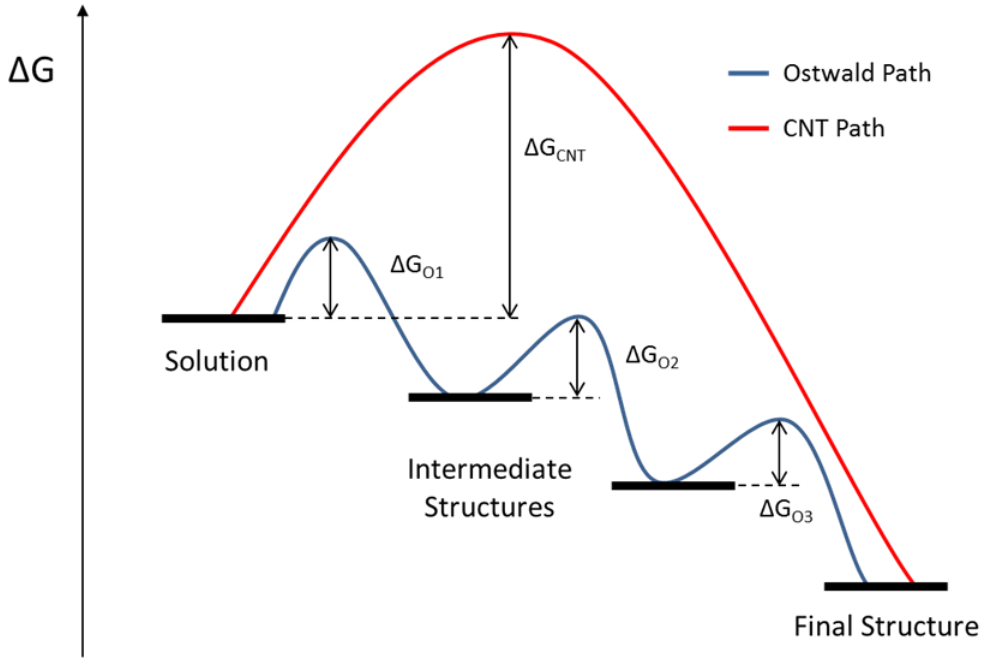

Figure 7: Free energy landscape of a multi-step Ostwald nucleation and growth pathway vs. a direct CNT ion-by-ion pathway. Reproduced from ref.[41]

The intermediate structures that form between the initial solution and final crystal product could be simply other solid polymorphs, or they could be amorphous solids or hydrated forms.[42] Additionally, the mechanism by which each transformation is made could be by the dissolution of one form and the re-precipitation of the next, by a solid-state transformation, or by a combination of the two.[43] For instance, Kim *et al*. frequently observed the nucleation of rhombohedral calcite ($CaCO_3$) crystals on the surface of amorphous calcium carbonate (ACC) spheres, which were subsequently depleted by continued crystal growth.[37] Here, the authors suggested that partial dissolution of the ACC led to the nucleation of calcite at the ACC-solution interface.

The dissolution-reprecipitation-based growth of each structure in a multistep pathway – and indeed primary nucleation itself – could be through simple ion-by-ion growth, but many other non-classical routes are possible. The simplest of these are so-called “two-step” models, where crystals form through the initial aggregation of solute molecules or ion complexes in solution (step 1), and these complexes subsequently arrange themselves into an ordered crystal nucleus (step 2).[44] A number of additional routes, such as those comprising liquid phase separation or oriented attachment of nanoparticles or nanocrystals, have also been proposed (Fig. 8),[1, 45] but there is recent evidence that even many of these more complex routes still fit within classical nucleation and growth theories.[46] However, further discussion of these routes or the universality of CNT is outside the scope of this thesis.

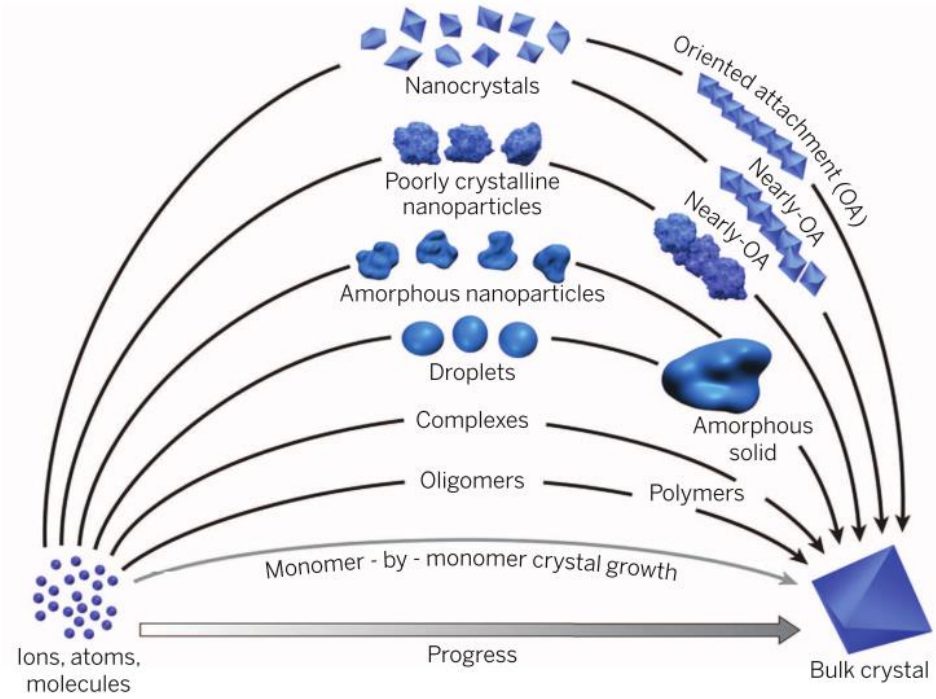

Figure 8: Some possible pathways for crystal nucleation an growth. Reproduced from ref.[1]

In summary, crystal growth can proceed by a variety of mechanisms, from direct ion-by-ion growth of a final crystal product to a multistep pathway containing multiple solid forms each produced through traditionally non-classical growth mechanisms. Indeed, it is for these reasons that such a wide variety of crystal morphologies and structures exist, and it is a major part of the motivation for studying crystallization processes. The myriad of possible synthesis pathways enable the creation of unique materials, but the selection, control, and observation of such pathways require precise experimental methods and high resolution analytical techniques. The next section will cover some of the previous work done in the crystal growth & design community to begin directing crystallization processes.

1.1.3 Crystallization in Confinement

One of the key focuses of crystallization research over the past several decades has been in replicating biological control over crystal nucleation and growth in the laboratory.[40, 47, 48] Such capability would enable materials chemists to synthesize crystals with desired morphologies and properties – all at energy efficient and under environmentally friendly reaction conditions. While this goal has not yet been fully realized, there has been progress in both understanding the methods organisms use to make biominerals and in developing synthetic analogues. There are a variety of mechanisms that biology utilizes to control crystallization, including chemical control of the reaction environment,[2, 49] introduction of soluble additives that can incorporate into and modify growing crystals,[50, 51] and utilization of insoluble protein matrices that can influence nucleation and act as frameworks for growth.[52, 53] An additional mechanism is the ability of organisms to delineate a region for crystal nucleation and growth and thus confine the crystallization volume.[54, 55] The focus of this section will be on synthetic attempts to apply this type of control over crystallization, and how confinement over different length scales can affect both the crystallization process and the properties of the final product, where this is especially relevant to crystallization in droplets and small milli-, micro-, and nano-fluidic devices.

Small Closed Compartments

One of the most obvious types of confinement present in biomineralization is that of small cellular compartments, such as vesicles, which are phospholipid membrane-bound structures of tens to hundreds of nanometers in diameter.[56] Biomineralizing cells can perform mineralization entirely within vesicles or use them to transport material to secondary sites for forming larger structures.[2] An example of this can be found in magnetobacteria, which form magnetite (Fe_3O_4) nanoparticles within vesicles and then assemble them into chains used for magnetic navigation.[54] Mann *et al*. mimicked the initial magnetite growth process in synthetic vesicles of 30 nm diameter, and found that different oxides of iron formed within vesicles and in bulk solution at the same concentrations.[57] They rationalized their results by taking into account ionic transport across the membrane, and showed that the process of material selection within vesicles was diffusion-controlled. Similarly, Tester *et al*. utilized synthetic vesicles for the biomimetic synthesis of $CaCO_3$ and found isolating the reaction within 100 nm and 1 µm vesicles resulted in the stabilization of ACC nanoparticles.[58] The authors suggested that crystallization of the ACC was inhibited due to the small size of the particles, which they estimated to be at most 1/3 the size of the vesicle.

Open Pores and Porous Networks

There are also confinement strategies more complicated than using single compartment-containing molecules, where complex extracellular structures can be used to provide confinement of varying geometry, over varying length scales.[2] The primary example of this is human bone, which contains – among other proteins – collagen filaments and fibrils that are assembled hierarchically over length scales varying by several orders of magnitude. The resulting structures contain various gaps and channels that can direct mineralization.[2, 53, 59] This type of confinement is extremely difficult to duplicate in the laboratory, and currently there are no synthetic tools which directly mimic such a process. However, there have been a variety of studies on simpler confined systems that can be more readily implemented in the lab.

Nanoporous membranes and networks enable the controlled study of varying degrees of confinement. A great deal of work has explored polycarbonate track-etch membranes that contain an array of high aspect ratio pores, where these are available in diameters ranging from tens to thousands of nanometers.[60] Loste *et al*. studied the formation of ACC in such membranes of 10 µm thickness with pores of 3 µm diameter.[61] At low temperatures, they found that ACC particles could be stabilized long enough to assemble together to form continuous rods which took the shape of the pore. In a subsequent work,[62] the authors studied the same system in a wider range of pore sizes (down to 0.2 µm) and found that the ACC rods could be transformed into single crystals of calcite that retained their cylindrical morphology. Crucially, this was only possible when ACC was able to completely fill the pores before the onset of crystallization, where smaller pores were shown to support this process over a wider range of conditions. Kim *et al*. precipitated ACC in even smaller pores (down to 50-100 nm) with the help of polymer additives which aided in complete pore infiltration.[63] Using this method they were able to generate long cylindrical calcite crystals with aspect ratios up to 100 (Fig. 9).

In contrast to structures with isolated pores, other researchers have utilized interconnected porous networks to confine crystallization. One of the traditional ways to do this is through the use of gels, which act as transparent diffusive barriers with tunable mesh/pore sizing.[40, 64] For example, Li and Estroff studied $CaCO_3$ crystallization in agarose hydrogels resting on carboxylate-functionalized SAM substrates.[65] Nucleation was shown to occur on the SAM surface from the (012) plane and growth continued as CO_2 was allowed to diffuse into the Ca^{2+}-containing gel.

However, as observed in many studies,[66, 67] one potential problem with the gel method is that gel fibers can become incorporated within the crystal, which may be undesireable.[62] Thus, many researchers have also employed rigid, insoluble

confinement networks. Anduix-Canto *et al*. crystallized potassium ferrocyanide ($K_4Fe(CN)_6$) in fragments of controlled porous glasses (CPGs) with interconnected pores of 8, 48, and 362 nm diameter.[68] Interestingly, while never seen in bulk at the same conditions, anhydrous $K_4Fe(CN)_6$ was the first phase to precipitate in all three CPG sizes. Further, in the smallest pores, stabilization of precursor phases was so strong that the most thermodynamically stable form was not observed for over a month.

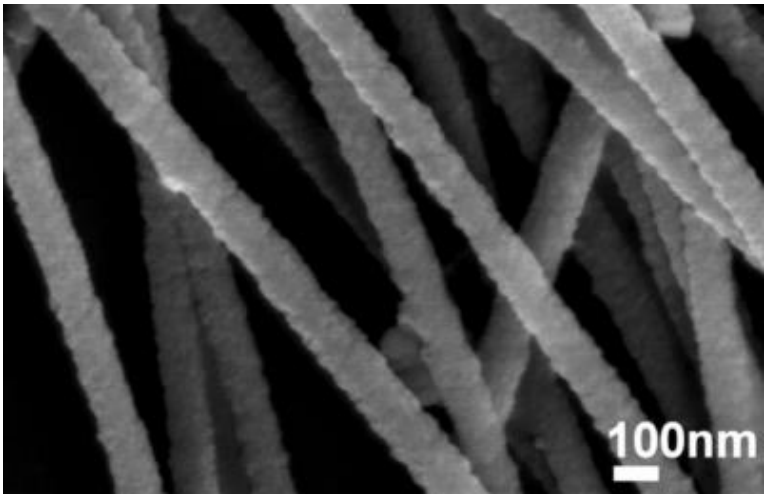

Figure 9: High aspect ratio calcite rods of ~100 nm diameter formed in track-etch membranes. Reproduced from ref.[63]

Engineered, Microfabricated, and Droplet-Based Confinement

Stephens *et al*. studied the growth of $CaCO_3$ in a "crossed-cylinder" apparatus which allowed a continuous range of surface separations to be tested simultaneously (Fig. 10a).[69] They found the effect of confinement on crystallization to extend up to surface separations of 10 µm, where above this distance normal rhombohedral calcite crystals formed and below this distance crystals exhibited increasingly flattened morphologies. At surface separations of approximately 1 µm, stabilized ACC was found and shown to crystallize if the confinement was removed. Similarly, Wang *et al*. studied $CaSO_4$ crystallization with the same apparatus and found that less stable hemihydrate ($CaSO_4 \cdot 0.5H_2O$) and amorphous phases were stabilized at separations of approximately 1 µm and 0.2 µm, respectively.[70]

In a subsequent work, Stephens *et al*. crystallized $CaCO_3$ within arrays of 4-10 µm sessile droplets on carboxylate-functionalized SAMs (Fig. 10b), where the finite solution volume halted growth at early reaction stages.[71] This enabled the observation of small, irregular tetrahedral-shaped calcite, which the authors suggested likely formed as a transient precursor to the standard rhombohedral morphology. The authors also found that the initial transformation of ACC into calcite was 2.5 to 15-fold slower on SAMs exposed to the droplets than SAMs exposed to bulk solution. In another study, Wolf *et al*. precipitated $CaCO_3$ in acoustically levitated droplets of 0.2-2 mm diameter.[72]

Supersaturation was induced slowly through droplet evaporation, and in combination with the low-convection environment, this resulted in the apparent formation of a dense liquid $CaCO_3$ precursor to ACC. In recent years, microfluidic devices have been exploited to provide similar confinement strategies, and these will be discussed in Section 1.2.3.

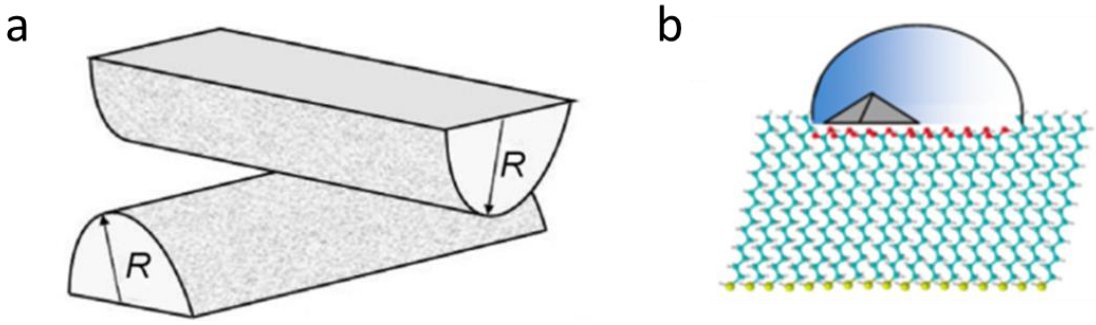

Figure 10: (a) Crossed-cylinder apparatus which enables simultaneous testing of known degrees of confinement based on the position from the contact point and cylinder radius, *R*. Reproduced from ref.[69] (b) Example of crystal growth in a picoliter droplet isolated on a hydrophilic SAM from Stephens *et al*.[71] Reproduced from ref.[71]

An important implication of the above works is that confinement in the micron range – not only confinement on the same length scale of the critical nucleus – can affect the crystallization process. Many theories for why this is the case have been proposed, including confinement limiting contact between the crystal surface and solution,[69] the elimination of convection,[37] and decreasing supersaturation profiles due to the finite reservoir of reactants.[73] However, exactly how confinement affects crystallization – at all length scales – is still poorly understood.[60] Nevertheless, it is clear that confinement over both nanometer and micrometer length scales can control the structure and morphology of crystals. It can also drastically alter the crystallization process by slowing down the rate of crystallization and stabilizing amorphous and other phases which might be short-lived or even completely absent in bulk syntheses. More detailed accounts of research into crystallization in confinement and other types of biomimetic control can be obtained from reviews by Meldrum and Cölfen,[40] Arakaki *et al*.,[74] and many others.[48, 75, 76]

1.1.4 Recent Advances in Analytical Techniques for Studying Crystallization

A critical component of controlling crystallization is in observing, and therefore, understanding the effect of processing parameters on the crystallization pathway. It is difficult to control something that cannot be observed and is not understood. Since the purpose of this thesis is to describe a new technique for probing crystal nucleation and

growth, the current state-of-the-art in analytical techniques for studying crystallization is now considered. The use of the word, “crystallization,” is important here, as opposed to the word, “crystal.” There are many techniques for studying static crystals *ex situ*, but this brief review will cover the highest resolution techniques which enable *in situ* study of the dynamic process of crystallization itself.

Atomic Force Microscopy (AFM)

Atomic force microscopy (AFM) is a scanning probe microscopy technique which allows the 3D imaging of surfaces with angstrom lateral resolution and sub-angstrom vertical resolution and the precise measurement of small forces exerted on the probe or tip.[77] It has been used to study crystallization processes for almost three decades,[78] but recent years have seen improvements in scan speed, resolution, and tip functionality.[79, 80] Many early AFM experiments with crystallization looked at slow surface dissolution and growth processes (over minutes)[78] and dried *ex situ* samples.[81] Due to the speed of crystal growth, which can occur at well over 100 molecular layers per second, *in situ* AFM imaging is challenging at high supersaturations.[81] However, utilizing low to moderate supersaturations and modern high speed AFMs enables many nucleation and growth processes to be observed. A typical AFM setup for studying crystallization *in situ* is shown in Figure 11. Here, the cantilever probe is situated within a sealed liquid cell, where reagents can be constantly replenished with the aid of external syringe pumps.

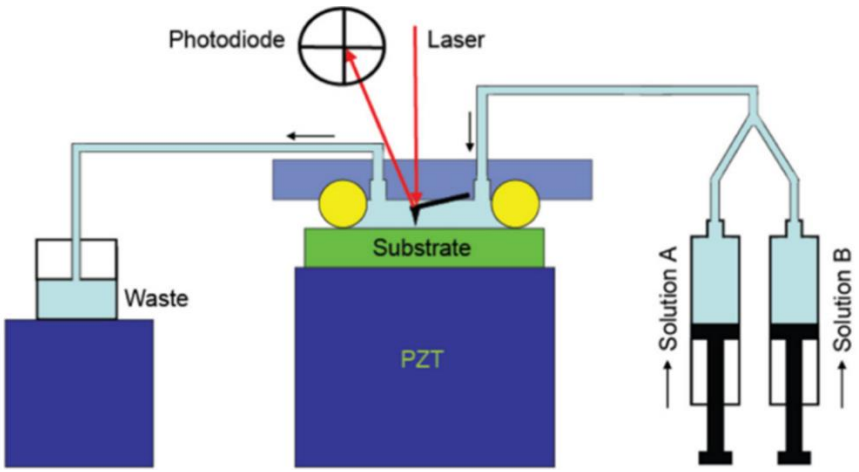

Figure 11: A liquid-cell AFM setup. New reactants are continuously flowed over the substrate to allow crystal overgrowth. Reproduced from ref.[79]

Recently, AFM studies have provided rich qualitative and quantitative information regarding a number of crystallization processes. One area of insight has been in obtaining nucleation rates on particular surfaces. For instance, Hamm *et al*. studied the nucleation of calcite on planar substrates with well-defined SAM surface chemistries (carboxyl, thiol, phosphate, and hydroxyl).[82] Their results directly confirmed CNT

predictions that nucleation rates should be substrate-specific, where surfaces with higher interfacial energy resulted in higher nucleation rates in order to minimize the free energy of the system.

Similarly, Habraken *et al.* studied the growth of calcium phosphate (CaP) on collagen surfaces – an important model for bone mineralization.[83] They recorded the heterogenous nucleation rate of CaP at supersaturations above and below the solubility of amorphous calcium phosphate (ACP) and found that the rates fit within CNT predictions in spite of the seemingly non-classical mechanisms observed. Namely, when ACP was undersaturated, apatite was the first and only phase to nucleate on the collagen. When ACP was slightly supersaturated, ACP nucleated first and then transformed into octacalcium phosphate (OCP) and finally apatite (Fig. 12), though such as process should be energetically unfavorable under CNT. However, cryogenic transmission electron microscopy (Cryo-TEM, to be discussed later in this section) revealed that, in both cases, nucleation was preceded by the formation of calcium triphosphate complexes in solution. While these pathways are not traditionally classical, the authors found that the presence of the calcium triphosphate complexes in solution lowered the energy barrier to ACP nucleation, and actually allowed for its formation within the framework of classical theory. More examples of AFM as a tool for studying crystallization can be found in the review by De Yoreo *et al*.[84]

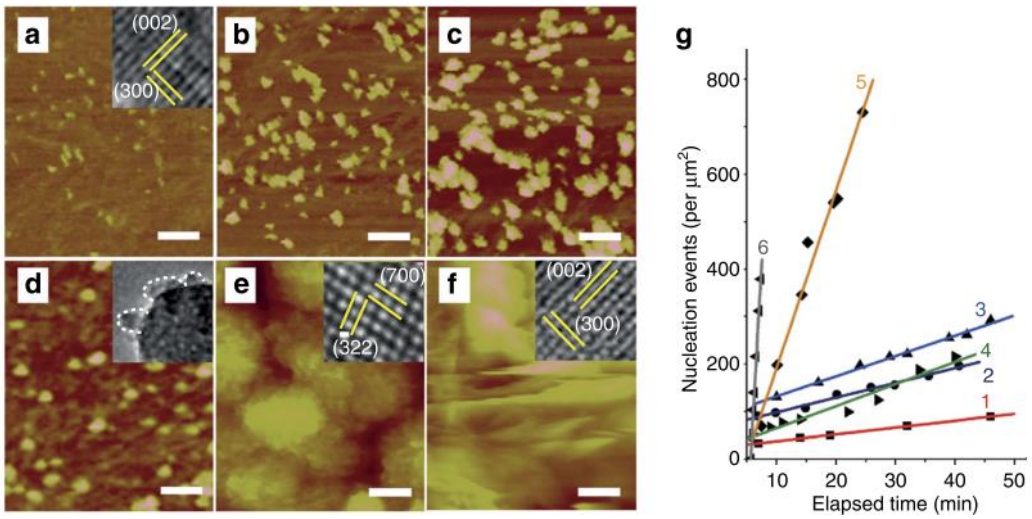

Figure 12: AFM analysis of CaP growth on collagen substrates. (a-c) Time-lapse images of the direct growth of apatite below the solubility of ACP. (d-c) Time-lapse images of (d) the nucleation of ACP, (e) transformation of ACP to OCP, and (f) transformation of OCP to apatite above the solubility of ACP. (g) Graph of CaP nucleation rate vs. time for six cases with increasing supersaturation. In 1-3 ACP is undersaturated and in 4-6 ACP is supersaturated. All scale bars are 100 nm. Reproduced from ref.[83]

It should be noted that there are many limitations to using AFM for studying crystallization. As mentioned above, AFM is relatively slow. It is also only able to observe processes occurring on surfaces and must be coupled with other techniques to

yield any chemical or structural information.[85] An additional limitation of AFM is that physical interaction between the probe and a surface can influence the outcome of an experiment. In contact mode, the probe creates a shear force which can deform surfaces,[79] and non-contact (or more accurately, tapping mode) data is more difficult to interpret, where its collection can still influence the sample.[79, 86] However, there are many other modern techniques which have the advantage of not requiring mechanical contact with a crystal for analysis. Perhaps the most significant of these is electron microscopy.

Liquid Cell Transmission Electron Microscopy (LC-TEM)

While electron microscopy normally requires vacuum conditions, a new technique known as liquid cell transmission electron microscopy (LC-TEM) enables solutions at ambient pressures to be analyzed. Williamson *et al.* developed the first sealed liquid cell for TEM analysis in 2003.[87] This was a simple cell containing two fluidic reservoirs connected by a thin 0.5-1 µm channel between two 80 nm silicon nitride (Si_3N_4) windows, which allow transmission of the electron beam. Such LC-TEM cells permit vacuum pressure to be maintained outside while also enabling samples inside to remain hydrated. Additionally, current LC-TEM sample environments (or "holders") are available commercially and can support fluid flow motivated by external syringe pumps (Fig. 13).

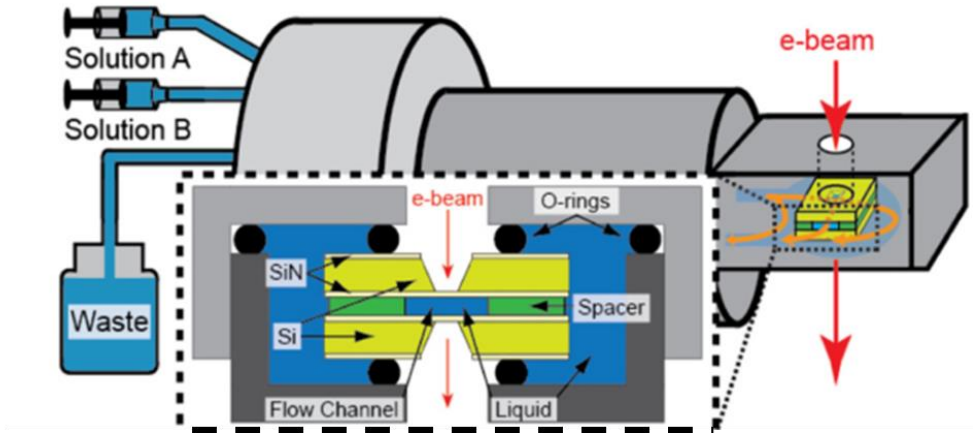

Figure 13: A liquid cell TEM setup with flow capability. Adapted from ref.[79]

Using a modern flow-enabled LC-TEM holder, Nielsen *et al*. studied the nucleation and growth of $CaCO_3$.[88] They observed that a variety of crystallization pathways to occur simultaneously. In some, ACC precipitated and transformed into either aragonite or vaterite (Fig. 14), and in others vaterite and calcite precipitated directly from solution. While it is often thought that a single pathway will dominate under particular solution conditions, their observation of many co-existing routes could imply that this is often the case, but is overlooked with lower resolution methods. However, they noted that they

could cause, delay, or prevent the formation of ACC by varying the electron beam intensity.

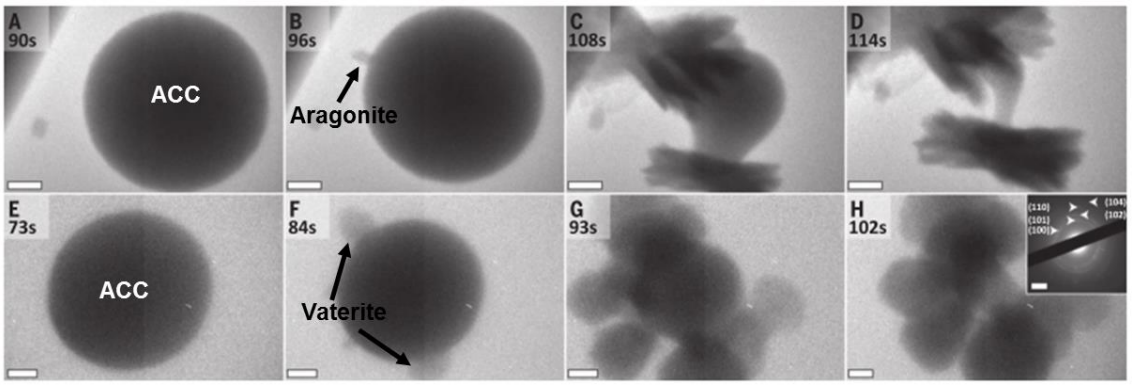

Figure 14: Liquid cell TEM study of $CaCO_3$ nucleation with polystyrene sulfonate (PSS). (a-d) Nucleation and growth of aragonite at the expense of ACC. (e-h) Nucleation and growth of vaterite at the expense of ACC. Inset: electron diffraction pattern confirming vaterite structure. Scale bars are 500 nm in (a-h) and 2 nm^{-1} in the inset. Adapted from ref.[88]

While not requiring mechanical contact like AFM, this highlights the fact that LC-TEM can still influence the sample. One of the major limitations of LC-TEM is the high electron dose required for high quality imaging, which can damage crystal structures and cause drastic changes in solution pH and composition.[89, 90] Such knowledge must be taken into account when designing LC-TEM experiments and interpreting any collected data. In fact, many studies have attempted to utilize beam effects for their advantage by investigating beam-induced nucleation processes.[85] However, unless such information is desired, experiments require extreme care to mitigate the effects of beam damage.

Cryogenic Transmission Electron Microscopy (Cryo-TEM)

Another important TEM technique, which does not encounter radiation damage issues as rapidly as LC-TEM, is cryogenic transmission electron microscopy (Cryo-TEM).[85] While not truly *in situ*, Cryo-TEM deserves mention since it is an important technique for studying crystallization. Time-resolution in Cryo-TEM is obtained by rapidly freezing thin liquid samples at particular reaction time points for subsequent static analysis (Fig. 15), which can consist of 2D imaging, selected area electron diffraction (SAED), energy-dispersive X-ray spectroscopy (EDX), and even 3D electron tomography (Cryo-ET).[85] Importantly, when done correctly, this type of “quenching” vitrifies the crystals and solution together in whatever state they are in, and does not include the washing and drying steps that are a part of sample preparation for conventional *ex situ* techniques.[91] Thus, Cryo-TEM enables quasi-time-resolved morphological, chemical, and structure characterization of materials synthesis.

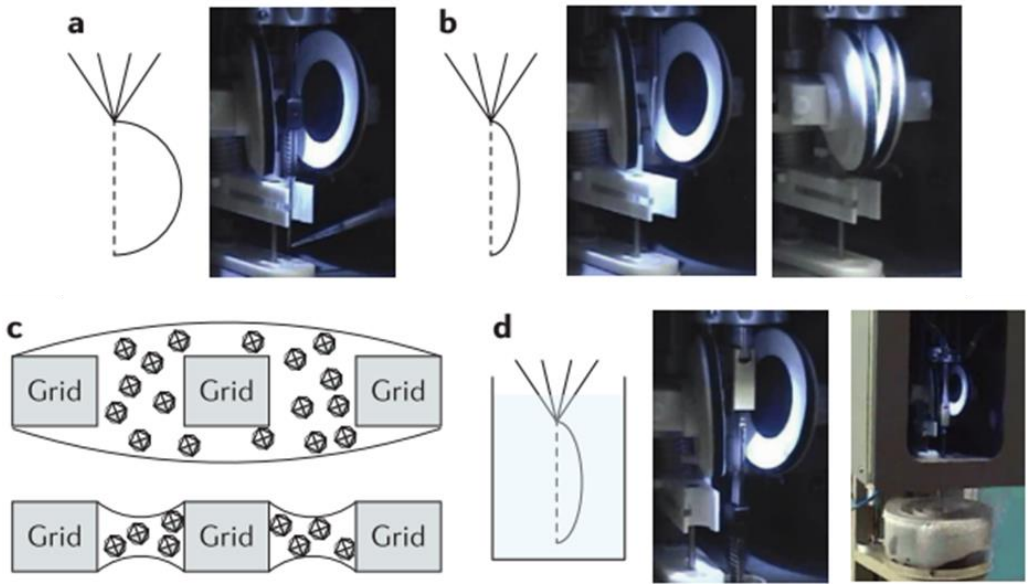

Figure 15: Sample preparation procedure for Cryo-TEM. The left images display a sketch of each step and the right images are photographs of the automated vitrification setup. (a) A drop of crystallizing solution is placed on a carbon TEM grip mounted on a robotic plunging arm. (b) Filter paper is automatically applied to the TEM grid to remove excess solution (c) which forms into a thin ~100 nm film. (d) The plunger vitrifies the solution in liquid ethane (-183 °C). Reproduced from ref.[85]

Several recent studies have made use of Cryo-TEM for analyzing the early stages of crystallization processes. A great example of the ability of this method for comprehensive analysis comes from Pouget *et al*., who studied the formation of $CaCO_3$ on steric acid monolayers.[92] They followed the crystallization pathway from the assembly of pre-nucleation clusters into ACC to the nucleation and growth of vaterite single crystals using a combination of imaging, SAED, and Cryo-ET (Fig. 16). Similarly, Van Driessche *et al*. tracked the crystallization of the protein, glucose isomerase, in the presence of varying concentrations of the precipitants, ammonium sulfate (AS) and polyethylene glycol (PEG).[93] They found that a variety of structures including single crystals, ordered nanorods, disordered aggregates, and gels could be formed through different pathways based on the relative concentration of each precipitant. Further information on both Cryo- and LC-TEM analysis of crystallization processes can be found in the recent review by De Yoreo and Sommerdijk.[85]

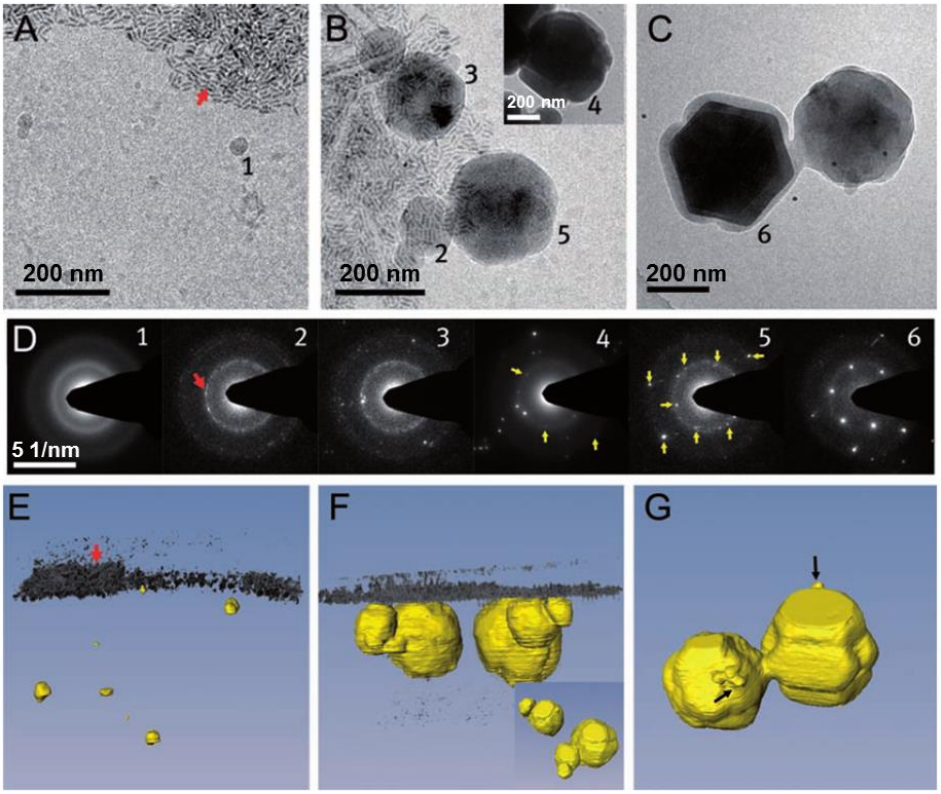

Figure 16: Cryo-TEM study of $CaCO_3$ formation on steric acid. (a-c) Time-resolved 2D images of the crystallization pathway. (d) SAED patterns corresponding to structures in (a-c). (e-g) 3D tomograms of areas corresponding to (a-c). Adapted from ref.[92]

Summary

In situ electron microscopy and atomic force microscopy have enabled a variety of new research into crystallization from solution, allowing many once only theoretical processes to be experimentally investigated and visualized for the first time. These results have, at times, reinforced or reconciled long-standing hypotheses,[46, 82, 83] and at others, suggested the possibility of new nucleation, growth, and dissolution mechanisms.[94-96] It is important to note that there are also many X-ray based techniques that have contributed to these efforts, and these will be covered in more depth in Section 1.3. However, first, let us take a deeper look into physics of the solutions and flows from which these materials are produced.

1.2 Droplet Microfluidics

One of the most important aspects of any branch of the physical or life sciences is that of scale – and this is no less true for fluid mechanics. The length scale indicates which forces must be considered and which can be neglected when seeking to accurately describe heat and mass transport within a target volume. The purpose of microfluidics research and technology is to understand and utilize the physics of flows

constrained to micrometer-sized dimensions, which can be useful for a variety of applications in synthesis and detection. This section will cover some of the background and theory of microfluidics, with a special focus on so-called “droplet” microfluidics and its usage for studying and growing crystals.

1.2.1 Microfluidics Background

Motivation and Early History

Since the development of the transistor at Bell Laboratories in the late 1940s,[97] humans have increased their mastery of electromagnetism at an unprecedented rate. As correctly predicted by Moore’s Law, the number of transistors that could fit on an integrated circuit has doubled every two years.[98] This has led to dramatic improvements in the performance of electronic devices, which are being made ever faster, smaller, and more powerful. *Wouldn’t it be nice* to exert that kind of control over other physical phenomena? This has been the exact goal of the microfluidics community over the past three decades.[99, 100] Since so much of chemistry, biology, and medicine happens in solution, constructing tools which allow the precise manipulation of fluids at small scales has the potential to accelerate and enhance synthesis, detection, and diagnostic processes.

Indeed, it was actually the microelectronics industry that provided the initial technical ability to begin fabricating what we now call “microfluidic devices” in the early 1990s. This was to fill the need for more sensitive and higher throughput analysis required for new genome sequencing and other bioanalytical technologies.[99] Early devices, such as those of Harrison *et al*., were fabricated out of glass or silicon via wet etching processes similar to those used in the fabrication of integrated circuits.[101] While originally these types of devices were used for biological separation, detection, and amplification applications, such as capillary electrophoresis and polymerase chain reaction (PCR),[99, 102] the focus of microfluidics began to shift to developing Micro Total Analysis Systems (µTAS) for a wider range of chemical applications.[103]

Soft Lithography of PDMS

The expansion of microfluidics outside of biotechnology was also aided by the development of soft lithography, which enabled more accessible fabrication and prototyping of microfluidic devices using soft elastomers such as polydimethylsiloxane (PDMS).[104, 105] The first step in fabricating a PDMS device is building a mold, where this is typically achieved through patterning a photoresist layer with UV radiation. Once a mold bearing the desired channel design is built, a liquid PDMS mixture containing a silicone base and a curing agent is poured in and allowed to cure with time and temperature. By creating molds with an array of several independent device patterns, a

few molding rounds can produce a large number of devices, which are easily assembled by exposing the cured PDMS pieces to a radio frequency plasma and bonding it with either a blank PDMS slab or a glass slide.[105] With channel dimensions in the range of tens to hundreds of micrometers, these devices typically consist of one or more fluid inlets, sections for mixing, merging, or other flow operations, a section for analysis, and one or more outlets (Fig. 17).

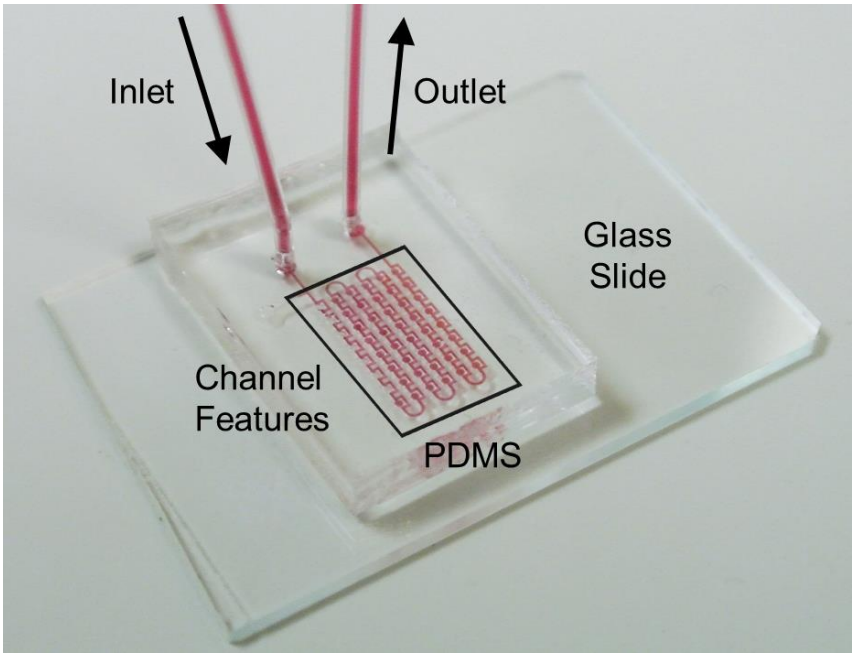

Figure 17: PDMS microfluidic device used by Kim *et al*.[37] filled with red dye for channel visualization. Photograph taken by the author.

While it will continue to be a popular and important material for device fabrication for years to come, there are some technical issues associated with the use of PDMS. Its optical transparency makes it a good material for optical microscopy, but it does not accommodate all types of analysis, e.g. X-ray scattering.[106] PDMS is also gas permeable, which is good for culturing living cells, but can lead to unwanted solvent evaporation in other contexts.[107, 108] The material also contains a large amount of uncured monomers that can leech out into solution[109] and swells in the presence of non-polar organic solvents.[105, 110] It is also not mechanically rigid[106] and lacks standardized world-to-chip connection.[111] For these reasons, other materials such as glass and rigid engineered plastics have been sought for more demanding scientific and industrial applications.[111-113] One area where this is true is in emulsion generation. Single droplets or emulsions can be generated fairly easily in PDMS devices, but double or multiple emulsions are much more difficult to obtain due to the need for strictly controlled surface chemistries.[111]

Emulsions and Droplet Microfluidics

An emulsion is formed when one fluid phase is dispersed in a second fluid phase with which it is immiscible, e.g. droplets of oil in water. These types of multiphase fluid systems are useful for a variety of industrial and commercial applications including food additives, cosmetics, and drug encapsulation and delivery[114-116] and can also be employed as a valuable scientific tool. As such, a subset of Microfluidics, called Droplet Microfluidics, is dedicated to the controlled generation and manipulation of individual emulsions or droplets within microfluidic devices.[117] Droplet microfluidic devices can be used for encapsulating single cells or biochemical reactions,[118-120] sorting and separating individual analytes/samples,[121-123] and controlled syntheses.[124-126] However, before droplets can be used to perform such functions, they must be controllably and reliably generated.

The standard large scale industrial method for producing emulsions is using a stirred vessel or high pressure nozzle to homogenize a mixture of two or more fluids.[116, 127] These methods are good for producing large volumes of emulsions, but result in polydisperse sizing which is not ideal for precise scientific applications.[128] Microfluidic devices are able to generate droplets with much more consistent sizing, where most modern devices use one of two methods: T-junction or flow focusing. The simplest of these, the T-junction, was first implemented by Thorsen *et al*. in 2001.[129] In this method, the phase to be dispersed is introduced perpendicularly into a channel containing an immiscible flow. As the dispersed phase enters the channel, a combination of pressure and shear force from the immiscible fluid causes the dispersed phase to break up into regularly sized droplets (Fig. 18a).[130]

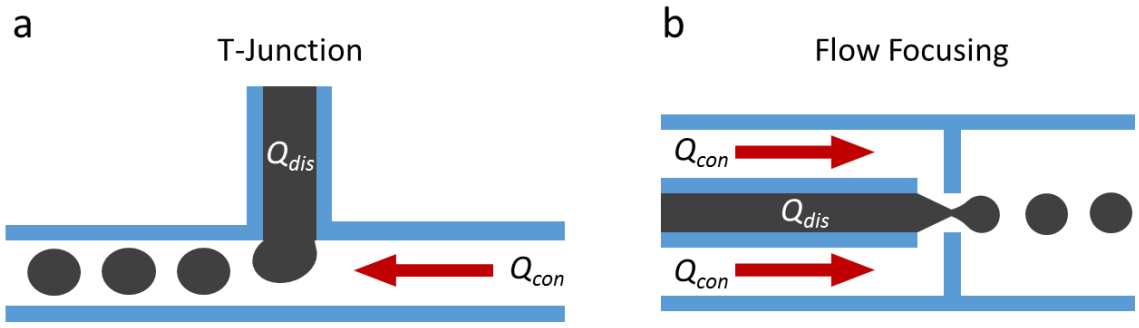

Figure 18: Diagrams of basic (a) T-junction and (b) Flow Focusing droplet generators. Q_{con} and Q_{dis} are the volumetric flow rates (m^3/s) of the continuous and dispersed phases, respectively. Adapted from ref.[41]

Shortly after the creation of the T-junction, Anna *et al*. introduced the flow focusing method of droplet generation.[131] In contrast to the T-junction, the dispersed phase and the continuous phase are introduced in a co-flowing geometry, where the continuous phase acts as a sheath flow around the dispersed phase. The two flows are directed

into a flow constriction which results in a local velocity increase, the elongation of the dispersed flow by the continuous flow, and ultimately, the break-up of the inner flow into droplets (Fig. 18b). Other types of devices, such as those for creating double, triple, or larger emulsion structures, typically use some variant of the above methods, e.g. two T-junctions in series[132] or a flow focusing junction with multiple layers of sheath flows.[133] These devices require careful patterning of the wettability of internal device surfaces to ensure smooth and consistent emulsification.[111]

Since its beginnings in the early 1990s, microfluidics technology has progressed in functionality and been adapted by a wider range of researchers. First restricted to specialist labs with only technical applications in mind, advances in device materials, construction, and reliability have opened up the technology to solving real scientific problems.[134-136] This has been achieved through a variety of ways, for example, with simple well-engineered devices that provide quick analytical results,[134] but also through more complex droplet microfluidic devices which provide completely new functionality not available with traditional laboratory equipment.[100] In order to understand what makes microfluidics so unique and attractive, let us delve into the physics of fluids and droplets at these small length scales.

1.2.2 Important Physics and Dimensionless Parameters

Laminar and Turbulent Flows

One of the first things that would be mentioned in an entry level fluid mechanics lecture is that, generally speaking, there are two types of flows: laminar and turbulent. Laminar flows are smooth, where streamlines flow parallel to one another in layered “lamina”. Turbulent flows are chaotic, where fluid paths meander in three dimensions due to random fluctuations in velocity.[137] This has a profound impact on mixing within flows. In laminar flows, mass transport perpendicular to the flow direction occurs only via diffusion, whereas in turbulent flows, transport is aided by chaotic changes in the velocity profile both parallel and perpendicular to the direction of the mean velocity, $\bar{u}$ (Fig. 19).

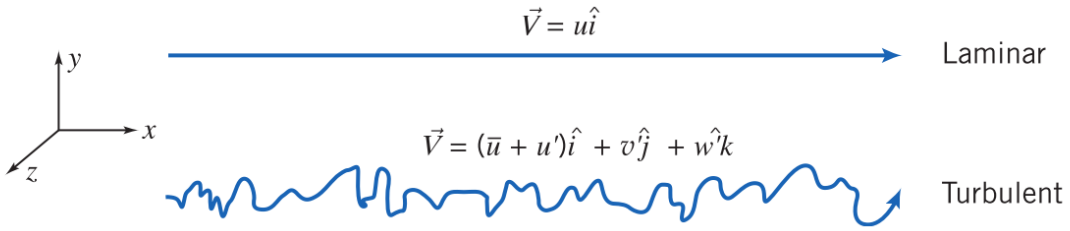

Figure 19: Laminar vs. turbulent flow particle pathlines, where *u’*, *v’*, and *w’* are terms representing time-dependent velocity fluctuations in the x, y, and z directions, respectively. Reproduced from ref.[137]

Whether a fluid exhibits laminar or turbulent behavior is determined by the ratio of inertial to viscous forces experienced by the fluid. This relationship is often expressed as the dimensionless Reynolds number (*Re*):

$$Re = \frac{\text{Inertial Forces}}{\text{Viscous Forces}} = \frac{\rho V L}{\mu} \quad \textbf{(6)}$$

where ρ is the density of the fluid, *V* is the fluid velocity, *L* is the characteristic length scale (e.g. the channel diameter), and μ is the dynamic viscosity.[137] At the scale and velocity of most microfluidic flows, the values of *Re* are typically ≤10. This means almost all microfluidic flows are laminar and dominated by viscous forces, with the transition to turbulent flow not typically occurring until *Re* values reach 2000-3000 depending on the channel geometry.[138, 139]

Although streamlines remain smooth and laminar, there are still velocity gradients across microfluidic flows. Due to friction at channel walls, fluid velocity at the wall in most situations is zero; this is referred to as the no-slip boundary condition. Since the fluid is viscous, this friction or shear force at the boundary propagates into the flow, slowing it layer-by-layer until a parabolic Poiseuille velocity field develops.[137] The result is that fluid in the center of a channel will move faster than fluid at the channel walls, and that fluid elements initially locked at the same x coordinate, but which vary in y coordinate, will grow farther apart along the flow (Fig. 20a). This is known as Taylor dispersion, and becomes important when considering mixing within microfluidic devices.[107, 138]

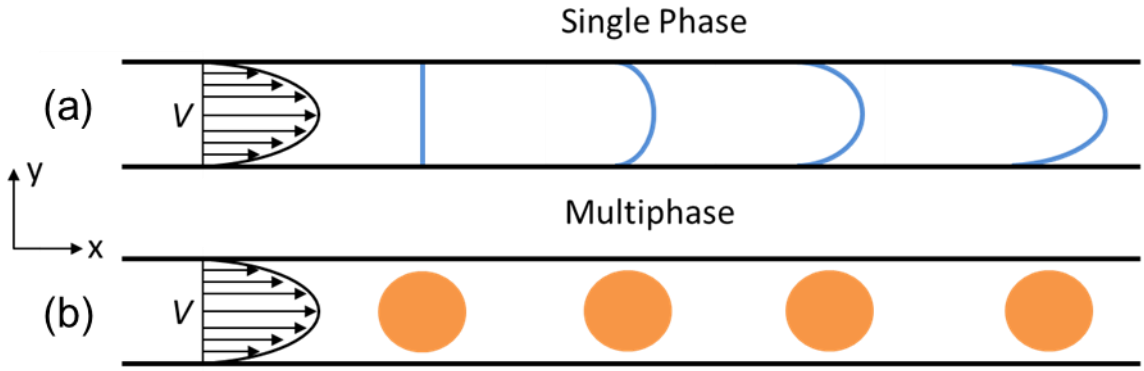

Figure 20: Illustration of mass transport due to the parabolic Poiseuille velocity profile in single phase and multiphase flow. (a) In single phase flow, fluid in the center of the channel travels faster than at the walls resulting in Taylor dispersion of the fluid element in blue. (b) In multiphase flow, fluid elements within droplets remain together in spite of any dispersion in the continuous phase. Adapted from ref.[41]

Mixing in Single-phase and Multiphase Flow

In long microchannels, Taylor dispersion can result in large concentration or residence time distributions which are not ideal in synthetic scenarios.[108] Over the

same channel length, reactions (e.g. crystallization) occurring at or near the walls of a channel will proceed for a longer time than those occurring in the center due to the difference in velocity. This can result in product inhomogeneity and also decrease the resolution of analytical measurements meant to monitor the reaction with time. To solve these and other problems with single phase flow, many have proposed the usage of multiphase or segmented flows comprising dispersed droplets travelling within a continuous fluid medium.[140-142] Since the continuous and dispersed fluids are not miscible, any solute trapped within a droplet will be confined within the droplet, provided the solute is not also soluble in the continuous phase or able to diffuse across the droplet interface (Fig. 20b).[143]

Multiphase flows can also be utilized to increase the slower rate of mixing usually found within single phase microfluidic devices. In continuous flow, the mixing of two parallel flow streams is completely reliant on diffusion, since there is no flow perpendicular to the direction of the average velocity. Depending on the width of the channel and diffusion coefficient of the material, complete diffusive mixing can take a long time. For instance, using the approximation for diffusion time (t_D):

$$\boldsymbol{t_D = \frac{x^2}{2D}} \quad \textbf{(7)}$$

where x is the mean distance travelled and D is the diffusion coefficient,[144] it takes a Ca^{2+} ion ($D \approx 0.79 \times 10^{-5}$ cm^2/s) ~6 sec to travel 100 µm and ~10 min to travel 1 mm. By slightly rearranging the above equation and accounting for the flow velocity (V), we can derive another useful dimensionless parameter, the Péclet number:

$$\boldsymbol{Pe = \frac{Vw}{D} = \frac{\text{Advection}}{\text{Diffusion}}} \quad \textbf{(8)}$$

where w is the channel width.[138] This number is useful for comparing the advective and diffusive transport rate, or the transport parallel and perpendicular to the flow direction, respectively. Practically, the *Pe* is roughly equivalent to the number of channel widths the flow would need to travel to be completely mixed,[138] e.g. a flow with a *Pe* of 100 and channel width of 100 µm would need to travel ~10,000 µm or 10 mm to be fully mixed.

Based on the needs of a particular application, diffusion time-scales of seconds and high *Pe* microfluidic flows may be sufficient, but droplets can achieve mixing more rapidly. This is because shear stress from the walls of a channel creates recirculating flow within droplets, such as that observed by Tice *et al*., who were able to achieve the mixing of an inorganic dye in under 25 ms within straight channels of 50 µm width (Fig. 21a).[145] They also showed that by varying the dispersed phase to continuous phase

volume fraction and the flow velocity they could obtain a range of mixing times. Moreover, when droplets are directed through curved microchannels they undergo chaotic advection, which compounds with the recirculating flow to enhance mixing even further. This process occurs when turns cause droplets to go through successive rounds of reorientation, stretching, and folding – similar to a baker's transformation (Fig. 21b).[146] Using this method, Song *et al*. achieved complete mixing of the same dye as in ref.[145], in approximately 2 ms.[141] Importantly, this potential for rapid mixing combined with their small surface area-to-volume ratio as compared to bulk solution means that microfluidic droplets have much greater chemical and thermal homogeneity than a traditional reaction environment (e.g. a glass beaker) or even a continuous microfluidic flow.[142]

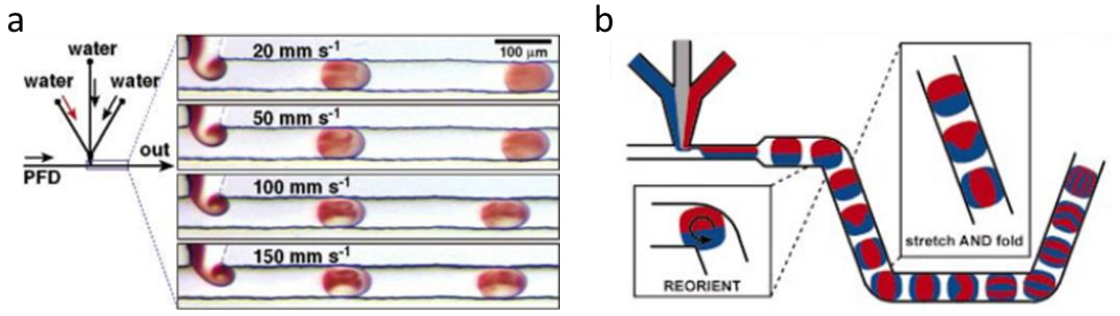

Figure 21: (a) Mixing of a red dye introduced into droplets at a T-junction at different flow velocities. Reproduced from ref.[145] (b) Illustration of mixing within droplets due to baker's transformation-like chaotic advection. Reproduced from ref.[146]

1.2.3 Droplet Microfluidics for Crystallization

Screening Crystallization Conditions

An important realization made in the 1940s and 1950s was that dividing up a single large reaction volume into a discrete number of finite elements could be a way of minimizing the effect of impurities.[147] Assuming there are x number of impurities in a volume, V, by dividing V into n separate elements where $n >> x$, one can ensure that the majority of elements or droplets are impurity-free. As such, droplet microfluidic devices can be used to create large numbers of clean, independent crystallization vessels with tunable, well-defined mixing rates as discussed above.

Since the advent of droplet microfluidics, several research groups have utilized these features to better grow and analyze crystals. An early example comes from Zheng *et al*., who used a T-junction device to screen conditions for creating protein crystals.[148] As mentioned in Section 1.1.1, a major problem in the study of structural biology is finding the right conditions for nucleating and growing large protein crystals suitable for XRD analysis. The authors used their microfluidic platform to continuously vary the flow rate ratio between their buffer and NaCl solutions to find the optimal

concentration range for the crystallization of a target protein (Fig. 22, top). Using this method, they were able to obtain crystals of a variety of proteins including thaumatin, catalase, and glucose isomerase (Fig. 22a-d).

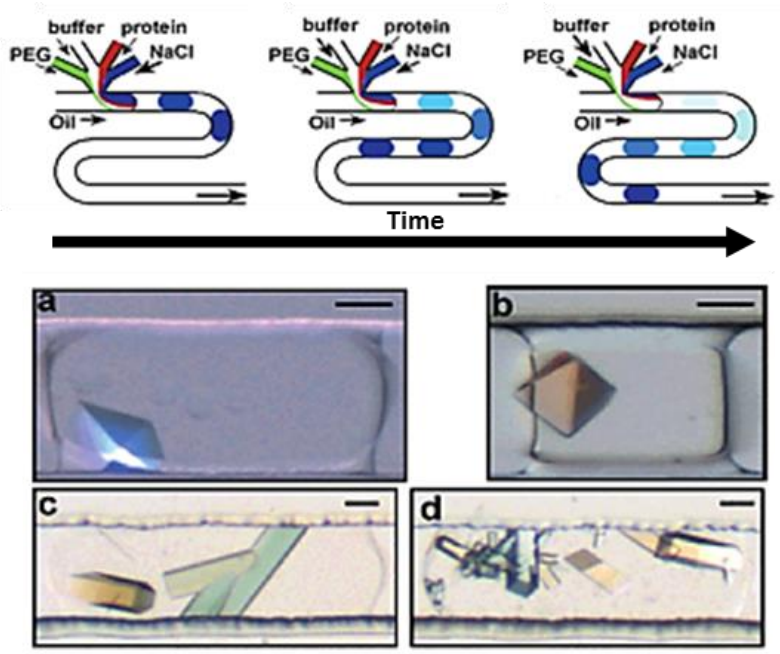

Figure 22: Illustration of the microfluidic technique of Zheng *et al*.[148] for creating a series of droplets with varying conditions for protein crystallization (top). (a-b) Examples of droplets with successful conditions containing crystals. Scale bars are 50 µm. Adapted from ref.[148]

Determining Thermodynamic and Kinetic Parameters

Such empirical studies for growing XRD-quality protein crystals have been a large focus of microfluidic crystallization work (covered more in Section 1.3.2). However many researchers have also utilized droplet devices for more quantitative study of crystal nucleation and growth processes. For instance, Laval *et al*. used a similar method to determine the solubility curve for adipic acid crystals.[149] They filled rows of microfluidic channels with droplets of varying concentration and allowed them to cool. Once all the droplets had crystallized, an elevated temperature gradient was applied across the chip, causing crystals within droplets at a concentrations and temperatures under the solubility limit to dissolve (Fig. 23a). Importantly, this was achieved with an experiment that required only 250 µL of solution and took less than 1 hr to complete. In another study, the authors precipitated potassium nitrate (KNO_3) crystals within droplets and followed their nucleation kinetics with time.[150] Subsequently, they initiated dissolution using a uniform temperature ramp across the device and observed two populations of crystals which dissolved at different temperatures (Fig. 23b). These populations were later identified by Raman spectroscopy and optical microscopy as representing two different polymorphs (Fig. 23c-d). In addition to these examples, a great deal of similar research investigating nucleation and dissolution rates and crystal

solubilities has been conducted.[151-153]

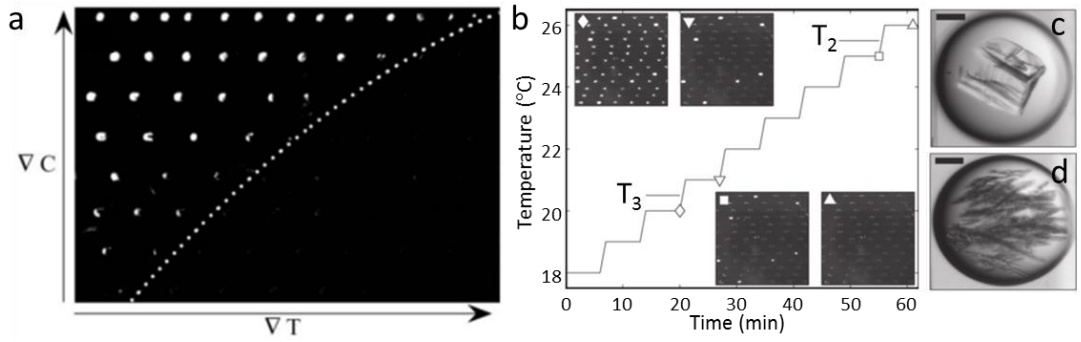

Figure 23: (a) Physical solubility diagram of Laval *et al.* (2007).[149] The white spots are crystals under polarized light. Dark regions are where crystals have dissolved. The while dotted line shows the solubility curve. (b) Temperature ramp-based dissolution curve of KNO_3 by Laval *et al*. (2008)[150] revealing the presence of two polymorphs with different solubilities: (c) Form III and (d) Form II. Scale bars are 100 µm. Adapted from ref.[149] and ref.[150]

Studying the Effects of Confinement

More recent research has sought to investigate the role of confinement on crystal nucleation and polymorphism. For example, Hammadi *et al*. performed an extensive study of protein, organic, and inorganic crystal nucleation in droplets of nL down to pL in volume.[154] Based on their results, they attributed the delayed nucleation behavior often observed in droplets to a combination of thermodynamic and kinetic effects. In nL sized droplets, the increase in induction time (i.e. the time between the application of a supersaturation and the nucleation of a crystal) was linked only to the nucleation rate, *J*, the number of crystal nuclei per unit time and volume.[155] Thus, the smaller the volume, the longer it should take to observe nucleation from a purely kinetic standpoint. However, in pL volumes they suggested there was an added thermodynamic effect inhibiting nucleation. Namely, that the size of the droplet compared to the size of critical nucleus meant that the droplet could no longer be considered an infinite reservoir of crystal monomers. Thus, a higher initial supersaturation was needed to produce a critical nucleus.

Likewise, Rodríguez-Ruiz *et al*. analyzed $CaCO_3$ phases precipitated from these same nL and pL droplets and found ikaite ($CaCO_3 \cdot 6H_2O$) and monohydrocalcite ($CaCO_3 \cdot H_2O$) – which are rarely observed at room temperature without additives.[3] Further, they did not find any evidence of the presence of ACC, which is the phase typically reported to occur at similar high supersaturations and small volumes. They rationalized their unusual results based on the mixing profile, small volume, and stoichiometry (1:1 $Ca:CO_3$ ratio), but could not fully explain the precipitation of these phases instead of ACC. Yashina *et al*. also precipitated $CaCO_3$ within droplet microfluidic devices, but at lower concentrations.[156] They found that they could

selectively control the precipitation of uniformly-sized pure calcite, pure vaterite, or a calcite/vaterite mixture by changing the $CaCO_3$ concentration within the droplets. In contrast, a continuous microfluidic reactor and bulk solution only yielded polydisperse mixtures of calcite and vaterite at the same concentrations. Similarly, while the reason for these differences was attributed to droplet confinement, the exact mechanisms of crystallization in confinement remain unknown – highlighting the need for further investigation. Additional information on the utilization of microfluidic devices for crystallization and inorganic materials synthesis can be found in reviews by Leng and Salmon,[157] Shi *et al*.,[158] Gunther and Jensen,[140] Phillips *et al*.,[159] and Abou-Hassan *et al*.[160]

Time-Resolved Analysis

A common link between all of the studies referenced above is that they use optical microscopy as their primary method of *in situ* or "on-chip" analysis. Other analyses, such as Raman spectroscopy, electron microscopy, and XRD were performed "off-chip", meaning that *in situ* analysis was limited to qualitative or statistical information (Fig. 22 and Fig. 23). However, a growing number of researchers have seen the potential of microfluidic "lab-on-a-chip" devices as tools for more in depth time-resolved analysis of crystallization and materials synthesis.[159]

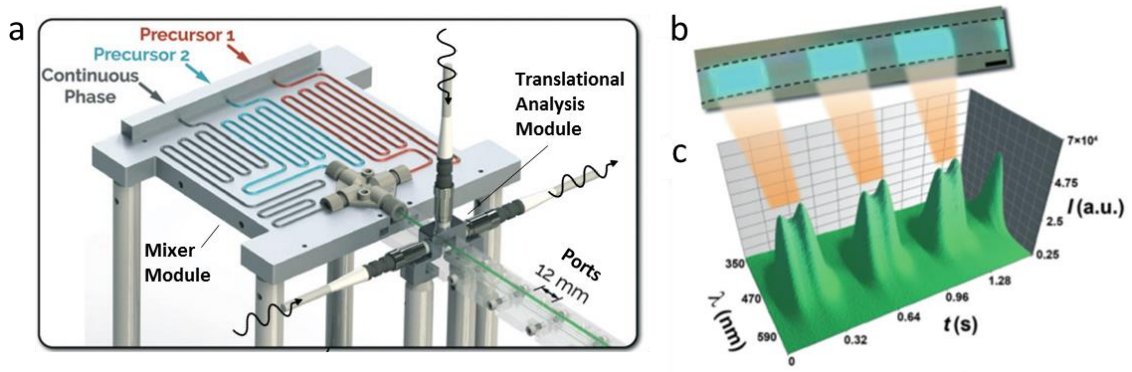

Figure 24: (a) Automated microfluidic device of Epps *et al*.[161] with a mixer/droplet generation module and a translational analysis module which can move to 20 independent sampling ports to monitor absorbance and emission. (b) Fluorescent droplets moving along the device and (c) the corresponding time-resolved emission spectra. Scale bar is 1 mm. Adapted from ref.[161]

Much of this work has focused on time-resolved absorption and emission characterization of photoluminescent nanoparticles or nanocrystals. For instance, Lignos *et al*. synthesized lead sulfide (PbS) and lead selenide (PbSe) nanoparticles and monitored their photoluminescence over different residence times and temperatures using near infrared (NIR) spectroscopy.[126] They showed the ability to carefully tune the size and emission characteristics of the nanocrystals by varying the reactor flow rate, and even used them to fabricate Schottky-type solar cells with greater

conversion efficiency than cells made with nanocrystals produced in bulk. Similarly, Epps *et al*. designed an automated microfluidic platform which enabled the characterization of perovskite nanocrystals over four orders of magnitude of residence time (100 ms – 17 min).[161] Post mixing, droplets were tracked with a translational analysis module which could be moved to different analysis ports along the flow (Fig. 24a). As droplets moved past these ports, their absorption and fluorescence could be monitored in real-time, allowing information to be collected from multiple droplets at a given residence time point (Fig. 24b-c).

The utilization of droplet microfluidics for time-resolved *in situ* analysis of crystallization processes has great potential, but is still in its infancy. Among other obstacles, the need for greater choice in the selection of analytical technique is evident. An exciting new area for growth is in on-chip XRD and other X-ray analyses, which have received some attention,[162] but have yet to be fully realized due to the challenge and expense of developing robust X-ray compatible devices. Nevertheless, such capability would be of tremendous value to materials scientists, who have used various forms of X-ray diffraction, scattering, spectroscopy, and imaging as a key form of materials characterization for decades.

1.3 Solution-State X-ray Scattering Analysis

First discovered in 1895,[163] X-rays have since been utilized for a variety of medical and engineering applications and many other forms of scientific analysis for over a century.[164] This final background section will focus on solution-state analysis facilitated by techniques based on the elastic scattering of X-rays with a sample.[165] There are a range of other important techniques based on the inelastic scattering, absorption, transmission, etc. of X-rays, but these will not be discussed here. After a brief introduction to the theory of X-ray scattering and diffraction, this section will cover scattering analysis of static and stopped solutions and then review recent advances in microfluidic and other flow-based approaches to X-ray scattering for the biological and physical sciences.

1.3.1 Introduction to X-ray Scattering and Diffraction

Background and Theory

When an X-ray beam encounters a material, individual photons interact with electrons in the sample and scatter off of them in all directions. Assuming these interactions are elastic, and neglecting any absorption or secondary scattering, the scattered X-rays will all have the same wavelength as the original incident X-rays.[165] An important property of such waves is that they can interfere with each other: when two

waves are in-phase they amplify each other through constructive interference and when they are out-of-phase they eliminate one other through deconstructive interference. Thus, X-rays scattered from adjacent atoms can interfere with each other both constructively and destructively based on their wavelength, direction, and importantly, the properties of the material by which they are scattered.[165]

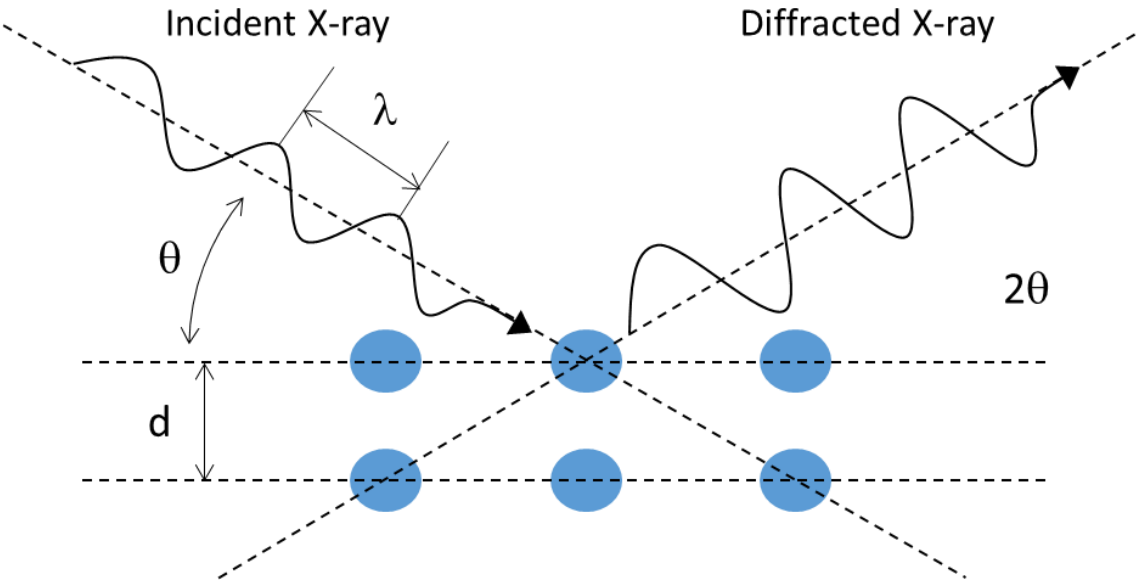

Figure 25: Diagram illustrating the diffraction of X-rays by the "diffraction grating" of a crystal lattice, where the blue circles are individual atoms. For simplicity, only a single X-ray is shown, scattering in a single direction. However, X-rays will be scattered in all directions, and it is only the constructive interference between them due to the particular d spacing that makes it appear that their scattering is so unidirectional. Adapted from ref.[41]

After Max von Laue confirmed the wave-like nature of X-rays in 1912, it was the father and son team of W. H. and W. L. Bragg that first realized that these above interactions could be used to investigate the structure of crystalline materials exposed to an X-ray beam.[166] Preliminary results showed that there were specific angles between an incident beam and particular crystal faces at which constructive interference occurred and produced a strong "reflection", and they reasoned this to be due to the periodic structure of the crystal's atomic lattice. Using this knowledge, they developed a simple geometric relationship, now known as Bragg's Law, to determine the atomic lattice spacing (d) corresponding to each reflection:

$$n\lambda = 2d \sin\theta \qquad \textbf{(9)}$$

where λ is the wavelength of the incident X-rays, θ is the angle of incidence (typically reported as 2θ for historic reasons), and n is an integer specifying the harmonic (strongest at n = 1).[167] If a material is completely amorphous, the spacing between atoms will be random, and constructive and destructive interference of scattered X-rays

will average out. However, if a material is crystalline, its lattice serves as a type of diffraction grating for the X-rays, where based on the regular spacing of the grating/lattice (d), particular angles 2θ will satisfy the Bragg condition and cause diffraction (Fig. 25).[166]

Single-Crystal X-ray Diffraction

Since this discovery, X-ray diffraction has been used to determine the structures of many thousands of materials including minerals,[168] proteins,[169] and nucleic acid.[170] The original method for achieving this, which is still popular today, is single-crystal X-ray diffraction. Here, a single crystal of a selected material is rotated on a goniometer, or other sample holder, to obtain reflections from every possible crystallographic orientation or d spacing (Fig. 26a).[171] These data can then be passed to software which fit a model to the calculated electron density distribution of the sample and produce a structure solution, where this is especially useful for complex structures such as those of large proteins.[172] Together, these methods of XRD and structure fitting are collectively known as X-ray crystallography.

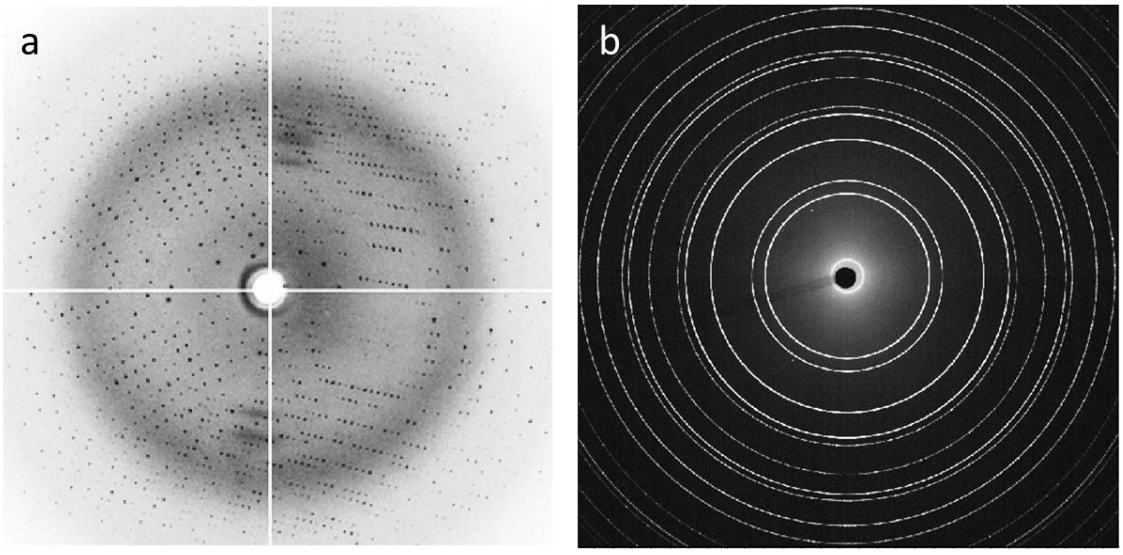

Figure 26: Examples of typical diffraction patterns obtained with 2D area detectors from either (a) single crystals or (b) ideal powders. (a) Black dots correspond to individual Bragg reflections. Reproduced from ref.[171] (b) White circles correspond to Debye-Scherrer rings resulting from an isotropic powder sample. Collected from a CeO_2 calibrant powder at Diamond beamline I11.

Powder X-ray Diffraction

Another important approach to XRD, especially in materials science, is powder X-ray diffraction (PXRD), where analysis is performed not on a single crystal, but on a powder of a selected material. This method can be preferred for materials that are difficult to grow into large single crystals or for real-world samples that often come in powder or polycrystalline form.[165] An ideal powder sample contains thousands of individual crystalline scatters oriented in random directions, i.e. without a preferred

orientation. When an X-ray beam encounters such a sample, the large number of crystals and orientations ensures that not only are reflections obtained from every d spacing, but that reflections from each d spacing are obtained at every possible azimuthal orientation perpendicular to the beam as well, producing a cone of diffraction (Fig. 27).[173] When these cones intersect with a 2D photographic film or electronic X-ray detector, they produce patterns known as Debye-Scherrer rings (Fig. 26b).[165, 174]

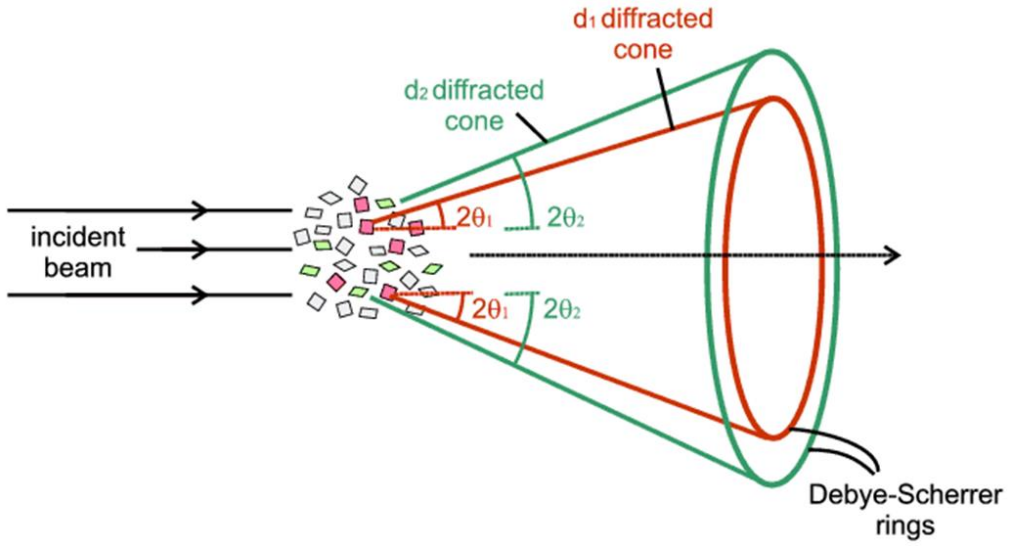

Figure 27: Illustration of the cone-like diffraction produced from powder samples. Reproduced from ref.[173]

The 2D patterns containing Debye-Scherrer rings are azimuthally integrated to obtain the 1D diffraction patterns that are normally used in all subsequent data analysis. In one-dimension, the rings appear as “peaks”, the positions of which can be used to index the corresponding lattice planes and identify the structure of the material (Fig. 28). The intensities of these peaks can also be used to determine the amount of crystalline material present or the relative amounts of different materials in multicomponent samples.[165] Also, there is a range of additional information that can be extracted from powder patterns of sufficiently high quality. Much of this comes from peak shape analysis, where as a general trend, more single crystalline materials have sharper peaks and polycrystalline and poorly crystalline materials have broader peaks.[165] Detailed analysis of peak shape through fitting routines such as those developed by Rietveld[175] and others[176] can yield quantitative information on the size and strain of individual crystal grains and can also be used to further refine the lattice parameters of a crystal.[165]

Powder XRD has some unique strengths that allow it to provide complementary information to what can be obtained from single crystal XRD,[177] which is traditionally used mainly for *ab initio* structure solution.[176] The first, and most obvious, is that since

information is acquired from a large population of crystals rather than a single crystal, the data is more representative of a sample as a whole. The second is that the high resolution in peak position and shape can be used to further refine structures previously solved by single-crystal XRD and extract additional information from a sample (as discussed above). The final strength, and the one most relevant to this thesis, is that powder or polycrystalline samples can be more easily subjected to external stimuli and measured under a range of conditions, making them better candidates for studying *in situ* processes.[177] This property has been exploited by a number of researchers for studying phenomena as diverse as phase changes in proteins,[178] high temperature gas-solid reactions,[179] micro- and nano-scopic fracturing of thin films,[180] and mineralization in simulated marine environments.[181]

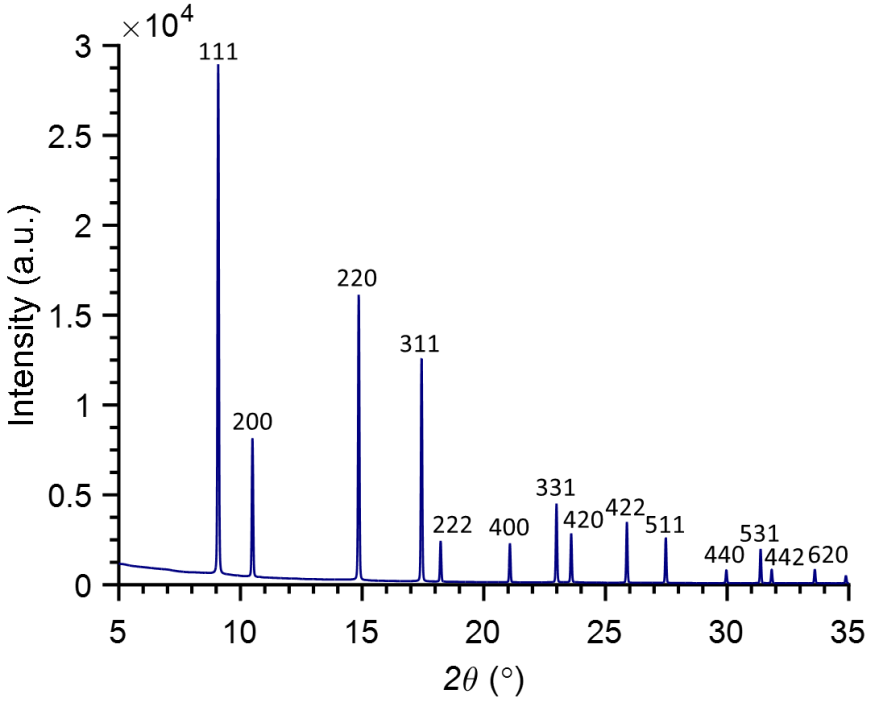

Figure 28: Integrated 1D pattern from Figure 26b. Peaks are labelled with the Miller indices of the matching reference for CeO_2 (ICSD: 61595).

Small Angle X-ray Scattering (SAXS)

While the above discussion was focused on crystalline diffraction, Bragg's law still holds true for non-crystalline materials as well. From Equation 9, it is clear that d and θ are inversely proportional, meaning that at very small angles 2θ, it is possible to probe features much larger than an atomic lattice. This type of analysis, known as Small Angle X-ray Scattering (SAXS), is then useful for crystalline and amorphous materials alike, and can be utilized to probe nanometer-scale features such as particle size, shape, and alignment.[164, 182] Similar to powder XRD, SAXS analysis is usually performed using a large number of sample particles, which can be in dry solid form or

dispersed in a liquid or gas. Consequently, SAXS benefits from the same representative averaging as PXRD and it can be used to study a huge variety of materials and processes occurring in the solid-, gas-, or solution-state.[183, 184] Further, SAXS analysis can be combined with PXRD to obtain both atomic and nanometer-scale information simultaneously, where PXRD is typically referred to as Wide Angle X-ray Scattering (WAXS) in this context (Fig. 29).[185] As will be seen below, SAXS is a popular technique for *in situ* solution-state analysis, with or without WAXS, and has received the most attention in flow-based studies to date.[186] By convention, SAXS and SAXS/WAXS data are typically plotted against the scattering vector (q) instead of 2θ, where $q = 4\pi\sin(\theta)/\lambda$.[187]

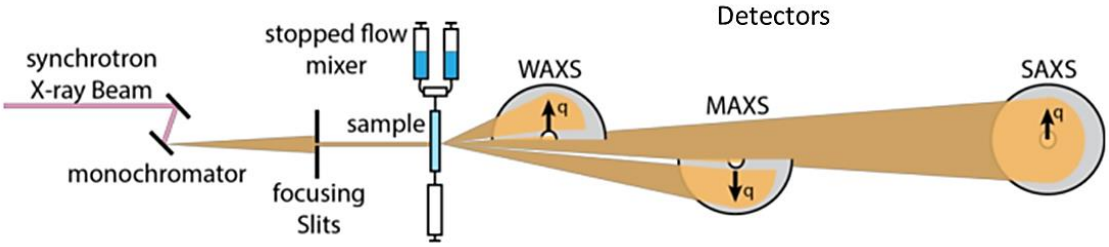

Figure 29: Typical setup for an *in situ* solution-state SAXS/WAXS experiment, where placement of the X-ray detector allows access to either SAXS, WAXS, or even medium angle X-ray scattering (MAXS). Adapted from ref.[185]

X-ray Total Scattering

Another related technique which is gaining interest for solution-state, and even flow-based studies, is X-ray total scattering, also known as atomic pair distribution function (PDF) analysis. The technique is a variant of PXRD, and finds its name due to the fact that it incorporates both crystalline Bragg scattering and so-called “diffuse” scattering from short range (i.e. local) ordering, which is not considered in standard PXRD experiments.[188] This combined data is then reduced and Fourier transformed to be analyzed as a PDF, which enables correlation between the measured scattering profile and the radial electron density distribution of a sample (Fig. 30).[189] Importantly, PDF analysis can utilize information contained in diffuse sample scattering even when crystalline Bragg peaks are weak or non-existent, making it incredibly powerful for analyzing poorly diffracting and dilute samples.[190] High incident X-ray energies, i.e. short wavelengths, are required to access a sufficient number of d spacings with the X-ray detector to provide enough data for an accurate correlation to be made, where energies are typically $\geq$ 45 keV.[191] As an added advantage, these high energy X-rays can penetrate far through even thick samples, allowing total scattering analysis to be coupled to large sample environments.[192]

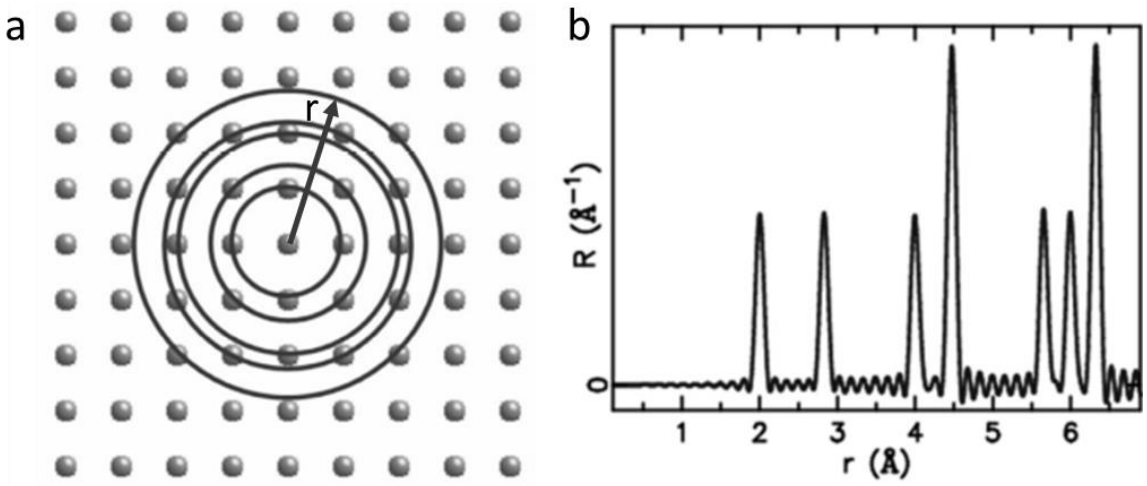

Figure 30: Example of information that can be obtained by PDF analysis of scattering data. (a) Radial distances from an arbitrary atom of a structure are indicated by circles which correspond to peaks on the (b) calculated radial distribution function (R) plot. Adapted from ref.[189]

Synchrotron Radiation Facilities

While most universities are equipped with laboratory X-ray diffractometers for single-crystal and powder XRD, these systems do not typically provide suitable photon flux (ph/s) or have sensitive enough hardware to perform high-resolution *in situ* analysis. Therefore, the majority of time-resolved and solution-based studies are performed at specialized national and international synchrotron radiation facilities.[193, 194] These facilities are based on particle accelerators that produce X-rays owing to a unique feature of sub-atomic particles, which causes them to release broad-spectrum electromagnetic radiation (including X-rays) when they are forced to change direction at relativistic speeds.[195] X-rays obtained in this way have a number of superior properties to those generated by the X-ray tubes in laboratory diffractometers, including much higher flux.[196, 197] This high flux, combined with the state-of-the-art X-ray optics and detectors available at synchrotrons makes them much better suited for time-resolved experiments.[198]

Each synchrotron comprises a number of independent end-stations, called “beamlines”, which obtain their own source of X-rays from the common electron or positron “storage ring”.[195] These beamlines are typically dedicated to a particular type of analysis (e.g. PXRD, single-crystal XRD, SAXS/WAXS), and have different hardware specific to their technique requirements and research focus.[181, 199, 200] A detailed discussion of the specific beamlines utilized in this project can be found in Section 2.2, and additional information on the merits of synchrotrons versus laboratory diffractometers for *in situ* analysis is included in Chapter 5.

Window Material Selection

Traditionally, X-ray analysis is performed with crystals resting on a flat plate or contained within thin-walled (~10 µm) glass capillaries (borosilicate or quartz) to prevent beam attenuation and minimize the effects of background scattering.[200] Therefore, when designing any type of *in situ* X-ray sample environment, one must select a suitable material for constructing the device. As a general rule, sample environments should be made as thin as possible, or at least comprise thin window sections where a portion of the sample volume can be analyzed. Of particular importance for microfluidic devices is that the popular material, PDMS, produces high background X-ray scattering, and is not ideal for fabricating X-ray sample environments unless used in very thin sections (<20 µm).[201] For this reason researchers have investigated a number of different materials as X-ray windows including, cyclo-olefin-copolymer (COC),[106, 202] poly(methyl methacrylate) (PMMA),[106] polystyrene (PS),[203, 204] silicon nitride,[205] silicon,[206, 207] and graphene.[208] Quite possibly the most popular material in such studies has been polyimide (sold as Kapton® HN by 3M), where it has been used for constructing a number of microfluidic and more general X-ray sample environments.[179, 209-211] Kapton is often the material of choice because of its high mechanical, thermal, and chemical resistance, and its added resistance and near-transparency to X-rays.[212] More recently, NOA-81 UV-curable adhesive (Norland) has gained popularity for its moldability and lower SAXS background as compared to Kapton,[213, 214] however this material struggles with radiation damage.[212] Ultimately, selecting the right window material and thickness for the a particular application or sample environment requires careful consideration of the available options. Particular attention should be paid to the resulting device rigidity, ease of manufacturing/assembly, background scattering, and overall cost, where there are often trade-offs between these properties.

1.3.2 Stopped-Flow and Static Analysis

Conventional Stopped-Flow

Solution-state XRD and SAXS/WAXS studies are often facilitated by a technique known as stopped-flow analysis. As its name suggests, this technique relies on an initial flow to mix reagents or introduce crystals into the beam path, before quickly stopping the flow and acquiring data.[215] The most common method for stopped-flow analysis utilizes systems marketed by the company, BioLogic (Fig. 31a).[216] These devices usually consist of two syringes that are linked to a glass capillary by a narrow mixer piece. At a designated time, the samples/reagents contained within the syringes are rapidly dosed into the capillary, where they are allowed to react under consecutive

X-ray exposures (Fig. 31b).[215] Mixing time-scales down to ~200-1000 µs can be achieved depending on the model of BioLogic system, where the time-resolution of subsequent of X-ray analysis is based on the capabilities of a particular beamline (e.g. detector speed, source flux) and the characteristics of the sample (e.g. density, concentration).[193] Depending on the scattering intensity of the sample and available flux, longer exposures might be required to enable detection, limiting analysis to concentrations that are detectable at the needed time-resolution.

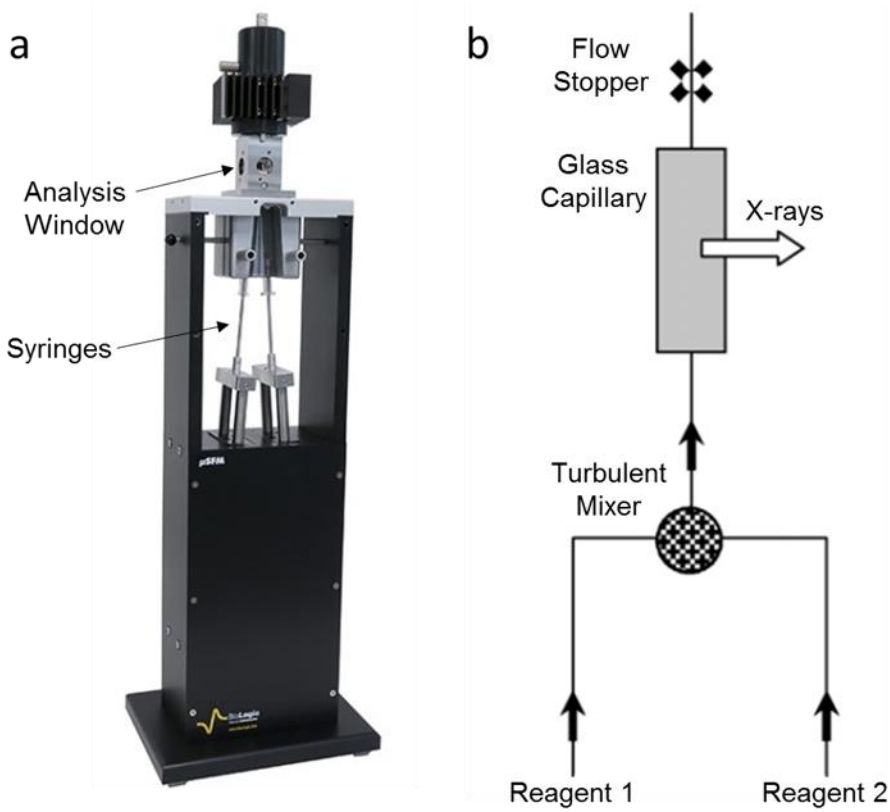

Figure 31: (a) Photograph of a BioLogic stopped-flow device (model µSFM). Obtained from company website. (b) Diagram of the stopped-flow apparatus. Adapted from ref.[215]

Stopped-flow devices haven been utilized for a number of SAXS studies of crystal nucleation and growth. For instance, Bolze *et al.* studied $CaCO_3$ crystallization with 100 ms time-resolution using a BioLogic stopped-flow device.[187] The authors observed the formation of ≤ 270 nm spherical particles of ACC as a precursor to calcite beginning ~20 sec after mixing 9 mM equimolar solutions of $CaCl_2$ and Na_2CO_3. Similarly, Abécassis *et al*. used a stopped-flow device to study the growth of gold nanoparticles in the presence of two different organic ligands with 200 ms time-resolution.[217] They found that nanoparticle production was dominated by nucleation with an alkylamine ligand, where final nanoparticles of 2 nm diameter were formed within 2 sec. Conversely, with an alkanoic acid ligand, nucleation occurred within 1 sec, followed by an ~11 sec growth phase that produced terminal nanoparticles of 7.4 nm diameter.

Finally, Stawski *et al*. used a BioLogic device to investigate the oft-disputed early formation stages of gypsum ($CaSO_4$).[218] Their SAXS results suggested gypsum crystallizes in a four-step process beginning with the formation of <3 nm primary species, followed by their aggregation and self-assembly into larger particles, and finally with an internal structural rearrangement producing a gypsum structure.

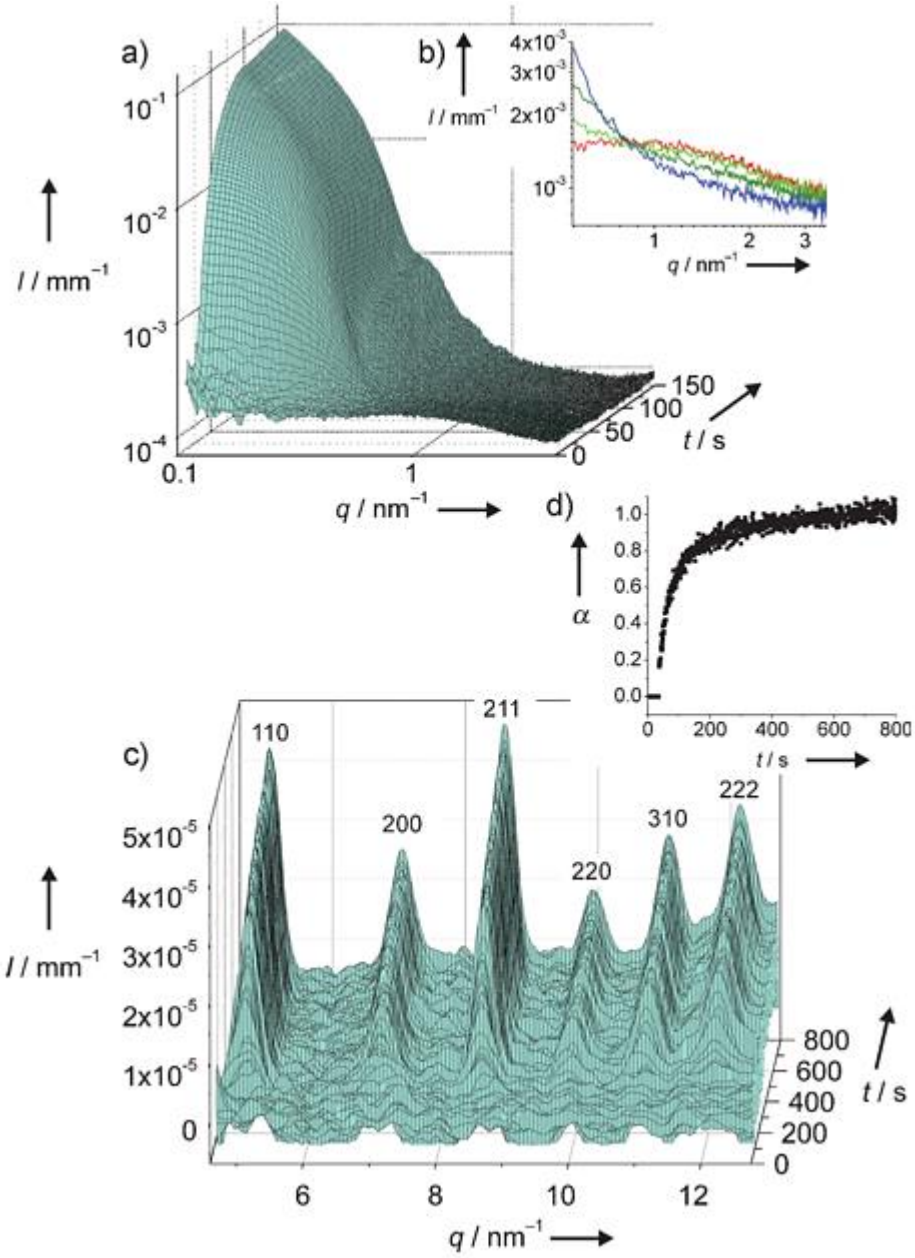

Figure 32: Stopped-flow SAXS/WAXS study from Cravillon *et al*. (a) SAXS data. (b) Higher *q* data from selected times: red 10 sec; light green 30 sec; dark green 50 sec; blue 70 sec. (c) WAXS data labelled with ZIF-8 peaks; (d) Plot of normalized integrated intensity of the 211 peak with time, demonstrating crystalline growth. Reproduced from ref.[219]

Likewise, stopped-flow devices have also found use in simultaneous SAXS/WAXS studies. For instance, Cravillon *et al*. studied the nucleation and growth of nanocrystals of the model zeolitic imidazolate framework (ZIF), ZIF-8, with 1 sec time resolution. The

authors observed the initial formation of ~2 nm Zn-ligand clusters within 1 sec of reaction time (Fig. 32a). After ~15 seconds, SAXS patterns indicated that larger particles had begun to form (Fig. 32b). However WAXS patterns corresponding to the ZIF-8 structure could not be detected until after approximately 35 sec (Fig. 32c and d). This led the authors to postulate that either the particles formed initially as an amorphous phase that later nucleated into a crystal, or simply that the lower detection limit of WAXS prevented Bragg peaks from being resolved until the crystals grew to a larger size.

A final example comes from Whittaker *et al*., who studied the crystallization of barium carbonate ($BaCO_3$) with not only SAXS/WAXS, but also with a third detector that allowed simultaneous collection of intermediate angles, so-called medium angle X-ray scattering (MAXS; Figure 29).[185] Here, the authors observed the initial formation of ~40 nm nanoparticles of amorphous barium carbonate (ABC) within 200 ms (with 100 ms time-resolution). However, instead of directly transforming into witherite, the most stable $BaCO_3$ polymorph, these ABC nanoparticles began to transform into thin crystalline sheets of a previously undiscovered $BaCO_3$ hydrate. Finally, after 30 sec these hydrate crystals, named gortatowskite by the authors, began to transform into witherite. This last example demonstrates the power of sensitive, high time-resolution *in situ* scattering, where it can even be used to discover new transient phases of a crystallization pathway.

Microfluidic Stopped-Flow and Static Analysis

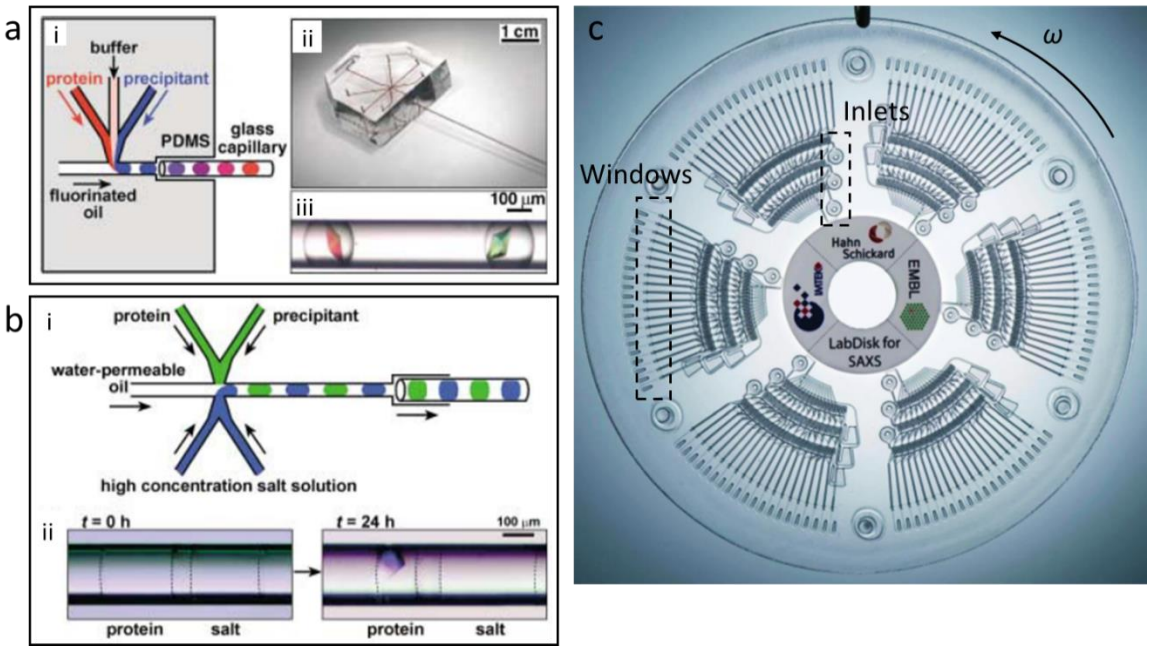

Figure 33: (a) Microbatch and (b) vapor-diffusion methods utilized by Zheng *et al*. for microfluidic stopped-flow X-ray crystallography. Adapted from ref.[220] (c) Centrifugal LabDisk for SAXS utilized by Schwemmer *et al*. for preparing an range of discrete sample conditions on a single chip. Adapted from ref.[221]

Stopped-flows have also been utilized in microfluidic devices, although generally for different applications and rarely for time-resolved analysis. Here, the primary aims have been to produce high quality crystals for single-crystal XRD and screen wide chemical parameter-spaces for both XRD and SAXS studies. For instance, Zheng *et al*. utilized PMDS-based microfluidic devices to prepare droplet crystallization environments for microbatch (Fig. 33a) and vapor-diffusion (Fig. 33a) protein crystal growth.[220] After droplets are formed at a T-junction, the flow is directed into a glass capillary attached to the device (Fig. 33a(ii)), where the flow is then stopped and droplets are allowed to incubate. Once suitable crystals have grown, the droplets can be probed by XRD without the need to remove crystals from the device. Importantly, this crystal preparation method also allows a range of crystallization conditions to be investigated simultaneously by systematically varying the solution flow rate ratios. In another example, Schwemmer *et al*. developed a particularly elegant centrifugal microfluidic stopped-flow device named the “LabDisk for SAXS” (Fig. 33c).[221] This device allows protein, buffer, and ligand solutions to be loaded into inlet wells with a pipette by hand, after which, the application of an angular velocity (ω) mixes the three solutions at 120 different dilutions and introduces them into individual wells for SAXS analysis.

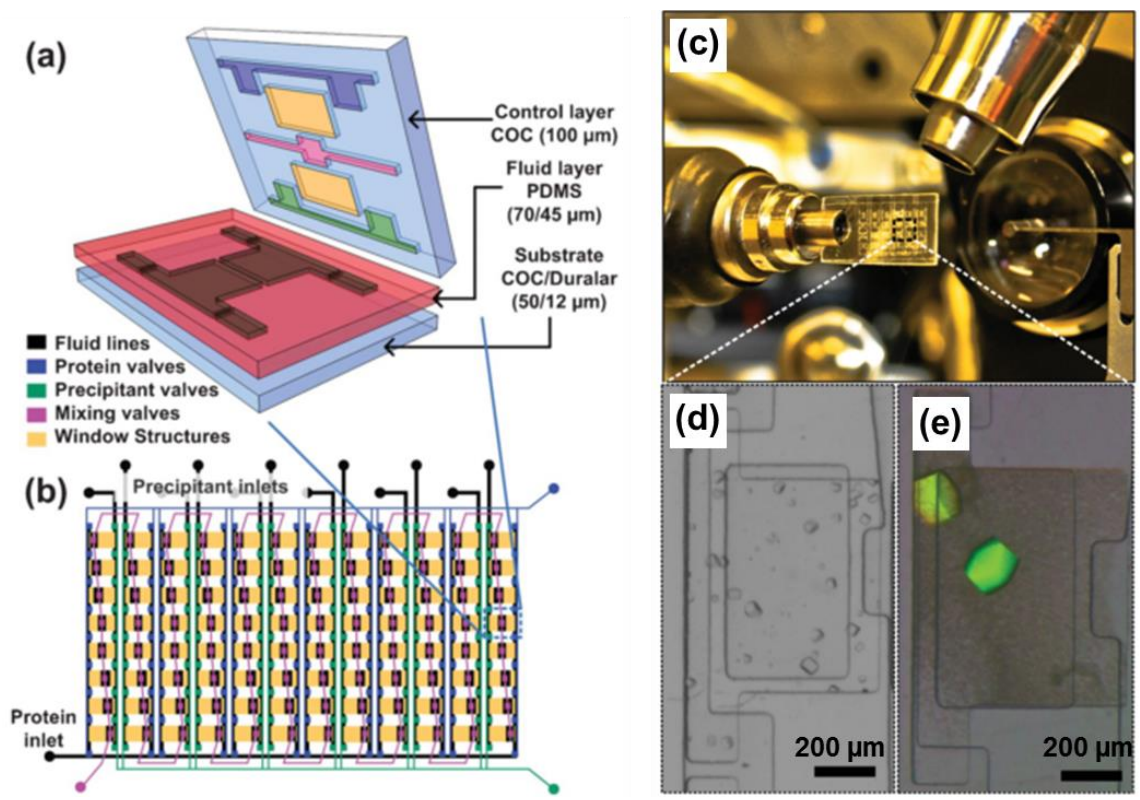

Figure 34: (a and b) Schematic of protein crystal growth chip of Perry *et al*. (c) Chip mounted at beamline 21-ID-G of the Advanced Photon Source. Crystals grown in microfluidic chambers under (d) initial and (e) optimized conditions. Adapted from ref.[222]

However, the vast majority of non-continuously flowing microfluidic X-ray studies to date have actually been of completely static solutions. The first example of this type of chip comes from Hansen *et al*., who used a PDMS device to grow protein crystals by free interface diffusion.[223] Using a series of valves, they loaded an array of different sized microfluidic chambers with a protein solution and precipitant solution. After filling all of the chambers, they sealed the device and then opened up the valves separating the solutions, allowing them to mix by diffusion. Subsequently, crystals that formed in the chambers with the best growth conditions could be removed and analyzed by single-crystal XRD. More recently, Perry *et al.* designed similar microfluidic chips, however, these were made from multiple layers of thin plastic films rather than PDMS alone (Fig. 34a and b).[222] This improved design allowed X-ray analysis to be conducted on-chip after optimizing solution conditions to produce suitable crystals (Fig. 34c-d).

Microfluidic Fixed-Target Serial Crystallography

In many situations, such as with difficult-to-crystallize membrane proteins, it is impossible to obtain large crystals suitable for singe-crystal XRD – even with successive rounds of condition optimization.[177, 224] Therefore, new research in this area has focused on growing crystals for fixed-target serial crystallography (SX).[225] In this technique, individual Bragg reflections are collected by scanning the X-ray beam across a large number of stationary micro- or nano-crystals, and these data are combined to create a composite single-crystal XRD pattern. For instance, Sui *et al*. fabricated a simplified version of the above single-crystal XRD chips comprising only one reaction chamber, which could be filled with microcrystals using microbatch or counter-diffusion techniques.[208] They sealed this device with a single layer of graphene on both sides, providing ultra-low background scattering in order to maximize the amount of diffraction that could be captured from the microcrystals.

Similarly, Ren et al. designed a simple device made from Z-cut single crystalline quartz.[226] Their device could also facilitate microbatch or diffusion-based crystallization and was shown to have much lower background scattering compared to other common device materials (e.g. Kapton, COC) as long as the device was oriented to prevent diffraction from the quartz chip. Heymann *et al*. took a very different approach to fixed-target SX using a droplet microfluidic device.[227] After optimizing droplet sizes so that one crystal would be generated per droplet, they created monodisperse emulsions with a T-junction droplet generator that led into a large storage array for crystal growth and on-chip diffraction. Although this final example did utilize active flow components, it and the other microfluidic studies discussed so far have *only* been focused on preparing crystals and solutions for analysis of final products or biochemical states. These studies have largely neglected the dynamic processes from which these products were

produced. The remainder of the section will be dedicated to the development of flow-based devices that *can* capture dynamic information from a range of processes.

1.3.3 Flow-Based X-ray Analysis of Biological and Soft Matter

One problem with the stopped-flow method for time-resolved analysis, is that data collection is limited by the experiment run time. In other words, to gain more statistics at a particular reaction time point, you have to repeat the experiment multiple times. In contrast, steadily flowing systems offer the ability to de-couple reaction time from the experimental run time, where different reaction time points can be accessed indefinitely by selecting particular beam positions downstream of the mixing point in steady flow operation.[215] Focusing on microfluidic sample environments, the majority of work in this area to date has looked at SAXS of biological and other soft matter systems.

Continuous Flow

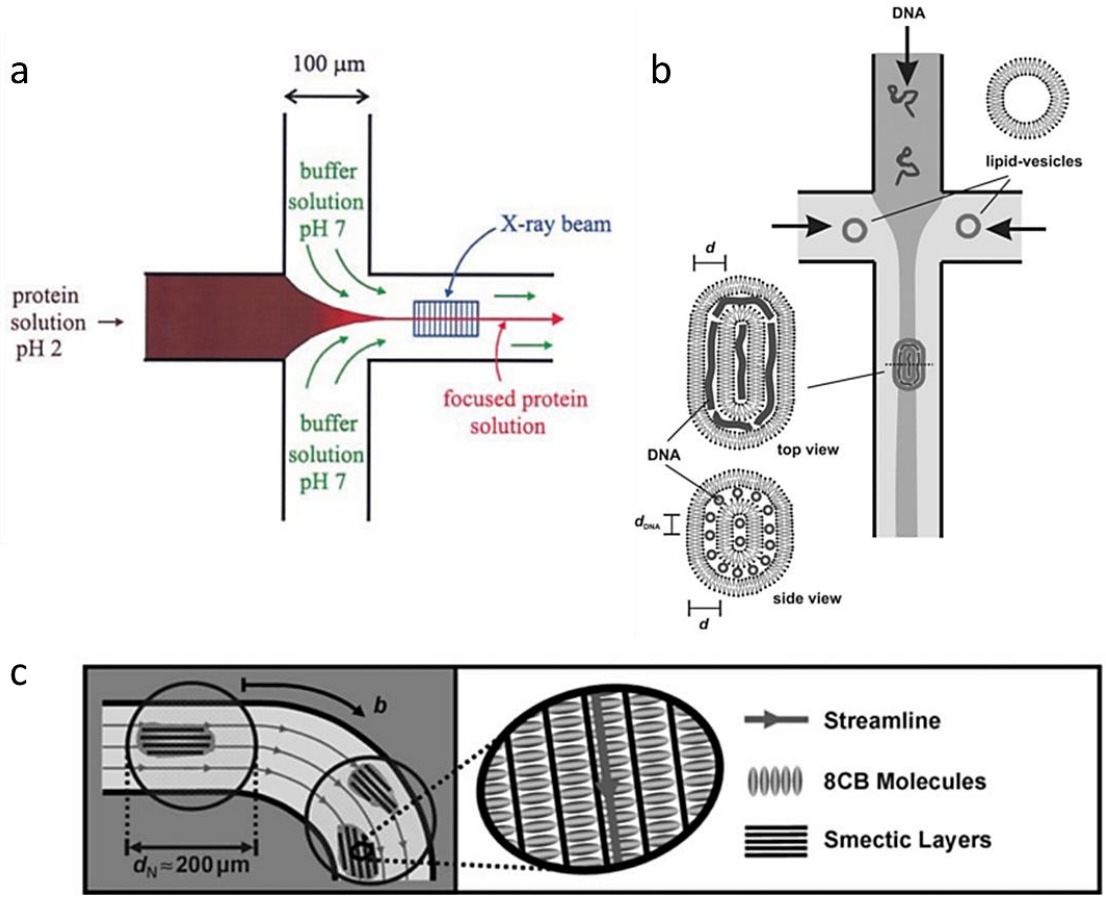

Figure 35: Early continuous flow SAXS studies of (a) protein folding by Pollack *et al*., (b) DNA-lipid assembly by Otten *et al*., and (c) liquid crystal alignment by Dootz *et al*. Reproduced from refs.[210, 228, 229]

Most microfluidic SAXS studies have made use of continuous flow. In one of the first microfluidic synchrotron-based studies, Pollack *et al*. studied protein deformation in response to a jump in solution pH (Fig. 35a).[228] Using SAXS combined with a

hydrodynamic flow focusing device, they observed an initially disordered cytochrome *c* protein at low pH collapse into a compact denatured state at pH ≈ 7 before quickly folding into its native ordered state – all within 10 ms. Likewise, Otten *et al*. used a similar flow focusing geometry to study the assembly of DNA and lipid vesicles into multilamellar structures that can be used for gene therapy (Fig. 35b).[229] By moving the X-ray beam downstream with the microfluidic jet they could observe the rapid formation of lipid lamella spaced 7.2 nm apart as well as the slower rearrangement of DNA trapped within the multilamellar structure.

As a final example, Dootz *et al*. studied the shear-induced alignment of a continuous flow of *n*-octyl-4-cyanobiphenyl (8CB) liquid crystals using a microfluidic chip with curved microchannels and narrow throats. They found that at room temperature the crystals aligned in smectic layers with the fluid streamlines – even as the flow turned around corners and accelerated into the channel constrictions (Fig. 35c). These three examples represent the large variety of sample types that can be investigated with microfluidic SAXS, and there have been many more such studies.[203, 204, 214, 230-234] Almost all of these have been in continuous flow, but there have been some important developments in adapting segmented flow devices for SAXS analysis.

Segmented Flow

In addition to studying DNA-lipid assembly, Otten *et al*. also studied the alignment of 8CB liquid crystals in microchannels, but in droplets rather than continuous flow.[229] They introduced the 8CB solution into a flow focusing junction and collected SAXS patterns before the junction, during flow focusing, and after droplet break-up. These patterns revealed that the crystal layers were oriented with the flow at each position, but that they were most closely aligned with the flow at the high-shear region of the junction just before break-up. In another study, Pham *et al*. used SAXS to investigate changes in lysozyme protein structure and shape as it crystallized from supersaturated solutions.[235] They used a microfluidic chip to mix a protein and precipitant solution at a T-junction just before droplet break-up, where droplets were then directed off-chip into a SAXS sample holder with a quartz capillary window.

The final example of segmented flow microfluidic devices for soft matter SAXS analysis comes from Saldanha *et al*.[236] The authors studied the assembly of vimentin filament proteins, where droplets containing the protein were generated on-chip and directed into a glass capillary similar to Pham *et al*. (Fig. 36a). They utilized high frame-rate X-ray exposures, which allowed them to observe the alternating scattering profiles of the water droplets and continuous fluorinated oil phase (Fig. 36b and c). Importantly, this enabled them to isolate scattering from each phase, and threshold out the patterns corresponding to oil and the oil-droplet interface (Fig. 36d and e). After this

thresholding step, the remaining patterns could be averaged and integrated to obtain statistically significant 1D patterns without any artefacts from oil or interfacial scattering. However, a weakness of the techniques of both Pham *et al*. and Saldanha *et al*. is that analysis is only facilitated in a small section of glass capillary at the device outlet. This limits the number of reaction times that can be accessed and also prevents the collection of data at early time points close to the droplet generation junction.

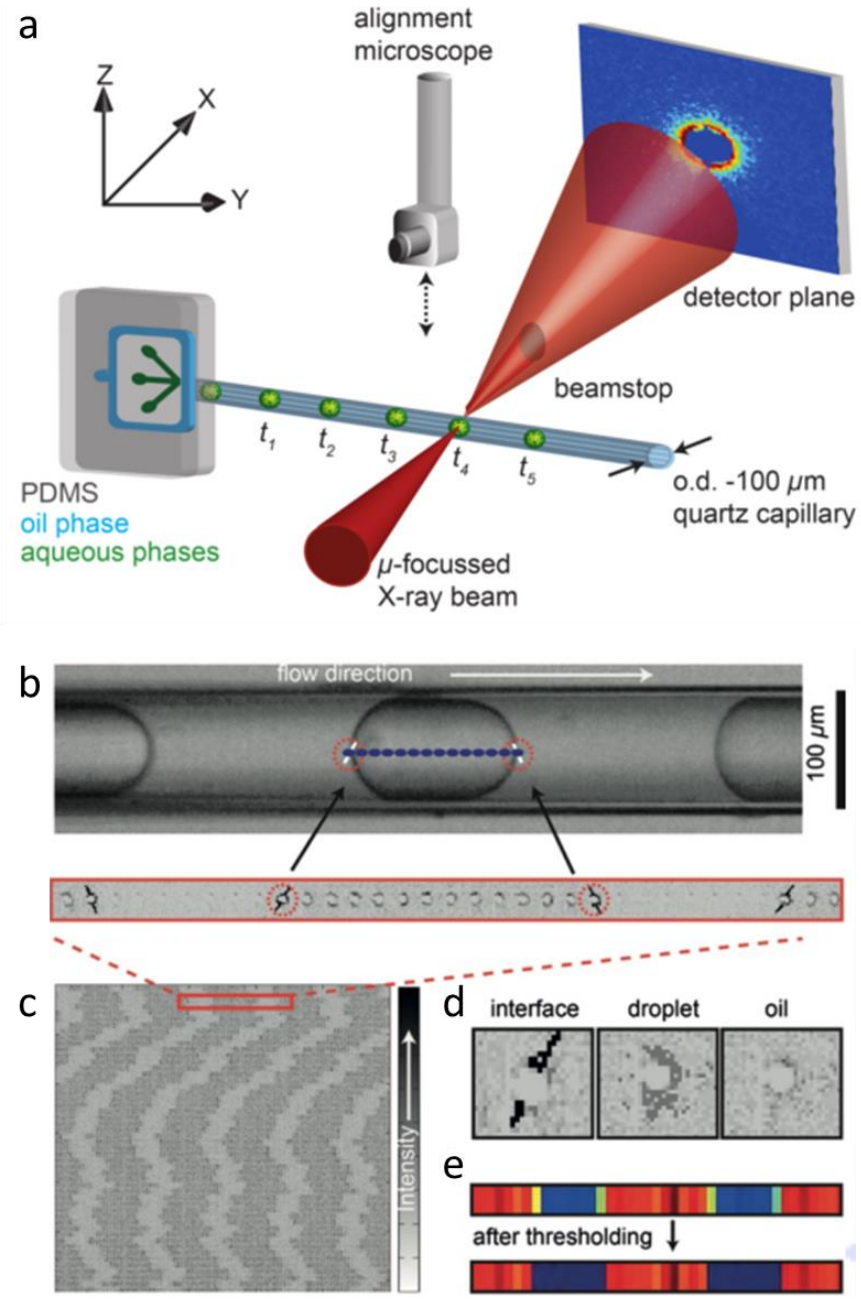

Figure 36: (a) Experimental setup of Saldanha *et al*.[236] (b) Optical micrograph of droplet flow within the analysis capillary and the corresponding 2D scattering patterns. (c) A montage of frame-by-frame 2D scattering patterns revealing the alternating w/o flow. (d) Representative 2D scattering patterns from droplets, oil, and the oil-droplet interface. (e) Example of thresholding technique to eliminate scattering from oil and the interface. Light blue and yellow/green frames corresponding to the oil and interfaces, respectively, are set to zero. Adapted from ref.[236]

Small Angle Neutron Scattering (SANS)

Although neutrons were not utilized as a part of this thesis, it is worth noting that similar progress has been made in flow-based sample environments for small angle neutron scattering (SANS).[237] For instance, Lopez *et al*. studied the flow behavior of two non-Newtonian fluids in continuous flow using a device fabricated from a photo-patterned polymer sandwiched between two glass plates.[238] Similarly, Adamo *et al*. recently demonstrated the suitability of droplet microfluidic devices for SANS, where they analyzed a range of soft matter model systems including surfactant mixtures and colloidal suspensions.[239] The authors also investigated the background scattering of various microfluidic carrier phases and discovered that fluorinated oils commonly used in droplet microfluidics provide suitably low background scattering for SANS analysis. Thus, there is also great potential for developing these types of flow devices for use at dedicated neutron facilities.

1.3.4 Flow-Based X-ray Analysis of Crystalline Material

Continuous Flow

There are fewer examples of flow-based X-ray studies of crystalline material, however this type of analysis is beginning to gain more popularity in the engineering and materials science communities. Much of the work in this area to date has studied corrosion and scale phenomena in continuous flow. For instance, Chen *et al*. used synchrotron-based WAXS and a millifluidic sample environment to study $CaCO_3$ scale formation.[240] They mixed a solution of two brines in a 1 mm inner diameter (ID) silicon capillary and studied the phases that precipitated at 25 °C and 80 °C. At 25 °C they observed the initial precipitation of aragonite and vaterite, but these polymorphs appeared to either precipitate in bulk or be easily washed off of the surface. Only calcite permanently attached to the surface, where it appeared to display only the (104) reflection. Conversely, at 80 °C they identified the presence of additional calcite orientations and also reflections from aragonite and vaterite polymorphs, where all the forms remained attached to the capillary walls.

In a follow-up WAXS study, Chen *et al*. investigated the effect of polyphosphinocarboxylic acid (PPCA) as a $CaCO_3$ scale inhibitor.[241] They found that the presence of PPCA both delayed the onset of surface deposition and also changed the primary scale at room temperature from calcite to vaterite. Further, they noticed that the inhibitor changed the lattice parameters of the deposited vaterite and calcite crystals, where they both displayed elongated c-axes. More recently, Burkle *et al*. utilized a millifluidic electrochemical flow-cell to investigate the relationship between corrosion and $FeCO_3$ precipitation on X65 carbon steel using grazing incidence X-ray

diffraction (GIXRD; Figure 37).[242] They introduced a CO_2-saturated NaCl brine into the device at 80 °C and found that $FeCO_3$ was the only phase to precipitate over the 4 hour long experiment. Additionally, they observed that the growth of $FeCO_3$ only began to inhibit corrosion after almost 45 min of reaction time once the layer blocked a sufficient number of active sites on the steel surface.

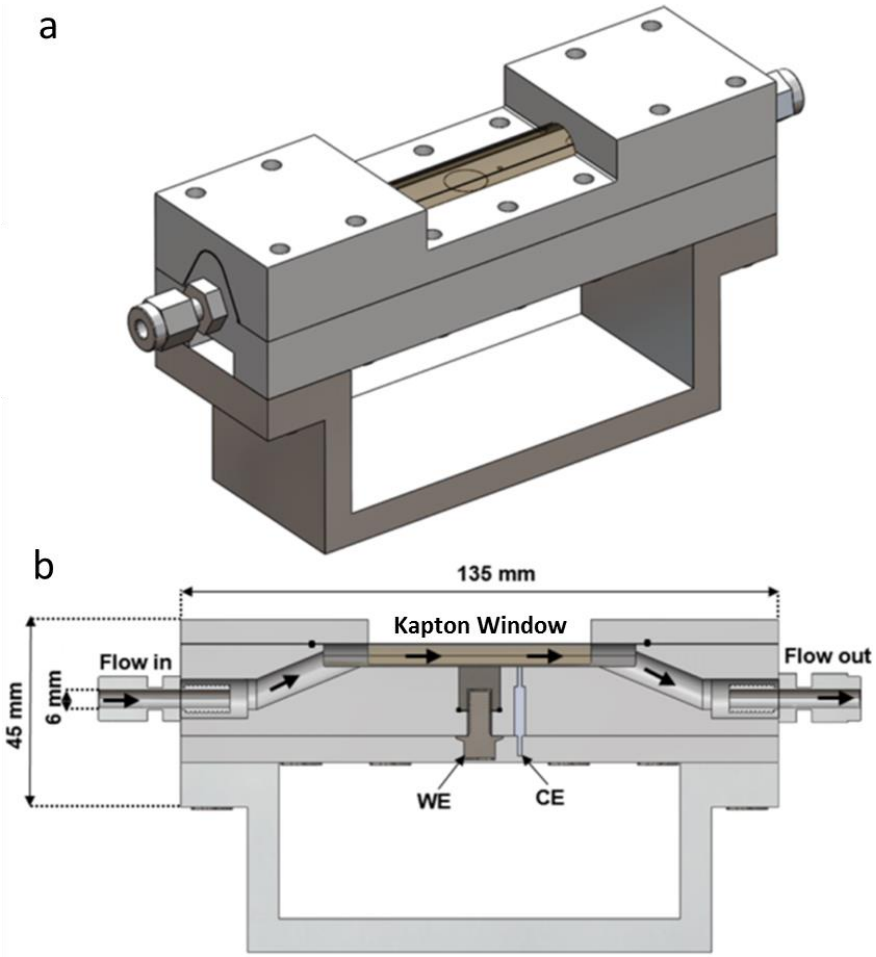

Figure 37: Design of the electrochemical GIXRD flow cell of Burkle *et al*. (a) Assembled flow-cell. (c) Cross-sectional view showing the Kapton window and working (WE) and counter (CE) electrodes. Adapted from ref.[242]

Continuous flow systems have also been utilized to study materials synthesis in bulk solution (i.e. not occurring at a surface), with several studies employing X-ray total scattering analysis. For example, Zobel *et al*. studied the formation of ZnO nanoparticles in a stainless steel millifluidic flow-cell with Kapton windows.[243] They mixed an ethanolic solution of zinc acetate (with or without specific organic ligands) and a methanolic solution of tetra-methylammonium hydroxide (TMAH), and recirculated it through the flow-cell with a peristaltic pump. Upon mixing, the authors observed the initial formation of ~1 nm diameter low coordinated Zn clusters. Subsequently, these clusters grew into ZnO particles of 2-4 nm diameter comprising a disordered shell and crystalline core, where the ratio of the core-shell thickness could

be controlled by the addition of different organic ligands. Recently, Terban *et al*. studied the formation of ZIF-8 nanocrystals in a flow-cell with a 2 mm ID Kapton analysis tube.[244] They mixed aqueous zinc nitrate and methanolic 2-methylimidazolate (2-MeIm) solutions at a 1:1 ratio and observed the simultaneous formation of both crystalline ZIF-8 and amorphous clusters of $Zn(2\text{-MeIm})_4$. They also noted the presence of a second amorphous $Zn_x(2\text{-MeIm})_y$ phase comprising short-range order related to ZIF-8 and suggested that this could serve as a precursor to the crystalline form.

Segmented Flow

To the best of the author's knowledge, there is only one example of segmented flow X-ray scattering analysis of crystalline material. This work comes from Stehle *et al*., who studied the nucleation of gold nanoparticles in water-in-oil emulsions with SAXS.[245] The authors utilized a glass capillary-based microfluidic device, where solutions of tetrachloroauric acid and sodium borohydride were mixed within the capillaries just before they were broken-up into droplets by a fluorinated oil (Fig. 38). After break-up, the droplets were directed immediately into a 0.3 mm ID, 10 µm wall thickness capillary for analysis. However, similar to the droplet devices for soft matter discussed above, this design limits the number of points at which the flow can be analyzed and does not permit the investigation of long residence times.

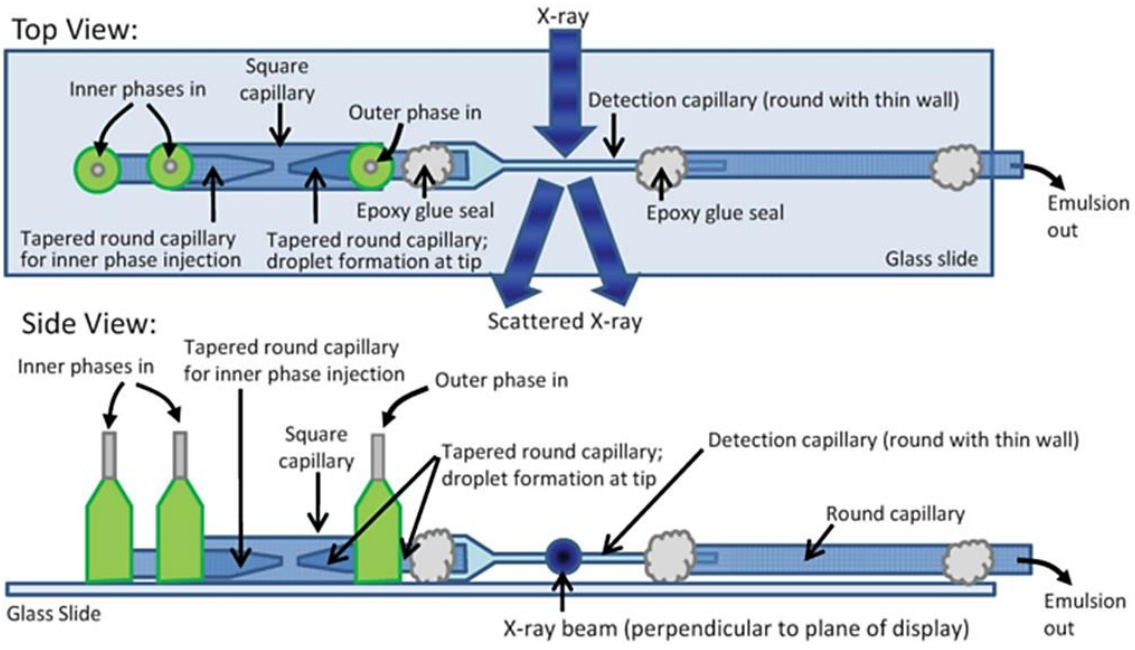

Figure 38: Illustration of the glass capillary device of Stehle *et al*. Reproduced from ref.[245]

Injector-Based Serial Crystallography

While approached from the perspective of structural biology rather than materials science, it is worth mentioning the large amount of effort devoted in recent years to injector-based serial crystallography (SX). Similar to fixed-target SX, the purpose of

injector-based SX is to obtain Bragg reflections from a large number of nanocrystals in order to solve the structure of difficult-to-crystallize proteins. In this technique, a pre-made suspension or viscous slurry of nanocrystals is introduced into the X-ray beam with a microfluidic nozzle that sprays out the suspension in a free flowing jet or in discrete droplets.[225] Before obtaining single-crystal patterns, this methodology was initially validated with serial PXRD studies at synchrotron facilities,[246, 247] where the collection of single-crystal reflections typically requires shorter pico- and femtosecond exposures from high-intensity pulsed X-rays, such as those produced by an X-ray free electron laser (XFEL). However, it is worth noting that such analysis is now also possible at synchrotrons, with a recent study reporting successful synchrotron single-crystal SX using a wider bandwidth “pink” X-ray beam.[248]

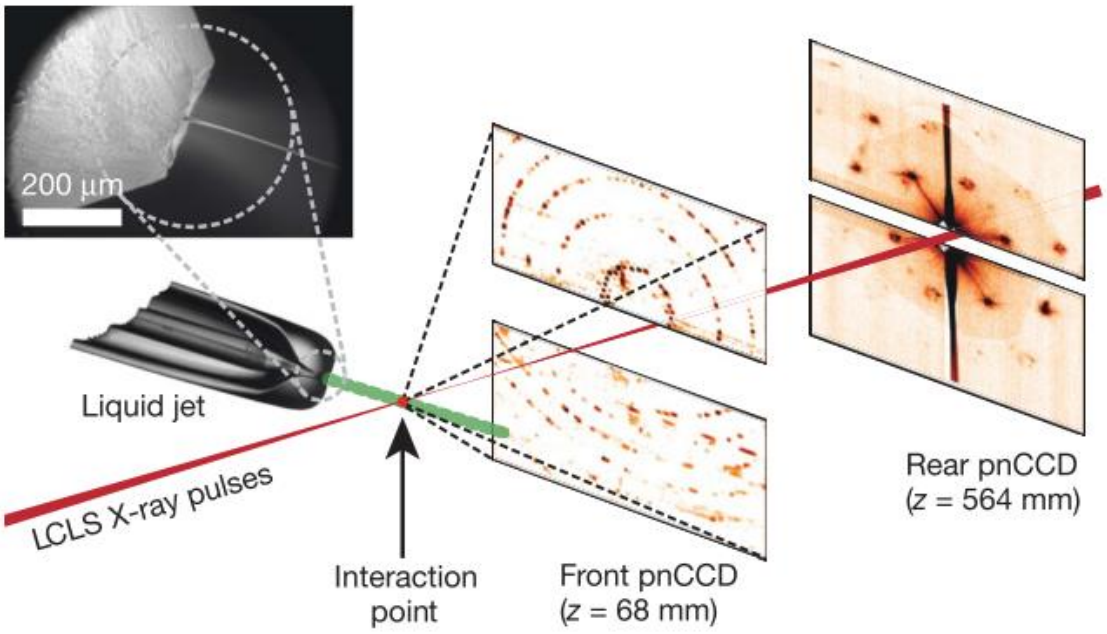

Figure 39: Injector-based serial crystallography setup of Chapman *et al*. Reproduced from ref.[249]

The first successful injector-based single-crystal SX experiment was conducted by Chapman *et al*. at the Linac Coherent Light Source (LCLS) XFEL in the USA.[249] Here, the authors used a gas-focused jet of 4 µm diameter to introduce nanocrystals of the photosystem I membrane protein into the X-ray beam (Fig. 39). With reflections captured from >15,000 crystals using millions of individual 70 fs exposures, they were able to solve the structure to 8.5 Å resolution. Since this first demonstration, subsequent studies have been able to obtain higher spatial resolution data in the range of 1-2 Å.[250-252]

More recently, research in this area has been focused on utilizing injector-based SX for time-resolved studies. This has led to the development of the “pump-probe”

method, where the sample jet is “pumped” with a pulse of laser light at a particular time delay before the arrival of an X-ray pulse “probe”.[253, 254] Based on the duration and spatial distance between the pulses and speed of the jet, this technique can be used to probe the photo-excitation and subsequent relaxation of proteins with millisecond to femtosecond temporal resolution.

Yet while these serial crystallographic approaches have proven effective in obtaining high-resolution structural data from difficult-to-crystallize proteins, it is the author’s view that the current ability of SX for time-resolved studies is often overstated. Although time-resolved pump-probe experiments enable femtosecond changes in proteins to be observed, a protein’s response to high intensity laser light is hardly relevant to the *in vivo* function of most proteins. Recognizing this, there have indeed been efforts to design experiments around photo-activated chemical triggers[193] or with injectors comprising mixing elements to initiate reactions,[255, 256] however these require a great deal of additional optimization to unlock their full potential. Further, it is difficult to access more than one time point per SX experiment, requiring it to be repeated multiple times at different pump-probe delays to truly observe the dynamics of a process.[257] Therefore, there appears to be significant room for improvement in SX sample environments and experimental techniques to acquire richer dynamic information from a wider range of proteins and also other materials.

Chapter 2:
Microfluidics-Coupled X-ray Powder Diffraction

2.1 An Insert-Based Reusable Microfluidic Device

2.1.1 Design, Fabrication, and Operation

Motivation

A common problem with many of the microfluidic devices discussed in Section 1.3 is their limited functionality. Most of these devices only permit analysis of single phase flows and room temperature reactions and they often have short channel lengths or small analysis windows, such that data can only be collected over short residence times. Typically, these devices are made of flexible materials like PDMS or other thin polymers, and utilize non-standardized inlets/outlets and mounting equipment, which together make interfacing with X-ray instrumentation difficult and inconsistent. In a university laboratory, these sorts of improvised devices and experimental setups are often satisfactory, where time is unlimited, and the user can make regular repairs to equipment and readily produce new devices. However, the current specifications of most commercial X-ray diffractometers at universities are not high enough to obtain useful data from microfluidic systems (see Chapter 5), so data must be collected at synchrotron radiation facilities. Unfortunately, time at these facilities, known as "beamtime", is granted through a competitive peer-review process, and even successful researchers may only be given a few days per year – at significant cost to the taxpayer.* Thus, it is of great importance to design more robust and reliable devices which make better use of precious beamtime.

Device Design and Operating Principles

In response to these shortcomings of previous X-ray compatible microfluidic reactors, the primary design goal of this project was to produce a device that offers multiple analysis points over long residence times (>1 min). Additionally, the device should enable reproducible mounting and dismounting in the beamline experimental hutch, have standardized world-to-chip connections, and of course, have as low a background X-ray signal as possible. The result was a plastic flow-cell made from multiple layers of thin inserts sealed between rigid poly(methyl methacrylate) (PMMA) base plates which provide structure, alignment, and fluid connections and that allow X-rays to enter and exit the device (Fig. 40). Additionally, the device is reusable, with

* The most recent 2017-18 estimate from Diamond Light Source is £19,188 per 24 hr.

many components having been used for several beamtimes over ~4 years. The original device configuration contained a central 300 µm-thick polytetrafluoroethylene (PTFE) insert bearing the channel design, two 75 µm-thick polyimide (Kapton) window inserts, and two 300 µm-thick silicone gaskets. However, this platform is versatile in that the inserts can be interchanged to allow different channel designs and materials to be used as required. Various other materials have been successfully tested, including nitrile gaskets and ruby mica and polyethylene terephthalate (polyester, PET) windows. The current iteration of the device uses a 250 µm-thick Kapton central insert, the original Kapton windows for WAXS analysis, and 50 µm-thick polyetherimide (PEI) windows for SAXS analysis (Fig. 40, detail).

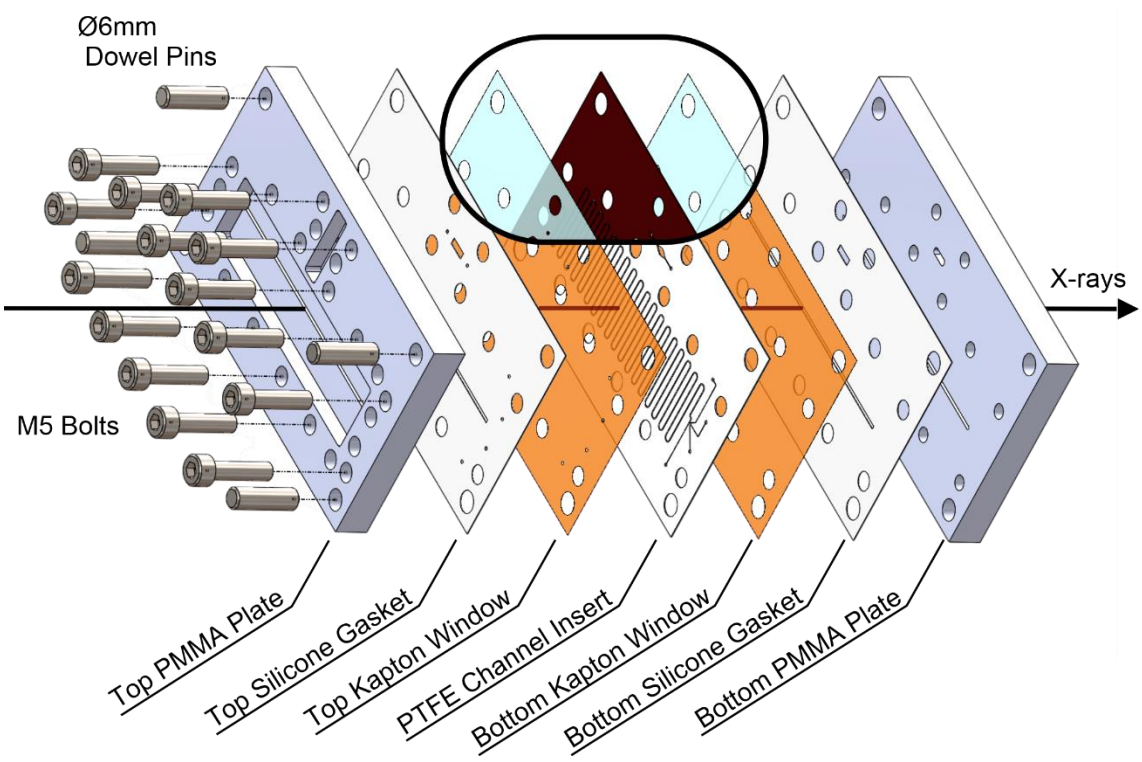

Figure 40: Exploded view of the insert-based device produced with SolidWorks CAD software. The main image shows the original components and the detail shows the current Kapton channel insert and PEI windows for SAXS.

The central insert was designed with a T-junction droplet generator and a long serpentine channel of 300 µm width and ~85 cm length to maximize potential residence time on-chip (Fig. 41a). The initial T-junction design had two dispersed phase inlets which met at a Y-junction, and was used for both continuous flow and segmented flow experiments (Fig. 41b). However, mixing between aqueous phases (e.g. Ca^{2+} and CO_3^{2-}) before droplet break-up can cause premature crystallization, resulting in fouling and blockage of the junction. For this reason, a new T-junction was designed to enable the addition of a “buffer” flow of water between the two reagent streams to delay mixing until after droplet formation (Fig. 41c). X-ray analysis of the flow is facilitated at each

position where the serpentine channel passes by the cut-out sections of the top and bottom PMMA plates (36 positions in total, Figure 41a).

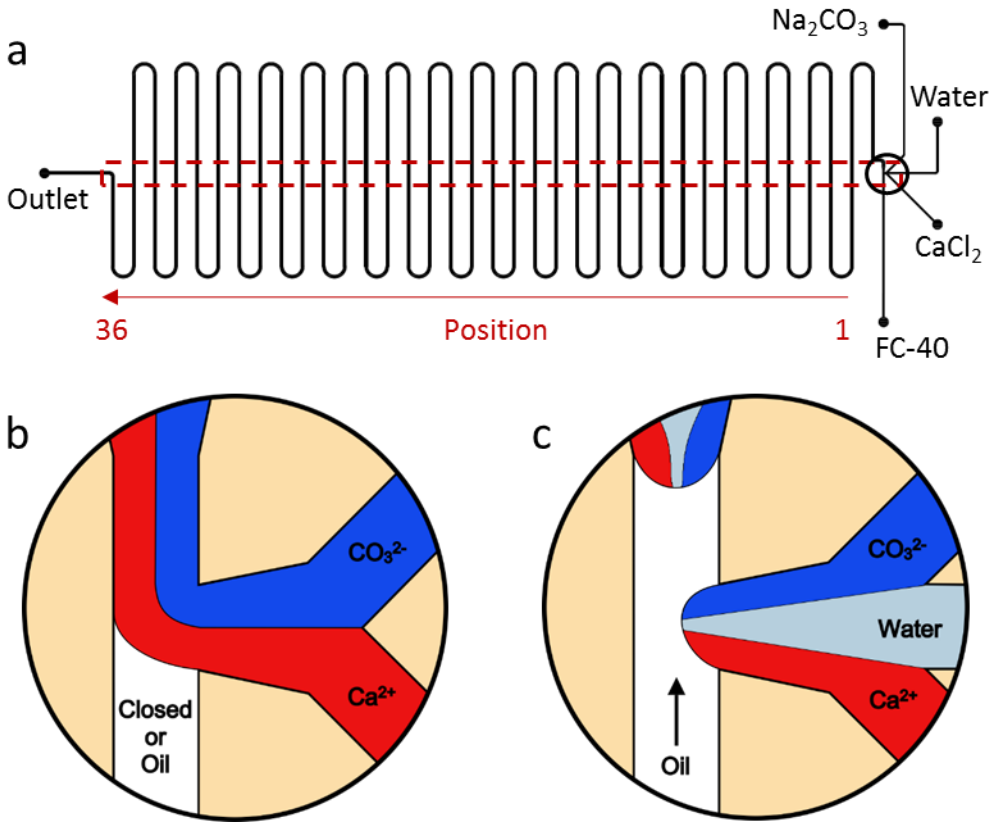

Figure 41: (a) Annotated channel design of the current central insert used in the insert-based device. The red dotted box shows the region visible through the cut-outs in the PMMA plates (not to scale). The red arrow shows the direction of flow over the 36 analysis positions. (b) Detail of the original T-junction design which could mix two reagents and was used for continuous or segmented flow by closing or opening the third inlet. (c) Detail of the current T-junction design which allows a buffer flow of water to be introduced between reagents.

The top PMMA plate utilizes UNF ¼ - 28 flat bottom ports for the connection of standard flangeless fittings for 1/16” tubing. It also contains through-holes for M5 bolts which fix to self-tapping stainless steel inserts embedded in the bottom PMMA plate. Both plates and all inserts comprise holes for 6 mm diameter dowel pins in each corner, which facilitate alignment of the inserts during assembly (Fig. 40). The top PMMA plate also has two M3 threaded holes for attachment of assembled devices to an optical rail carriage. This carriage facilitates the quick, easy, and reproducible exchange of devices on an optical rail, which can be mounted on an translational XYZ stage (goniometer) within a beamline experimental hutch (Fig. 42). More detailed computer-aided design (CAD) drawings of the device are available in Appendix I.

Device Fabrication

Fabrication of devices was performed at the EPSRC National Facility for Innovative Robotic Systems at the University of Leeds School of Mechanical

Engineering. All inserts were cut with a UV laser (Protolaser U3, LPKF), with the exception of the PTFE channel inserts, which were cut by Laser Micromachining Ltd. (St Asaph, UK). This was due to the difficulty of precisely cutting PTFE without access to a high repetition pico- or femto-second laser. PTFE was initially chosen as the channel material for its hydrophobic properties in order to facilitate water-in-oil emulsion formation. Later, a hydrophobic chemical treatment using a commercial water repellant was employed for segmented flow experiments,[118] rendering the use of PTFE unnecessary. This enabled Kapton to be used for the channel insert as well, which allowed all inserts to be fabricated in-house. The top and bottom PMMA plates were computer numerical control (CNC) machined with a 5-axis milling machine (DMU 40 eVo, DMG Mori).

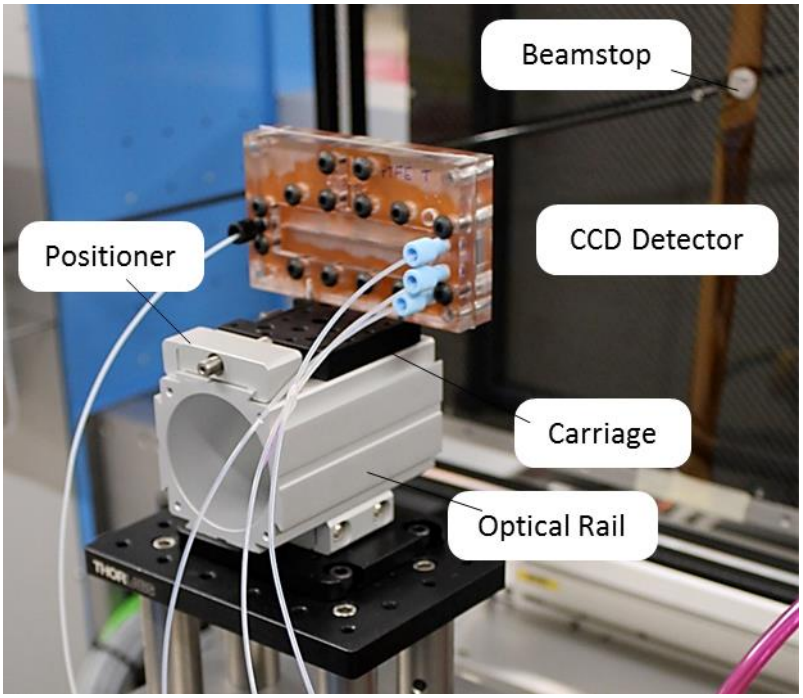

Figure 42: Insert-based device mounted in Experimental Hutch 2 (EH2) of Diamond beamline I11 before an experiment. Light blue fittings are attached to fluid inlets and the black fitting is attached to the device outlet.

Device Treatment and Mounting

After device assembly, fluidic connections are made and devices can be mounted on the optical rail for X-ray analysis. For segmented flow experiments, a chemical treatment adapted from Mazutis *et al*. is performed prior to mounting.[118] All inlets are plugged except the inlet for the continuous phase, and Aquapel solution (Pittsburg Glass Works) is injected into the device and allowed to coat the channel for ~30 seconds. The Aquapel is expelled from the device with a flow of clean dry air (CDA), and the device is subsequently filled with the continuous fluorinated oil phase (Fluorinert FC-40, 3M) until it has flowed through the entire channel length. Finally, the

FC-40 is expelled with another flow of CDA, and the devices are mounted. After mounting, the device must be aligned with the X-ray beam. This alignment process is different at each beamline, and will be discussed in Section 2.2.

Device Start-Up and Operation

Fluid flow is motivated via a syringe pump (neMESYS, Cetoni), where syringes are filled and tubing is primed prior to being connected to the device. The flow start-up process begins with the FC-40, which is allowed to enter the device and wet the T-junction first. Subsequently, the aqueous reagents are injected, removing the head of air formed between the oil in the T-junction and reagents in the tubing. In experiments with the buffer water flow, the water is dosed and allowed to enter the T-junction before the aqueous reagent flows are started. Once all air from the device has been removed and droplet generation has equilibrated, the experimental hutch is locked and experiments can begin. For experiments conducted at the university, devices were assembled, treated, and operated similarly, but simply placed on the stage of a stereo optical microscope (M165 FC, Leica Microsystems) for recording video or still frame images. PDMS devices with a similar serpentine channel design and made using the method discussed in Section 1.2.1 were also utilized for easier optical analysis.

2.1.2 Flow Characterization

Mixing in Continuous Flow

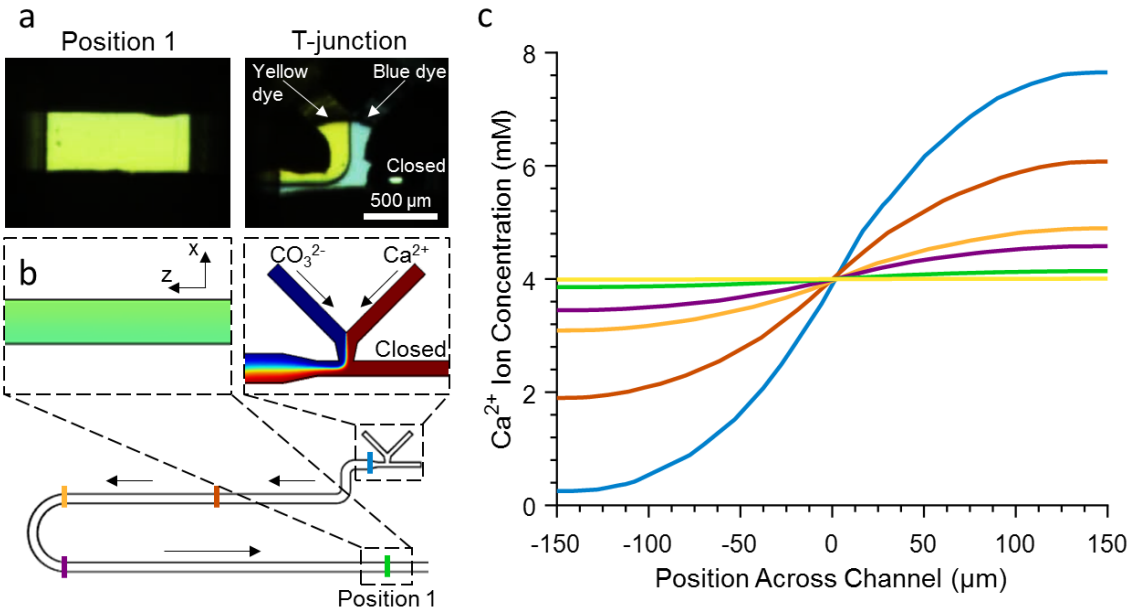

Figure 43: (a) Mixing of dyes within the insert-based device at a total flow rate of 14 µL/min. (b) A corresponding COMSOL simulation of Ca^{2+} ion diffusion under the same flow conditions. (c) Line profiles of Ca^{2+} ion concentration at the corresponding colored channel positions in (b), showing the concentration to be nearly uniform at Position 1.

A combination of flow visualization and finite element analysis (FEA) was used to characterize mass transport within the device under the same conditions used for crystal growth in continuous flow. Crystallization experiments with continuous flow were performed with 8 mM $CaCl_2$ and 8 mM Na_2CO_3 solutions set at a volumetric flow rate (Q) of 7 µL/min each (yielding a final $CaCO_3$ concentration of 4 mM and a total flow rate of Q_{total} = 14 µL/min). This condition was first modelled using flows of food dyes in the place of the Ca and CO_3 solutions (Fig. 43a). As expected due to the low *Re* number (≈ 1.44 in main channel), a well-defined interface between the yellow and blue dye flows developed at the T-junction, and no turbulent mixing was observed. Subsequently, the two streams slowly mixed by diffusion, with the flow appearing almost uniformly green at analysis Position 1, or after 9.7 seconds based on the mean velocity (Q_{total}/Area) of the flow. This is in spite of the high *Pe* number (≈ 985) implying that the flow should not be completely mixed until it travels 295 mm, somewhere between Positions 12 and 13.

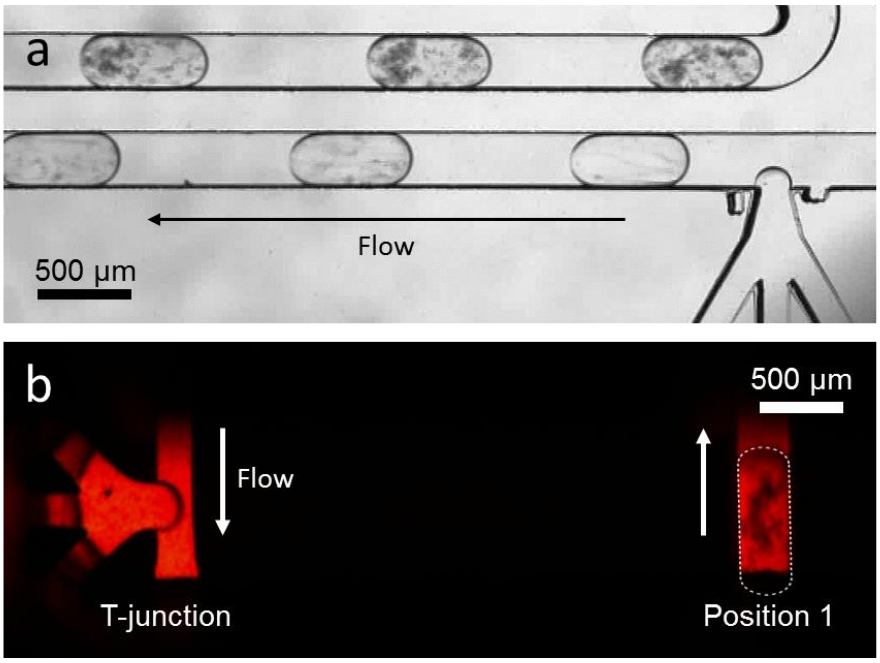

Figure 44: (a) Droplet flow in a PDMS device with total flow rate of 32 µL/min showing immediate precipitation after break-up. (b) Droplet flow in an insert-based device with a precipitate-filled droplet at Position 1 after ~5 s. The $CaCO_3$ concentration in (a) and (b) is 50 mM.

Actual ion transport was simulated with COMSOL Multiphysics FEA software, where results correlated well with the dye-based experiment (Fig. 43b). Cross-sectional distributions of the Ca^{2+} ion concentration (x-axis) analyzed at different points along the flow (z direction), revealed the concentration to be 4 ± 0.15 mM across Position 1, where zero is the xy center of the channel (Fig. 43c). So while the *Pe* number suggests that this flow condition will not be completely mixed at Position 1, it should nonetheless

contain a near-uniform Ca^{2+} ion distribution within ± 3.75% of the target concentration. However, it is important to note that this model is only valid until precipitation occurs, which will begin to lower the ion concentration, and therefore the supersaturation, of the solution as a function of time and channel position.

Mixing in Segmented Flow

Higher concentrations and flow rates were utilized for crystallization experiments with droplets. In a typical experiment, total flow rates of 22-32 µL/min and 25-50 mM final $CaCO_3$ concentration were employed, yielding total device residence times of ~2.4-2.9 min and droplet velocities of ~5-6 mm/s depending on the channel cross-sectional area. Visualization of these conditions in optically transparent PDMS chips revealed that precipitation in droplets begins immediately at droplet break-up, with material seen distributed throughout the droplet in <1 sec (Fig. 44). Mixing within insert-based devices is expected to be even faster due to the series of turns directly following the T-junction (Fig. 43b, channel diagram),[146] with droplets being mixed long before they reach the first X-ray analysis position after ~4-5 sec (Fig. 44b).

2.1.3 Thermal Characterization

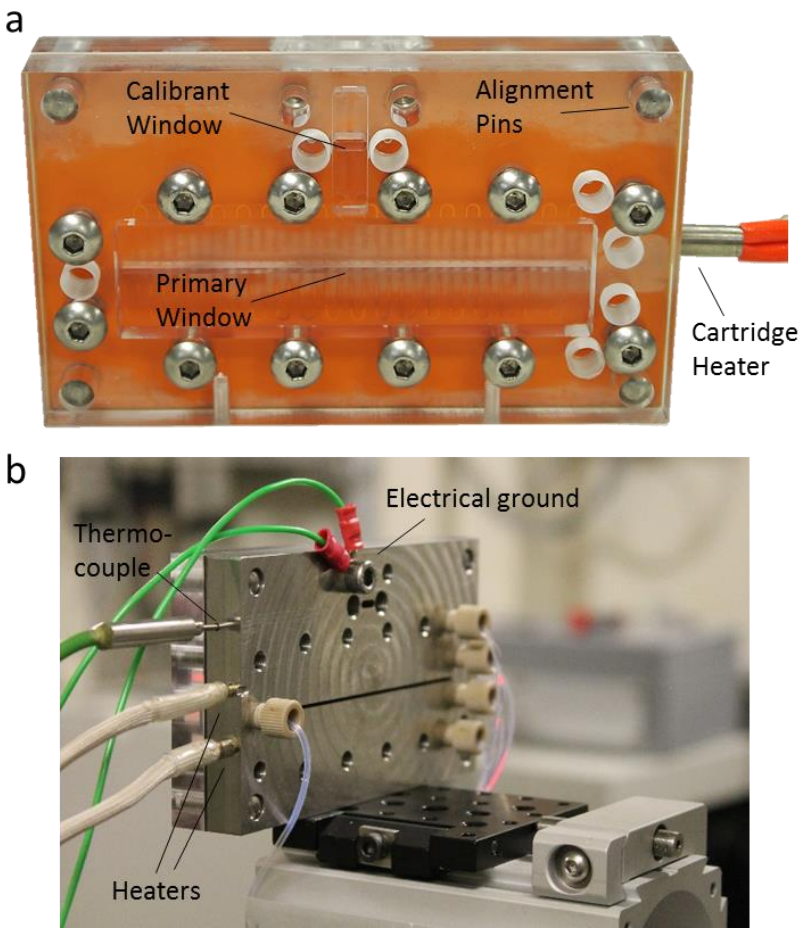

Figure 45: Modified devices for (a) generating temperature gradients and (b) sustained heating.

Two variants of the insert-based device were designed to investigate heated reactions. The first contains a small blind bore in the bottom PMMA plate underneath the inlets where a small ceramic cartridge heater and K-type thermocouple can be inserted (Fig. 45a). This design can be used to create a temperature gradient along the channel, initiate a reaction with localized heating, or potentially be combined with a heated syringe and tubing line to allow a hot solution to be pumped on chip to subsequently cool and crystallize. The second variant utilizes a stainless steel top plate with two blind bores along the length of the serpentine channel for insertion of custom-made stainless steel cartridge heaters (Tecnologic UK, Figure 45b). This design can be used to heat the entire length of the channel.

Temperature Gradient Device

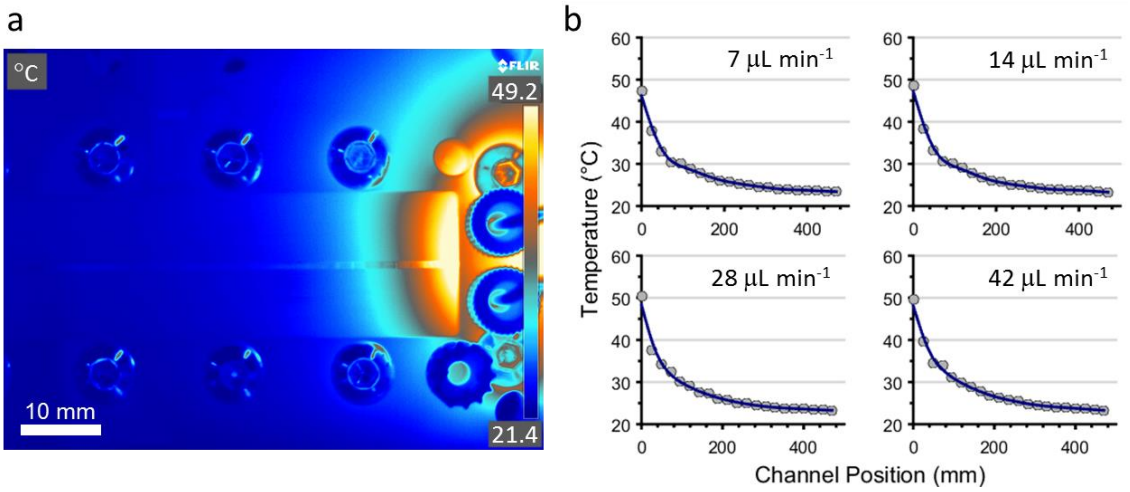

Figure 46: (a) IR image of the thermal gradient insert-based device. (b) Temperature vs. Channel Position plots of the flow at the indicated total flow rate.

Thermal imaging was used to measure the channel temperature at different positions depending on the experimental flow rate and the temperature of the thermocouple placed close to the heater. The first device was evaluated at a cartridge heater temperature of 130 °C utilized for synchrotron experiments. Video and images were captured with a X6540sc IR camera (FLIR). These showed the heat distribution across the device surface (Fig. 46a). Pixel values over each analysis position were extracted to generate plots of flow temperature vs. channel position at different flow rates, assuming the surface temperature of the thin, high-emissivity Kapton windows to be equivalent to the temperature of the adjacent flow (Fig. 46b).[258] As expected, the temperature at the T-junction was the highest, with the flow rapidly cooling from the T-junction to Position 3, and then slowly cooling to room temperature from Position 3 to 20. At the same flow rate as utilized in crystallization experiments, 14 µL/min, the fluid temperatures at the T-junction, Position 1, and Position 2 were 48.6 ± 1, 38.3 ± 1, and

33.3 ± 1 °C, respectively. These were the three main positions of interest during synchrotron XRD analysis of crystallization in continuous flow.

Constant Temperature Device

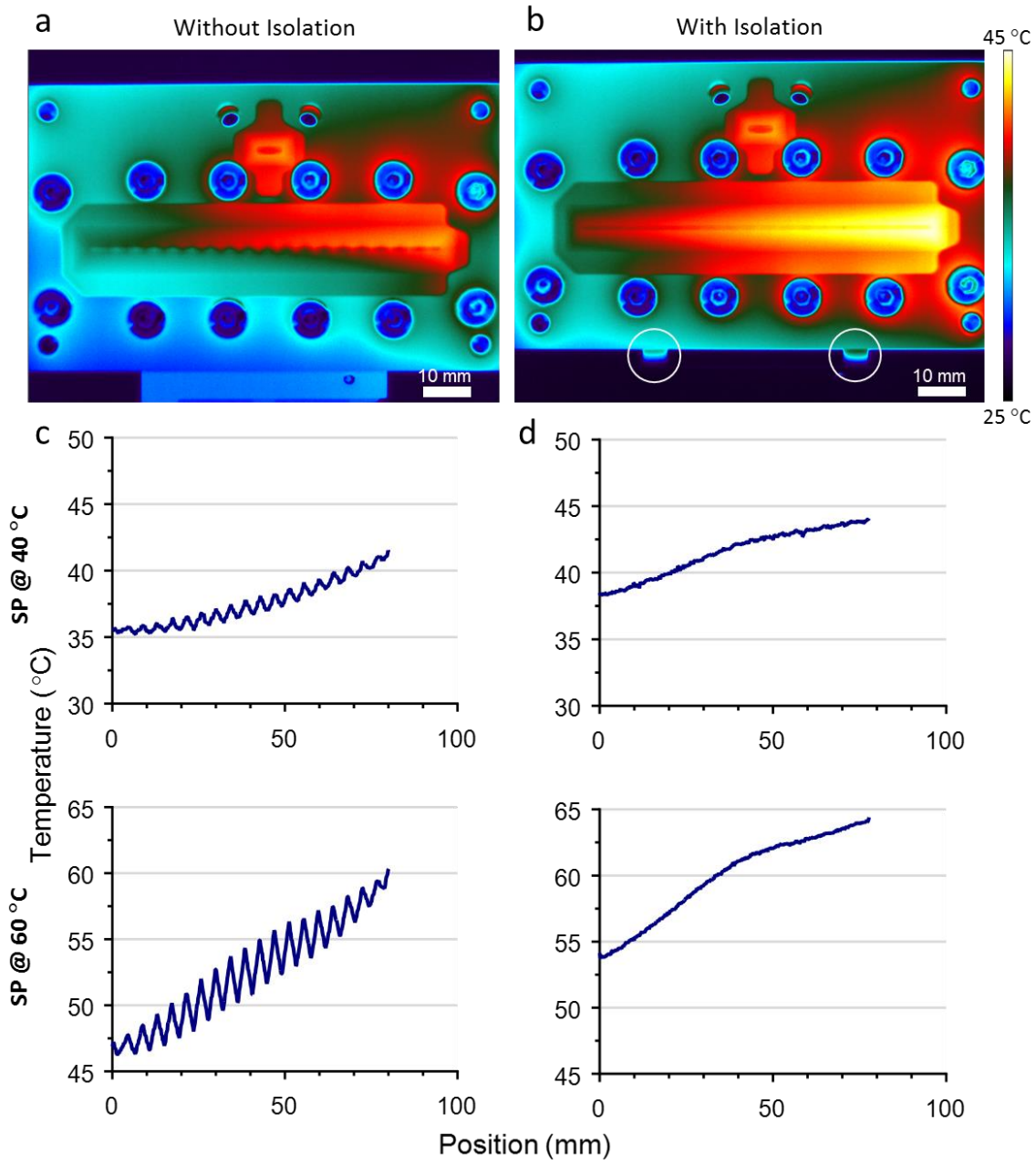

Figure 47: Thermal analysis of the stainless steel heated device (viewed from the back). IR image of the device set to 40 °C (a) with and (b) without thermal isolation from rail carriage. Nylon spacers identified with white ovals. (c) Temperature line profile across cut-out window at set points (SPs) of 40 °C and 60 °C showing sawtooth pattern due to lack of isolation. (d) Temperature line profile across cut-out window at SPs of 40 °C and 60 °C with thermal isolation.

Heating in the stainless steel device variant was investigated using a 640sc IR camera (FLIR). In contrast to the thermal gradient device, the thermocouple in this device monitored the temperature of the stainless steel top plate rather than the heater itself, enabling the desired temperature of the plate to be set with a proportional-

integral-derivative (PID) controller (RS). However, thermal imaging of the device revealed that this design did not result in uniform heating of the plate or the channel (Fig. 47). Heating was greater at the end of the channel (right side of device) where the cartridge heaters were inserted. This problem was exacerbated by heat loss due to direct contact between the stainless steel plate and the aluminum rail carriage mount, causing the bottom of the device to be colder than the top (Fig. 47a). The serpentine design of the channel carried the flow alternately between the hot and cold areas resulting in a sawtooth-like heating/cooling cycle (Fig. 47c). Thermally isolating the device from the mount using Nylon spacers solved this problem (Fig. 47b), however it did not eliminate the large temperature gradient along the channel and also resulted in temperature overshoots of ~5 °C at both the 40 °C and 60 °C set points (Fig. 47d). It is possible that selecting a higher conductivity material (such as aluminium) for the top plate and also choosing a back plate material that is less insulating than PMMA could lower the thermal mass of the device and allow for greater control. In the future, the device could also be redesigned to enable better placement of cartridge heaters. However, further optimization of the heated device was outside the scope of the project, the main focus of which was to develop *in situ* X-ray scattering methodology.

2.2 Beamline Specifications and Experimental Setup

Figure 48: Diamond Light Source (left) and the ESRF (right) indicated with red arrows.

The microfluidics-coupled XRD techniques presented here were developed over the course of six beamtimes at three different beamlines across two synchrotrons, Diamond Light Source and the European Synchrotron Radiation Facility (ESRF; Figure 48). Differences in instrumentation and equipment available at each beamline required that the microfluidic setup and experimental procedure be slightly modified for each facility. However, these differences also allowed comparison of the features and capabilities of each beamline, enabling the identification of critical detector and X-ray

source parameters and the most useful beamline hardware. The specifications and experimental procedure for each beamline as well as a discussion of important differences between beamlines are included below.

2.2.1 Diamond I11 (High-Resolution Powder Diffraction)

General Beamline Information

The United Kingdom's national synchrotron radiation facility is Diamond Light Source, which is located in Didcot, Oxfordshire at the site of Rutherford Appleton Laboratory. Two beamlines at Diamond were utilized for this project, the first being its powder diffraction beamline, I11. This beamline comprises a control room and two radiation-controlled experimental hutches, EH1 and EH2, where EH2 is the more versatile of the two. EH2 contains a 2D charge-coupled device (CCD) X-ray area detector and a number of motorized XYZ sample stages where microfluidic devices or other sample environments can be mounted (Fig. 42). Typical powder diffraction experiments make use of a wide X-ray beam (several mm in length) to irradiate segments of horizontally mounted sample capillaries, and thus I11 is optimized to provide a beam of this size.[200] In order to obtain a smaller beam comparable to the size of a microfluidic channel, vertical and horizontal slits upstream from the device were narrowed to cut the beam to a roughly 200 x 200 μm^2 area.

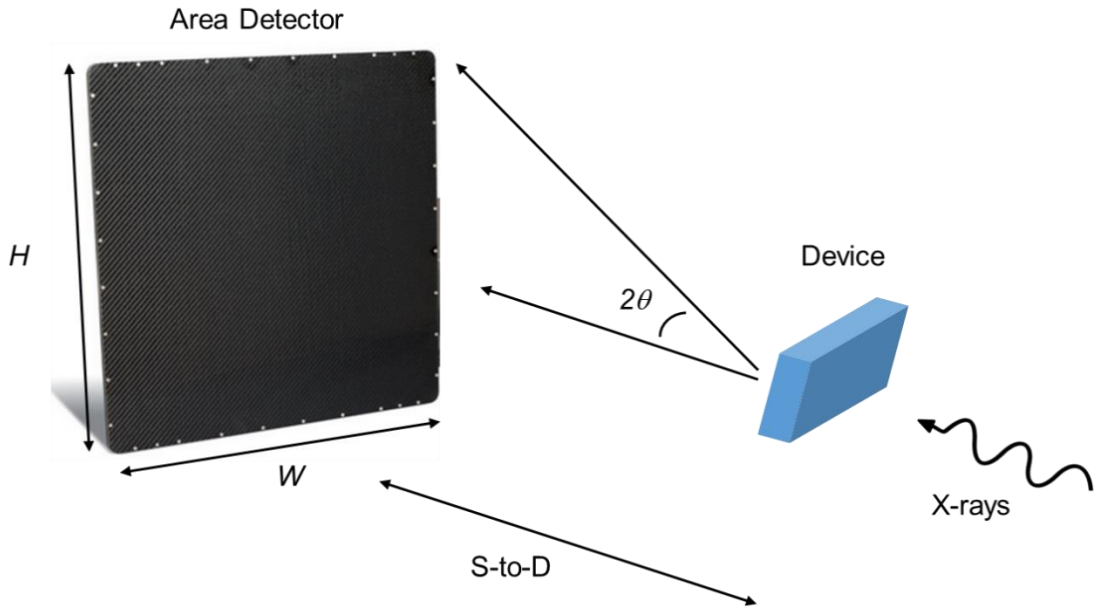

Figure 49: Basic geometry of a microfluidic X-ray experiment with important dimensions labelled. Based on the height (*H*) and width (*W*) of a detector and the sample-to-detector distance (S-to-D), there is a maximum angle 2θ which can be accessed.

Distance Calibration

The standard geometry of a microfluidics-coupled X-ray experiment is shown in Figure 49. One of the most important dimensions of any X-ray experiment is the

sample-to-detector (S-to-D) distance, which determines where a particular angle 2θ will intersect with the plane of detector. This distance must be determined accurately in order to convert from units of distance on a detector into units 2θ, and thus process any experimental data. The standard way of doing this is utilizing a calibrant (a strongly diffracting powder of known structure) and using basic trigonometric functions to back calculate the S-to-D distance. Ideally, this is done for each experiment or after any movement of the equipment, in order to ensure the highest accuracy possible. For this reason, a dedicated calibrant channel, with its own X-ray window, was integrated into the insert-based device (Fig. 45a). During device assembly a small amount of cerium oxide (CeO_2) or silicon powder is deposited in the chamber before sealing the device. Then, once the device is mounted and fluid connections are made, a short scan is performed at this location to calibrate the S-to-D (Fig. 50a).

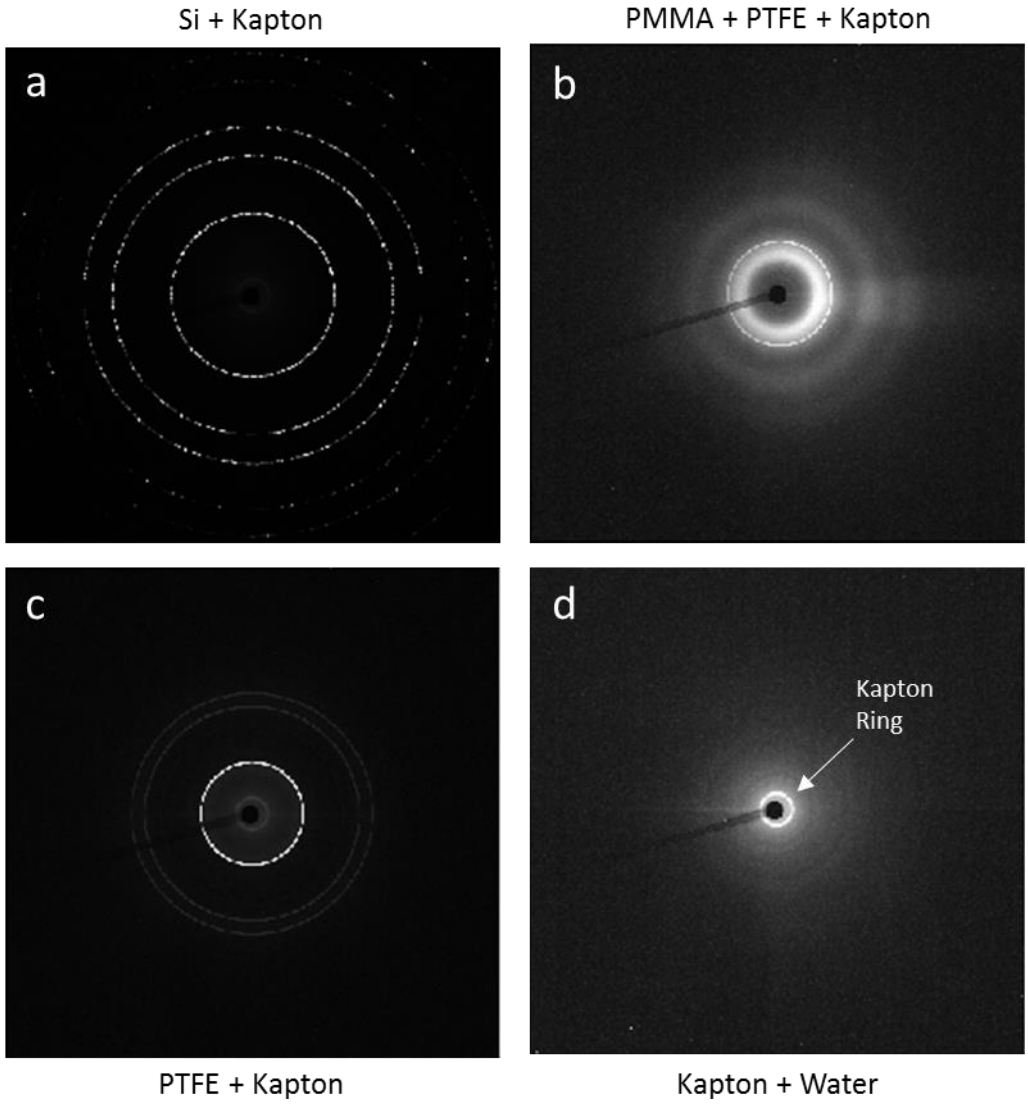

Figure 50: XRD patterns of various positions on the device taken at I11. (a) Silicon in the calibrant channel. (b) Misaligned position with beam hitting PMMA and PTFE. (c) Misaligned position with beam clipping a PTFE channel wall. (d) A refined analysis position filled with water.

Device Alignment

After calibration, the sample stage is raised to expose the main channel to the X-ray beam, and the location of each analysis position is refined. Preliminary alignment is supported by using X-ray sensitive paper to locate the beam and combining this knowledge with the CAD drawing of the device. The final refinement of individual analysis positions is aided by the characteristic diffraction patterns of the various device components. Firstly, the two edges of the main cut-out in the PMMA plates can be found by determining the locations where PMMA scattering ceases (Fig. 50b), with the center of the cut-out being the midpoint between these two locations. Similarly, individual channel crossings through the cut-out are found by minimizing the scattering from PTFE that occurs when the beam clips the side wall of a channel (Fig. 50c). By repeating this process at each analysis position for every experiment, XRD patterns can be reliably obtained from every position on the device (Fig. 50d).

General Remarks

Two beamtimes were conducted at I11, typically utilizing an X-ray beam of 15 keV (additional source and detector data are available in Table 1 and Table 2 of Section 2.2.4). The first of these beamtimes was a part of the earlier MSc project and produced only proof-of-concept data.[41] Even in the second beamtime, usable data could only be collected from continuous flow – not from droplets. As will be discussed later in the section, although the long scan times used at these beamtimes (minutes to hours) are common in powder X-ray diffraction to collect sufficient scattering statistics, these scan times proved to have the opposite effect on the segmented flow system and resulted in the signal being masked by the background. Shorter scan times were not used due to the limitations of the I11 detector and the lack of user and support staff experience with segmented flow XRD. However, it is important to note that improvements have been made to detector operation at I11 and some segmented milli-fluidic results from this beamline are presented in Chapter 4.

2.2.2 ESRF ID13 (Microfocus)

General Beamline Information

Three beamtimes were conducted at beamline ID13 of the European Synchrotron Radiation Facility. This beamline is quite different than Diamond I11, as it is designed for producing micro- and nano-focused X-ray beams for a variety of different techniques, not only XRD. The typical microfocused spot size of an ID13 beam is ~5 µm, so to illuminate a larger region of the flow channel, the device was defocused to provide a beam of approximately 12 x 15 μm^2. Since the beam is focused to attain this size rather than simply cut with slits, the photon flux at the sample was effectively

double that achieved at I11 (Table 1). This also meant that since the spot size was much smaller than the spot at I11, the flux density (flux per unit area) was more than two orders of magnitude larger.

In addition to a smaller, higher flux beam, ID13 also possesses a much faster and more sensitive hybrid photon counting X-ray detector (Eiger X 4M, Dectris).[259] Unlike more standard CCD detectors, these types of detectors are sensitive to single photons and operate digitally – allowing high frame rates (up to kHz) and fast readout times (down to 4 µs) with almost no noise.[198, 260] Such detector speed coupled with high flux density permits the collection of high contrast diffraction patterns in a very short period and with low readout times – meaning that multi-frame data are essentially gapless. This enables fast and dynamic processes to be analyzed, for instance, the flow of droplets past a beam.

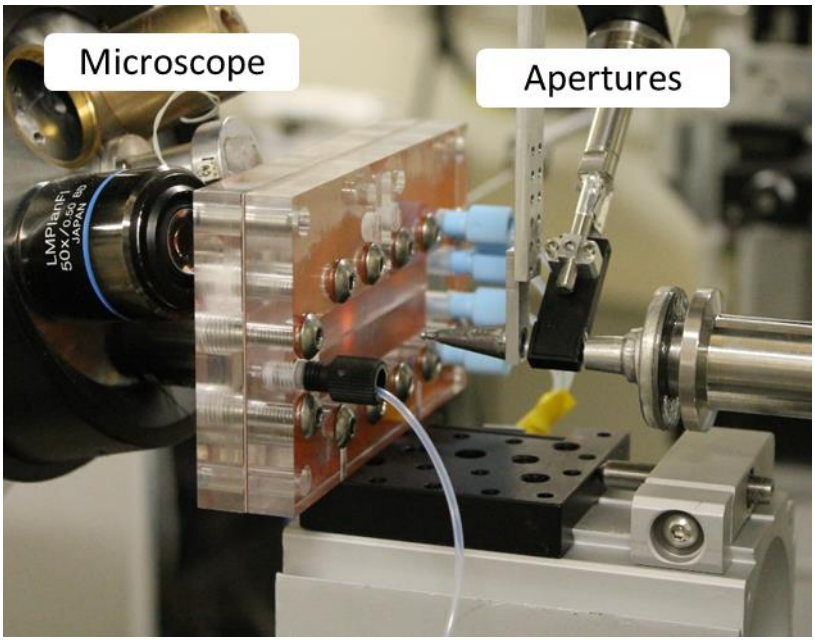

Figure 51: The insert-based device mounted at ID13 with the inline positioning microscope deployed.

Alignment and Calibration

From a practical experimental standpoint, aligning the device with the beam was also much easier at beamline ID13 compared to I11. The experimental hutch at ID13 is equipped with an optical positioning microscope which can be lowered into the beam path while the X-ray shutter is closed (Fig. 51). The focal point of the microscope is pre-aligned with the beam focal point. Thus, each analysis position can be aligned with the beam by simply bringing the position into the focal plane of the microscope and saving the corresponding motor position of the XYZ sample stage. Further, a simple interpolation program was implemented in the control room computer to automatically find and move to any channel position based on the location of the first and last

analysis positions. Similarly, to calibrate S-to-D distance, a calibrant-filled capillary was moved into the beam focal point and a scan was taken at the same detector position utilized during experiments. This meant that only one calibration scan was necessary, and calibrant powders were not required to be loaded into the device during assembly. This combined functionality significantly reduced the time spent on device assembly and alignment per experiment.

Experimental Information

The inline optical microscope could also be utilized to observe the flow start-up procedure during each experiment. At Diamond I11, the inability to visually inspect the flow channel made it difficult to determine when the flows had equilibrated. However, at ID13 this ambiguity was eliminated and the flows could be monitored until droplet production was stabilized. Then, once steady-state droplet generation was observed, the microscope could be raised out of the beam path and the X-ray detector could be moved into its analysis position close to the device. Subsequently, X-ray exposures could be collected at different positions on a device, where the typical exposure settings utilized at ID13 were 50 frames per second (fps) over 10 sec for a total of 500 frames per scan. This data collection strategy implemented at ID13 for segmented flow will be discussed further in Section 2.3.1.

2.2.3 Diamond I22 (SAXS/WAXS)

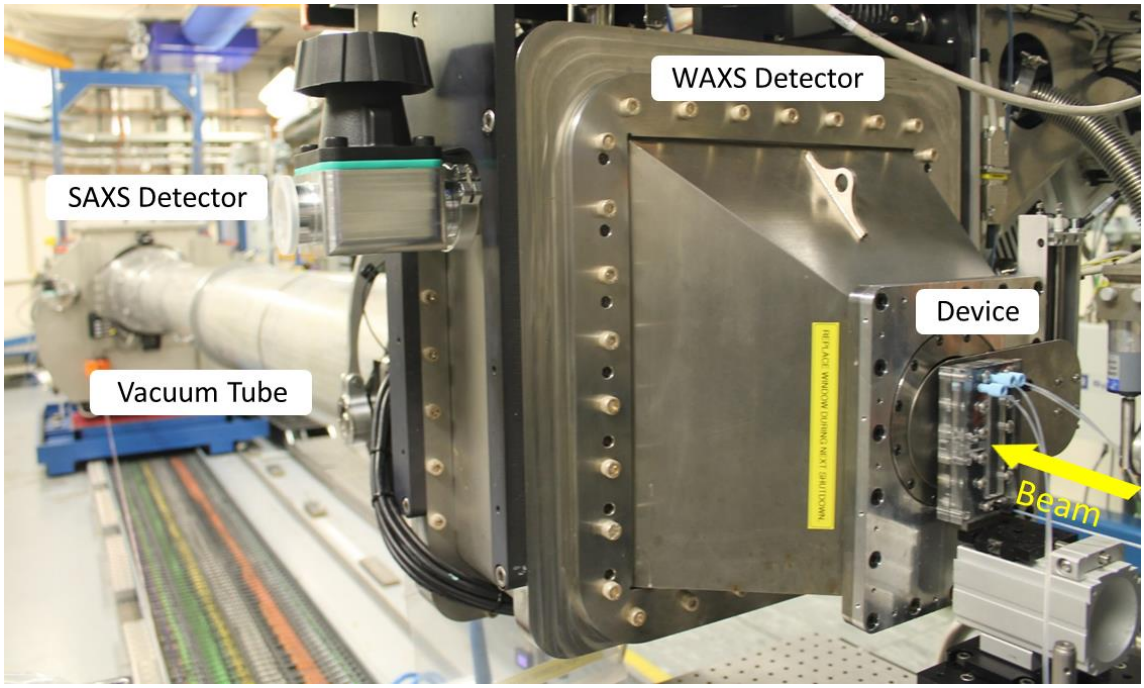

Figure 52: Insert-based device mounted vertically in the experimental hutch of beamline I22.

General Beamline Information

The most recent beamline to be utilized as a part of this thesis was Diamond's SAXS/WAXS beamline, I22. This beamline was chosen over I11 for its specifications, which more closely resemble those of ESRF ID13. While not a microfocus beamline, it has a smaller standard beam size (80 vertical x 320 horizontal μm^2) and a similar hybrid photon counting detector to ID13 (Pilatus 2M, Dectris).[261] Due to the dimensions of the beam, the insert-based device needed to be mounted vertically to prevent the beam from clipping the side walls of the channel. This was achieved using a stainless steel bracket which enabled the device to be mounted using the same optical rail setup as at I11 and ID13 (Fig. 52). Additionally, this beamline is equipped with a second Pilatus detector which allows SAXS and WAXS data to be collected simultaneously. The SAXS detector is situated several meters downstream from the sample stage through a large vacuum tube to minimize beam scattering with air. SAXS results obtained with the device are not included as a part of this thesis. However, the feasibility of droplet microfluidics SAXS has been previously demonstrated by Saldanha *et al*.[236] as discussed previously in Section 1.3.3.

Alignment, Calibration, and Scan Settings

A major difference between I22 and ID13 was the lack of an inline optical microscope for calibration and positioning.† Therefore, to make calibration as simple as possible, a calibrant-filled capillary was used to obtain the S-to-D distance of the first mounted device. Subsequently, care was taken not to move the optical rail mount or positioner (Fig. 42) during the exchange of devices over the course of the beamtime, enabling the same S-to-D distance to be used for all experiments. Analysis position refinement was conducted in a manner similar to at I11, but with an automated process as follows: X-ray exposures were taken while scanning the device vertically and horizontally across the analysis position. The control computer software then generated plots of X-ray transmission vs. position and automatically moved the device into the center of maximum transmission. This procedure was performed at the first and last analysis positions, and a similar interpolation program to at ID13 was utilized to navigate to each analysis position during experiments. After the initial device was mounted, the refined position of all subsequent devices was found to be within ~50 µm – illustrating the reproducibility of the device exchange system. After alignment, data were collected in a similar manner to at ID13 (and with similar results), with typical scan settings of 100 fps over 20 sec for a total of 2000 frames per scan.

---

† It should be noted that an inline microscope is planned as a part of a forthcoming I22 upgrade.

2.2.4 Comparison of Beamlines

Beamlines are unique facilities made up of any number of control rooms, experimental hutches, instruments, and support laboratories, and have many different technical and practical facets. They are also typically optimized for a particular application or technique, making general comparison of a beamline's overall quality difficult, if not completely unproductive. Thus, this section will seek to merely identify important beamline characteristics and practical features which were most beneficial in conducting microfluidics coupled X-ray diffraction experiments.

Table 1: X-ray Beam Characteristics

Beamline	Energy (keV)	Beam size (H x W μm^2)	Flux at sample (ph/s)	Flux Density (ph/s/μm^2)
Diamond I11	15	~200 x 200	~7.12 x 10^{11}	1.78 x 10^7
ESRF ID13	13	12 x 15	~1.5 x 10^{12}	8.33 x 10^9
Diamond I22	12.4	~80 x 320	~6 x 10^{12}	2.34 x 10^8

Comparison of X-ray Beams

The X-ray energy used at all three beamlines was comparable (Table 1), and each beam had the power to easily transmit through the device windows and solution without significant attenuation.‡ Additionally, all beamlines had the ability to produce beams smaller than the microchannel/ analysis position dimensions. These two characteristics together enable each beamline to be utilized for less demanding continuous flow microfluidics experiments, where crystals grow on device surfaces and no fast processes (< seconds) need to be captured. However, there are significant differences between the beamlines which have profound implications on their effectiveness for segmented flow analysis.

Table 2: Detector Characteristics and Experimental Sample-to-Detector Distance

Beamline	Detector	Pixel Size (μm)	Aspect Ratio (H x W)	Sample-to-Detector Distance (mm)
Diamond I11	Pixium RF4343	148	2880 x 2881	261
ESRF ID13	Eiger X 4M	75	2167 x 2070	116
Diamond I22	Pilatus 2M	172	1475 x 1679	164

In technical terms, it is clear from Table 1 and Table 2 that the greatest differences between the beamlines utilized during this project were in X-ray flux/ flux density, beam size, and detector type. Beamline ID13 stands apart from both Diamond beamlines with

‡ At all energies there should be >97% photon transmission through the Kapton windows according to the absorption calculator from the Advanced Photon Source (APS) found at https://11bm.xray.aps.anl.gov/absorb/absorb.php

a two orders of magnitude smaller beam size. At a similar overall flux value, this translates into much larger flux densities in the irradiated area. Practically, this means that when a flowing crystal does pass by the beam, a much higher percentage of photons should encounter the crystal than with a larger, lower density beam where many photons are “wasted” on the solvent. The result is that higher signal-to-noise ratio data should be obtained from smaller, higher flux density beams.

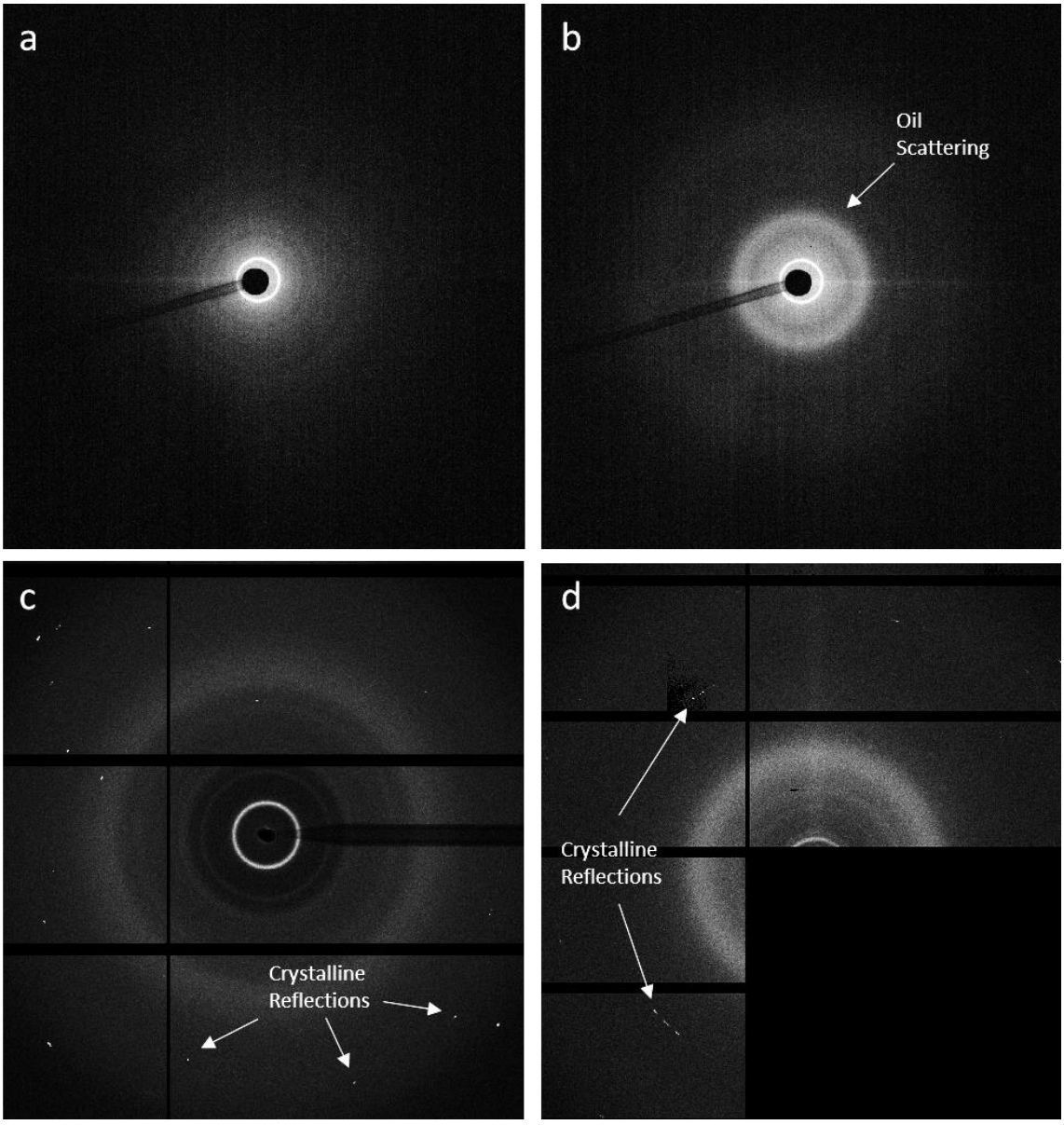

Figure 53: Raw diffraction frames from (a and b) Diamond I11, (c) ESRF ID13, and (d) Diamond I22. (a) 60 sec exposure of water flow. (b) 60 sec exposure of droplet flow with no crystalline diffraction visible. (c) 20 ms and (d) 10 ms frames from transiting droplet showing crystalline diffraction.

Comparison of X-ray Detectors

Nevertheless, the data obtained at ID13 and I22 from droplet microfluidics experiments was of a similar quality. While undoubtedly there is a flux limit to

performing experiments on dynamic systems, e.g. flowing droplets, it appears that this was not the limiting factor of the experiments presented here. Instead, the detector speed and sensitivity proved to be much more important for capturing data from segmented flow than originally anticipated. This is illustrated in Figure 53, which contains raw diffraction frames taken from similar experiments at all three beamlines. Figure 53a displays a 60 sec exposure from I11 of the continuous flow of water in the device. The only features visible are low intensity diffuse water scattering and a low angle Debye-Scherrer ring characteristic of the Kapton windows. However, when the oil flow was initiated and Ca^{2+} and CO_3^{2-} reagents added, rather than displaying the accumulation of crystalline reflections, a 60 sec exposure is completely dominated by diffuse scattering from the electron dense fluorinated oil phase (Fig. 53b). Conversely, in the high frame rate scans collected on the hybrid photon counting detectors at ID13 and I22, 10 and 20 ms frames captured during droplet transit display only water scattering and diffraction spots from the crystals of interest (Fig. 53c and d). At I11, the high scattering intensity from the oil continuous phase effectively blurs the signal from passing droplets, with longer integration times appearing to make the problem worse, not better. Therefore, information from the crystals of interest can only be obtained by isolating the scattering of the dispersed phase from the continuous phase, where this was achieved here through utilizing a series of consecutive, short exposures.

General Comparison

Some other important considerations in beamline selection are the ease and efficiency with which an experiment can be conducted and the overall “user friendliness” of a beamline. The quicker an experiment can be set up, the more experiments can be run per beamtime and the more results that can be collected. The most helpful feature encountered in this project was the inline microscope at ESRF ID13, which was an invaluable tool in the positioning and alignment of devices. Loading a calibrant powder into each device to determine S-to-D, as required at Diamond I11, is time-consuming and also risks contaminating the main flow channel if static electricity disperses the powder. Also, combining the optical refinement of each analysis position with automated interpolation saves a great deal of time during the mounting of each chip. Finally, the ability to visualize the flow, just like in the home laboratory, makes device start-up and inspection much easier.

However, one of beamline ID13’s greatest strengths, namely its flexibility, is also a major weakness. For maximum versatility, all hardware and scan parameters are

controlled via command line scripts in the SPEC coding language,[§] and there are no graphical user interfaces (GUIs) to simplify beamline operation. While this provides a huge range of executable functions, it amounts to a steep learning curve for new users. It also means there is a great risk of damaging beamline hardware, which was intentionally designed with a large range of motion and many degrees of freedom to facilitate different experimental setups. Since every microfluidics experiment requires movement of the sample stage, inline microscope, and detector, there are many opportunities for failure. This risk of hardware damage is epitomized by the beamstop alignment procedure – an essential part of any synchrotron experiment to protect the detector from being hit by the main beam. At ID13, the beamstop is not integrated into the detector or fixed in place, and must be moved and realigned after device start-up for every experiment. Failure to do this could result in catastrophic damage to the detector. Yet, it is important to note that beamlines are constant "works-in-progress", and many of these features will inevitably improve over time.

In spite of not being equipped with an inline microscope, Diamond I22 has many features which make beamline operation simpler and safer than at ID13. Automation and GUIs make device alignment fairly straightforward, and careful set up of the optical rail mount means that a single S-to-D value can be used for an entire beamtime – assuming movement of the setup is not required. There are also many safety features in place to prevent hardware damage. The sample stage is in a designated area, and when the X-ray shutter is closed, hard covers can be lowered to prevent damage to detectors and beamline optics during device mounting. No movement of detectors is required during set up or operation, and no WAXS beamstop is required, as the detector panel in line with the main beam has been removed to allow transit of low angle X-rays to the SAXS detector (Fig. 53d). Finally, the beamstop for the SAXS detector remains fixed in place, so not to be vulnerable to human error.

2.3 Droplet Microfluidics-Coupled X-ray Diffraction (DMC-XRD)

2.3.1 Analysis Concept

Working Principle

As previously discussed in Section 1.2.2, droplet microfluidic devices offer a way to eliminate Taylor dispersion, ensuring uniform concentration and residence time distributions along a flow channel. Researchers can profit from this feature of

[§] At the time of writing, beamline ID13 and the entire ESRF are being updated to a new Python-based control language called Bliss (BeamLine Instrument Support Software).

segmented microflows to perform time-resolved analysis of reactions, where spatial resolution can be converted into time resolution based on the flow rate/velocity of the fluid droplets. Here, utilization of this principle has led to the development of a new technique for studying crystallization: Droplet Microfluidics-Coupled X-ray Diffraction (DMC-XRD). This technique allows complete powder diffraction patterns to be collected from crystals encapsulated in continuously flowing microfluidic droplets, where correlation between the position of the droplet and its residence time on-chip permits structures to be probed as a function of reaction time (Fig. 54).

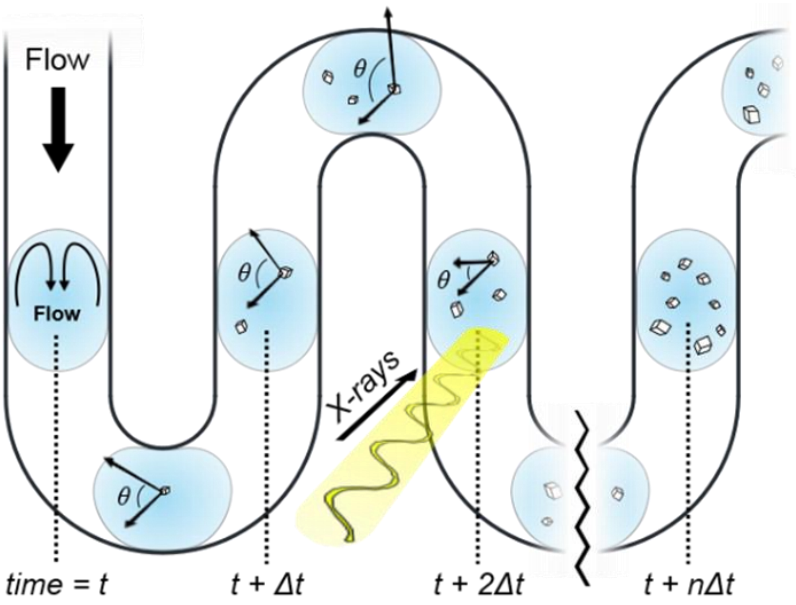

Figure 54: Droplet microfluidics-coupled XRD concept. Moving the device with respect to the X-ray beam allows access to different time-points, while the internal droplet flows rotate crystals to diffract from different orientations.

While the steady, global flow in the microchannel provides accurate time-resolution, the internal recirculating flows within each droplet work to rapidly mix the solution (see Section 2.1.2) and continually rotate the growing crystallites. This latter function ensures that crystals present different orientations to the beam, allowing reflections from different angles (θ) satisfying the Bragg condition (Equation 9) to be collected (Fig. 54). In this way, the droplets themselves serve the same role as the goniometers utilized in single crystal diffraction experiments to rotate crystals[262] and the capillary spinners utilized in powder diffraction experiments to reduce preferred sample orientation.[200] Therefore, DMC-XRD is similar to injector-based serial crystallographic techniques (see Section 1.3.4), which obtain a complete diffraction pattern from a flow of randomly oriented crystallites rather than from a single crystal or powder.[249]

Mitigation of Beam Damage

Also, like serial crystallography, each new reflection is obtained from a fresh crystal replenished by the flow, so that the effects of beam damage are minimized, if not eliminated completely.[246] The radiation dose (*D*) sustained by a flowing crystal can be approximated by the equation,

$$\boldsymbol{D = \mu E I_0 t} \qquad \textbf{(10)}$$

where μ is the mass attenuation coefficient (~21 cm^2/g for calcite at 13 keV)[263], *E* is the X-ray energy in eV, I_0 is the incident flux density, and *t* is the dwell time in the beam.[246] For experiments at beamline ID13 the maximum dwell time of a crystal in the beam is approximately 2.5 ms, resulting in a dose of ~9.1 x 10^4 Gy (J/kg) for each irradiated calcite crystal. Comparatively, this figure is more than two orders of magnitude lower than the Henderson limit (2 x 10^7 Gy), which is a guide for radiation damage in macromolecular crystallography and the value at which the original diffraction intensity is roughly halved.[264] Therefore, there should be no changes in diffraction intensity in DMC-XRD and radiation damage can be safely neglected. This feature of DMC-XRD will become increasingly important if analyzing biological and other types of materials that are much more sensitive to radiation than compared to calcite.

Data Collection Method

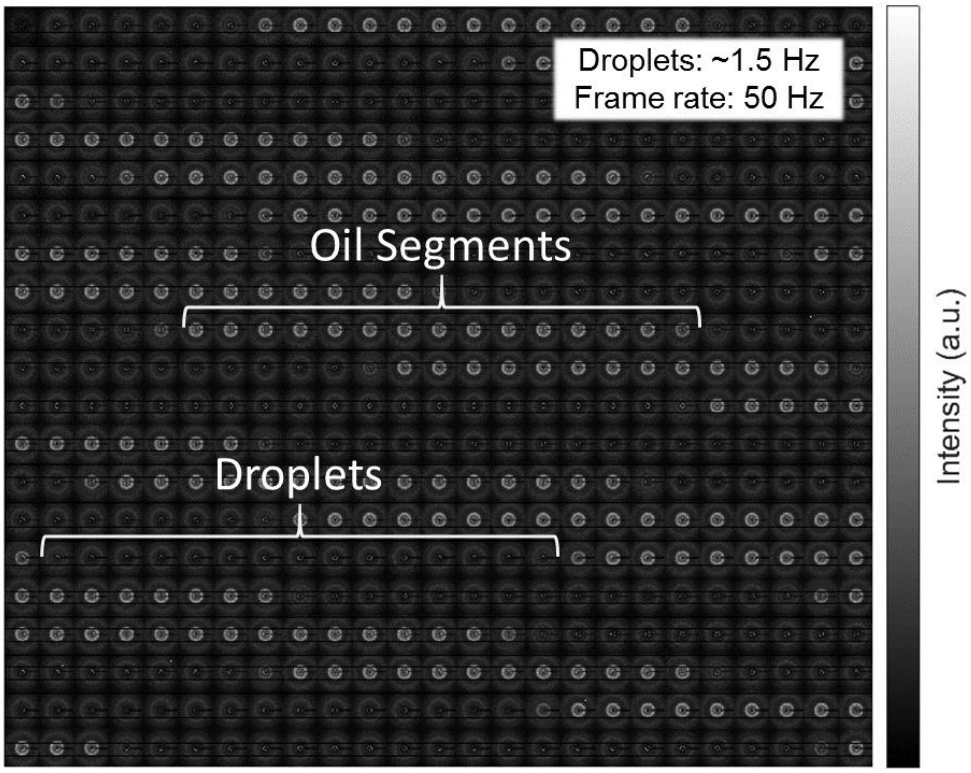

Figure 55: Collage of a frame-by-frame X-ray exposure (20 ms for a total of 10 sec) from beamline ID13 revealing the alternating flow of water and fluorinated oil.

Since long X-ray exposures were found to obscure signal from droplets (Fig. 53b), short exposures are needed to capture and isolate each diffraction event that occurs during droplet transit. However, this presents a problem as there are not enough reflections in a single frame to build a full diffraction pattern. In order to overcome this challenge, many individual frames containing crystal 'hits' must be compiled to generate a complete diffraction pattern comprising reflections from each d spacing and with sufficient statistics to produce peaks at the appropriate relative intensities. Hence, many frames are collected consecutively from a particular position to capture multiple diffraction events, where the alternating scattering profiles of the water and oil phases reveal the flow of droplets in the device (Fig. 55). Such analysis also confirms the large difference in scattering intensity between the water droplets and continuous oil phase.

Yet, this additional information comes at a cost. Rather than having a single diffraction pattern to process, many hundreds to thousands of patterns are generated in only seconds of analysis, where a large percentage (depending on the w/o volume fraction and nucleation rate) of these do not contain information of interest. Consequently, the ability to perform DMC-XRD analysis requires a method for efficiently sorting and selecting data to incorporate into a final diffraction pattern. The next section will discuss the strategies implemented herein to select and process such large volumes of synchrotron data.

2.3.2 Data Processing Method

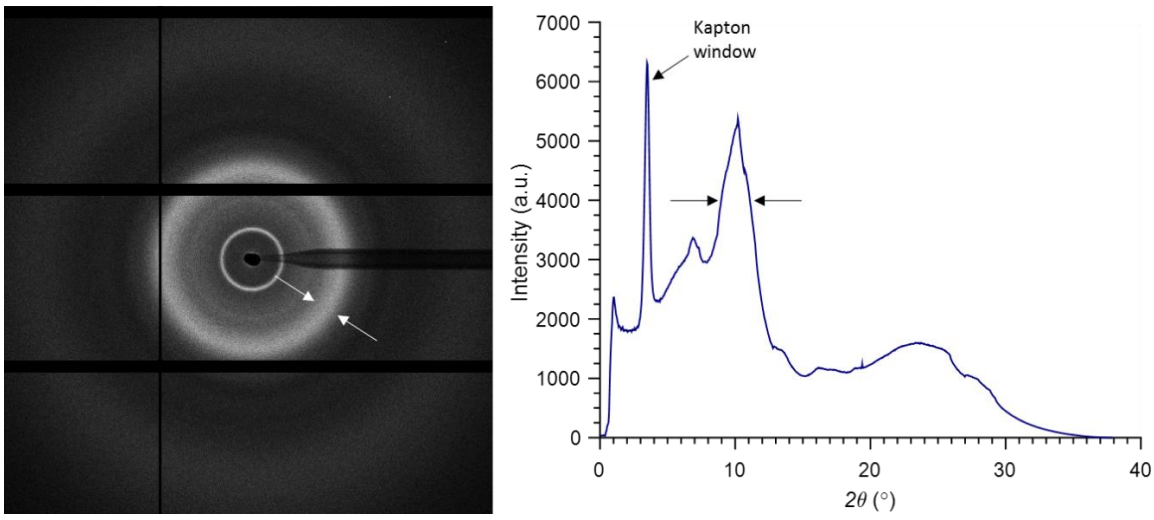

Figure 56: A raw 2D (left) and 1D (right) diffraction pattern revealing the characteristic scattering band of FC-40 fluorinated oil from 8.5-11.5° 2θ at 13 keV (arrows).

Frame Sorting and Selection

A MATLAB (MathWorks, Natick, MA) program was developed to convert raw 2D data obtained from a beamtime into usable 1D diffraction patterns for identifying crystal structure. The first processing step is selecting which frames should be analyzed (i.e.

aqueous droplets) and which should be ignored (i.e. oil segments). Fortunately, due to the large intensity difference between frames containing scattering from oil and frames containing scattering from water, distinguishing between them is relatively straightforward. There is a large scattering band from the fluorinated oil at around 10° (Fig. 56), which is used to identify oil frames. The MATLAB program interrogates test pixels over this band for each frame, and if the intensity value of any test pixel is above an arbitrary value, the frame is discarded. Selection of this value is determined empirically for each experiment to ensure the threshold is sufficiently low to exclude all oil frames, but not so low as to potentially lose some frames of interest. This is most important for frames taken while the droplets are entering or exiting the beam, which often contain several crystal hits, but also a larger proportion of oil scattering than in the center of a droplet. Conversely, the summed intensity value of a larger region of interest (ROI) over the scattering band can be interrogated instead of test pixels, where this is preferred if the contrast between individual band pixels in water and oil frames is low (utilized for the results presented in Chapter 5.3).

Background Subtraction and Thresholding

Once frames are sorted and the frames of interest are identified, these frames must be processed to remove any scattering from device materials or solvent. The MATLAB processing routine uses two mechanisms to achieve this: *(1)* background subtraction and *(2)* thresholding. The general processing method implemented in this work is demonstrated by the following equation:

$$\mathbf{n}_{processed} = \mathbf{n}_{raw} - \boldsymbol{\alpha} \cdot \mathbf{n}_{background} \quad \textbf{(11)}$$

where n is a particular pixel located at (x_i,y_i) and α is a background intensity modifier. The first step in applying this routine is in selecting a suitable background frame. Initially, scans were taken of the insert-based device filled with water to be used as dedicated background reference patterns. However, frames from these scans were found to be unsuitable references because they did not contain a thin layer of oil around the water phase, and more importantly, because unique texturing in the device windows, small changes in S-to-D distance, and other unaccountable differences between scans make the application of a universal background reference impossible. Therefore, a unique frame containing only water scattering must be selected from each individual scan to serve as that scan's background.

Next, a suitable α factor must be selected. Since intensity values are directly related to the number of photons which hit a particular detector pixel in a given amount of time (a quantum phenomenon),[265] even two exposures of the same duration will have a slightly different intensity distribution across pixels. Thus, subtraction of one

frame containing only water scattering from another frame containing only water scattering will leave a residual value. Additionally, the presence of crystalline sample within droplets changes the solvent:sample ratio occupying the beam path, varying the background intensity. To compensate for these effects, a factor of α = 2 was typically used to account for background scattering. Lastly, a threshold determined for each experiment is applied to the entire image (typically 25-30 arbitrary units, a.u., for ID13 and I22 data). This sets any pixels less than the threshold value to zero, to eliminate any remaining low intensity scattering that could add noise to the final pattern.

Combination and Integration

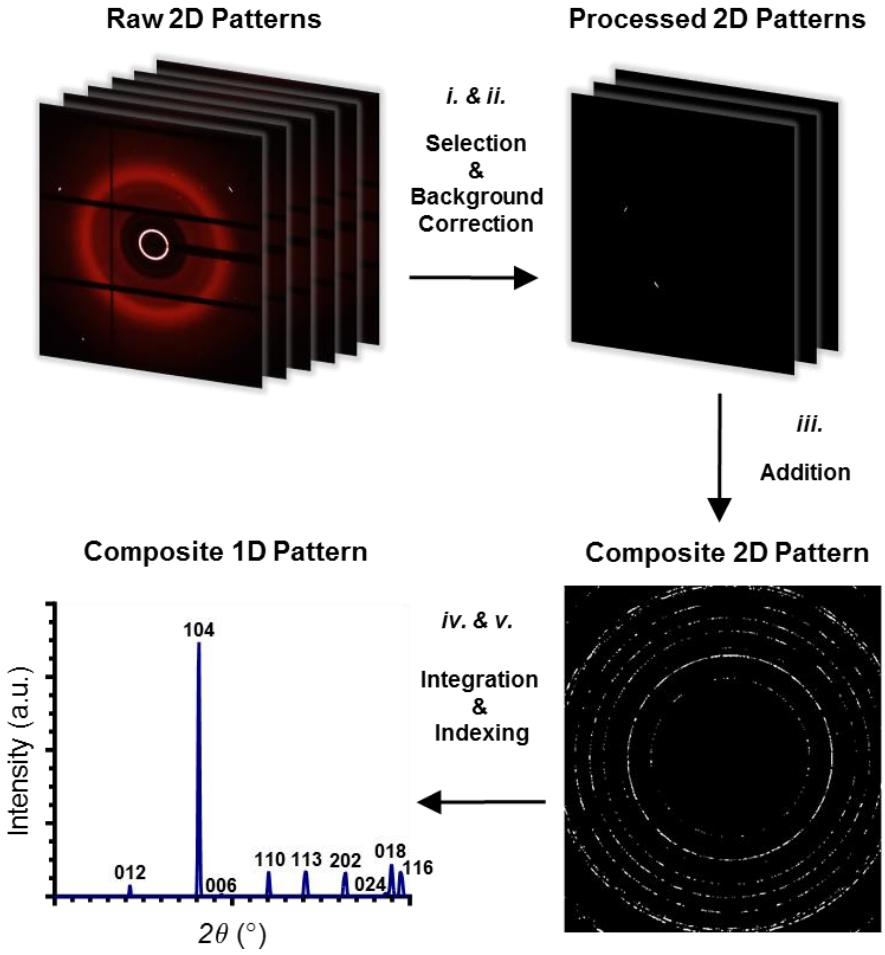

Figure 57: Standard data processing workflow for DMC-XRD using the example of calcite growth observed at beamline ID13.

After all target frames have been processed, these frames are combined to produce a composite 2D diffraction pattern containing all the crystalline reflections observed in a particular scan. This pattern is then azimuthally integrated to obtain the 1D diffraction pattern displaying intensity as a function of scattering angle, 2θ. Integration is conducted with minimal binning to preserve spatial resolution while also avoiding oversampling, where the number of samples taken at a given radius (*r*,

number of pixels from beam center) is equal to the circumference ($2\pi r$) converted into units of radians. Finally, the 1D patterns can be indexed using reference data to identify particular reflections and determine the structure of the materials present. An overview of the entire DMC-XRD processing workflow is illustrated in Figure 57 and copy of the general MATLAB script can be found in Appendix II.

Continuous Flow Data Processing

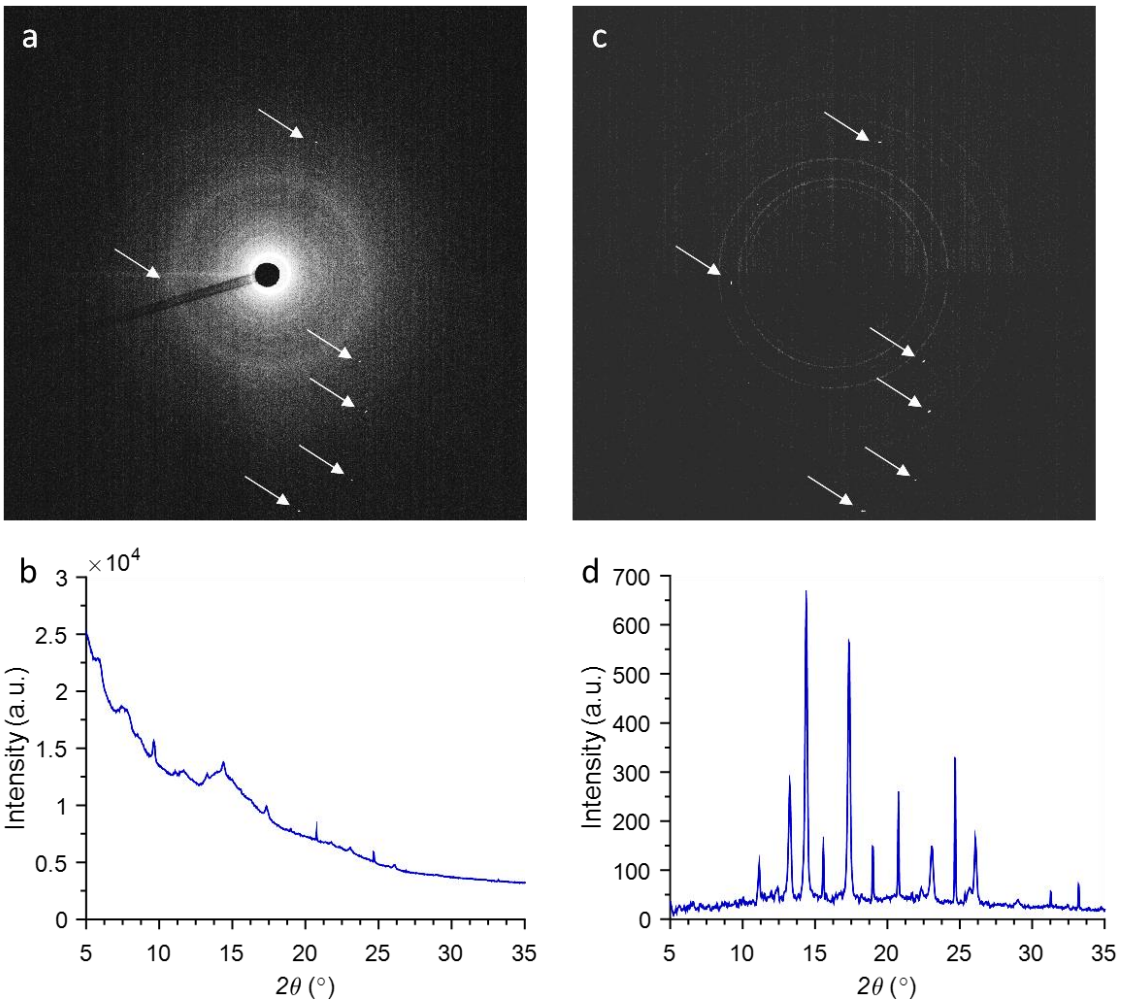

Figure 58: Raw (a) 2D and (b) 1D diffraction patterns of $CaCO_3$ crystallization in continuous flow collected from a 60 sec exposure at Diamond I11. The same (c) 2D and (d) 1D patterns processed with background subtraction, thresholding, and a median filter. The white arrows indicate diffraction spots from single crystals, where some faint Debye-Scherrer rings from polycrystals can also be seen in (c).

Data processing was also required for diffraction patterns obtained from continuous flow experiments at Diamond beamline I11. While the ionic conditions employed during this beamtime caused significant crystal deposition on channel walls, long exposure times (1-2 min) resulted in the collection of a great deal of background scattering from the device windows and solution in addition to crystalline reflections. This is clearly illustrated by the 1D and 2D patterns presented in Figure 58. In the raw

patterns, crystalline reflections are barely visible above diffuse background scattering (Fig. 58a and b). Further, so few reflections were seen – and at such low contrast – that the standard background subtraction and thresholding routine implemented for DMC-XRD data was not sufficient to extract the data. More complicated image processing methods utilizing filters, i.e. median or Gaussian, can also be employed, however must be used with caution so as to not overly manipulate the underlying data. As a test, a conservative median filter was applied after background subtraction and before thresholding to provide greater contrast in the 2D pattern prior to integration to 1D (Fig. 58c). This filter sets the intensity of each pixel to the median intensity value of a surrounding 3 x 3 pixel neighborhood. Adopting this processing workflow for the continuous flow data produced much better 1D patterns to be used for indexing (Fig. 58d), and therefore, all continuous flow XRD data presented here were processed using this strategy.

2.3.3 Detection Limit Measurements

Dilution Experiments

In order to estimate the detection limit of this new technique, pre-made nanoparticles (NPs) of known size and composition were introduced into water droplets and measured using DMC-XRD at decreasing concentrations until their signal could no longer be detected. The limit of detection of a particular crystalline material in the wide-angle X-ray scattering region is determined by factors such as particle size and orientation, crystal symmetry, electron density and the amount of scatterers (i.e. concentration/ weight percentage),[266-268] and in practice, is also affected by background scattering (e.g. from the device windows, solvent, or amorphous content) and data processing parameters.[269] Two types of NPs were selected for these measurements: magnetite (Fe_3O_4) and gold (Au) of 11.6 ± 2.3 nm and 15.2 ± 1.5 nm diameter, respectively (Fig. 59a and b).

Due to their larger size and electron density ($n_{e\ Au} \approx 4.67 \times 10^{24}$ e^-/cm^3), the gold NPs were detectable at a lower concentration, down to between 0.05 wt% and 0.0167 wt%. Conversely, magnetite NPs ($n_{e\ Mag} \approx 1.47 \times 10^{24}$ e^-/cm^3) were only detected down to between 0.3125 and 0.25 wt%. When the diffraction intensity of both NPs was plotted as a function of concentration, the trends followed a logarithmic decay (Fig. 59d), where the last data point shown for each NP is the last concentration at which the main Bragg peak of the particular material was observed. The level of sensitivity displayed by DMC-XRD puts it in the same league as second harmonic generation (SHG) microscopy-guided PXRD, the most sensitive XRD technique to date, which has

been reported to enable detection of crystalline material down to 100 parts per million (ppm, 0.01 wt%).[267]

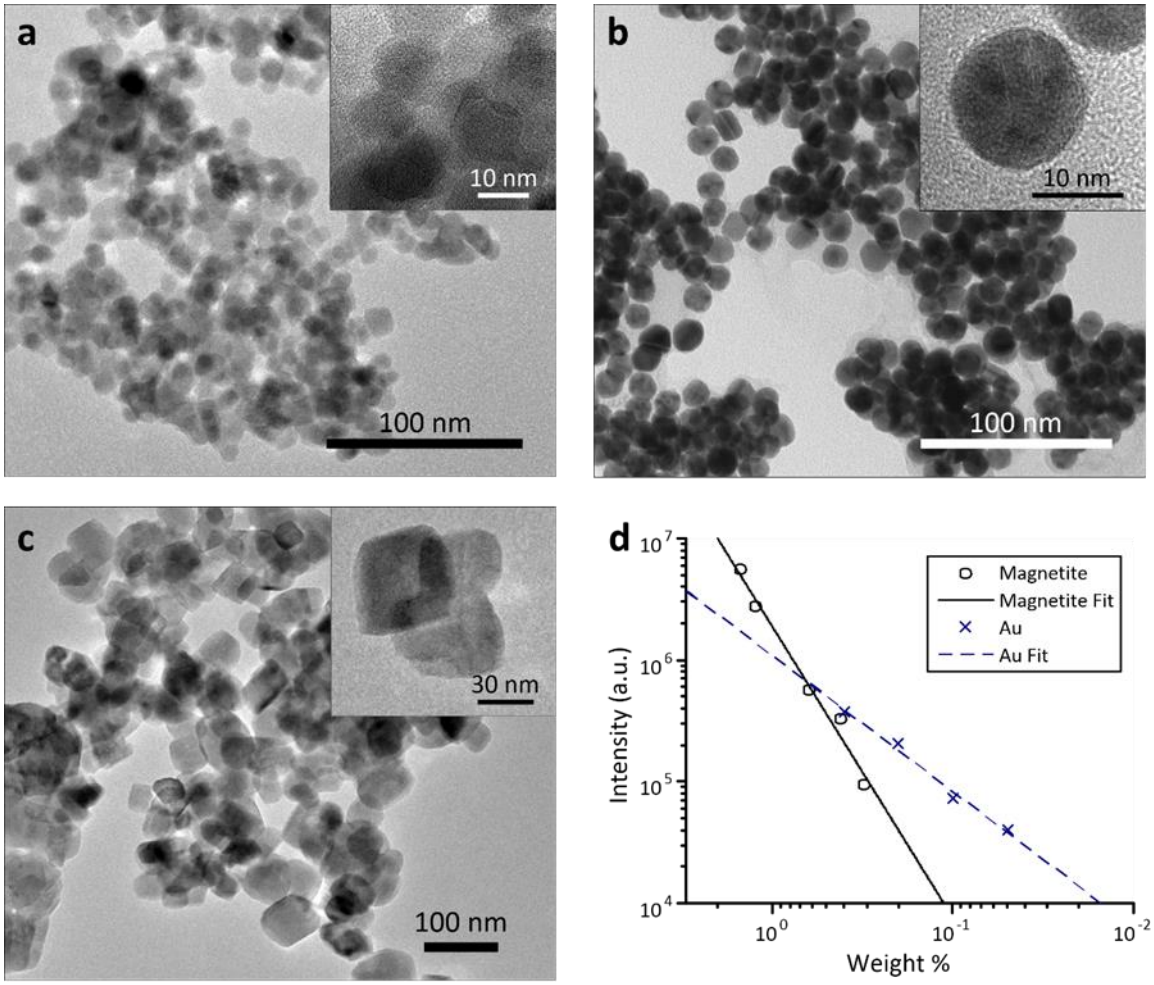

Figure 59: Transmission electron micrographs revealing the size of (a) magnetite, (b) gold and (c) calcite nanoparticles. (d) Diffraction signal decay of nanoparticles measured by the heights of the (311) and (111) reflections of magnetite and gold, respectively, at their indicated concentration within droplets.

These measurements can also be used to estimate the required signal-to-noise ratio, or contrast, needed for DMC-XRD based on the current window materials and processing parameters. The highest Bragg reflections of both magnetite and gold were lost due to noise in the order of 10^4 a.u. (Fig. 59d). This noise value was accumulated over the 500 frames collected per scan, of which ~115-188 are actually from the droplets based on the volume fractions of the dispersed phase needed to obtain the required NP dilutions. Thus, there was a baseline noise of roughly 53-85 a.u. per single frame from a droplet. For context, a single (104) reflection from calcite typically produces pixels with intensity values on the order of 10^2 to 10^3 a.u. (Fig. 60).

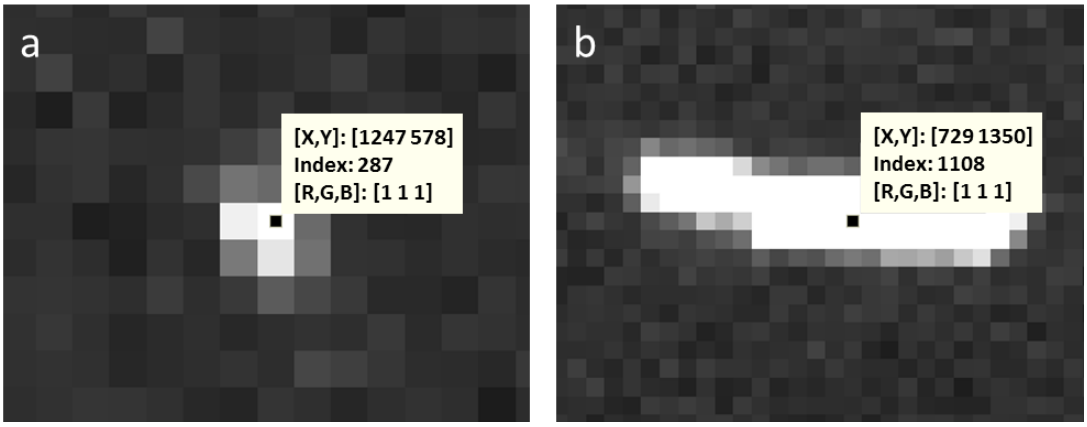

Figure 60: Representative single calcite (104) reflections from raw single 20 ms frames taken at beamline ID13. (a) Image from Position 2 and (b) image from Position 20 during a calcite nanoparticle-seeded experiment. The [X,Y] values are the pixel coordinates, and the Index value is the intensity in arbitrary units.

Calcite Detection

A similar detection experiment was performed with pre-made calcite NPs of 50.3 ± 11.6 nm (Fig. 59c). However, even at the highest concentration attempted, 1.0 wt%, no diffraction could be observed, where this is attributed to the lower electron density of calcite ($n_{e\ Cal} \approx 0.82 \times 10^{24}$ e^-/cm^3). This result demonstrates the sensitivity of diffraction intensity to electron density: the calcite NPs are five times larger than the magnetite ones and only half as electron dense, yet they cannot be detected at more than three times the weight percentage. While not yielding the minimum detectable concentration for calcite NPs of this size, this experiment did confirm that in the subsequent experiments which utilized these same NPs as seed crystals (see Chapter 3), the measured diffraction was from actual crystal growth and not simply from the detection of the initial seeds.

General Remarks

These experiments provided a helpful estimation of the detection limit and required signal-to-noise ratio of the current DMC-XRD method. However, it is important to note that it is difficult to predict the precise size at which a particular material will be detected in a less-controlled scenario. This is due to the dependence of the detection limit on not only intrinsic properties of the crystal, but also extrinsic ones – the most important being the number of crystals which nucleate and subsequently grow. Therefore, to accomplish such a task, a complex model which incorporates device and solvent background measurements, data processing parameters, intrinsic material information, and experiment-dependent kinetic properties (e.g. nucleation and growth rates) would be required.

2.4 Preliminary Data Collection

Calcium Carbonate as a Model System

DMC-XRD and continuous flow diffraction analysis with the insert-based device were trialed using the crystallization of calcium carbonate ($CaCO_3$). This material is a good model system for studying crystallization since it can be precipitated easily using a range of methods (including direct mixing) and has three anhydrous polymorphs with unique morphologies: calcite (rhombohedral), aragonite (needle-like), and vaterite (spherical or plate-like), in order of descending stability at room temperature.[40, 270] $CaCO_3$ is also an important geological and industrial material, and is utilized by Nature as the primary component of a variety of biominerals.[48, 271] Further, $CaCO_3$ is known to form from an amorphous precursor, amorphous calcium carbonate (ACC), in a number of contexts,[91, 272] where elucidating the mechanisms of $CaCO_3$ crystallization remains an active area of scientific research (Section 1.1). For these reasons, $CaCO_3$ was utilized as a well-characterized, yet still fascinating system with which to compare continuous and segmented flow data collection.

2.4.1 Continuous Flow Results

Experimental Conditions

$CaCO_3$ crystallization due to the direct mixing of aqueous $CaCl_2$ and Na_2CO_3 solutions in continuous flow was studied within the insert-based device at Diamond I11. Final concentrations of 4 mM Ca^{2+}/CO_3^{2-} were employed, with all solutions being filtered with a 0.22 µm Millipore membrane prior to being loaded into syringes. Reactions were studied at constant ambient temperature (23 °C) along the flow channel and also using the temperature gradient device characterized in Section 2.1.3 (with positions of interest at 49, 38, and 33 °C). Results obtained at beamline I11 were supplemented by optical and electron microscopy at Leeds and equilibrium modelling of the solution chemistry with Visual MINTEQ (KTH, Sweden). This software considers the sorption and complexation of the ions and chemical species in solution to simulate parameters such as pH, ionic strength, and the saturation index (*SI*) of common mineral phases, where the K_{SP} values for ACC and for the other polymorphs at non-ambient conditions were supplemented using the accepted models from Brečević and Nielsen[273] and Plummer and Busenberg,[274] respectively.

Table 3: Solution Conditions from Visual MINTEQ for Continuous Flow Experiments

Temperature	Polymorph	SI (log IAP - log K_{SP})	pH	Ionic Strength
23 °C	Calcite	2.536	10.683	0.0157
	Aragonite	2.391		
	Vaterite	1.964		
	ACC	0.446		
33 °C	Calcite	2.524	10.457	0.0153
	Aragonite	2.386		
	Vaterite	1.979		
	ACC	0.489		
38 °C	Calcite	2.516	10.347	0.0151
	Aragonite	2.381		
	Vaterite	1.982		
	ACC	0.511		
49 °C	Calcite	2.492	10.116	0.0145
	Aragonite	2.364		
	Vaterite	1.984		
	ACC	0.561		

The modelling results for the solution conditions utilized during synchrotron experiments can be found in Table 3. The supersaturation of vaterite and ACC were shown to increase at higher temperatures, while the supersaturation of the other phases decreases. However, the supersaturation of calcite decreases slightly more than that of aragonite. Additionally, the solution pH and ionic strength also decreased with increasing temperature.

Ambient Temperature Experiments

At ambient conditions the onset of crystallization was fast, with crystals visible at the T-junction within 2 min experiment time, and a clear line of crystals was visible at the interface between the $CaCl_2$ and Na_2CO_3 flows after 5 min (Fig. 61d). The morphology of the crystals appeared to be rhombohedral, and the first diffraction pattern taken at 10 min contained a single (104) peak – confirming the polymorph was calcite (Fig. 62a, blue). Crystals were also observed by microscopy at Positions 1 and 2 within 5 min, where surface growth was found along the entire channel width, yet appeared to be intensified at scratches on the Kapton windows (Fig. 61e and f). Over the course of the ~45 min long experiment, further growth was observed at all three positions of interest (Fig. 61g-l), but subsequent channels contained less and less growth, with Position 6 containing almost none.

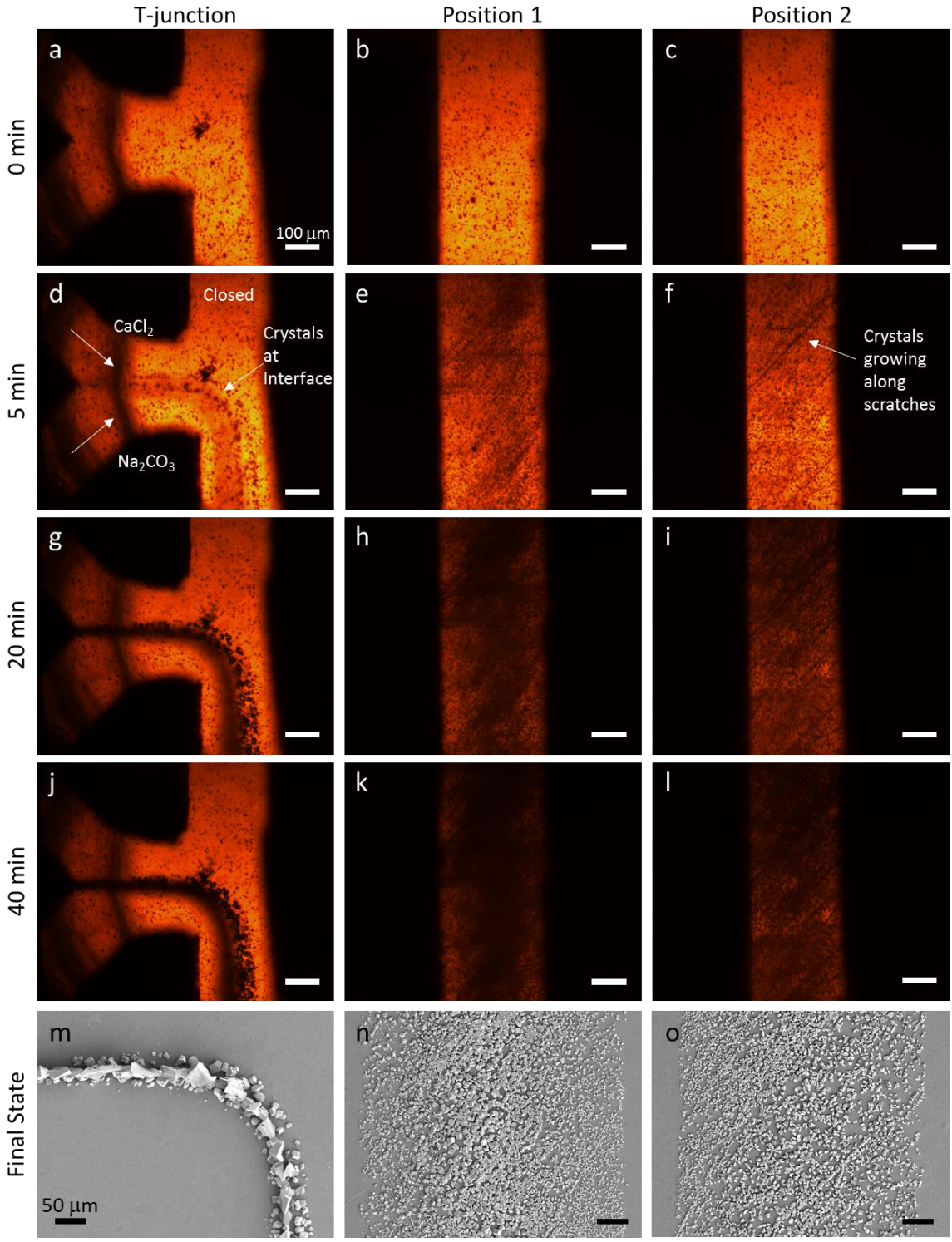

Figure 61: Optical micrographs of the bottom Kapton window at the indicated channel position of the insert-based device at (a-c) 5 min, (d-f) 20 min, and (g-i) 40 min reaction time during a continuous flow experiment at ambient temperature. The blurred feature next to the line of crystals at the $CaCl_2$ and Na_2CO_3 interface is caused by out-of-focus crystals on the top window. (m-o) SEM micrographs of the dried device after ~40 min of reaction time. Scale bars in optical images are 100 µm and in SEM images are 50 µm.

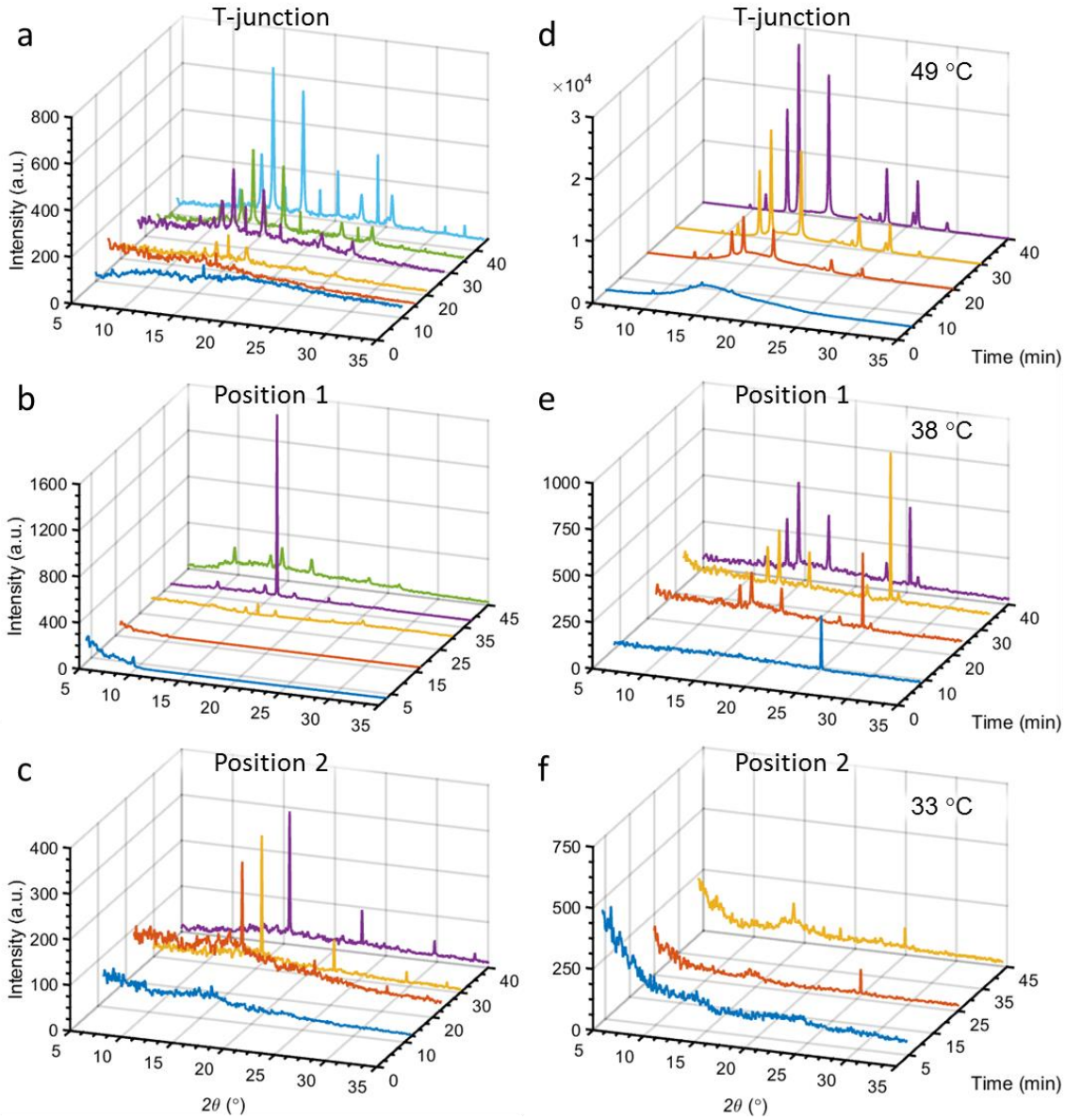

Figure 62: Time-resolved diffraction patterns from the indicated channel position taken from the (a-c) ambient temperature and (d-f) temperature gradient experiment at the indicated temperature.

XRD peaks were not discernable at Position 1 until after 30 min, and showed a mixture of calcite and vaterite (Fig. 62b, orange). At 38 min, a large calcite (104) reflection was observed, but then was lost by 45 min of experiment time, presumably because the diffracting crystal shifted or was pulled into the flow (Fig. 62b, purple and green). At Position 2, calcite appeared to be the only polymorph growing for the duration of the experiment, as no peaks corresponding to vaterite could be identified (Fig. 62c).

Ultimately, concomitant growth of calcite and vaterite was observed at the T-junction and Position 1, while only calcite growth was detected at Position 2 by XRD.

This could be due to the lessening supersaturation of the flow as it travels downstream and ions are sequestered by surface growth, or simply due to the lower contrast of polycrystalline vaterite reflections that are harder to resolve from background scattering. Reflections from calcite appeared as single spots that resulted in sharp diffraction peaks, whereas reflections from vaterite appeared as faint rings that resulted in broader diffraction peaks (Fig. 58c and Figure 63). Indeed, subsequent SEM analysis revealed the presence of hexagonal plate-like vaterite crystals at both Positions 1 and 2 in addition to large rhombohedral crystals of calcite (Fig. 64).

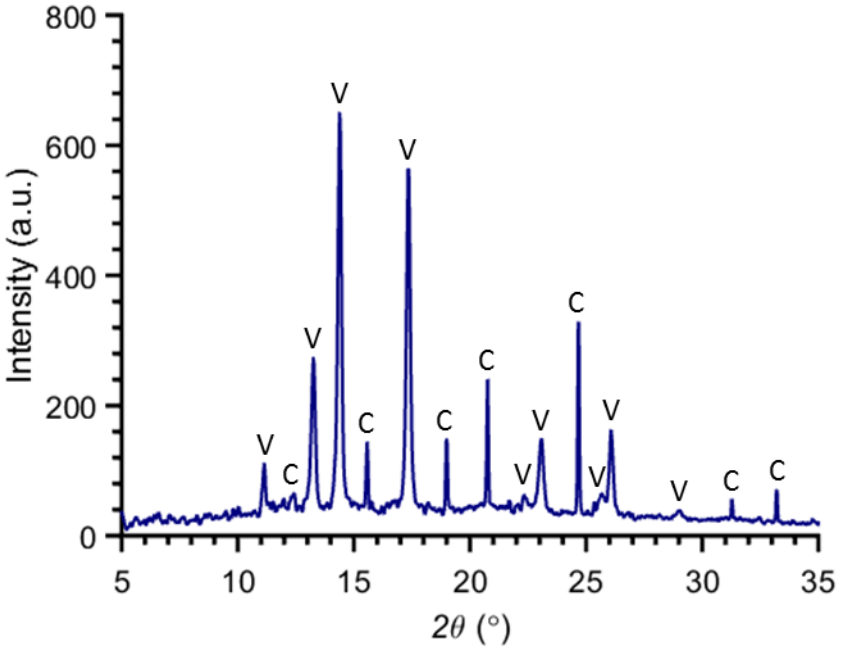

Figure 63: Indexed diffraction pattern taken from the T-junction after 43 min reaction time in the ambient temperature experiment. Sharp peaks correspond to calcite (C) and broader peaks to vaterite (V).

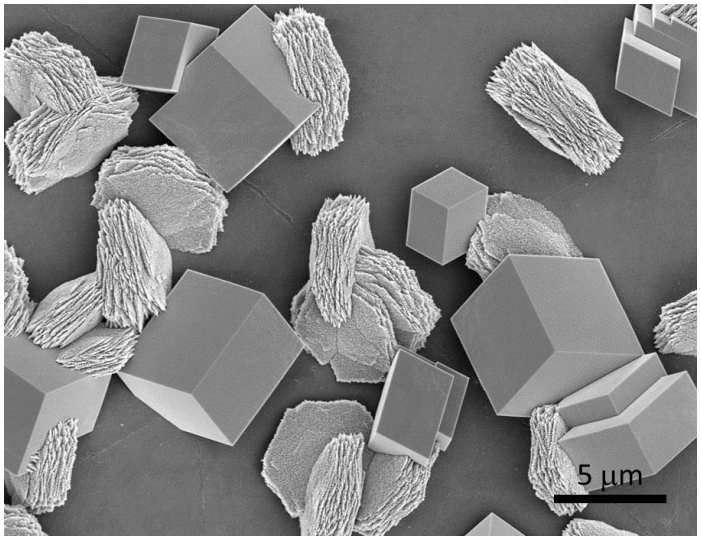

Figure 64: Large single crystals of calcite and polycrystalline vaterite platelets at Position 2 after an ambient temperature continuous flow experiment.

Temperature Gradient Experiments

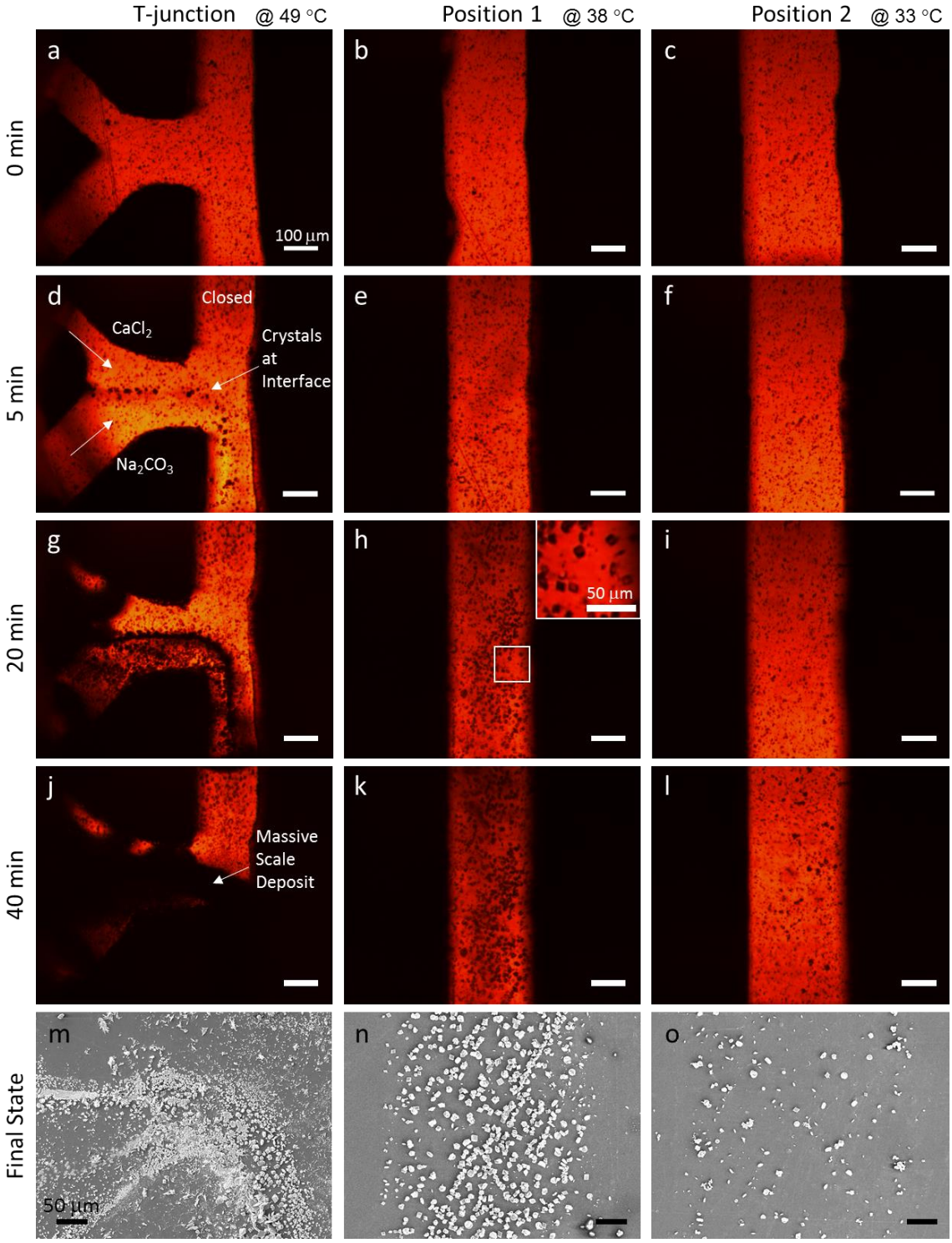

Figure 65: Optical micrographs of the bottom Kapton window at the indicated channel position and temperature at (a-c) 5 min, (d-f) 20 min, and (g-i) 40 min reaction time during a continuous flow experiment. (m-o) SEM micrographs of the dried device after ~40 min of reaction time. Scale bars in optical images are 100 µm and in SEM images are 50 µm.

In the temperature gradient experiment, similar fast precipitation at the T-junction was observed (Fig. 65d). However, growth at Positions 1 and 2 was much slower than in the ambient temperature experiment (Fig. 65e and f). The high supersaturation and

temperature (~50 °C) of the T-junction resulted in the rapid accumulation of vaterite (Fig. 62d), which eventually led to massive scale deposits that fouled the mixer (Fig. 65j). This high amount of precipitation at the junction was likely responsible for the relatively low amounts of crystal deposition at Positions 1 and 2 (Fig. 65k and l), as most ions would be sequestered by the scale.

At Position 1 the first polymorph to be detected was aragonite at 8 min experiment time (Fig. 62e, blue). Subsequently, XRD indicated the concurrent growth of primarily aragonite and vaterite over the remainder of the experiment, yet one calcite peak could be observed at 23 min (Fig. 62e, red) and some apparent calcite-like rhombohedral crystals could also be seen in the optical microscope (Fig. 65h, inset). The aragonite appeared to have a preferred orientation along the flow channel as only the (041) reflection was observed, in contrast to the many peaks observed for polycrystalline vaterite (Fig. 66). At Position 2, calcite was the first polymorph to be detected by XRD after 25 min of experiment time (Fig. 62f, red), with the concurrent growth of vaterite detected after 43 min (Fig. 62f, orange). Thus, vaterite was seen at every position, joined by aragonite and calcite at Position 1, and by calcite alone at Position 2.

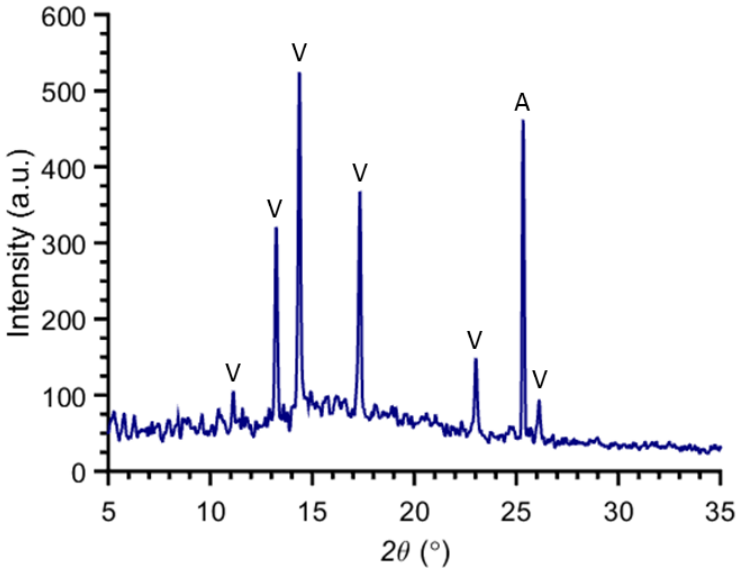

Figure 66: Diffraction pattern from Position 1 during the temperature gradient experiment after 40 min. Labelled peaks correspond to vaterite (V) and aragonite (A).

While the presence of ACC in these continuous flow experiments cannot be ruled out – and indeed is likely – for both conditions in light of the high supersaturations, direct confirmation of this is difficult considering the high background scattering from the windows and solution and relatively low signal-to-noise ratio in continuous flow. However, the evidence for ACC precipitation is most clear from the diffuse scattering band seen around 15° in the early diffraction patterns from the T-junction in the temperature gradient experiment (Fig. 62d, blue and red). When the initial pattern

collected was compared to literature references for ACC scattering,[275, 276] there was good agreement in the position of the main characteristic scattering band at ~28° (for Cu Kα, Fig. 67). This suggests that ACC was present in large amounts, at least initially, in the temperature gradient experiment.

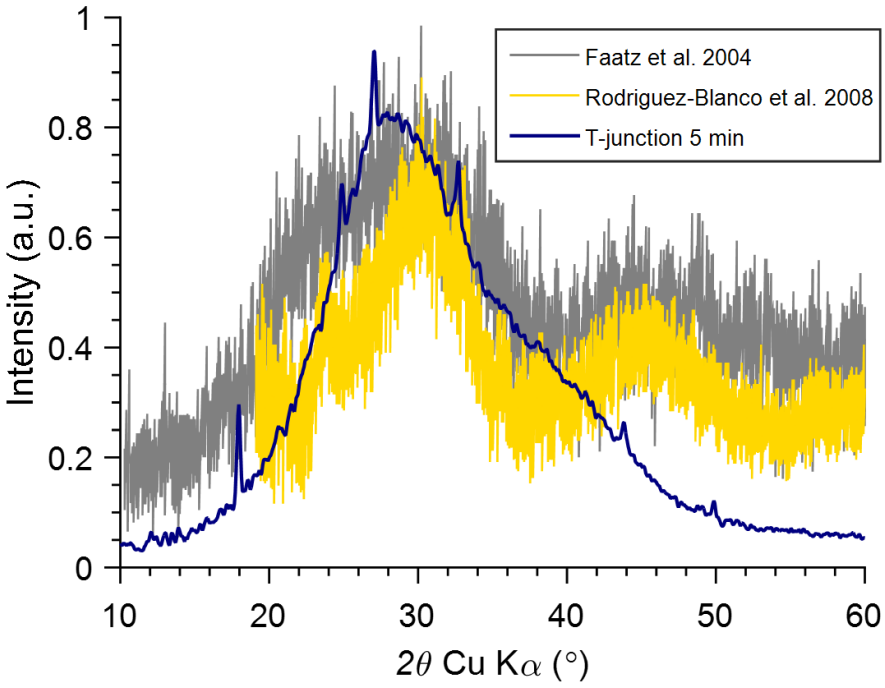

Figure 67: Processed diffraction pattern from the T-junction at 5 min reaction time in the heated experiment compared with literature references for ACC scattering. The diffraction pattern was converted into Cu Kα wavelength (1.5406 Å) and normalized for comparison. Small peaks above the possible ACC band belong to vaterite.

2.4.2 Segmented Flow Results

Experimental Conditions

Two different chip/flow configurations were employed for segmented flow analysis, both utilizing FC-40 with 2.5 wt% PFPE-PEG-PFPE triblock copolymer surfactant[277] as the continuous phase. The first was with a PTFE channel insert using the standard 3-inlet configuration with $CaCl_2$ and $NaCO_3$ meeting at a Y-mixer before encountering the FC-40 oil flow (Fig. 41b). The second made use of a chemically treated PTFE insert (see Section 2.1.1) with an additional inlet between the $CaCl_2$ and $NaCO_3$ flows to introduce a buffer flow of water (Fig. 41c). Experiments using the first configuration were conducted with final concentrations of 12.5 mM Ca^{2+} and 50 mM CO_3^{2-}, and experiments using the second configuration employed a final equimolar concentration of 25 mM Ca^{2+}/CO_3^{2-}. The solution in the latter experiments also contained porous bioactive glass powder, which was introduced with the $CaCl_2$ flow for a final concentration of 0.01 wt% in the droplets. This powder was used as a nucleating agent to encourage precipitation within the bulk of the droplets, and will be discussed in detail

in Chapter 3. The simulated solution conditions for both types of segmented flow experiments can be found in Table 4. These different conditions/configurations were utilized at two different beamtimes (>1 year apart) and reflect the laboratory conditions that were being investigated at the time.

Table 4: Solution Conditions from Visual MINTEQ for Preliminary Segmented Flow Experiments

Condition	Polymorph	SI (log IAP - log K_{SP})	pH	Ionic Strength
12.5 mM Ca^{2+} / 50 mM CO_3^{2-}	Calcite	3.287	11.161	0.1153
	Aragonite	3.142		
	Vaterite	2.715		
	ACC	1.197		
25 mM Ca^{2+} / CO_3^{2-}	Calcite	3.451	10.902	0.0821
	Aragonite	3.306		
	Vaterite	2.879		
	ACC	1.361		

First Configuration (No Buffer Flow)

The first configuration produced crystals within the droplets, yet resulted in the immediate scaling of the Kapton windows at the mixing region leading up to the T-junction (Fig. 68). Initially, the scale was not as strongly attached to the window surface as in continuous flow experiments, and the oil flow periodically removed aggregates once their size resulted in large enough pressure or drag forces to dislodge them (Fig. 68, 5 min experiment time). However, over time, precipitation at the mixer and T-junction became too great to be counter-acted by the oil flow, and complete fouling of the junction ensued. Scaling was not limited to the T-junction, and delayed droplet break-up caused by the foul also resulted in scaling of the channel downstream towards Position 1 (Fig. 69a).

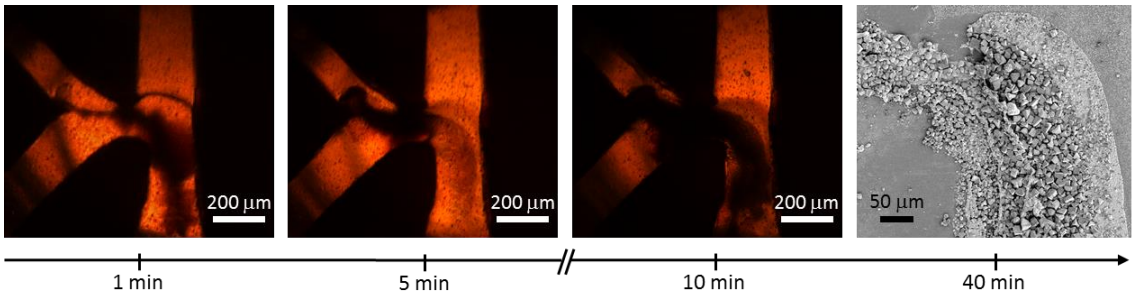

Figure 68: Optical and SEM micrographs of T-junction fouling over 40 min of experiment time with the first segmented flow configuration.

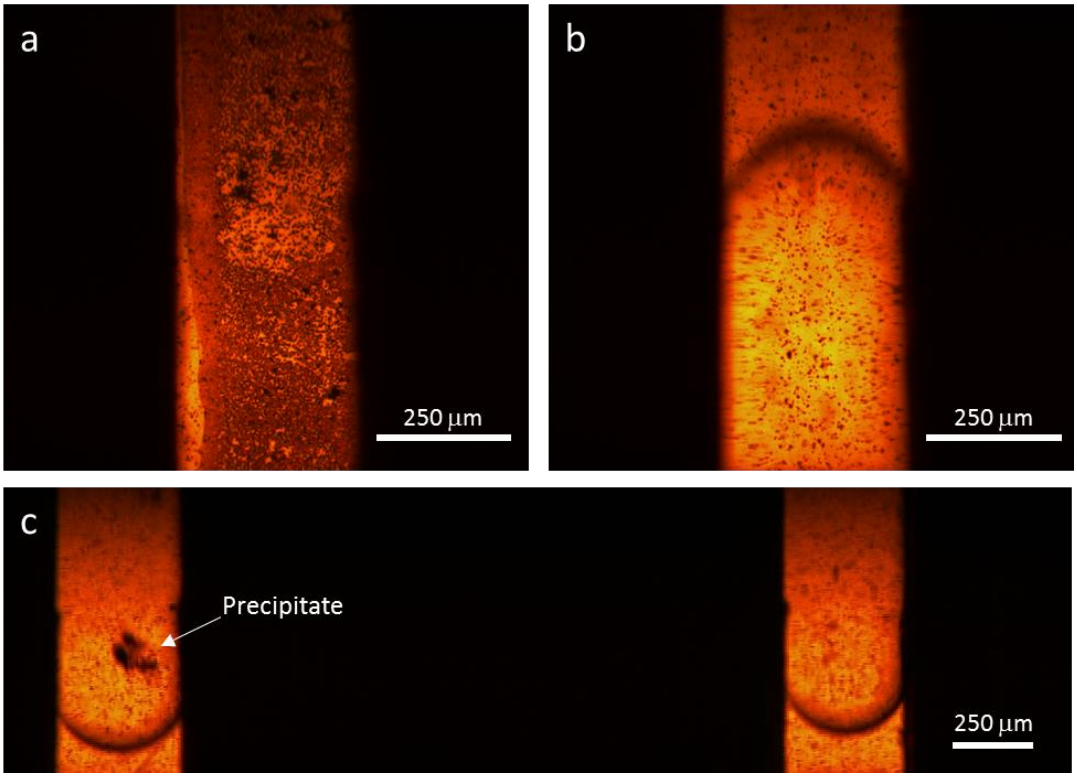

Figure 69: Optical micrographs of (a) scale at Position 1 after 10 min reaction time, (b) a droplet passing by Position 2 at 25 min reaction time, and (c) precipitate encapsulated in a droplet at Position 4 after 40 min reaction time.

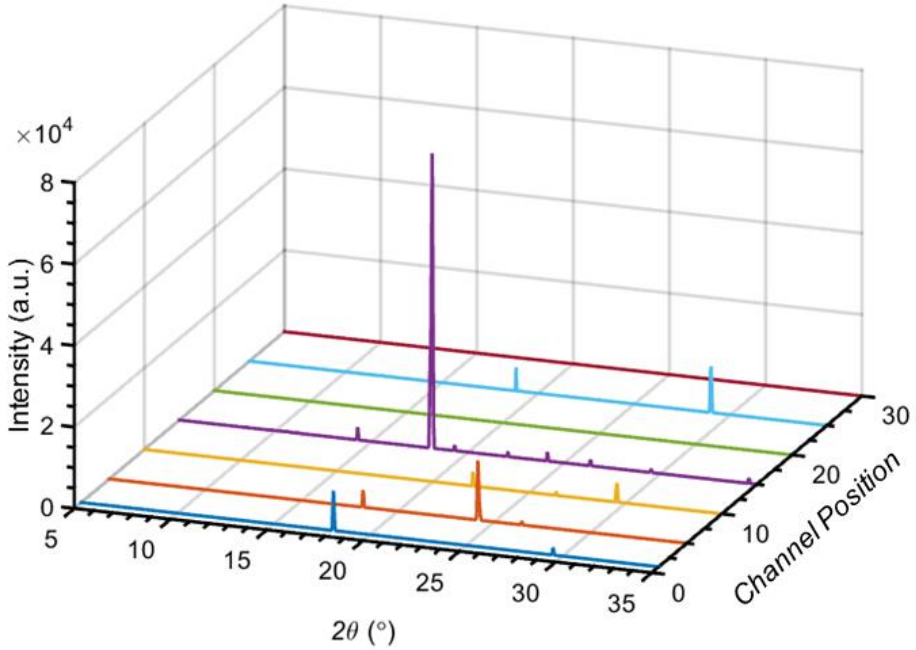

Figure 70: DMC-XRD patterns as a function of channel position in the insert-based device with the first segmented flow condition. All peaks correspond to calcite

However, at no time during the ~45 min experiment was the T-junction completely blocked, and no scaling was observed from Position 2 onwards (Fig. 69b). Uniformly sized and spaced plugs continued to form, with most plugs containing clumps of

precipitates for the duration of the experiment (Fig. 69c). While undoubtedly, many of these aggregates were ACC, considering their irregular shapes, DMC-XRD patterns collected from many positions confirmed the presence of calcite crystals (Fig. 70). Nonetheless, it is unclear whether the observed material and crystals nucleated within the droplets or were merely encapsulated fragments broken off of the fouling upstream. Overall, the XRD patterns increased in intensity with increasing channel position, as would be expected if crystals were indeed growing in the droplets as they travelled downstream. Yet, several positions contained less intensity than previous positions or even zero intensity, demonstrating the inconsistency of the flow resulting from the fouled mixer.

Second Configuration (Buffer Flow and Nucleating Agent)

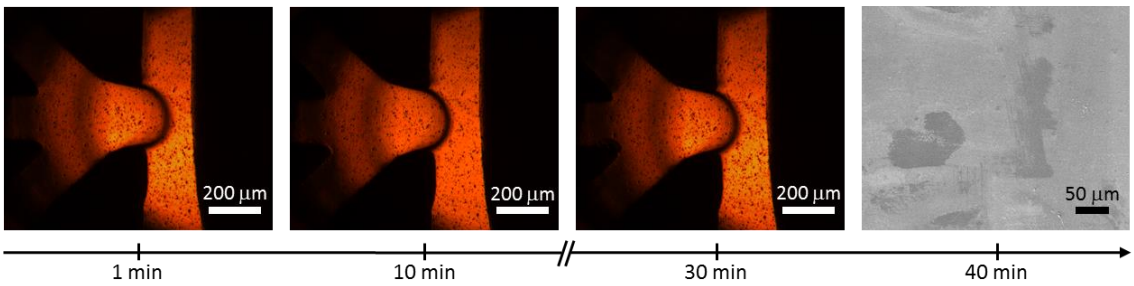

Figure 71: Optical micrographs of T-junction fouling over 40 min of experiment time with the second segmented flow configuration.

Figure 72: Precipitates encapsulated in flowing droplets at Positions 4 and 5 after 40 minutes of experiment time. Due to the speed of droplets and spotted features of Kapton windows, they are difficult to resolve.

In spite of having a higher supersaturation, the second flow configuration prevented scaling and produced much more consistent DMC-XRD patterns. Even over 40 min of experiment time, no scale build-up was observed at the T-junction or anywhere else on-chip (Fig. 71). Additionally, droplet production was consistent for the duration of the experiment, with growing material visible in each droplet beginning from Position 1 (Fig. 72). Diffraction was first detected at Position 5, at 20 sec solution residence time, where the pattern corresponded to calcite (Fig. 73). Subsequently,

increasingly intense diffraction patterns were collected from Positions 6-15 (~24-60 sec), until the intensity settled to near a constant value over Positions 20-34 (~79-135 sec, Fig. 73).

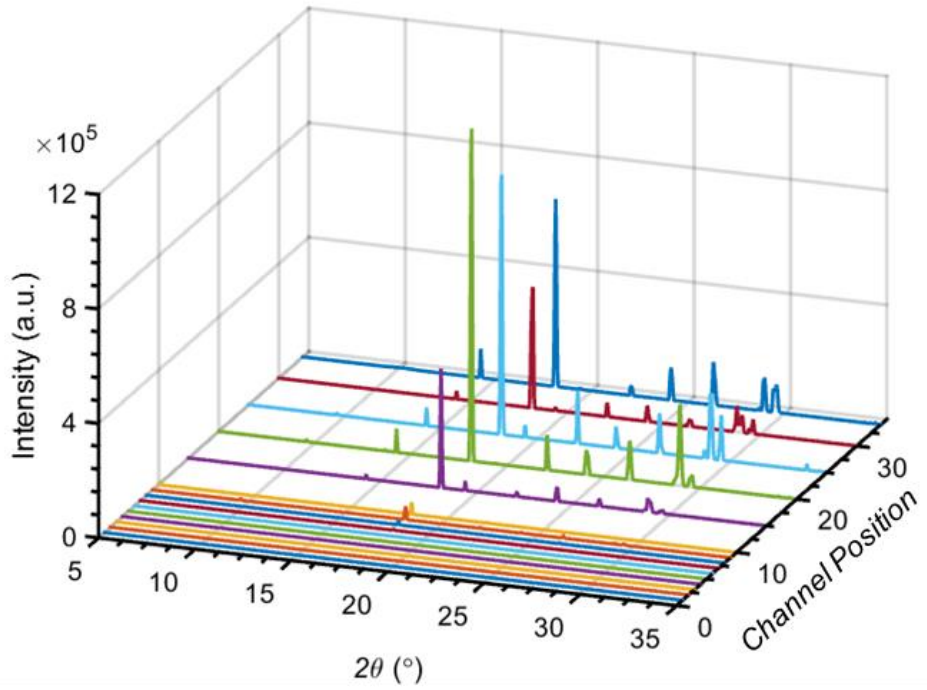

Figure 73: DMC-XRD patterns as a function of channel position in the insert-based device with the second flow condition. All peaks correspond to calcite

The presence of ACC in the droplets can be indirectly inferred since material visibly precipitates almost immediately after droplet break-up, yet crystalline reflections cannot be seen until Position 5. Thus, the likely crystallization pathway that explains the combined optical and DMC-XRD data is that immediate ACC precipitation was followed by calcite nucleation sometime before crystals were first detected (after 20 sec). Then subsequent growth in diffraction intensity was caused by the growth of calcite crystals at the expense of ACC, which was depleted once the diffraction intensity leveled off at around 79 sec residence time. However, it is challenging to directly confirm the presence of ACC using X-ray scattering since the volume fraction of the ACC in the droplets was very low compared to in the continuous flow experiments where ACC scattering could be detected. It is probable that most DMC-XRD frames from a droplet will simply not contain ACC scattering, and current background processing routines are not sensitive enough to preserve ACC scattering in the final composite pattern if it is only found in a select number of single frames. In the future, an extra processing step which inspects each frame for characteristic ACC scattering bands could be implemented, but this was not investigated here.

2.4.3 Discussion of Surface vs. Bulk Crystallization

The critical difference between continuous flow and segmented flow analysis is that they are studying two fundamentally different things: surface crystallization and bulk crystallization, respectively. As was discussed in Section 1.1.1, surfaces play an important role in crystal nucleation; one that cannot be neglected in a high surface area-to-volume ratio environment such as a microfluidic channel. Ultimately, the continuous flow experiments presented above were studying the interaction between the growing crystals and the Kapton substrate, where the continual injection of fresh reactants fueled time-dependent growth at each analysis position (Fig. 62) rather than spatially-dependent growth in the solution as it travelled downstream (Fig. 74a and b and Fig. 75a and b). This is further evidenced by crystals growing along surface scratches in the Kapton windows (Fig. 61), and preferred orientation of growth as observed by XRD (Fig. 66).

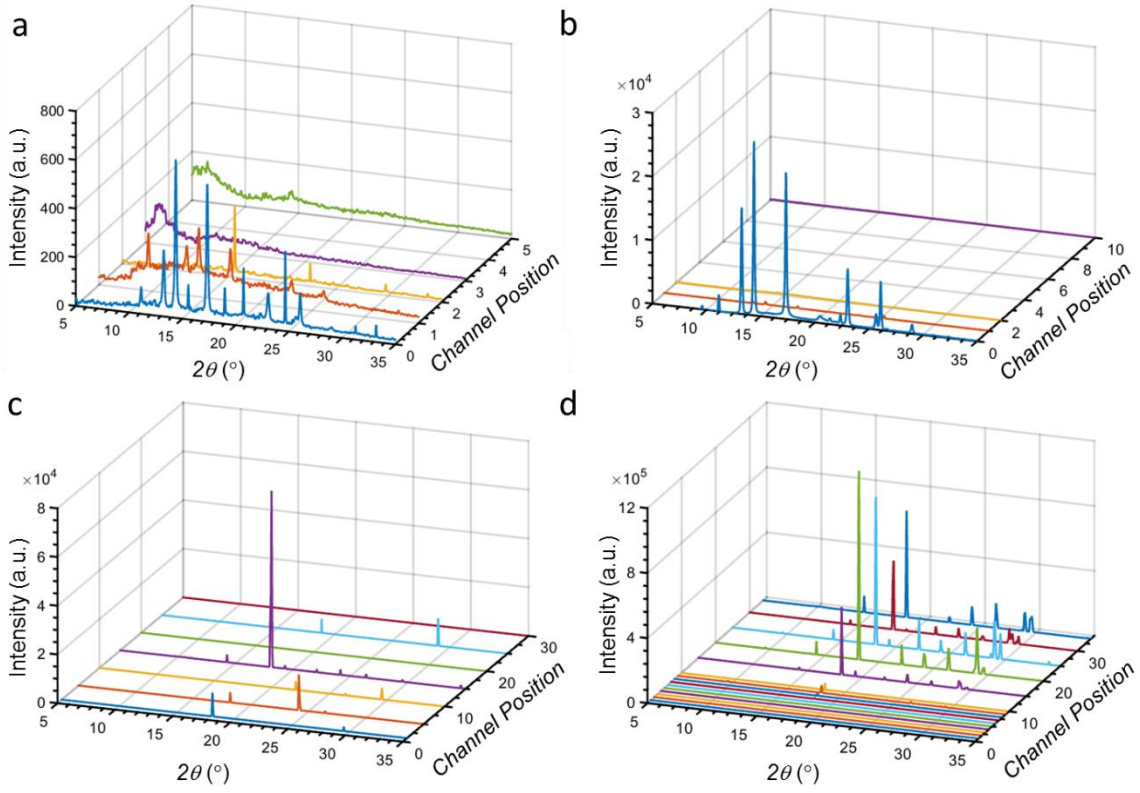

Figure 74: Spatially-resolved diffraction patterns as a function of analysis position from (a) ambient temperature continuous flow, (b) temperature gradient continuous flow, (c) 12.5/50 mM Ca/CO_3 no buffer segmented flow, and (d) 25 mM Ca/CO_3 with buffer segmented flow experiments. Patterns in (a) and (b) are the last captured from each position, showing the final state of the channel.

Conversely, in an idealized segmented flow experiment, fluid interaction with the channel walls is effectively eliminated, meaning growth can proceed within the “bulk” of

the droplet.** Therefore, since growth is tied to the position of a droplet and not to a fixed position along the channel, crystal growth and thus, diffraction signal, increase within droplets as the travel downstream (Fig. 74c and d and Fig. 75c and d). Importantly, this allows length scale (i.e. channel position) to be converted into time scale (i.e. solution/crystal residence time) under steady flow operation, where droplets at a particular location will always have the same residence time independent of the total experimental run time (Fig. 75).

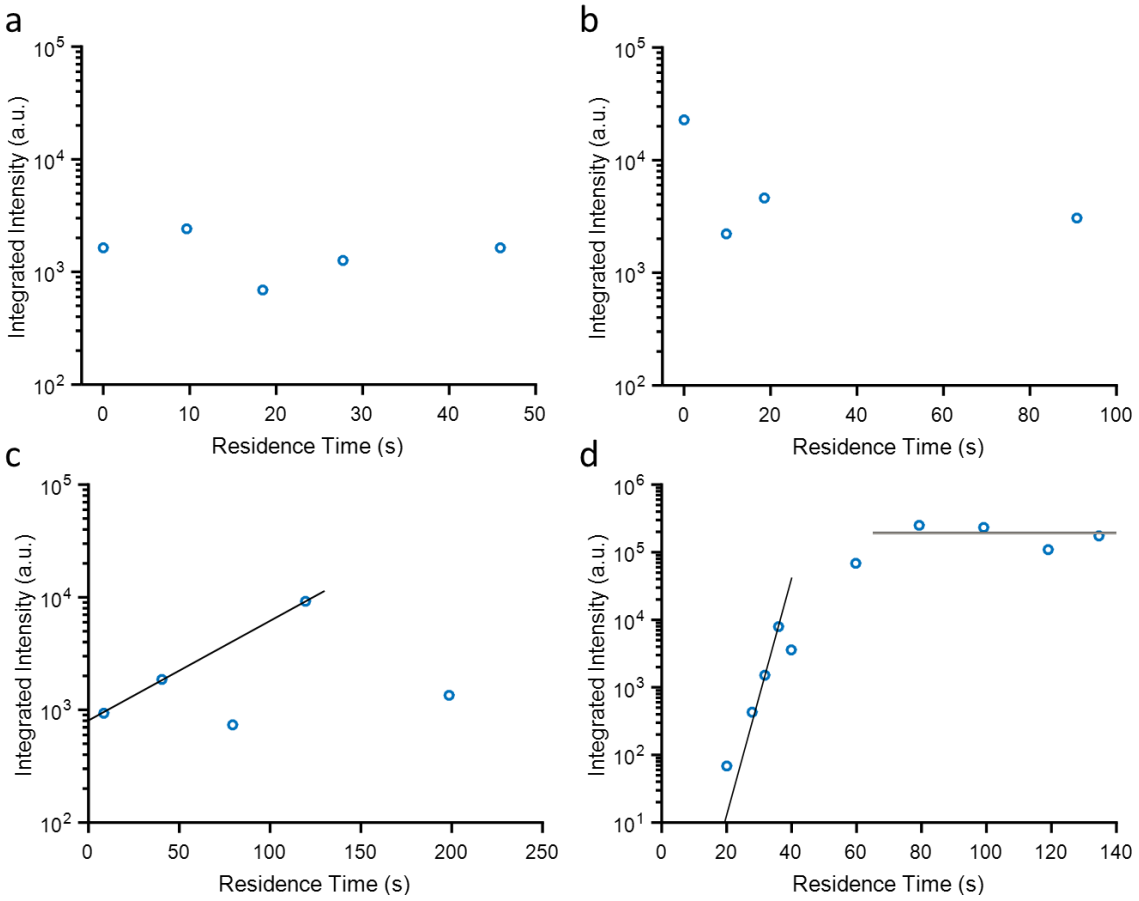

Figure 75: Integrated intensity (area under the curve) of diffraction patterns as a function of solution residence time for (a) ambient temperature continuous flow, (b) temperature gradient continuous flow, (c) segmented flow no buffer and (d) segmented flow with buffer and nucleating agent experiments. The black lines in (c) and (d) are an exponential fit of the initial increase in intensity. The horizontal grey line in (d) is a guide to the eye.

The choice of flow configuration then depends on the goal of an experiment. If the goal is to understand surface-driven phenomena such as scale,[240] weathering,[278] or corrosion,[242] then continuous flow may be the best option. Even a hybrid system like the first segmented flow configuration (without buffer) – where surface interactions

** Typically “bulk” is used to contrast a conventional, large reaction environment and a micro or nano-sized compartment, but here it is used to distinguish between surface-dominated and solution-dominated crystallization.

were modified, but not eliminated – could be useful for studying multiphasic phenomena, such as oil recovery.[279] However, if the goal of an experiment is to reproducibly study crystallization or synthesis processes with an experiment time-independent serial approach, then the reaction must be completely isolated from the device surface.

Here, this could only be achieved with the second flow configuration, which made use of a buffer water flow to maintain segregation of the reagents until after droplet formation alongside of a hydrophobic surface treatment to minimize droplet wetting. While both segmented flow setups enabled crystals to be encapsulated into droplets, the fouling of early channel positions in the first condition made the flow unstable and inconsistent over time. DMC-XRD patterns taken later in the device deviated from the trend of increasing diffraction intensity (Fig. 75c), with some patterns collected near the end of the experiment even yielding zero intensity (Fig. 70, Positions 20 and 30). In contrast, no fouling was observed using the second configuration and diffraction signal increased until leveling off near a constant value, presumably due to the depletion of all ions/amorphous precursors (Fig. 75d). Of course, the condition studied with this configuration was not truly homogenous from a nucleation perspective, since nucleation was heavily influenced by the addition of the nucleating agent powder, itself a surface. However, crystal growth and nucleation in this experiment was successfully de-coupled from device working surfaces, allowing the observation of droplet-encapsulated processes in a well-controlled, reproducible environment.

The suitability of the second buffer flow configuration for performing serial diffraction experiments is further validated by comparing DMC-XRD patterns obtained from the same position at different times throughout the experiment. Consider the patterns in Figure 76 collected from Position 20 ten minutes apart from each other. Qualitatively, both the 1D and 2D patterns from the different experiment times appear similar, and contain all of the of the same calcite peaks. The relative intensity of some peaks in the second plot is slightly lower than in the first, but several peaks are actually higher, including the (113), (202), (116), and very small (006), which is not even visible in the first pattern plotted at this scale. Quantitatively, the two patterns are also comparable. Image analysis of the 2D patterns revealed that there were 435 connected components (i.e. discrete features) in the first pattern and 472 in the second, suggesting a similar number of individual Bragg reflections were captured (within 92%). Additionally, comparison of the integrated intensity, or area under the curve,[165] of each 1D pattern shows that total diffraction intensity was in a similar order of magnitude (2.48×10^5 a.u. vs. 2.04×10^5 a.u., respectively). These analyses demonstrate the statistical variability of the technique, which is dependent on capturing a large number

of random diffraction events. However, these two plots align incredibly well considering they were produced from such a small sample (500 frames coming from only ~10-15 droplets over 10 s), and should converge even further over longer collection times.

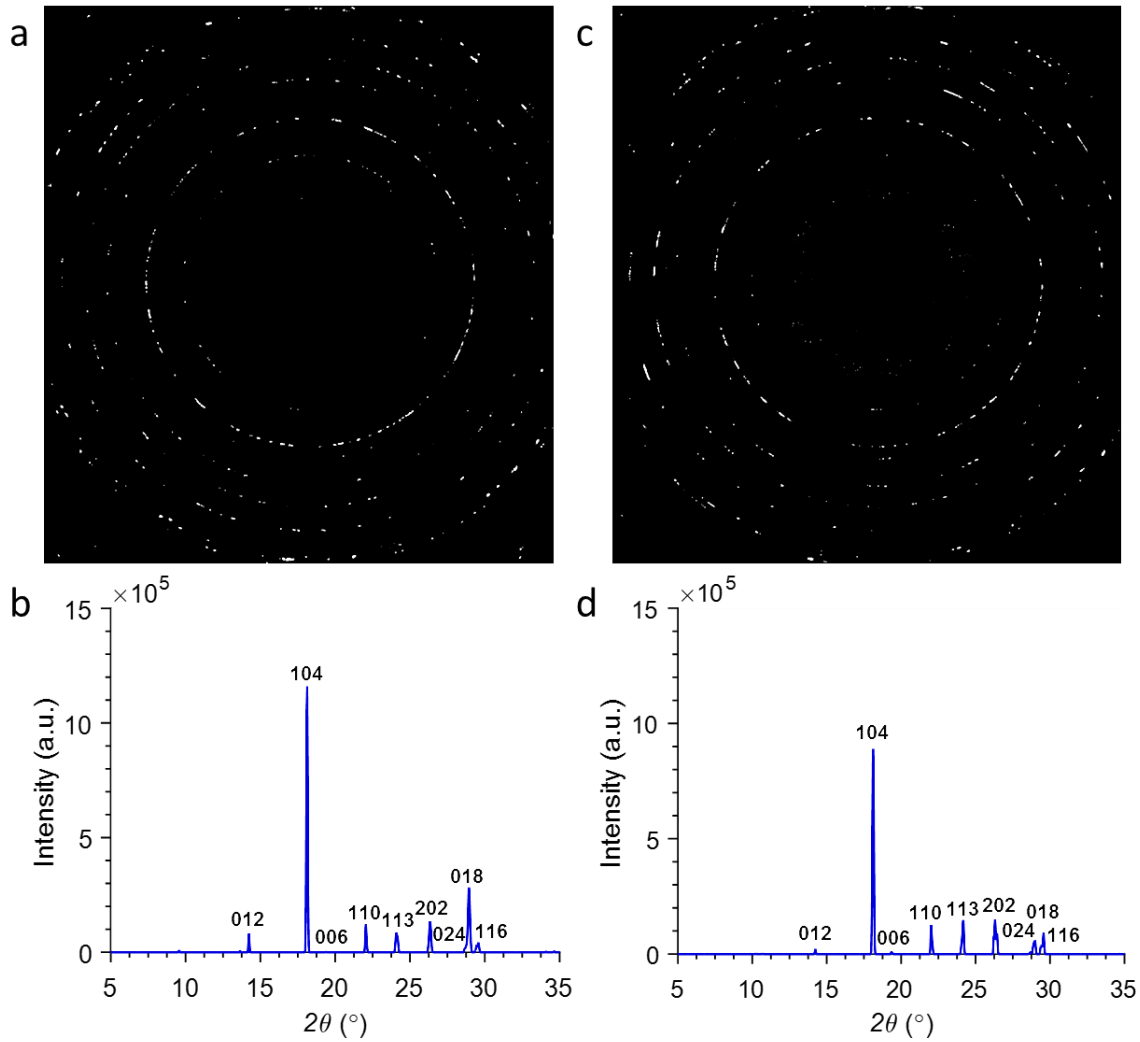

Figure 76: 2D and 1D DMC-XRD patterns from Position 20 during an experiment with the second segmented flow condition after (a and b) 10 min and (b and c) 20 min experiment time. All peaks correspond to calcite and are labelled with their corresponding lattice plane.

2.4.4 Summary

A new reusable flow-cell that enables crystallization to be studied under different temperatures and flow configurations was characterized. Its utility as an X-ray analysis sample environment for continuous and segmented flow experiments was also demonstrated, where the choice of flow configuration was shown to allow access to information on different types of processes: whether at a surface or in bulk. Adopting a segmented flow condition that completely isolated the crystallization reaction from device surfaces allowed serial crystallography-like data to be collected from individual positions on the device, which in the context of segmented flow, translates to a time from mixing. Such a technique is valuable, since it permits data from individual time

points to be pieced together to create a time-resolved structural representation of a crystallization pathway.

Chapter 3:
Nucleant-Mediated Crystallization of Calcium Carbonate

A critical component of developing DMC-XRD was finding good candidate systems for initial analysis: ones that would provide growth in diffraction signal over the device residence time and that would also be interesting from a crystallization perspective. A problem often encountered with the crystallization of $CaCO_3$ in microfluidic devices was that low supersaturations resulted in crystallization induction times much longer than the device residence time, while high supersaturations caused fouling at the T-junction (see Section 2.4.2) and/or the precipitation of long-lived ACC. For this reason, and due to the tremendous interest in understanding the mechanisms of heterogeneous nucleation (see Section 1.1.1), DMC-XRD analysis was focused on identifying effective nucleating agents or "nucleants" for $CaCO_3$.

3.1 Selection and Characterization of Potential Nucleants

3.1.1 Nucleant Selection and Solution Conditions

While there has been a great deal of work identifying different nucleants for materials such as ice and protein crystals, inorganic crystals have received relatively little attention. For the case of $CaCO_3$, most work has focused on identifying specific amino acids and functional groups of proteins which facilitate the crystallization of biominerals in nature,[9, 280, 281] and then implementing biomimetic alternatives such as substrates with functionalized SAMs.[6, 75, 82] To date, few comprehensive studies have investigated a diverse range of materials, surface chemistries, and topographies that could promote $CaCO_3$ nucleation. One inorganic material that has received more treatment in this regard is calcium phosphate (CaP), which is a primary component of human bone in its hydroxyapatite form.[59] A class of partially soluble bioactive glasses (BG) containing varying ratios of SiO_2, CaO, P_2O_5, and sometimes other oxides, have been demonstrated to be good nucleants for hydroxyapatite,[282] finding applications in dentistry and biomedical implants.[283] Interestingly, a porous form of BG (type 58S) has also been shown to have good nucleating properties for a number of protein crystals.[23]

This rich range of materials serving as nucleants for other crystal systems provided a good starting point for selecting potential nucleants for $CaCO_3$. A representative group of particulate additives was chosen to investigate the effect of different features (e.g. porosity, surface chemistry, topography) on $CaCO_3$ crystallization. Porous 58S BG was selected due to its proven ability to nucleate proteins and hydroxyapatite. In order to compare porous and non-porous bioactive

glasses, the original 45S5 Bioglass® composition was also selected (non-porous BG). Controlled porous glass (CPG), consisting primarily of SiO_2, was chosen for its similarly large surface area and pore sizing to 58S BG, yet its lack of surface bioactivity.[68] CPGs with added carboxylate functionalization (CPGs+COOH) were also investigated, since substrates patterned with COOH SAMs are often used as models for biomineralization.[82] A number of minerals that are used as models of atmospheric dust in ice nucleation studies were also tested. After preliminary trials of 0.025 wt% dispersions of the minerals, kaolinite, NX illite, amazonite, and montmorillonite, NX illite was shown to be the most effective and was selected for further analysis along with the other additives (Fig. 77).

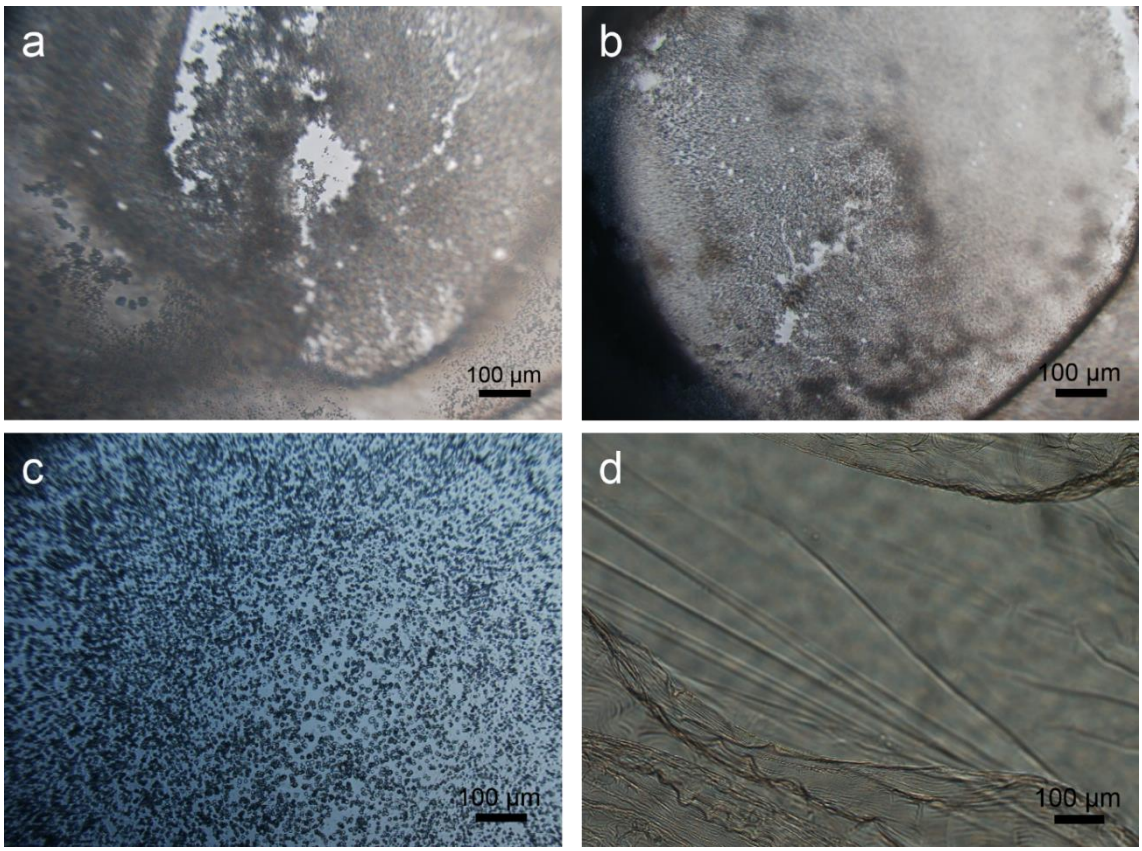

Figure 77: Optical micrographs from preliminary mineral trials in 2 µL sessile droplets on hydrophobic petri dishes. (a and b) Representative images of metastable ACC before nucleation in control experiments and experiments with poor nucleants. The droplets appear opaque and contain mainly large amorphous aggregates. (c) Image from a droplet containing 0.025 wt% NX illite 3 min after mixing. All ACC appears to have been depleted and replaced by rhombohedral calcite crystals of ~5-10 µm in size. (d) ACC film developed in droplets with 1 M Ca^{2+}/CO_3^{2-} concentration.

The activities of these nucleants were also compared to those of calcite nanoparticles (CNP) of 50.3 ± 11.6 nm diameter (Fig. 78), and control experiments were conducted without nucleants. CNPs should result in the shortest possible calcite induction time, and control experiments the longest, providing good points of reference.

Ionic conditions of 50 mM Ca^{2+}/CO_3^{2-} ($SI_{calcite} \approx 3.8$) obtained through direct mixing of aqueous equimolar solutions were chosen for all experiments to allow the precipitation and depletion of ACC to be used as an indicator of nucleation efficiency. Initial aqueous solutions of either 100 mM $CaCl_2$ and Na_2CO_3 or 300 mM $CaCl_2$ and Na_2CO_3 diluted using the buffer flow configuration (1:6 dilution; Figure 41c) were utilized. Lower supersaturations (at ~1-2 mM) crystallized too slowly and higher supersaturations (at ~0.5-1 M) formed an apparently continuous ACC film that did not nucleate crystals without nucleants for 7-20 min (Fig. 77d). In all subsequent experiments, nucleants were pre-dispersed in the $CaCl_2$ solution at 0.01 wt% and sonicated for 5 min before mixing with the Na_2CO_3 solution, where the 1:6 dilution results in final nucleant concentrations of 0.0017 wt% in droplets.

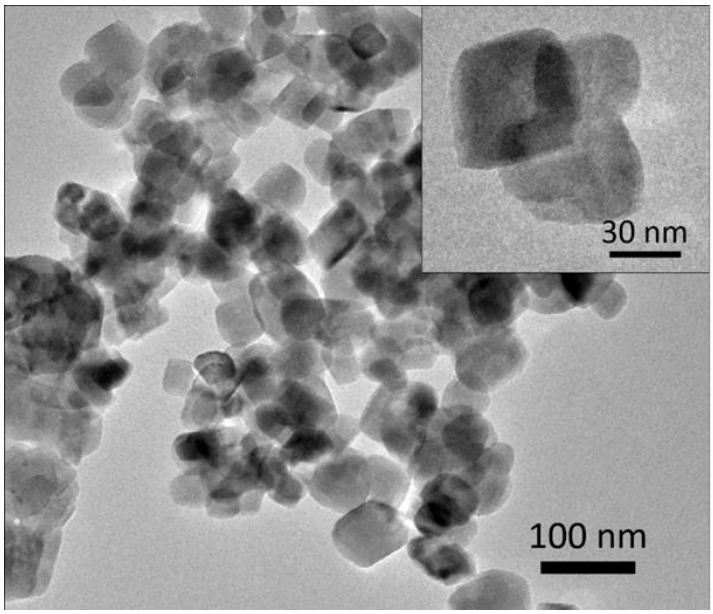

Figure 78: TEM micrographs of the calcite nanoparticles (CNPs) used for the seeding experiments.

3.1.2 Nucleant Preparation

The final selection of nucleants used in all subsequent experiments were *(1)* porous BG, *(2)* non-porous BG, *(3)* CPGs, *(4)* CPGs+COOH, and *(5)* NX illite. The porous and non-porous BGs were obtained from Molecular Dimensions (Naomi's Nucleant) and XL Sci-Tech, respectively. The CPGs were obtained from Schott (CoralPor® 1000), and the NX illite was obtained from B + M Nottenkämper (Arginotec® NX). All nucleant powders were ground with a mortar and pestle prior to use and before characterization. Some nucleants received additional treatment. The NX illite was cleaned to remove possible organic contamination and any inorganic salts (primarily calcite). For organic removal, NX illite powders were placed in a 3% NaClO solution overnight with constant agitation. Afterwards, the powders were sonicated and

centrifuged, the supernatant was removed and replaced with fresh deionized (DI) water, and then this centrifugation/wash cycle was repeated three times. Finally, the cleaned powder was washed with ethanol and dried overnight at 60 °C. For inorganic removal, the powder was sonicated for 10 min in a 1% HCl solution (pH = 4). Afterwards, the same centrifugation/wash cycle as above was repeated.

The CPGs+COOH were prepared using a chemical vapour deposition method adapted from Le Caer *et al*.[284] Stock CPG powders were placed in a vacuum chamber at room temperature for 1 hr with an open vial containing 1 mL of 3-aminopropyl-triethoxysilane. After removing the silane vial, excess silane was removed from the pores by reapplying the vacuum and leaving the CPGs for another hour at 45 °C. Subsequently, the CPGs were washed with toluene and ethanol and dried at 60 °C for 2 hr. Carboxylate functionalization was then achieved by placing the CPGs in a 10% succinic anhydride and 1% 4-dimethyl(amino)pyridine solution of N,N-dimethylformamide (DMF) overnight.[285] Lastly, treated CPGs were rinsed with DMF, DI water, and ethanol and placed in the oven at 60 °C for 2 hr.

3.1.3 Scanning Electron Microscopy

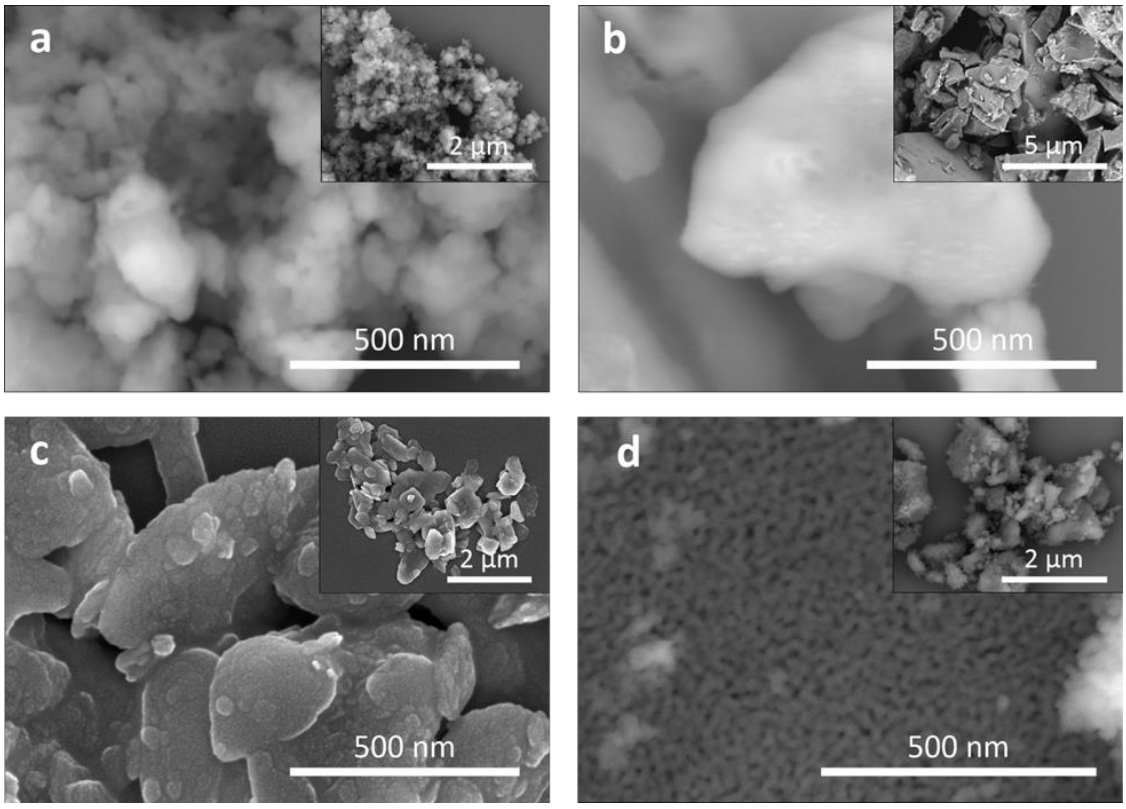

Figure 79: SEM micrographs of (a) porous BG, (b) non-porous BG, (c) NX illite and (d) CPG fragments. Images were obtained with an FEI NanoSEM 450.

The treated nucleants were characterized with a range of techniques. Scanning electron microscopy (SEM) revealed the heterogeneous sizing of all of the nucleant

species, where the imaged particles ranged from hundreds of nanometers to several microns in size (Fig. 79). Additionally, the high-magnification SEM images illustrate the surface topography of the nucleants. The porous BG displays a granular texture comprising irregular gaps and voids (Fig. 79a), while the non-porous BG has a much smoother surface (Fig. 79b). The NX illite has a similar appearance to the porous BG, but with larger voids and a rougher surface (Fig. 79c). Finally, the CPGs have a visibly porous surface, with the sizing and spacing of pores appearing fairly uniform (Fig. 79d).

3.1.4 Brunauer-Emmett-Teller and Barrett-Joyner-Halenda Analysis

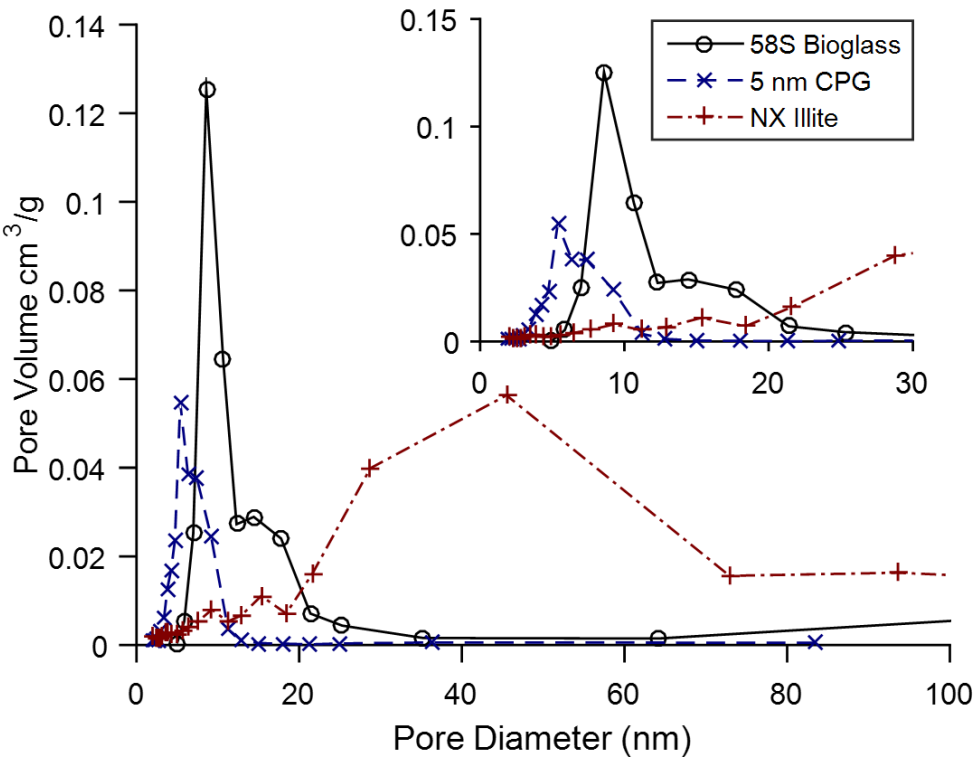

Figure 80: Pore size distribution of nucleants from Barrett-Joyner-Halenda (BJH) desorption measurements. Data were obtained with a Micrometrics ASAP 2020 Plus system.

The pore volume and pore size distribution of the porous BG, CPG, and NX illite particles were quantified through Barrett-Joyner-Halenda (BJH) analysis of N_2 gas desorption curves (Fig. 80). Porous BG and the CPGs had pores with diameters in the range of ~6-21 nm and ~3-11 nm, respectively. The NX illite had a small volume of pores in this range, however most of its pore volume comprised pores greater than 20 nm in diameter. Unsurprisingly, there were no detectable pores in the non-porous BG, which had a specific surface area approximately 180 times less than the porous BG. Table 5 contains a summary of the Brunauer–Emmett–Teller (BET) surface area and BJH results as well as the composition of each nucleant.[286, 287]

Table 5: Physical and Chemical Properties of Nucleants

Nucleant	Surface Area (m^2g^{-1})	Total Pore Volume (cm^3g^{-1})	Average Pore Diameter (nm)	Chemical/Mineral Composition
Non-porous BG	0.52 ± 0.10	-	-	46.1% SiO_2, 24.4% Na_2O, 26.9% CaO and 2.6% P_2O_5 [ref.[286]]
Porous BG	92.36 ± 0.46	0.33	10.34	60% SiO_2, 36% CaO and 4% P_2O_5 [ref.[286]]
CPG	146.79 ± 0.47	0.23	5.51	95-97% SiO_2 [manufacturer]
NX Illite	76.92 ± 0.60	0.23	15.65	6.6% Quartz, 9.8% Feldspar, 2.1% Calcite (removed), 60.5% Illite, 13.8% Mixed illite-smectite and 7.2% Kaolinite [ref.[287]]

3.1.5 Powder X-ray Diffraction

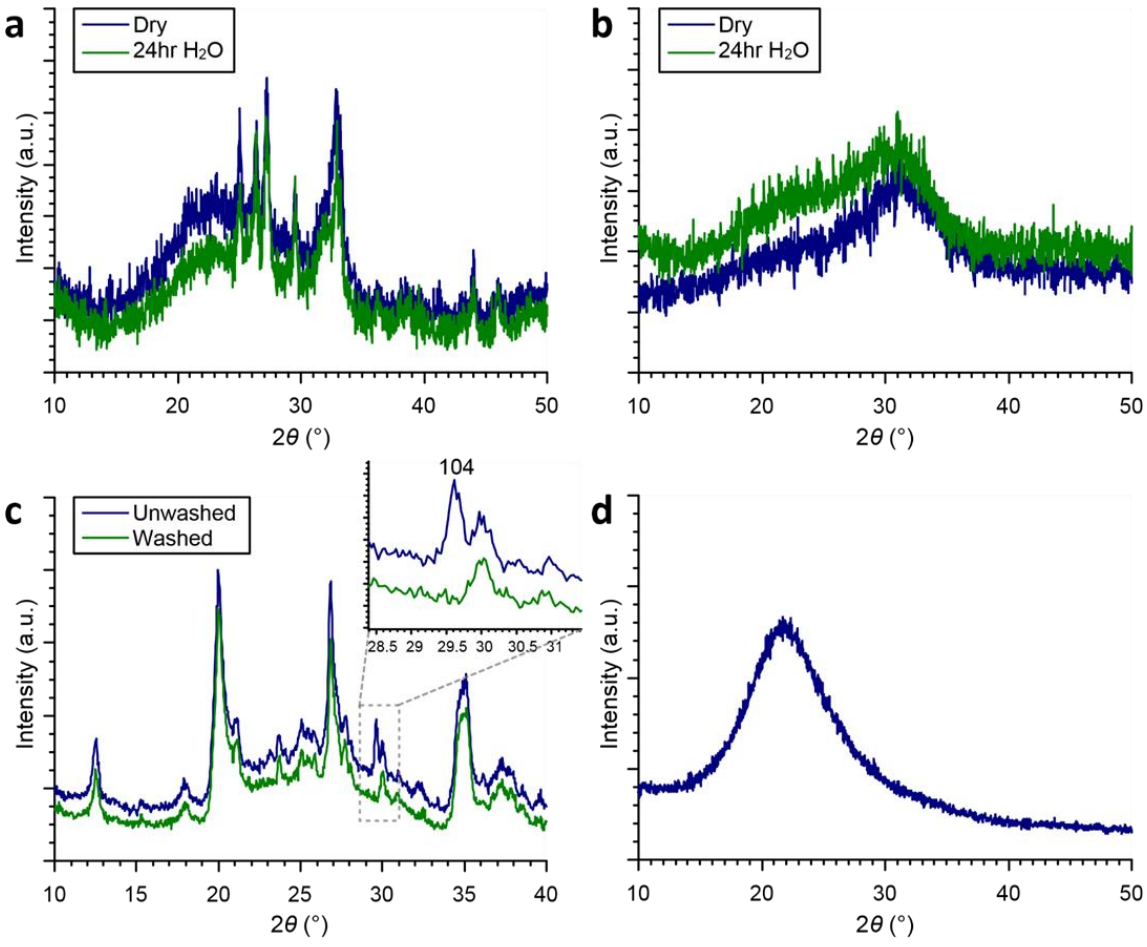

Figure 81: PXRD patterns of (a) porous BG, (b) non-porous BG, (c) NX illite, and (d) CPGs. Data were obtained with a Bruker D2 Phaser with steps of 0.02° and 0.8 s exposure per step.

Powder X-ray diffraction (PXRD) was used to examine the crystallinity of the powders, and if any change in the crystallinity of the BGs could be observed due to storage in DI water (Fig. 81). None of the nucleants had very sharp or high contrast peaks in relation to the background, but the NX illite and the porous BG appeared to have some more internal order than either the non-porous BG or CPGs. No significant changes in structure were observed between dry BGs and those stored in DI water for 24 hr prior to analysis (Fig. 81a and b). PXRD was also used to confirm the removal of trace calcite from NX illite samples after chemical treatment, as evidenced by the disappearance of the (104) reflection (Fig. 81c, inset).

3.1.6 Atomic Absorption Spectroscopy

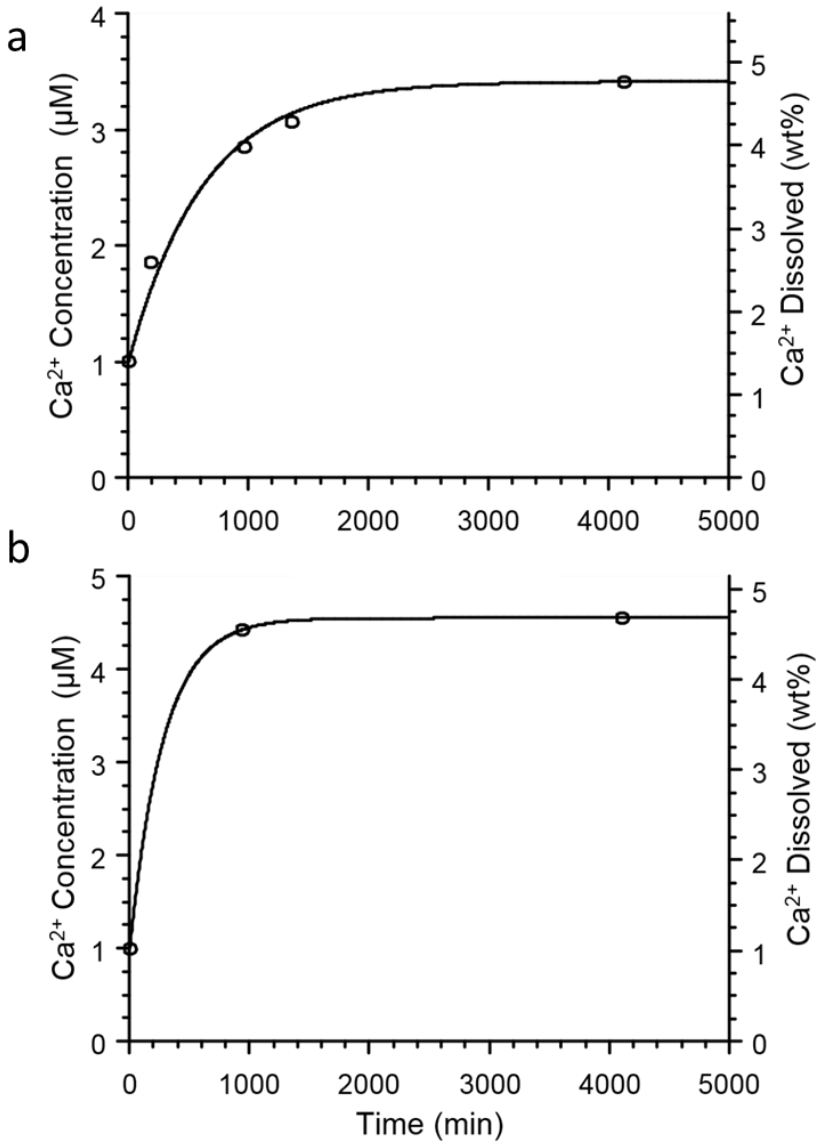

Figure 82: AAS results from solutions incubated with (a) non-porous and (b) porous BG for the indicated time. The left y-axis shows the [Ca^{2+}] that would be added to the final mixed droplets during a standard microfluidic experiment, and the right y-axis shows the percentage of calcium that has been dissolved of the total amount of Ca^{2+} present in 5 mg of porous or non-porous BG. Data were obtained with a Perkin Elmer Atomic Absorption Spectrometer.

Finally, due to their partial solubility, BG powders were incubated in DI water to investigate the amount of calcium leached into the solution, in case this could affect the final [Ca^{2+}] in crystallization experiments. Solutions were made with 5 mg of the BG in 5 mL of water (0.1 wt%) and incubated at room temperature with no agitation. This simulated the way nucleant stock solutions were prepared and stored prior to synchrotron experiments. Aliquots were taken from solutions after varying times and were analyzed with Atomic Absorption Spectroscopy (AAS). At the indicated time, the solutions were filtered with a 0.22 μm syringe filter to remove the BG and halt dissolution. ASS revealed that the non-porous BG solution equilibrated after roughly 2 days, and the porous BG in about half a day due to its higher surface area (Fig. 82). This confirmed that, regardless of the time stored in the stock solution, neither sample could increase the final [Ca^{2+}] of the mixed droplets in the microfluidics experiments by more than 5 μM. Since this represents less than 0.01% of the calcium present during crystallization with the 50 mM Ca^{2+}/CO_3^{2-} concentration utilized, storage of BG powders in water is not expected to affect subsequent crystallization experiments.

3.2 Crystallization Results

3.2.1 Polarized Light Microscopy in PDMS Devices

Crystal growth in flowing droplets containing porous and non-porous BG, NX illite, CPGs, CPGs+COOH, CNPs, and no nucleant was followed with polarized light optical microscopy; only particles that are birefringent are observed such that amorphous material is not seen. In a typical experiment with a good nucleant, droplets at early stages appear dark, then slowly begin to lighten, and then finally display individual birefringent crystals (Fig. 83a). Such experiments provided a qualitative understanding of crystal growth in the droplets, where precipitation was shown to occur in a series of stages. *Stage 1*: In all cases, immediate precipitation of ACC occurred after droplet break-up, yielding a turbid solution (Fig. 83b). *Stage 2*: Large aggregates of ACC formed, the highest concentration of which gathered near the droplet tail (Fig. 84a). *Stage 3*: These aggregates subsequently broke-up as crystals nucleated and grew, leading to more homogenous dispersal of material within the droplets (Fig. 83a). Additionally, the droplets became less turbid as the crystals grew larger, indicating that they grew at the expense of the ACC. In the CPG, CPG+COOH, and control experiments, no apparent depletion of ACC or crystal growth was observed within the residence time of the chip (2.35 min), and these experiments did not progress beyond *Stage 2*.

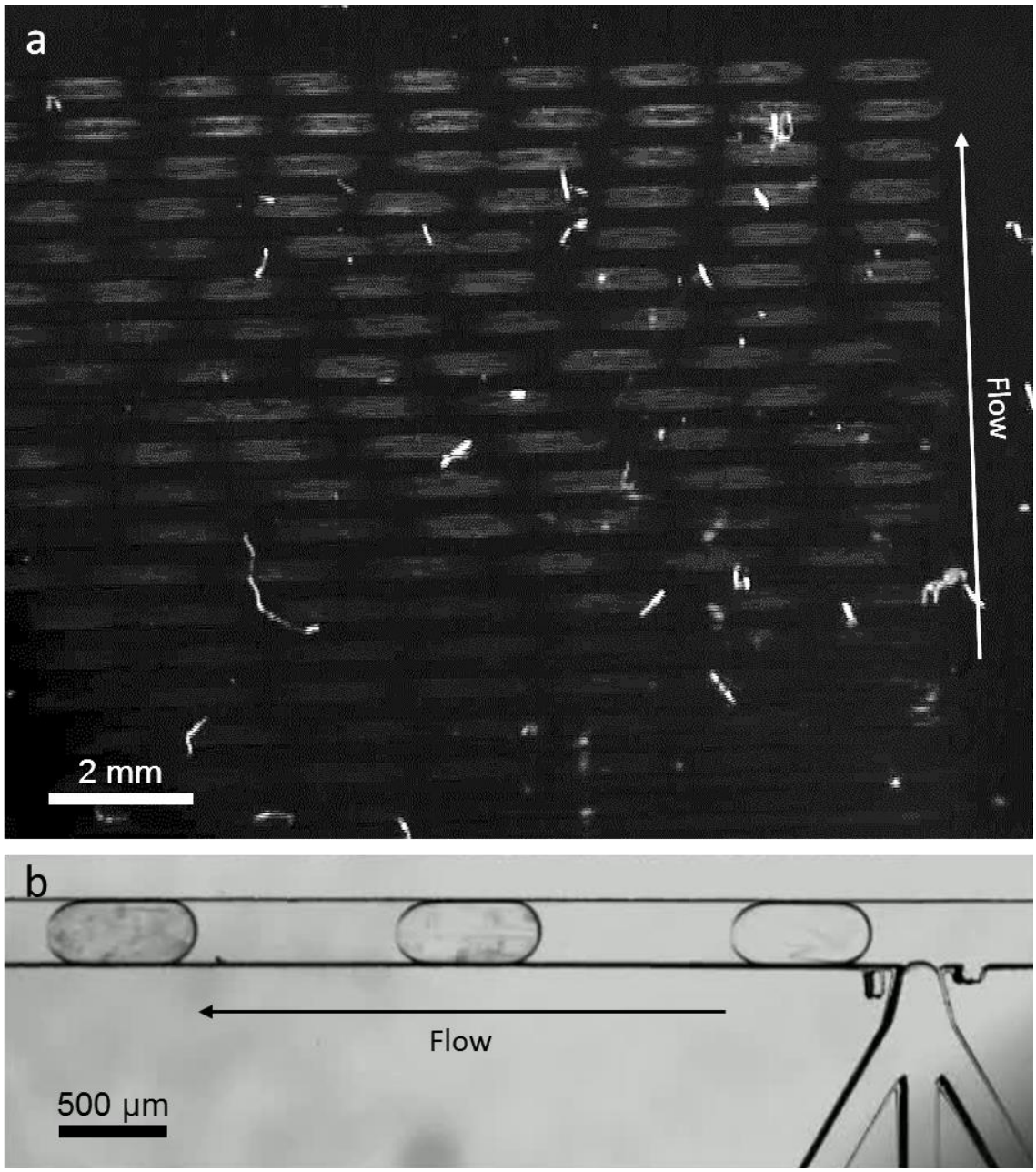

Figure 83: Optical snapshots of flowing droplets with 50 mM Ca^{2+}/CO_3^{2-} concentration and (a) 0.0017 wt% CNPs or (b) 0.0017 wt% CPGs. (a) Image acquired using cross polarizers to observe growth of birefringent crystals. Images and video were captured with a Leica M165 FC stereo microscope.

To study longer residence times in these systems, the flows were stopped to incubate the droplets on-chip. In the control experiment, many droplets still did not contain crystals after 30 min (Fig. 84a). After 2-5 min, some droplets containing CPGs and CPGs+COOH displayed 1 or 2 crystals, but still contained ACC (Fig. 84b). Immediately after flow stoppage, droplets containing CNPs and porous BG had more than 50 crystals of several microns in size and appeared to be depleted of ACC (Fig. 84c and d). Most droplets containing NX illite and non-porous BG had 2-10 crystals still retained some ACC (Fig. 84e and f).

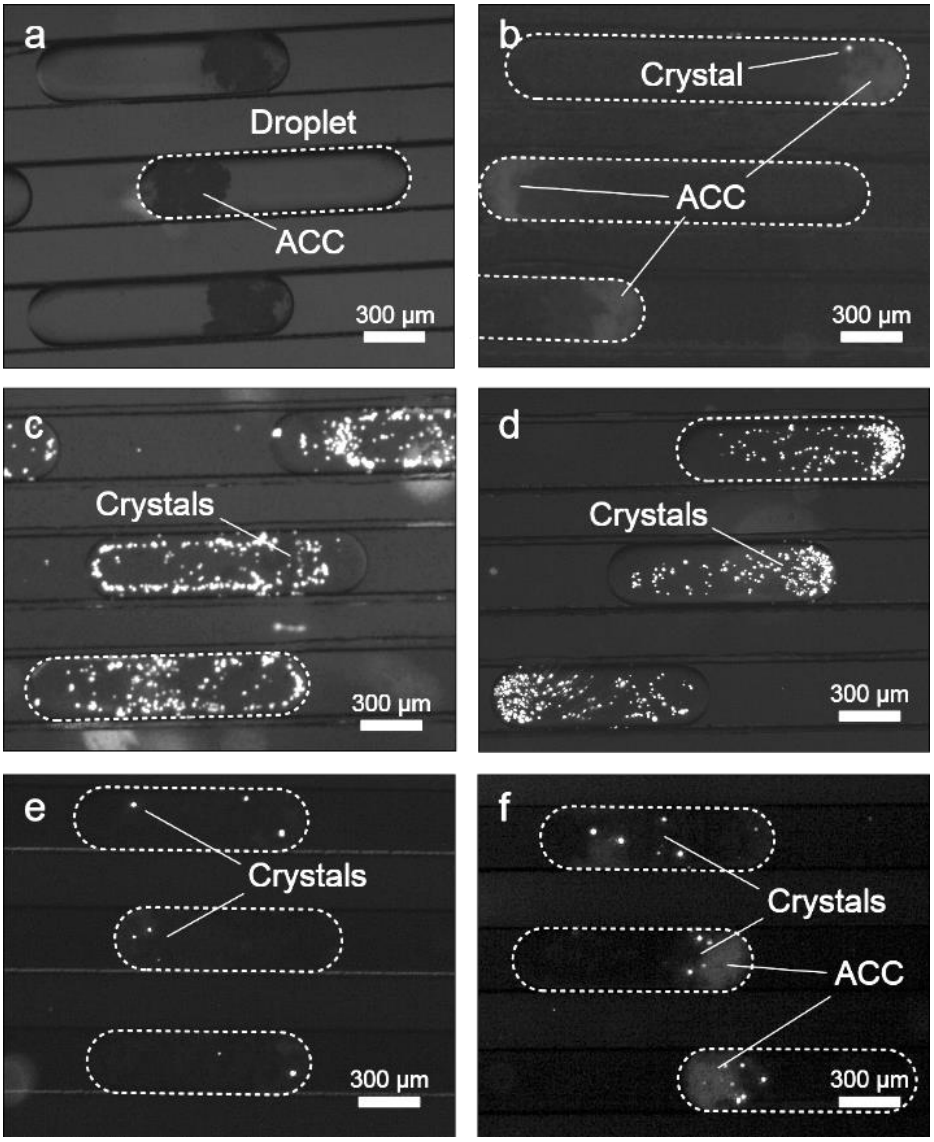

Figure 84: Optical micrographs with ~90° oriented cross polarizers obtained after flow stoppage in experiments with (a) no nucleants, (b) CPGs, (c) CNPs, (d) porous BG, (e) NX illite and (f) non-porous BG.

While these experiments provided some general insight into the efficacy of the nucleants, the low light level, the high frame-rates needed to capture droplet motion, and the slow/sporadic crystal growth in the presence of some nucleants made it difficult to obtain high resolution data, and thus gain more quantitative information. Further, since nucleation is not detectable with optical microscopy until crystals are micron-sized, and crystals can be easily obscured by the ACC aggregates, it is difficult to assign a precise induction time for crystal nucleation. For these reasons, other techniques were needed to quantify the nucleation efficiency of the nucleants.

3.2.2 UV-Vis Turbidity Measurements in Bulk

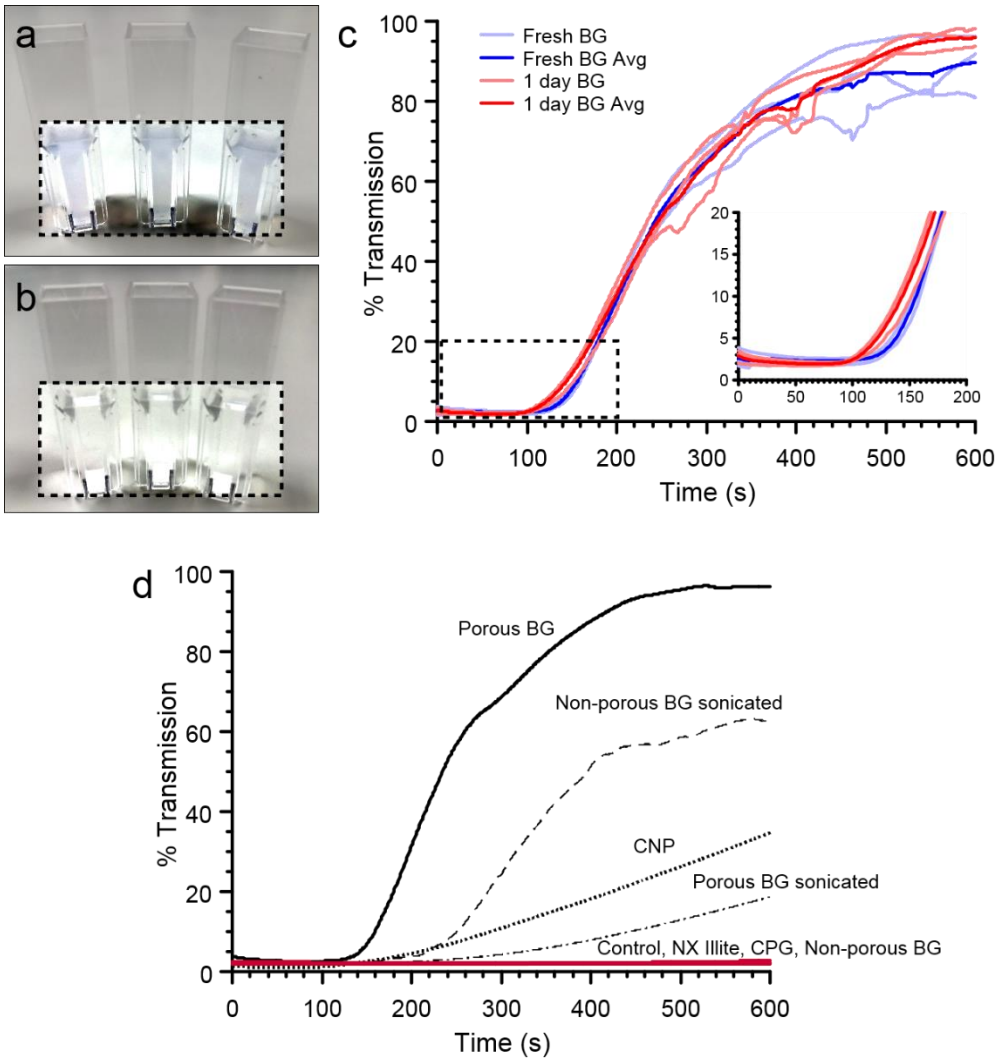

Figure 85: Photographs of cuvettes filled with (a) metastable ACC and (b) after settling of crystals. (c) Time-resolved turbidity plots of $CaCO_3$ crystallization from freshly mixed porous BG solutions (blue) and 1-day old porous BG solutions (red). (d) Time-resolved turbidity plots of crystallization with the indicated nucleant. Turbidity data were collected with a Perkin Elmer Lambda 35 UV-Vis double-beam spectrometer with 2 nm slit width and λ = 500 nm.

Light transmission through $CaCO_3$ solutions can be used as an indicator of the precipitation and dissolution of ACC.[288] The precipitation of ACC increases the turbidity of the solution, which grows more transparent as ACC dissolves, crystals nucleate, and solid materials settle on the bottom of the reaction vessel due to gravity. Here, time-resolved turbidity measurements were conducted to evaluate nucleant efficiency. When 100 mM $CaCl_2$ and Na_2CO_3 solutions were mixed in a cuvette, the immediate formation of uniformly distributed gel-like ACC throughout the solution could be observed. By eye, this material did not settle or appear to crystallize even after several hours (Fig. 85a). However, the addition of nucleants sped up this process, where near-full recovery of transparency could be achieved within 10 minutes depending on the nucleant (Fig.

85b). First, the performance of freshly mixed and 1-day old stock solutions of porous BG was compared to investigate if possible changes to the BG surface from incubation in solution could result in a difference in nucleating efficiency. Three experiments were conducted for each case, and these runs and their averages can be seen in Figure 85c. Little difference was seen between the two populations in both recovery of optical transparency (~7-10 min) and induction time (~70-80 s), where the induction time in turbidity measurements was taken to be the time when there was an inflection point, i.e. the transmission minimum just before recovery began.

Next, turbidity plots were generated for crystallizations in the presence of each nucleant (Fig. 85d). Surprisingly, solutions with porous BG recovered their transparency faster than solutions with CNP seeds. However, this is attributed to the higher nucleation efficiency of CNPs, which resulted in smaller crystals that were more resistant to settling. In fact, when porous BG solutions were sonicated for better dispersal, crystals appeared to settle at a slower rate similar to in the presence of the CNPs (Fig. 85d). Importantly, the induction time of the CNPs was shorter than that of the porous BG, and the induction times of the sonicated and unsonicated porous BG runs were the same. This suggests that regardless of settling efficiency, the turbidity measurements were equally sensitive to nucleation. The control and CPG runs showed no recovery of transparency in the observed time frame, and the NX illite run recovered less than 0.2% transmission. With the exceptions of porous and non-porous BG, sonicated and unsonicated nucleants performed similarly, and the turbidity induction times for each nucleant can be found in Table 6.

Table 6: Comparison of Induction Times with Different Nucleants

Nucleant	Turbidity Induction Time (s)	Diffraction Induction Time (s)
CNPs	≤ 68	≤ 4.23
58S BG	≤ 83	≤ 12.15
NX Illite	≤ 134	≤ 16.00
45S5 BG	≤ 93	≤ 40.77
CPG	> 600	> 142.76
CPG+COOH	–	> 142.76
None	> 600	> 142.76

Generally, the performance of nucleants correlated to the polarized light experiments. However, the unexpectedly poor performance of NX illite and the reverse trend of non-porous BG settling efficiency highlight the shortcomings of the turbidity technique. The transmission profile is the product of a convolution of ACC dissolution, crystal nucleation and growth, and gravitational sedimentation, and is therefore not sensitive enough to nucleation alone. An ideal technique should be able to sense

nucleation directly, in a small analyte volume, and provide precise data-rich information.

3.2.3 DMC-XRD in Insert-Based Devices

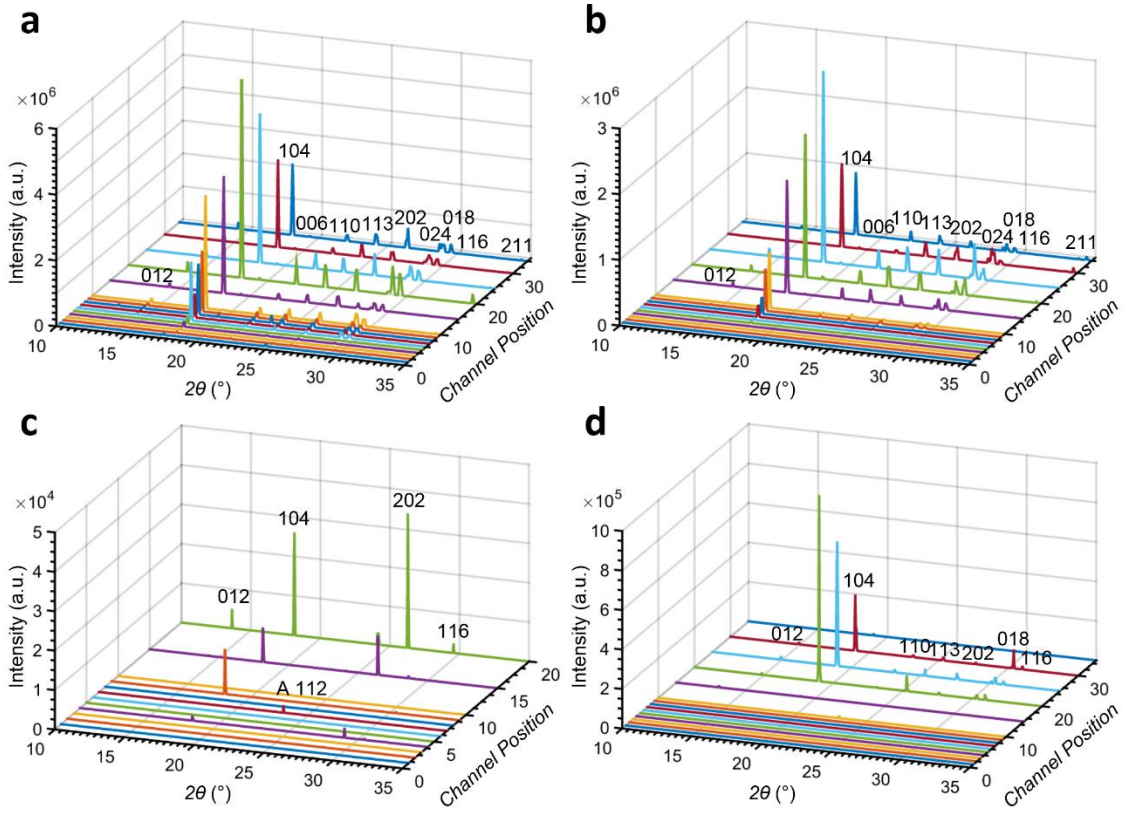

Figure 86: DMC-XRD patterns from experiments with (a) CNPs, (b) Porous BG, (c) NX Illite, and (d) Non-porous BG. Labelled peaks correspond to calcite except for the peak labelled A 112, which corresponds to aragonite.

DMC-XRD was utilized to obtain more precise quantitative data from crystallizations in the presence of the selected nucleants. XRD data collected for each nucleant was compared on the basis of induction time (i.e. position on the device where diffraction was first observed), diffraction signal growth rate, overall diffraction intensity, and consistency of measurements. The diffraction induction time for each experiment can be found in Table 6, where nucleation was detected much earlier than with turbidity measurements. Unsurprisingly, the experiment with CNPs had the shortest induction time, since $CaCO_3$ is the ideal nucleant. The induction time for the control experiment was greater than the residence time of the chip (142.76 s) due to the stability of amorphous calcium carbonate (ACC) at this supersaturation and within droplets more generally,[71] as indicated by the lack of consistent crystal growth. Porous BG induced nucleation and growth of calcite almost as rapidly as CNPs, and non-porous BG and NX illite also decreased the induction time compared to the control

experiment. Neither the CPGs nor the CPGs+COOH had a noticeable effect on induction time within the observed time frame.

DMC-XRD patterns collected from each analysis position for each dataset are shown in Figure 86 and Figure 87. Rapid increases in peak height and the number of detectable peaks are apparent for the CNP and porous BG runs (Fig. 86a and b). The results from the non-porous BG and NX illite experiments also show growth in diffraction pattern intensity. However, they are less consistent (e.g. sometimes diffraction is not observed at positions after crystals have nucleated; Figure 86c and d). Some limited diffraction was also observed in the CPG, CPG+COOH, and control experiments. However, diffractions patterns obtained from the same positions changed with time, and no consistent crystal growth was observed. For these reasons, these diffraction peaks are attributed to crystals that managed to grow on and foul device surfaces, and so do not accurately represent the residence time of the indicated positions (Fig. 87).

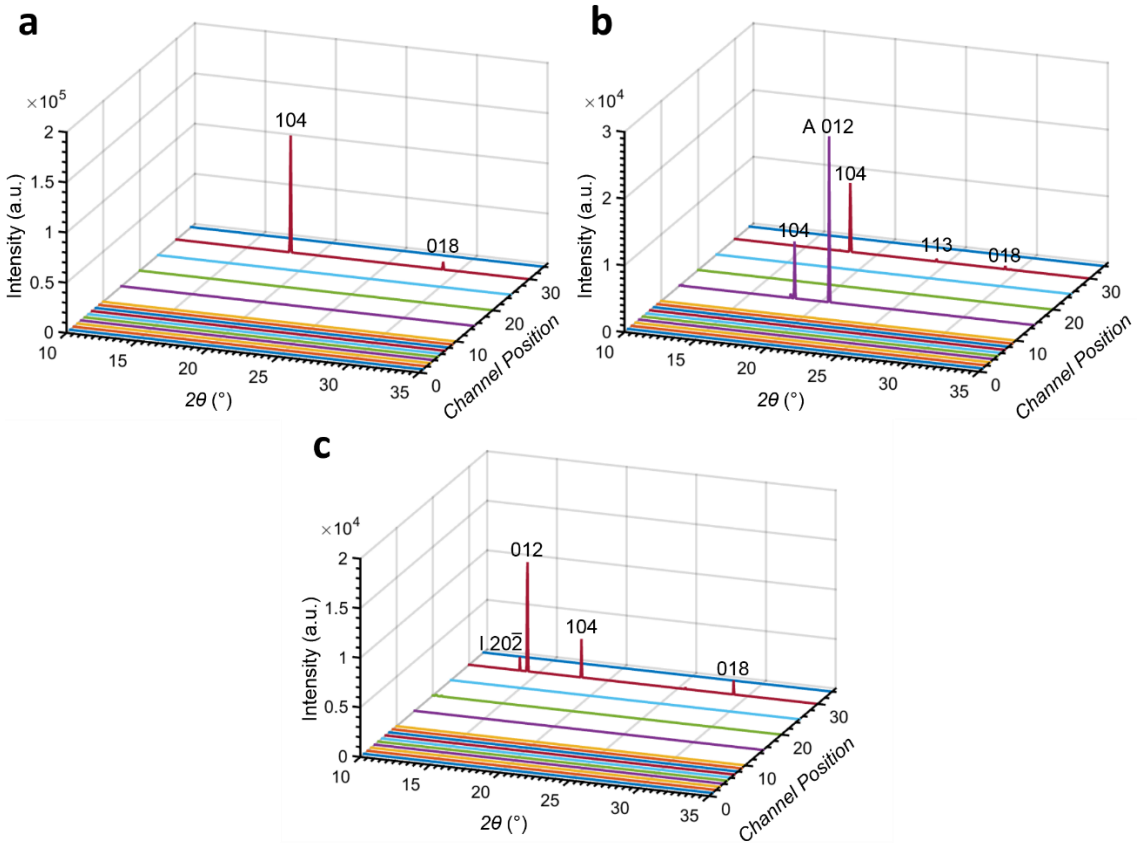

Figure 87: DMC-XRD patterns for experiments with (a) CPGs, (b) CPGs+COOH and (c) control. Labelled peaks correspond to calcite, except for peaks labelled A and I, which correspond most closely to aragonite and ikaite ($CaCO_3 \cdot 6H_2O$), respectively.

The vast majority of diffraction patterns in all experiments matched with calcite, with the notable exception of several peaks observed in the NX illite run. While many peaks corresponding to calcite were also seen in this experiment, some peaks

corresponding to aragonite were observed at Positions 7 and 9 (Fig. 88). Then, beginning at Position 15 and continuing to Position 20, there was a large increase in the relative intensity of the calcite (202) peak, so that it became larger than the (104) peak (Fig. 89). A few peaks not corresponding to calcite were also seen in the CPG+COOH and control experiments (Fig. 87b and c). However, it is important to note that in runs with low nucleation rates, the observed diffraction likely comes from device scale, and the low number and intensity of reflections and low signal-to-noise ratio makes processing and indexing more difficult.

The diffraction data from each experiment was also integrated to obtain the total area under the patterns at each position, and thus compare the relative amount of material present at each time point.[165] After initial detection of crystals, the integrated intensity from the CNP and porous BG experiments grew exponentially and then subsequently settled to near a constant value (Fig. 90). Slower growth was observed in the NX illite and non-porous BG runs (Fig. 90), and no consistent growth pattern emerged from the CPG, CPG+COOH, or control experiments (Fig. 91).

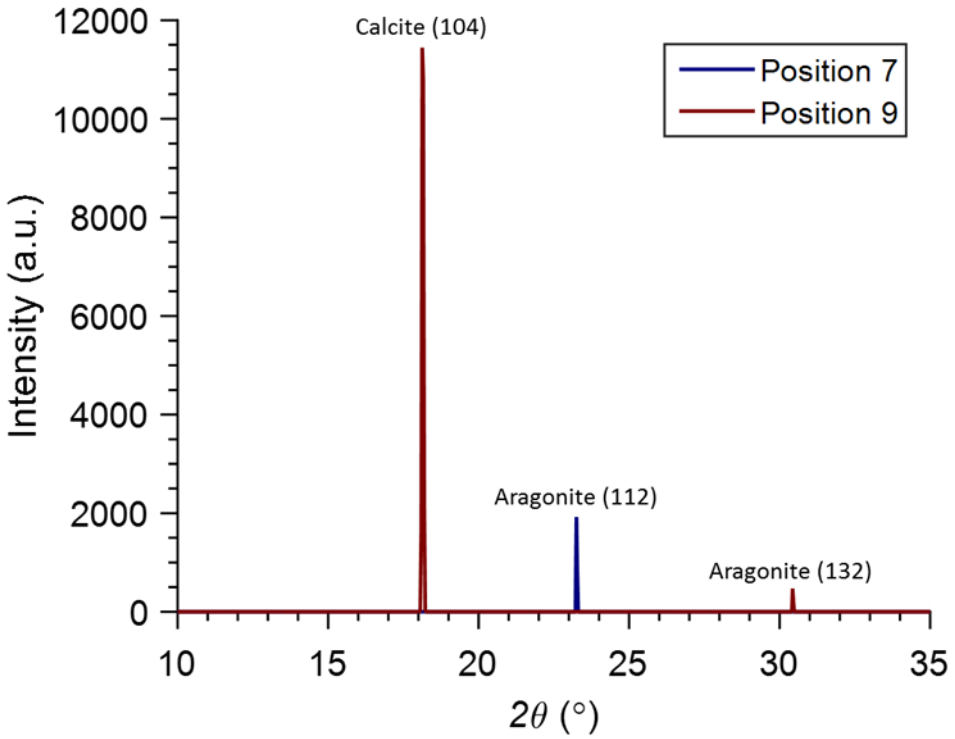

Figure 88: Diffraction patterns from Position 7 (blue) and Position 9 (red) from an NX illite experiment. These patterns contain some peaks which correspond only to aragonite and not calcite or vaterite.

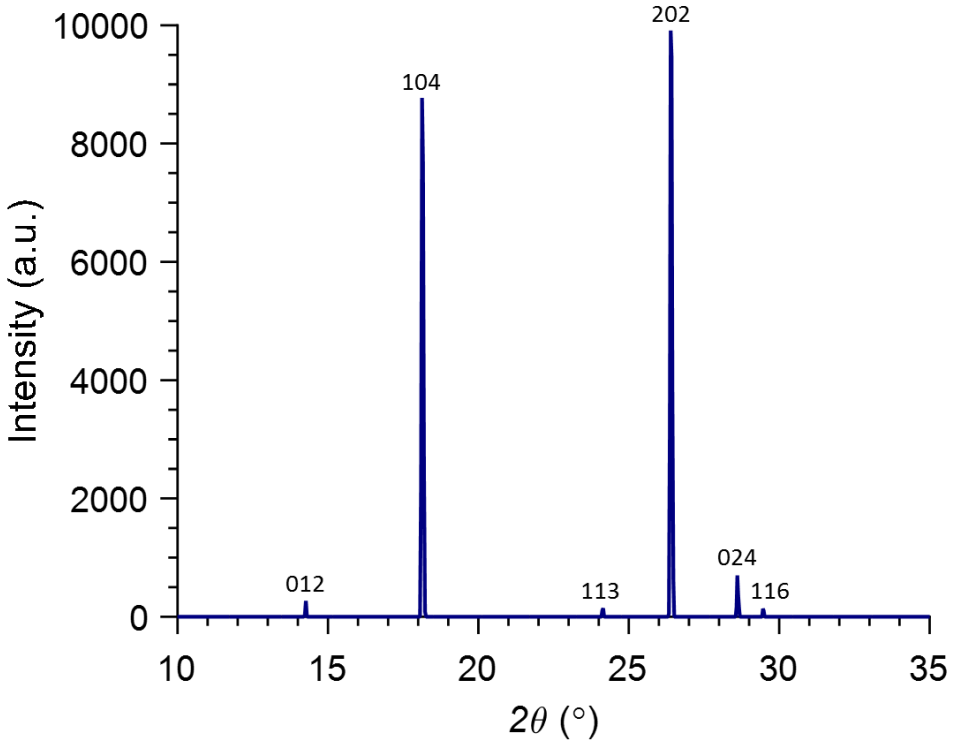

Figure 89: Diffraction pattern obtained from Position 15 during an NX illite experiment with calcite reflections labelled. The relative intensity of the (202) reflection in relation to the (104) reflection is much higher than in a standard calcite sample.

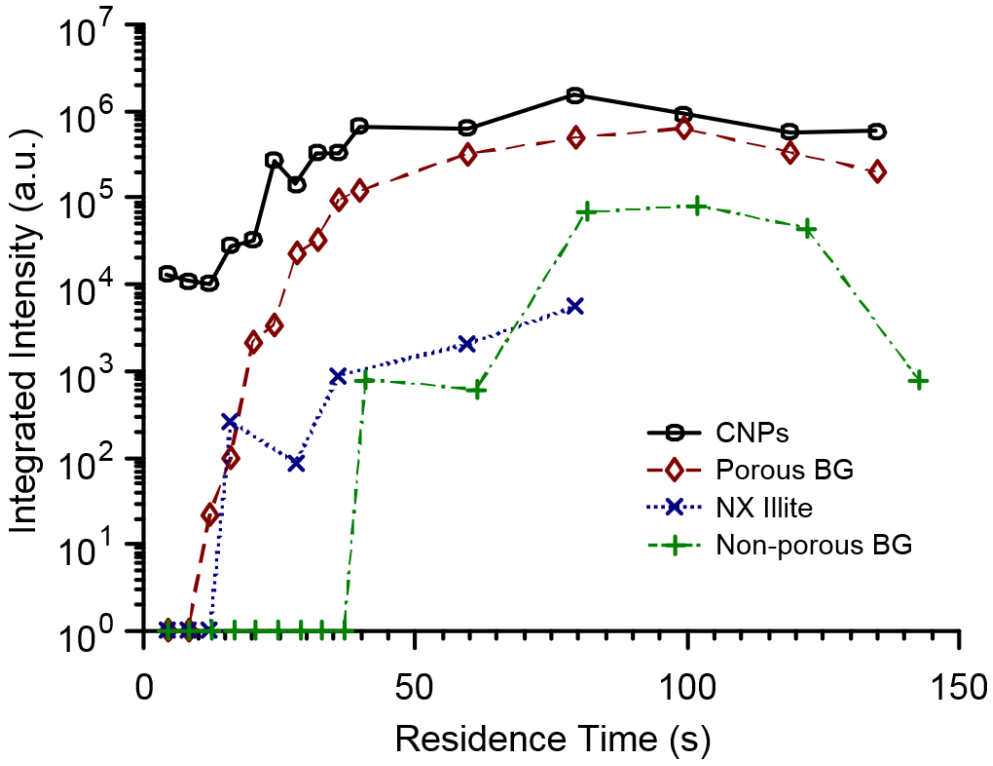

Figure 90: Time-resolved integrated intensity plots from experiments where consistent nucleation was observed on-chip. A value of 1 was added to each data point to allow patterns with zero integrated intensity to be plotted on the semi-log graph.

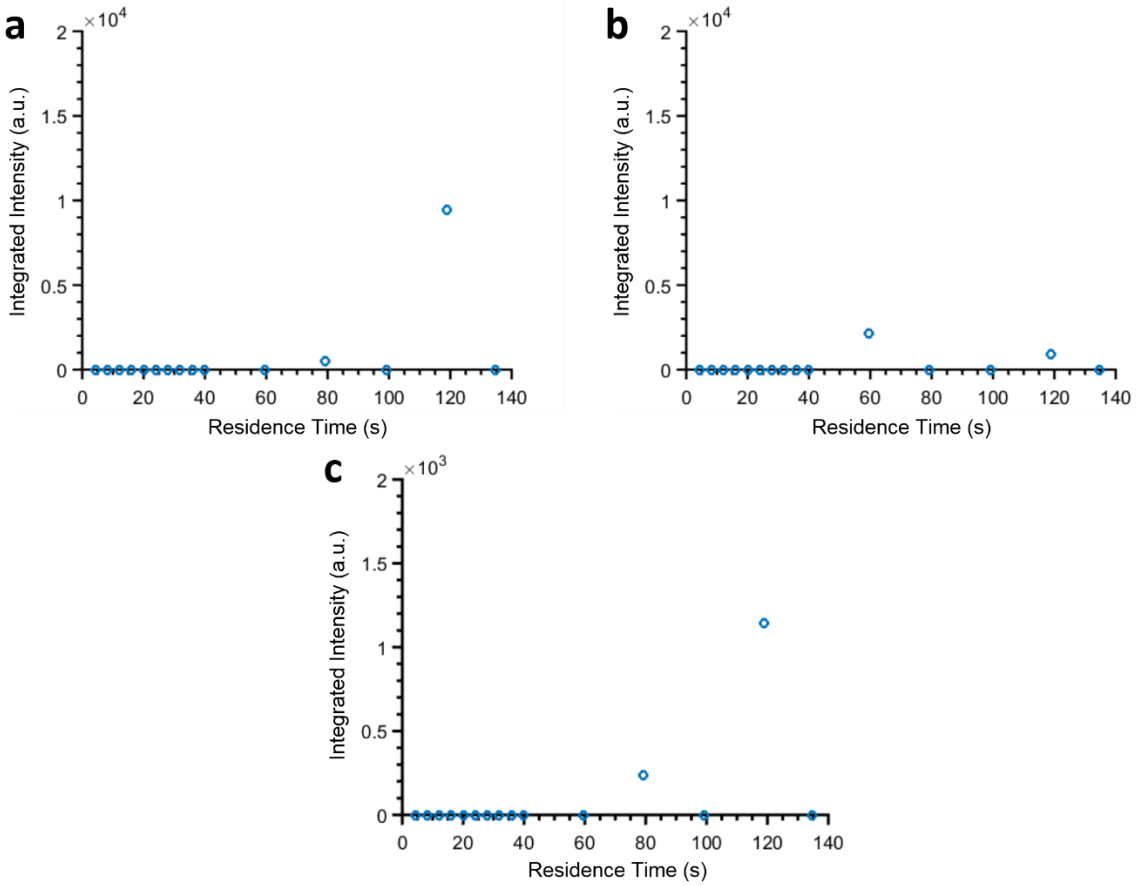

Figure 91: Integrated intensity plots from experiments with (a) CPGs, (b) CPGs+COOH, and (c) control.

3.3 Discussion

3.3.1 Bioactive Glass Nucleation Mechanisms

The clear winner of the above $CaCO_3$ nucleant trials was porous bioactive glass. Its presence in solution resulted in detectable nucleation almost as quickly as in the presence of CNPs (Table 6), fast growth in diffraction signal, and then steady diffraction intensity on the same order of magnitude as with CNPs (Fig. 90). The original hypothesis for why porous BG was such an effective $CaCO_3$ nucleant was that its wide range of pore sizes enabled it to stabilize a range of critical nucleus sizes, similar to its proposed role in protein crystallization.[8] However, that non-porous BG also nucleated $CaCO_3$ and CPGs with similarly-sized pores had no effect on nucleation suggest that the nucleating ability of bioactive glasses may not be due to pore sizing alone. For this reason, a range of other experiments were conducted to investigate the mechanism of bioactive glass-mediated $CaCO_3$ nucleation.

The nucleant trials were all done at equal mass percent, but another important way of comparing nucleants is by utilizing equalized surface areas.[289] Due to the large difference in the specific surface area (m^2g^{-1}) of porous and non-porous BG, this could

explain their differing nucleation ability. Indeed, in bulk experiments where a higher concentration of non-porous BG was utilized, ACC was depleted and all material was crystallized at a similar rate to with porous BG (Fig. 92). These experiments suggest that the surfaces of non-porous and porous BG are equally effective at crystallizing $CaCO_3$, and that the presence of pores only served to increase the interfacial area between the surface and the solution.

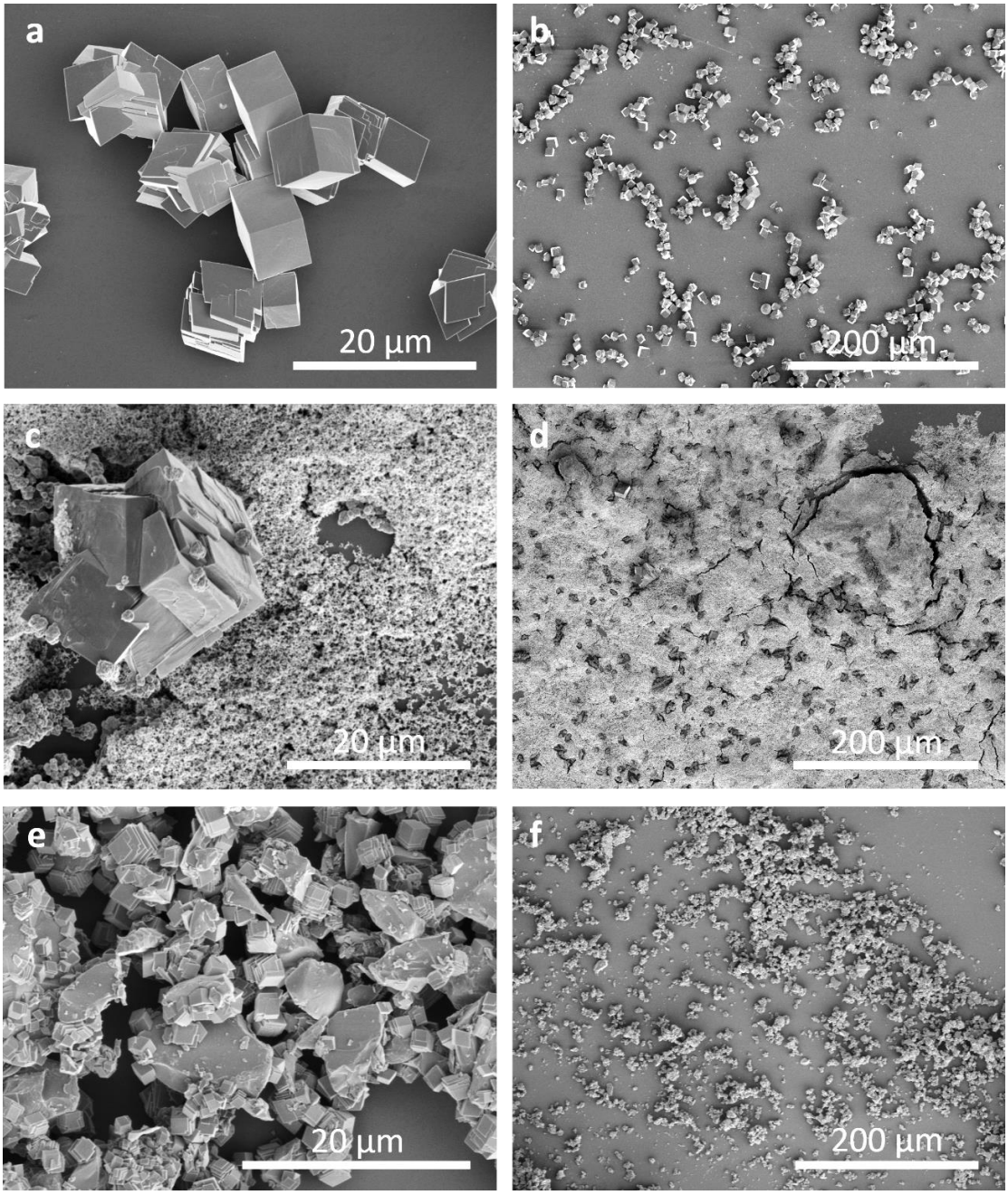

Figure 92: SEM micrographs of $CaCO_3$ precipitated after 10 min at 50 mM Ca^{2+}/CO_3^{2-} concentration in the presence of (a and b) 0.005 wt% porous BG, (c and d) 0.005 wt% non-porous BG, and (e and f) 0.89 wt% non-porous BG to match the total surface area of 0.005 wt% porous BG. (a and b) Only large rhombohedral calcite crystals are observed and no ACC remains. (c and d) Most material appears to be ACC though there are some large calcite crystals. (e and f) All ACC appears to have been depleted similar to (a and b), although a large number of non-porous BG fragments are also observed due to their high concentration.

Since it is likely that pores *do not* play a direct role in bioactive glass-mediated $CaCO_3$ nucleation, the question arises: what then *does* cause BG to nucleate calcite? While the mechanism by which it operates for $CaCO_3$ appears to be different to that for protein crystals, insight can be gained from studies of hydroxyapatite formation on BG for dental and orthopedic applications. The mechanisms of BG-mediated hydroxyapatite nucleation have been known for decades in the bioceramics community. BGs produce a highly carbonated apatite phase known as hydroxycarbonate apatite, or HCA, which forms due to a series of dynamic processes that occur at the BG surface *in vivo* or in simulated body fluids (SBFs).[290, 291]

Previous FTIR studies have revealed the different stages of these surface reactions which begin immediately upon immersion in solution.[292, 293] First, there is a cation exchange between H^+ ions in solution and Na^+ or other metal cations at the BG surface. This results in the formation of surface silanol (Si-OH) groups and the partial dissolution of the silica (SiO_2) network of the glass. Next, this silicate dissolution leads to the formation of more silanol groups, some of which condense to form a hydrated silica-rich gel layer. Ca^{2+} and PO^{4-} groups in the bulk of the glass and ions (including CO_3^{2-}) from solution migrate into this gel layer and create a carbonate-rich amorphous calcium phosphate (ACP), which finally crystallizes into HCA.

Notably, it is already recognized by some groups within the bioceramics community that calcite can form in competition with HCA on the surface of BGs. This effect has typically been attributed to the slight supersaturation with respect to both mineral phases in simulated body fluids (SBFs), which can be exacerbated at high BG loadings that quickly deplete PO_4^{3-} ions and increase the concentration of Ca^{2+} ions in solution.[294-298] Some have suggested that poor mixing leads to calcite precipitation,[299] but recently it was shown that calcite precipitation could even dominate over HCA in a well-mixed flow reactor.[300] Interestingly, Mačković *et al*. suggested that ACC could form as a precursor to a calcite.[301] However, the specific mechanisms that result in $CaCO_3$ growth on BGs have never been directly investigated until now.

When $CaCO_3$ is precipitated by direct mixing of $CaCl_2$ and Na_2CO_3 solutions, all of the necessary chemical species are present to allow these surface BG reactions to proceed. In low PO_4^{3-} environments, an ACC layer may then form in place of the ACP layer, which then quickly transforms into calcite. In nucleation trials, ACC was highly supersaturated ($SI_{ACC} \approx 1.7$), making the precipitation of ACC inevitable. However, if the surface of the BG promotes the formation of ACC in its local environment, conceivably it could still nucleate calcite via this proposed mechanism even if the solution were not globally supersaturated with respect to ACC. This proved to be true in experiments conducted with 1 mM final Ca^{2+}/CO_3^{2-} concentration ($SI_{ACC} \approx -0.38$),

where 2 μL droplets with CPGs or no nucleants contained little to no evidence of precipitation, but droplets with porous BG contained hundreds of small precipitates after an hour (Fig. 93). Subsequent UV-Vis turbidity measurements of the same conditions were in agreement with this optical data (Fig. 94). Control experiments with no nucleant showed almost no loss in optical transmission over 1 hr. The addition of CPGs resulted in lower light transmission, however when compared to measurements of control CPG suspensions in DI water, it became apparent that most of the loss of transmission was due to the scattering/absorption of light by the glass particles rather than precipitation. Conversely, in experiments with porous BG, a sharp drop in transmission corresponding to precipitation could clearly be observed within 5 min of reaction time. This confirms that BG particles can induce $CaCO_3$ precipitation even below the supersaturation of ACC.

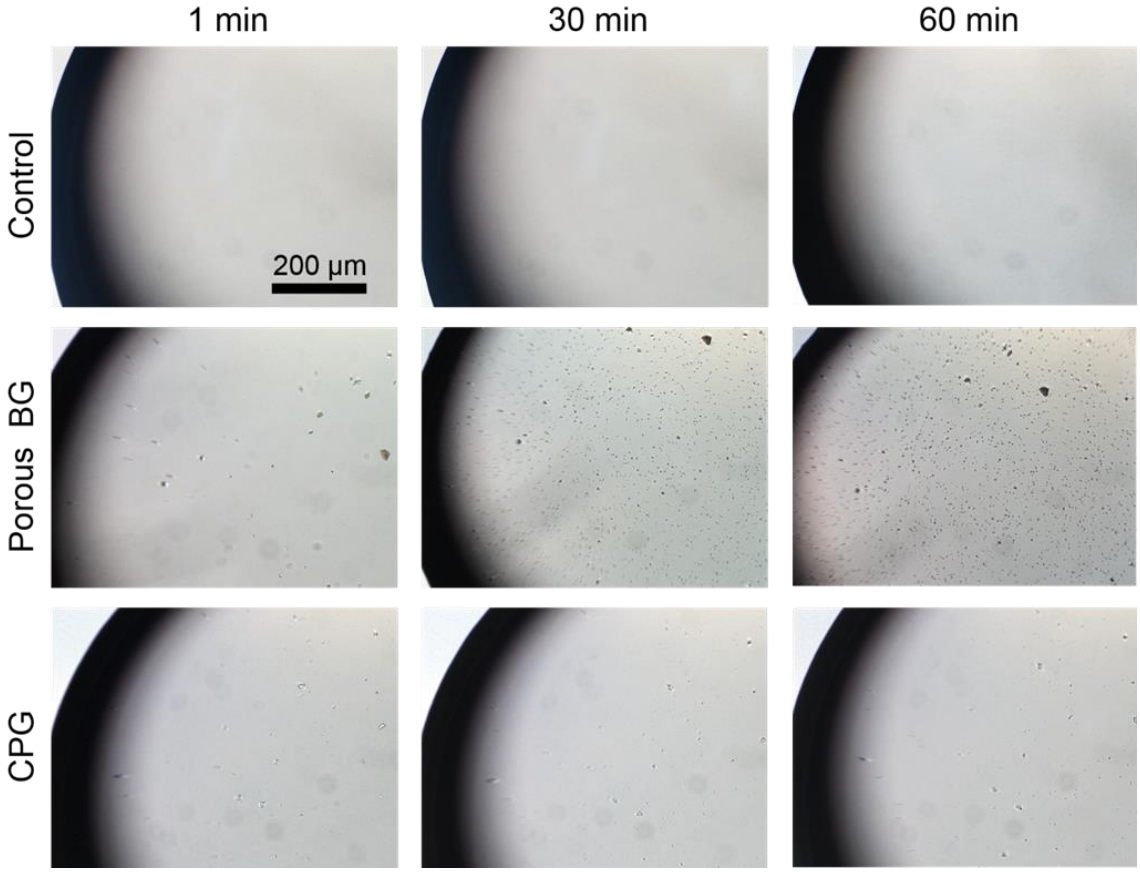

Figure 93: Time-resolved optical microscopy of 2 μL droplets of 1 mM Ca^{2+}/CO_3^{2-} containing no nulceant or 0.005 wt% of the indicated nucleant.

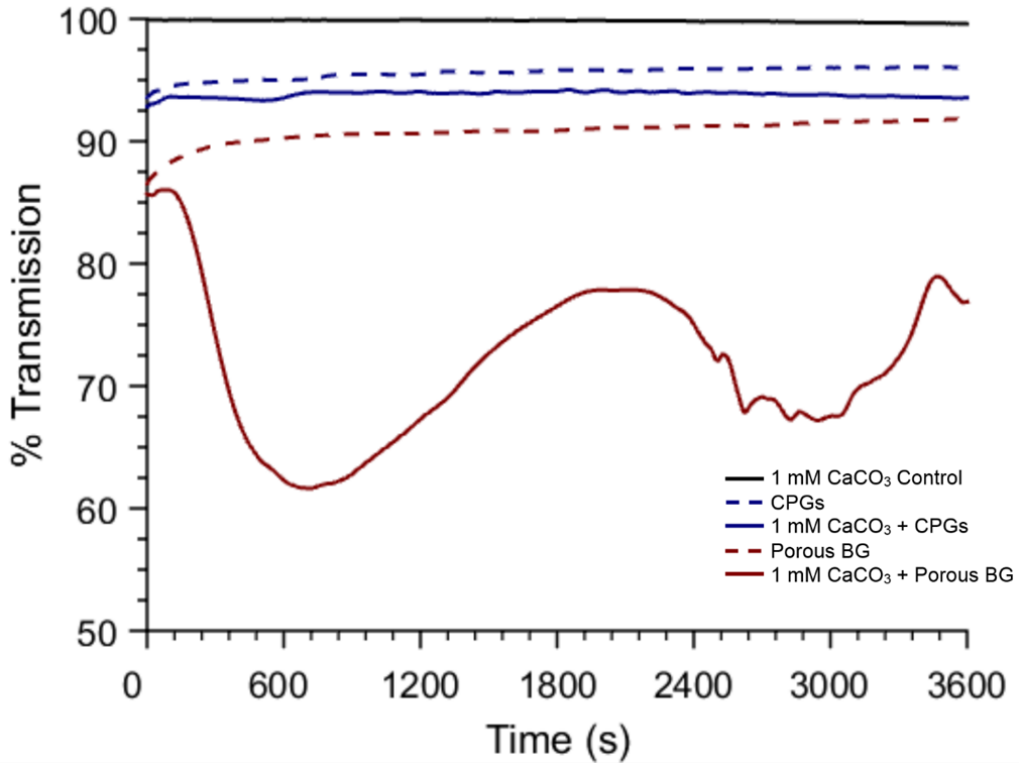

Figure 94: Time-resolved turbidity measurements of experiments at 1 mM final Ca^{2+}/CO_3^{2-} concentration and 0.005 wt% of the indicated nucleant. The control experiment contains no nucleant, and the dotted lines refer to experiments with just the indicated nucleant in DI water.

Another question is how material-specific is the nucleation mechanism of the BG. For instance, HCA and calcite both contain calcium and carbonate, so it is possible that the effect of BG is limited to materials made from these compounds. Therefore, a range of experiments were conducted with barium carbonate ($BaCO_3$) and sulfate ($BaSO_4$) to investigate the crystallization of non-calcium and/or -carbonate-containing materials on BGs and CPGs. $BaCO_3$ experiments were conducted at equimolar concentrations of 20 mM $BaCl_2$ and Na_2CO_3, and $BaSO_4$ experiments were conducted at equimolar concentrations of 1.25 mM $BaCl_2$ and Na_2SO_4. These concentrations were chosen to match the supersaturation of the thermodynamic phases of $BaCO_3$ and $BaSO_4$, witherite and barite, respectively, with the supersaturation of calcite at the 50 mM concentration of the nucleant trials ($SI_{witherite} \approx SI_{barite} \approx SI_{calcite} \approx 3.8$; Visual MINTEQ).

Interestingly, both materials crystallized faster in the presence of porous and non-porous BG than in control experiments, and CPGs also had an effect (Fig. 95). Results with $BaCO_3$ are less clear than with $BaSO_4$, as mixing resulted in the immediate precipitation of what appeared to be amorphous barium carbonate (ABC).[185] It is more difficult to distinguish between clusters of ABC and growing witherite crystals than between ACC and calcite by eye. However, after 5 minutes of reaction time, droplets containing CPGs appeared to be the least turbid and contained more distinct and homogenously dispersed material than in the other conditions (Fig. 95). Porous BG

appeared to be the second least turbid, followed by non-porous BG, and finally control. In experiments with $BaSO_4$, there was no apparent precipitation of amorphous material, and it was clear that droplets containing porous BG had a greater number of smaller crystals, suggesting a higher number of independent nucleation events (Fig. 95).

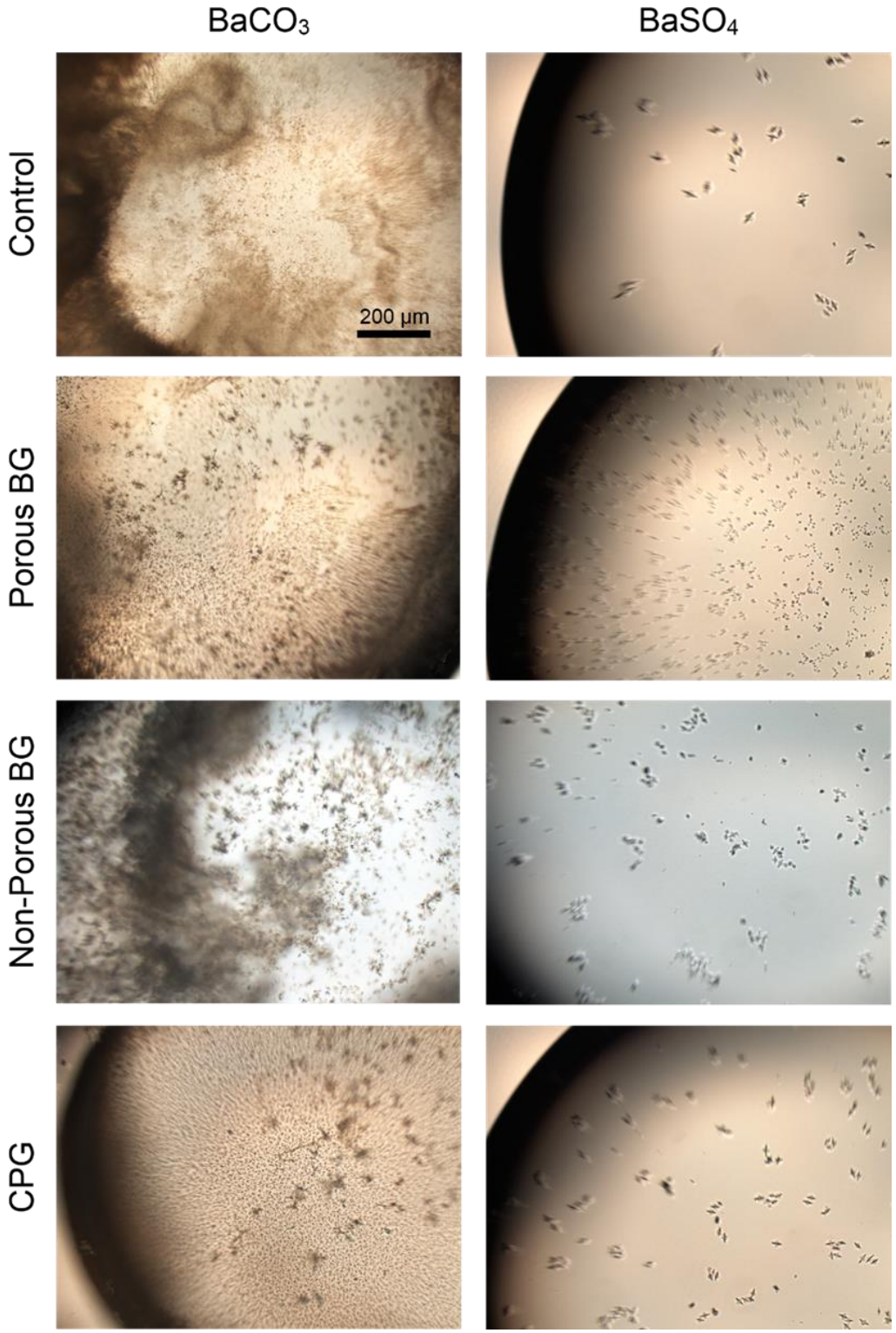

Figure 95: Optical micrographs of 2 µL droplets of either 20 mM Ba^{2+}/CO_3^{2-} or 1.25 mM Ba^{2+}/SO_4^{2-} with no nulceant or 0.005 wt% of the indicated nucleant after 5 min reaction time.

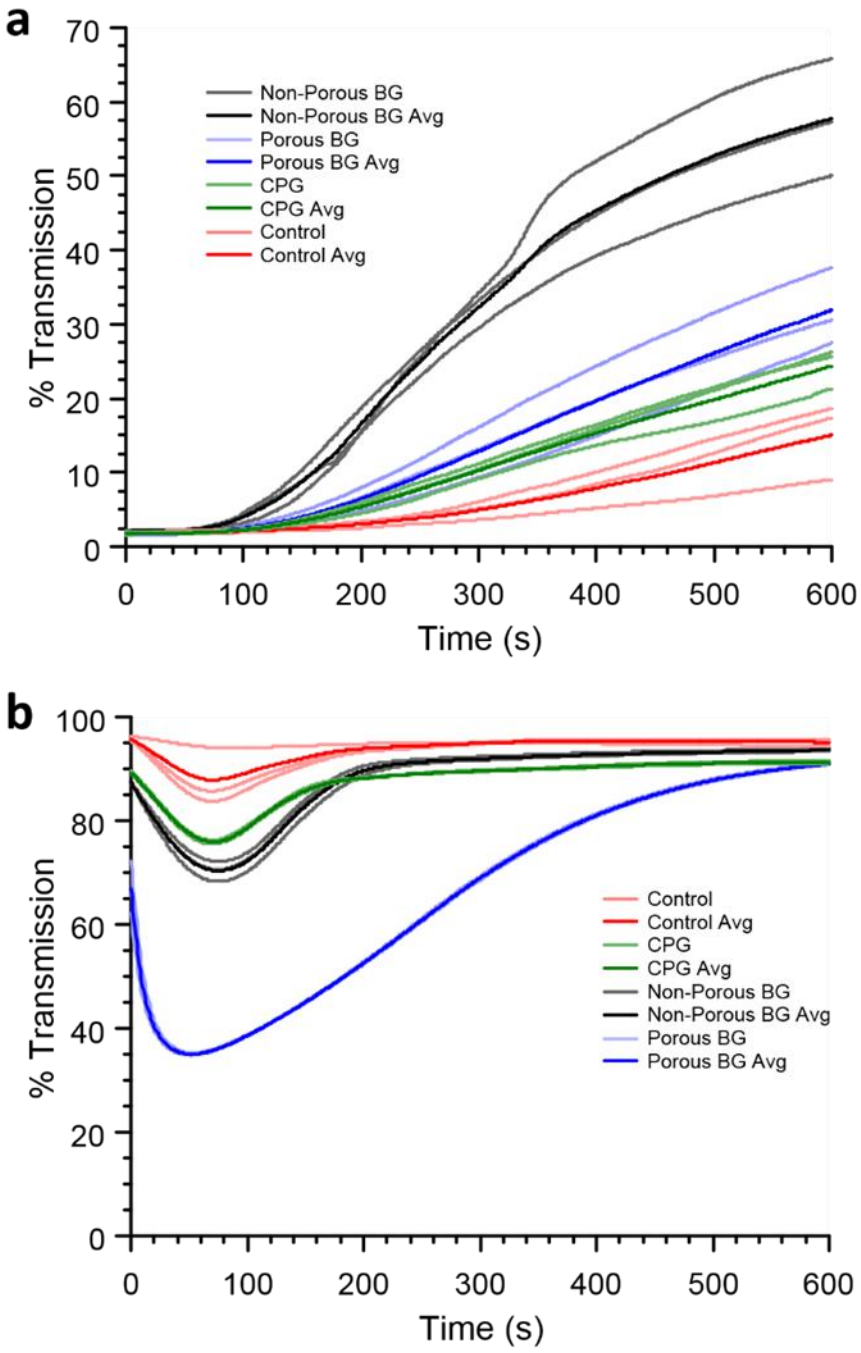

Figure 96: Time-resolved turbidity measurements of experiments with (a) 20 mM Ba^{2+}/CO_3^{2-} and (b) 1.25 mM Ba^{2+}/SO_4^{2-} with 0.005 wt% of the indicated nucleant or no nucleant (control).

The same conditions for both materials were also investigated with time-resolved turbidity measurements (Fig. 96). Immediate precipitation of ABC in $BaCO_3$ experiments caused initial transmission values to be low and then increase with time. Surprisingly, Non-porous BG resulted in the fastest recovery of optical transmission (Fig. 96a), in spite of porous BG and CPGs appearing to result in more nucleation and conversion of ABC by eye (Fig. 95). Thus, it is inconclusive which of the three powders are the best nucleant for $BaCO_3$, but all three appear to have some effect. It could be that each nucleant aids in $BaCO_3$ nucleation simply by providing a surface for

heterogeneous nucleation, rather than through a more complex recognition mechanism. In this case it would be expected that CPGs would be the best nucleant, followed by porous BG, and then non-porous BG due to their respective surface areas. If this is true, the slower recovery in optical transmission by CPGs and porous BGs could be explained by their presence resulting in the nucleation of smaller crystals which settle slower. Again, this highlights the limitations of turbidity measurements, where convolution of precipitation, crystallization, and sedimentation can make data interpretation difficult for some systems. DMC-XRD measurements could provide more conclusive results for $BaCO_3$ nucleation, making this a good candidate system for a subsequent beamtime.

Turbidity data interpretation was simpler for $BaSO_4$ since there was no initial amorphous precipitation. Here, any drop in transmission corresponds to the precipitation of barite crystals, and recovery corresponds to sedimentation of these crystals. From these data, porous BG clearly results in the most $BaSO_4$ precipitation, where optical transmission dropped to almost half that with any of the other nucleants (Fig. 96). Notably, it also appears that non-porous BG resulted in more precipitation than CPGs. This suggests that surface area is not the main contributor to nucleation efficiency here, and that there is a unique interaction between BGs and $BaSO_4$. Therefore, it is likely that the effect of bioactive glasses is not limited to calcium and carbonate-containing materials like HCA and calcite, and they can also nucleate other inorganic materials.

3.3.2 NX Illite Nucleation Mechanisms

Porous BG was the best nucleant studied here, but NX illite also clearly promotes the nucleation of $CaCO_3$. While the exact mechanism of BG-induced nucleation is still unknown, it seems very likely to be related to the dynamic surface reactions which produce ACP/HCA. However, identifying the mechanisms of NX illite-induced nucleation is more difficult than with BG. NX illite is a heterogenous material made from a variety of minerals, including feldspar, kaolinite, and illite (Table 5), and has received attention in the ice nucleation community due to the fact that is comprises so many materials often found in atmospheric dust samples.[287, 302] Thus, it is not trivial to determine which component or group of components is acting to induce $CaCO_3$ nucleation.

There are a couple of unique features of the DMC-XRD patterns that could provide some insight. The first is the detection of aragonite at two early channel positions (Fig. 88). Aragonite is not normally found at room temperature without the presence of specific soluble additives,[303] so the fact that NX illite can promote it suggests that the surface could have a chemical affinity for the structure of aragonite. Magnesium (Mg^{2+})

ions in solution can induce the room temperature formation of aragonite, and NX illite has been shown to leach Mg^{2+}.[302] However, it takes several minutes to obtain even μM quantities, and nucleation in the presence of Mg^{2+} is typically retarded.[304] Even in the presence of porous BG, solutions with enough Mg^{2+} to produce aragonite take >10 min to crystallize (Fig. 97). These make it unlikely that NX illite-induced aragonite formation is due to Mg^{2+}.

Another interesting result from DMC-XRD is the unusual relative diffraction peak heights of the calcite formed at later channel positions (Fig. 89). Such patterns are usually the result of poor scattering statistics due to preferred orientation in the sample, but can also be due to large changes in crystal morphology.[305] One possible explanation for both of these diffraction features is that structural matching resulted in the initial formation of aragonite, which converted into calcite with an unusual anisotropic morphology. However, the only evidence of this is from a single synchrotron DMC-XRD experiment. At least five other NX illite experiments were attempted over the course of three different beamtimes, but poor flow and device fouling caused by build-up of amorphous material prevented consistent data collection. Additional laboratory experiments were conducted to investigate this hypothesis, but PXRD of samples collected from bulk reactions showed no aragonite or preferred calcite orientation (Fig. 98), and SEM of samples collected from droplets did not show any atypical morphologies in experiments with NX illite or any other nucleant (Fig. 99).

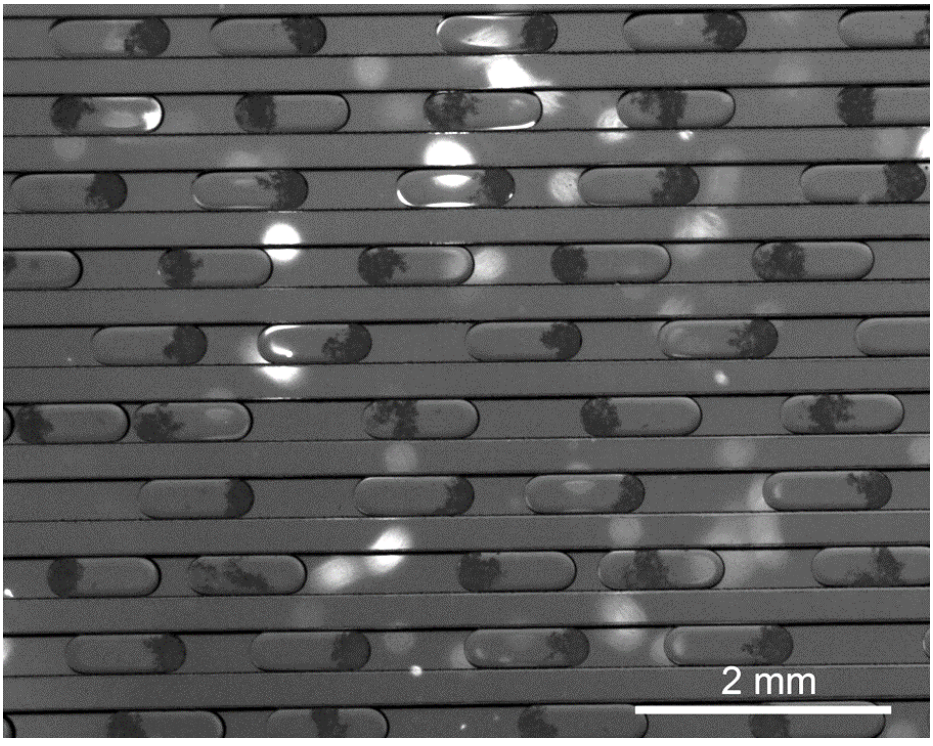

Figure 97: Optical polarized light micrograph of droplets with 0.0017 wt% porous BG, 50 mM Ca^{2+}/CO_3^{2-}, and 75 mM Mg^{2+} containing metastable ACC even after 10 min. Bright spots are due to light reflected off of out-of-focus dust fibers.

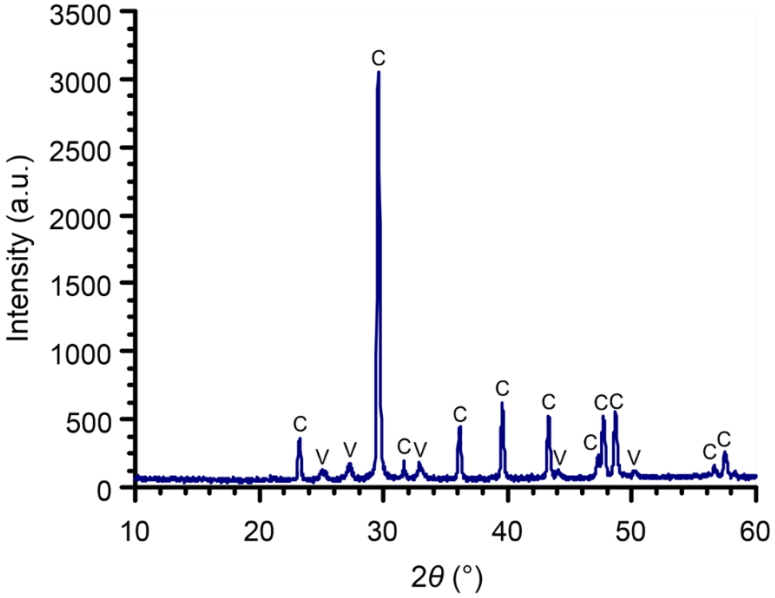

Figure 98: PXRD pattern of sample collected from crystallization with 50 mM Ca^{2+}/CO_3^{2-} and 0.005% NX illite in 1 mL under constant stirring after 10 min. Peaks are labelled calcite (C) and vaterite (V).

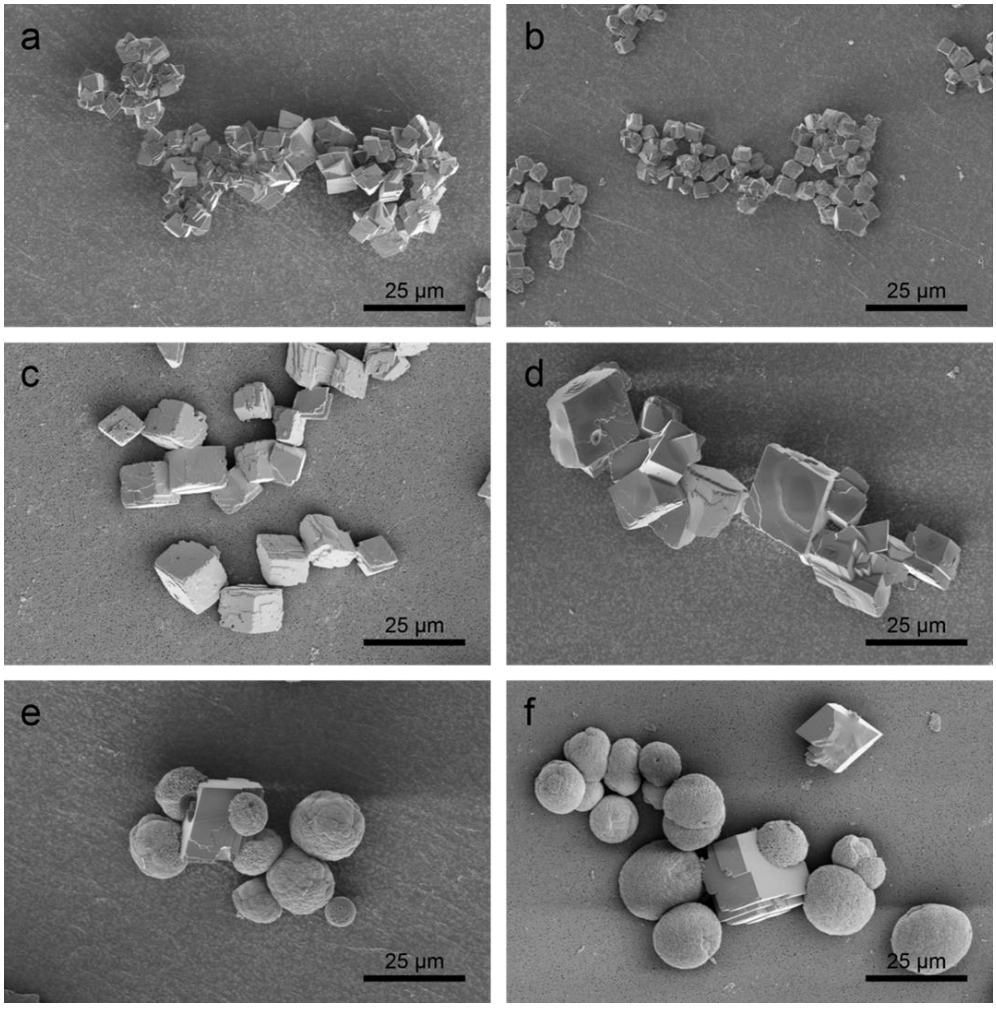

Figure 99: SEM micrographs of sample collected after 2 days from droplets from experiments with (a) CNPs, (b) porous BG, (c) NX illite, (d) non-porous BG, (e) CPGs, and (b) no nucleant.

While it is difficult to make any additional or specific claims about NX illite-mediated $CaCO_3$ nucleation based on the data collected here, previous studies of nucleation on mineral surfaces may provide some more general insights. Earlier studies of $CaCO_3$ nucleation on the minerals montmorillonite, kaolinite, and quartz showed montmorillonite to be the only effective nucleant, and suggested this was due to an epitaxial match between montmorillonite and calcite.[306, 307] This is in contrast to the results from the preliminary nucleant trials conducted as a part of this project (Section 3.1.1), where montmorillonite did not appear to be an effective nucleant for calcite. However, there are some key experimental differences between the studies. For example, they utilized lower supersaturations, did not clean mineral samples, and also soaked montmorillonite in various salt solutions before experiments ($MgCl_2$, $CaCl_2$, or NaCl). Perhaps not surprisingly, they found that the most effective montmorillonite samples were the ones soaked in $CaCl_2$,[306] suggesting that epitaxial matching alone is not responsible for calcite nucleation.

Recent studies of heterogeneous ice nucleation on mineral samples propose that nucleation is caused by surface “active sites” such as cracks or pits, which may reveal favorable underlying surface chemistries or structures,[22] be of a size or shape that promotes nucleation,[308] or work through a combination of surface chemistry and topography.[309] Additional studies of mineral-based ice nucleation have identified alkali feldspars as the most effective components of atmospheric dusts,[17] where their effectiveness has been linked to surface features at grain boundaries between Na- and K-rich domains.[7] Therefore, it may be that NX illite – containing a range of minerals, including feldspars – nucleates $CaCO_3$ due to its unique surface topography resulting from its heterogeneous nature. In the future, additional characterization of NX illite, trials with a wider range of crystal systems, and *in situ* experiments which allow the precise location and structure of an active site to be identified, should help to provide a more defined nucleation mechanism.

3.4 Summary

Herein, several orthogonal time-resolved methods (polarized light, turbidity, and DMC-XRD) were employed to investigate the nucleant-mediated crystallization of calcium carbonate. Of the nucleants studied, porous bioactive glass was clearly the most effective in terms of both shortening induction time and increasing overall growth. Surprisingly, controlled porous glass having a similarly high surface area and pore volume to porous BG did not significantly promote $CaCO_3$ nucleation. CPGs functionalized with COOH groups were also ineffective, despite the fact that COOH SAMs on planar substrates can promote nucleation.[6, 82] This puzzling result seemed to

indicate that it could be the larger pore size range of the porous BG compared to the CPGs that enabled it to function as such an efficient nucleant.[8] However, non-porous BG was also shown to nucleate calcite, although to a lesser extent than porous BG. That porous and non-porous BGs both promote nucleation suggest that their ability to nucleate calcite is a chemical property of BG rather than a physical property of pore sizing, where both BGs appeared equally effective when their surface areas were normalized (Fig. 92).

The relatively small amount of calcium released by BGs, the slow rate of this release (Fig. 82), and the fact that freshly suspended and day-old bioactive glass-containing solutions performed no differently (Fig. 85c), make it unlikely that nucleation is due solely to a transient localized Ca^{2+} ion release or by a global increased Ca^{2+} concentration. Equally, the poorly crystalline nature of both bioactive glasses, especially the non-porous BG, makes epitaxial growth unlikely (Fig. 81a and b). Finally, the porous BG is fabricated using a sol-gel method and the non-porous BG from a melt, with both containing similar amounts of SiO_2, CaO, and P_2O_5, but the non-porous BG additionally containing some Na_2O (Table 5). These large differences in the syntheses, in the surface topographies of the bioactive glasses as observed by SEM (Fig. 79a and b), and the rapid dissolution/restructuring of BG surfaces that occurs in solution, also make it unlikely that a particular surface feature is responsible for triggering nucleation. Therefore, it is plausible that calcite nucleation is promoted due to the formation of a surface ACC layer resulting from the same mechanisms that lead to ACP and HCA production. Perhaps a similar amorphous phase-mediated pathway leads to $BaSO_4$ and/or $BaCO_3$ crystallization, however more experiments are necessary to provide more conclusive evidence for this theory. Importantly, these results also clearly show that BGs can act as effective nucleants in a matter of seconds, not just over timescales of hours and days such as those often studied in bioceramics assays.[310]

These results also highlight the utility of DMC-XRD, which provides highly sensitive analysis of crystallization in clean, controlled, and reproducible environments. It permits the correlation of material structure to residence time and also enables quantitative information, such as induction time and crystallographic parameters to be gathered – where DMC-XRD was close to one order of magnitude more sensitive to nucleation than turbidity measurements (Table 6). Such data, coupled with other *in situ* and *ex situ* analyses, has revealed new insight into the mechanisms of calcite growth on bioactive glasses, NX illite, and nucleant-induced $CaCO_3$ crystallization more generally. Counter to conventional wisdom, high surface area and porosity alone do not necessarily make a good nucleant. Neither do the combination of high surface area

and beneficial surface chemistry, e.g. CPGs+COOH. While it is difficult to predict such combinations and select or design effective nucleants, the methods presented here should find use in evaluating potential nucleants and investigating their mechanisms.

Chapter 4:
Millifluidics-Coupled Powder X-ray Diffraction

The previous two chapters introduced a new droplet microfluidic technique for powder X-ray diffraction analysis (Section 2.3), tested it against conventional continuous flow type operation (Section 2.4), and utilized it for studying heterogeneous crystal nucleation and growth (Section 3.2.3). The remainder of the thesis investigates the use of similar flow systems at different length scales and with different X-ray sources.

This chapter explores synchrotron-based analysis through case studies with two different milli-fluidic X-ray sample environments. The first environment (Section 4.1) is analogous to DMC-XRD, but using millimeter-sized aqueous plugs containing crystals that are probed using a serial crystallographic approach. The second environment (Section 4.2) is a continuous flow crystallization platform based on cascaded stirred-tank reactors, where bulk crystal growth can be observed over the device residence time and surface crystallization is not as dominant with a lower surface area-to-volume ratio than compared to microfluidics.

4.1 The Kinetically Regulated Automated Input Crystallizer – Diffraction (KRAIC-D)

4.1.1 Background

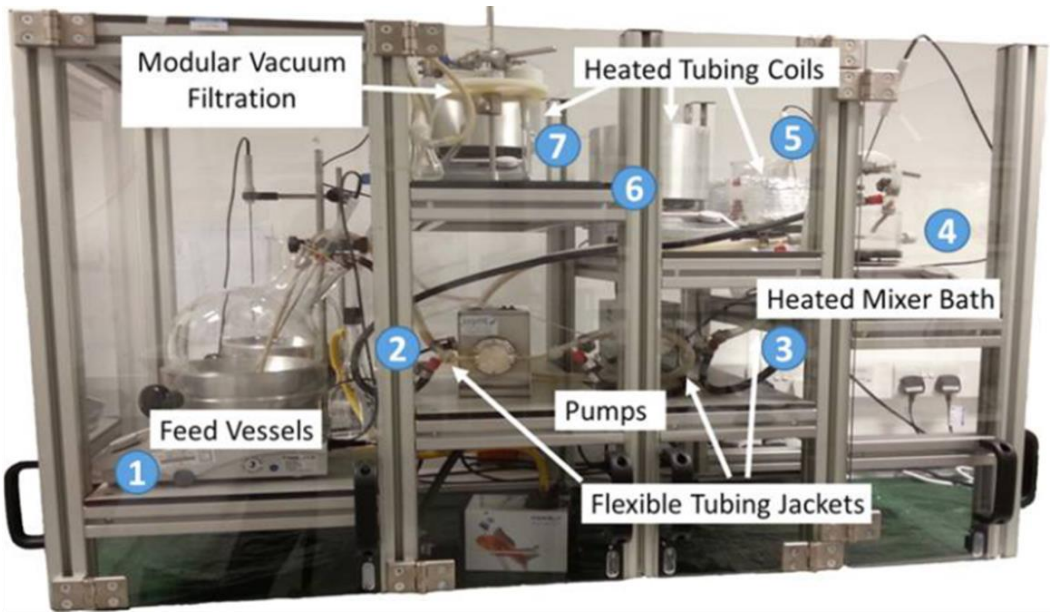

Figure 100: Original laboratory KRAIC. Numbered regions indicate temperature zones; (1-4) Feed/mixing region at 40 °C; (5) Heated cool 1 at 30 °C; (6) Heated coil 2 at 24 °C; (7) Heated coil 3 at 22 °C. Reproduced from ref.[311]

The kinetically regulated automated input crystallizer, or KRAIC, is a mesoscale flow reactor developed by Robertson *et al*. at the University of Bath.[311] It consists of two gear pumps that transport an undersaturated solution and a carrier oil phase from their respective heated and stirred feed vessels into a mixer piece. Downstream of the mixer is a 15 m long fluorinated ethylene propylene (FEP) tubing reactor wound into a series of heated coils (Fig. 100). The mixer generates a steady plug flow of the solution in the carrier fluid (Fig. 101a and b), and the series of coils in the reactor allow the solution to cool, become supersaturated, and crystallize at a controlled rate (Fig. 101b and c). As an added benefit, a separation mechanism at the device outlet enables the carrier fluid to be recovered and continuously reused. This recycling process together with the plug flow operation of the device allow for long (>2 hr) production cycles to be completed with a single batch of feed solutions and without device scaling.

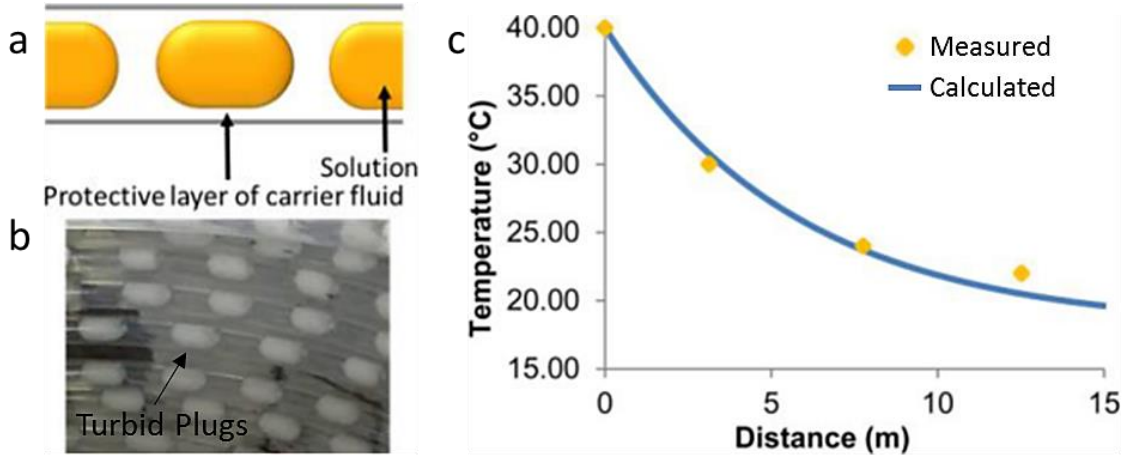

Figure 101: (a) Diagram of the KRAIC solution-in-carrier fluid plug flow. (b) Photograph of turbid plugs at a heated coil segment revealing the presence of crystals. (c) Graph of the temperature gradient along the reactor tubing. Adapted from ref.[311]

While enabling high-throughput materials production, the materials characterization capabilities of this original KRAIC were limited. For example, characterization could only be performed by collecting products at the device outlet for subsequent *ex situ* analysis. Collecting data from different time points then required multiple experiments utilizing different total reactor tubing lengths, where this was time-consuming and entailed making major modifications to the device in order to set-up each experiment. For this reason, the developers of the KRAIC became interested in modifying its design to perform *in situ* analyses, including X-ray diffraction. After a chance encounter at Diamond Light Source between one of the KRAIC developers and the author of this thesis, a collaboration was born to design a new KRAIC system using the principles of DMC-XRD: the KRAIC-D (D for diffraction!).

4.1.2 Device Design and Fabrication

Conceptual Design

As is clearly seen from Figure 100, the original laboratory KRAIC is not easily adapted for use at a beamline. It is far too large and cumbersome to fit on a translational sample stage, and more importantly, has no easy access point for X-rays. Thus, an entirely new design concept was needed. For simplicity, the feed vessels and pumps would be separated from the crystallization/analysis section of the reactor, which would be built on an optomechanical breadboard for easier mounting on a goniometer. The CAD design of this new streamlined section of the KRAIC-D can be found in Figure 102. It comprises three main components: *(1)* a base, *(2)* two cylinders for wrapping tubing, and *(3)* two central support rails to hold X-ray window segments between tubing coils. These rails ensure that analysis windows will be fixed in place in order to provide consistent spacing and sample-to-detector (S-to-D) distance.

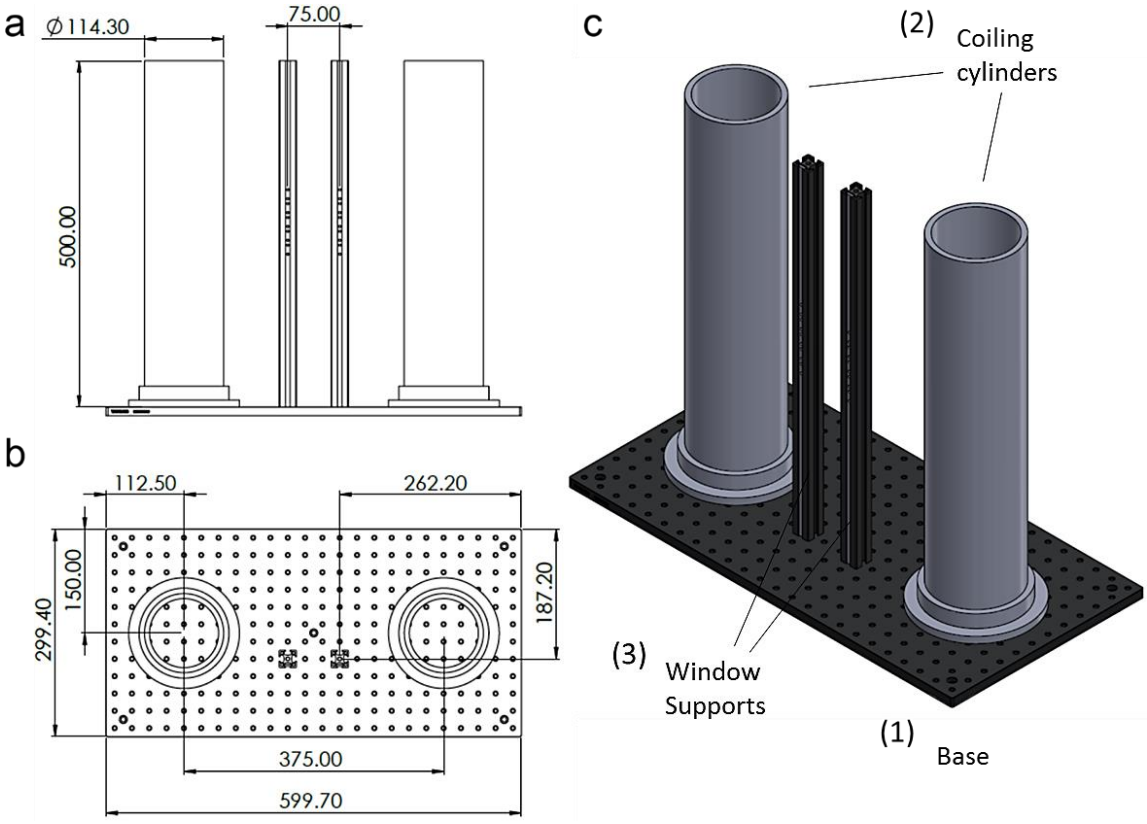

Figure 102: CAD design of the KRAIC-D. (a) Front view. (b) Top view. (c) Isometric view showing the base, coiling cylinders, and central window support rails. All dimensions in mm.

Since the FEP tubing that composes the reactor section of the original KRAIC is thick and has high background X-ray scattering, analysis sections would need to be made from another material. Keeping with the design of the insert-based microfluidic device (Chapter 2), Kapton was selected due to its high mechanical, thermal, and chemical stability, its low X-ray absorbance,[212] and because it can be easily obtained in

not only sheet, but also tube form. However, since Kapton tubing does not have the flexibility to be coiled without buckling and is also expensive to obtain in large quantities, the majority of the flow system would still be made out of FEP. This meant that a suitable interface between the Kapton windows and the FEP tubing would need to be designed to minimize flow disturbance and to prevent leakage. The design of this Kapton-FEP tubing union is presented in Figure 103. One side contains a bore that matches the outer diameter of the FEP tubing (~4.8 mm), and the other side contains a bore which matches that of the Kapton tubing (~3.4 mm). In the center of the union is a cylindrical channel that matches the inner diameter of both the Kapton and FEP tubing (~3.2 mm each), so that there is no cross-sectional area change – which could cause flow disturbance – flowing into or out of the union. There is also a notch around the middle of each union, where bolts can be used to fix the union to the window support rails (Fig. 102c).

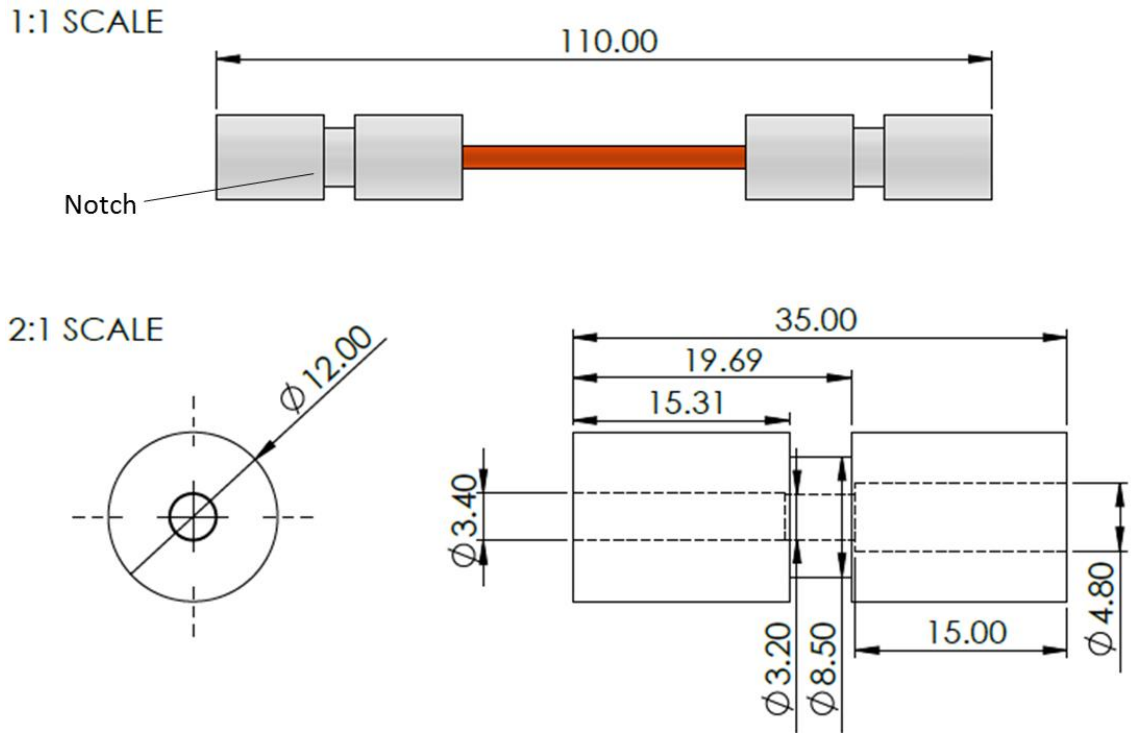

Figure 103: CAD design of the Kapton-FEP unions showing an assembled window section (1:1 scale) and a single union piece (2:1 Scale). All dimensions in mm.

Device Construction

The base of the KRAIC-D is a 300 x 600 mm aluminum breadboard purchased from Thorlabs. The coiling cylinders were cut into 500 mm tall sections from polyvinyl chloride (PVC) solvent weld pipes (E Class; OD: 114.3 mm; ID: 97.7 mm) and fixed to the base using 114 mm diameter acrylonitrile butadiene styrene (ABS) flange pipe fittings. FEP tubing making up the majority of the flow reactor was obtained from Omega (OD: 4.763 mm; ID: 3.175 mm). FEP tubing segments totalling approximately

10.5 m in length (between the first and fifth window section) were wrapped around the cylinders and fixed in place using laser-cut PMMA brackets, which fasten to M5 internal threads equally-spaced along the side of the cylinders (Fig. 104a). Each FEP segment is inserted into the outlet of a window section, wrapped 2.5 times around two coiling cylinders (~10 mm pitch), and inserted into the inlet of the next window section. The z-positions where the FEP tubing crosses between the cylinders were carefully selected to ensure that the tubing did not block the beam path to any Kapton window.

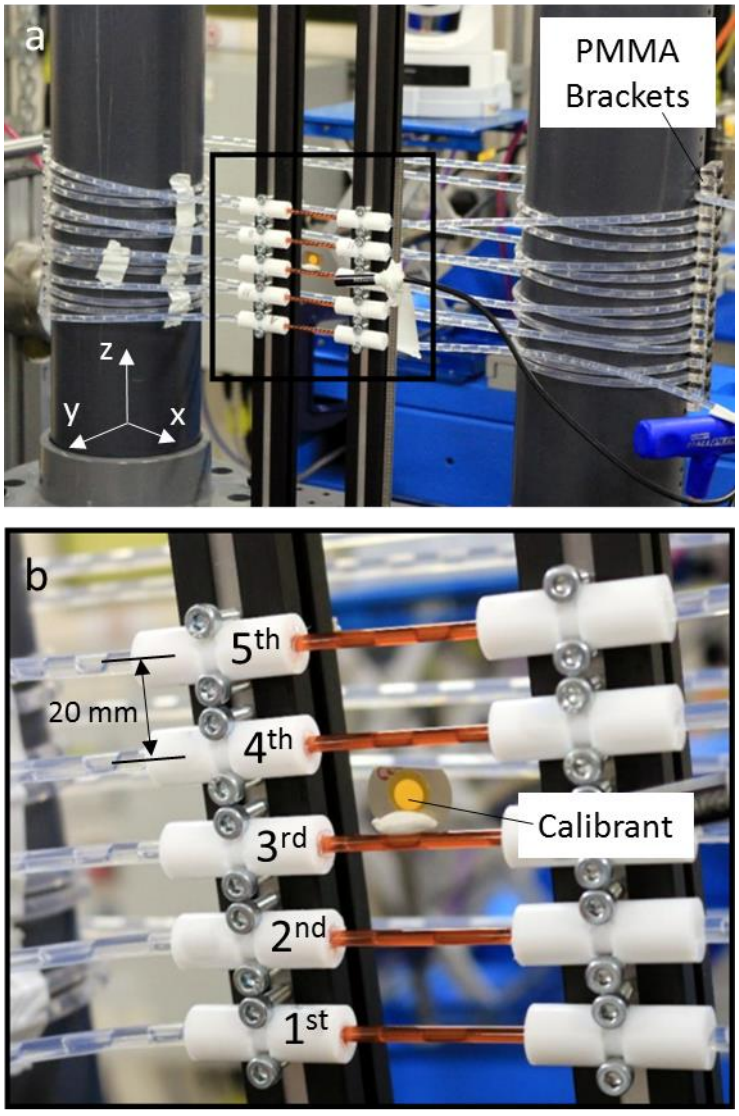

Figure 104: (a) Photograph of the completed KRAIC-D mounted in the hutch at Diamond beamline I11. The beam path is in the positive y-direction. (b) Close-up photograph of the five analysis window sections.

Kapton-FEP tubing unions were machined out of 12 mm diameter PTFE rods using a sliding head lathe (Cincom L12, Citizen). PTFE was selected since it is the thermosetting version of FEP and has similar wetting properties. Each Kapton window section is supported at both unions by a 500 mm tall aluminum construction rail (Thorlabs; Figure 104b). The unions were fixed to the rails with the help of long 500

mm pieces of stainless steel comprising appropriately-spaced M5 internal threads that slot into the rails to serve as drop nuts. Additionally, a thin metal shim containing some CeO_2 calibrant powder was placed on top of the middle Kapton tube to determine the sample-to-detector distance of the windows (Fig. 104b).

Analysis Window Preparation

Analysis windows were made from seamless Kapton tubing obtained from American Durafilm (ID: 3.188 mm; wall thickness: 0.095 mm). This tubing was required because preliminary flow experiments showed that the seams between each wrap of more standard spiral-wound Kapton tubing disturbed the plug flow. Before assembly into window sections, each Kapton piece must be cut to size and chemically treated. Kapton tubes were cut into 7 cm long sections using a razor blade, where the tubes were held in a cutting-block with a narrow slot for entry of the blade. This setup aids in making smooth cuts perdindicular to the tube axis which are necessary to create a clean interface within the PTFE unions. A similar cutting setup was utilized for the same reason for the FEP tubing. After cutting, the Kapton tube surfaces are rendered hydrophobic using an Aquapel-based method similar to the one utilized for microfluidic device treatment,[118] where five tubes are processed at a time. First, the Kapton surfaces are activated by placing the tubes in a radio frequency plasma chamber (Harrick Plasma) for 60 sec. The tubes are then placed in a 15 mL Eppendorf centrifuge tube with a whole ampule of Aquapel and gently agitated for 30 sec while ensuring all surfaces are contacted by the solution. The Kapton tubes are then removed from the solution, rinsed with ethanol, DI water, ethanol again, and dried with clean dry air. Finally, window sections are assembled by placing a union on each end of a treated Kapton segment and applying a small amount of transparent silicone rubber sealant (RS Components) to prevent leaking.

4.1.3 Urea-Barbituric Acid: A Case Study with KRAIC-D

The Urea-Barbituric Acid Co-Crystal System

The organic co-crystal system, urea-barbituric acid (UBA), was selected as the initial KRAIC-D test material. Organic crystallization is an important aspect of the production of active pharmaceutical ingredients (APIs), where the formulation of co-crystals containing an API and a suitable coformer provides additional parameter space for optimizing properties including product stability, bioavailability, and manufacturability.[312, 313] However, the design of co-crystals is complex, since they can form in multiple polymorphs – just like their single-component crystal counterparts.[312] UBA is a good model system for co-crystals since it has three known anhydrous polymorphs, which can be formed from cooling crystallizations in methanol or ethanol.

All three forms have a 1:1 mole ratio of urea to barbituric acid, with Forms I and III being the most commonly observed and Form II being more elusive.[312] Additionally, Forms I and III have very similar solubilities, to the point that it is still unclear which is the most stable polymorph.[312-314]

Experimental Setup at Diamond beamline I11

Here, the cooling crystallization of UBA in methanol was studied in a tri-phasic methanol-oil-air system (Fig. 105a). A methanolic solution of 13.21 g/L urea and 14.09 g/L barbituric acid was combined with a flow of air plugs in fluorinated oil (Galden SV110) at a T-piece mixer, where introducing air segments between each solution plug prevented the coalescence of plugs at inclined sections of tubing. The solution was dosed with an SF-10 pump (Vapourtec), and the air and oil were dosed with chromatography pumps (Asynt) for a combined flow rate of approximately 12.4 mL/min (N.B. due to the compressibility of air and the pump precision, the set flow rate is not exact). The residence time of plugs in the reactor (14.38 m from the mixer to the outlet) was observed to be 8.33 min, where this corresponds to a true average flow rate of 13.7 mL/min and plug velocity of 28.8 mm/s. Assuming this flow rate to be constant across the device, the residence times of windows 1 to 5 (see Figure 105b) were 0.73, 2.29, 3.85, 5.41, and 6.97 min, respectively.

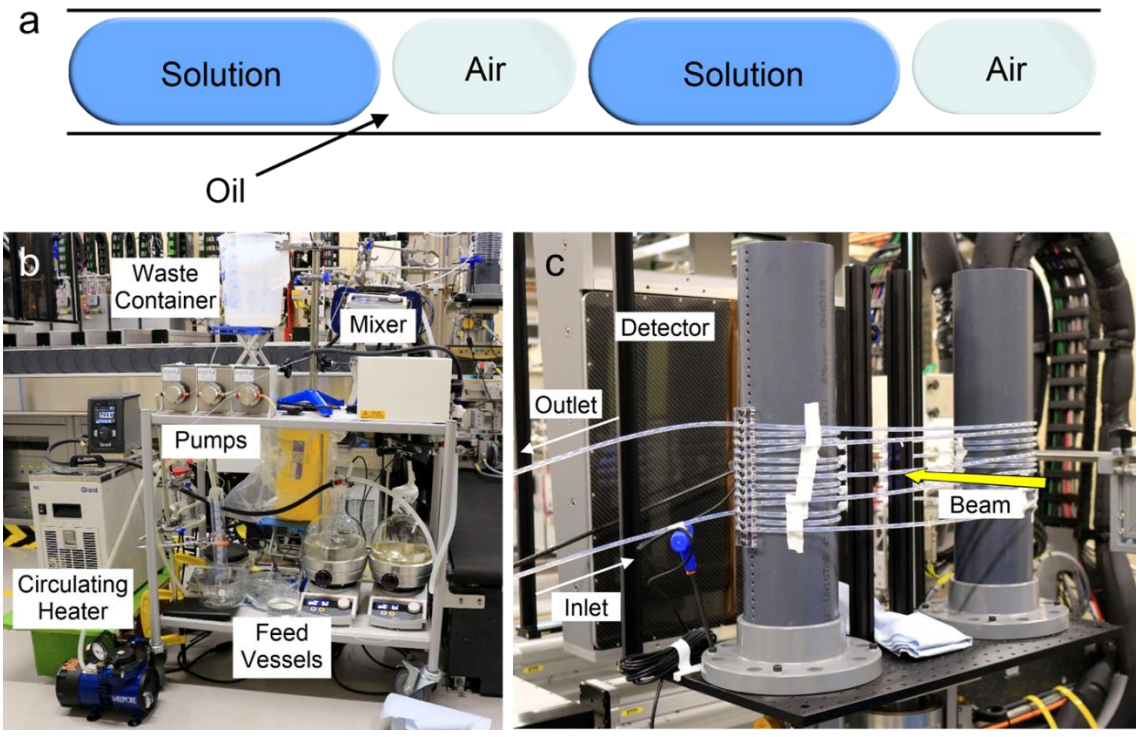

Figure 105: Experimental setup at Diamond beamline I11. (a) Schematic of tri-phasic methanol-air-oil flow. (b) Flow control section of the KRAIC-D. (c) Crystallization/Analysis section of the KRAIC-D.

The T-piece mixer was situated in a hot water bath kept at 55 °C, after which the flow was allowed to cool to room temperature. The coiling cylinders could be used for active or controlled cooling/heating, but this was not implemented here. Due to the distance between the mixer section and the analysis section of the KRAIC-D (~120 mm; Figure 105b and c), the flow was found to have already cooled to 27.3 °C before entering the first analysis window. Subsequently, crystals were first observed by eye just after the third analysis window (~4-5 min residence time), by which point the flow had cooled to room temperature (~23 °C).

X-ray analysis was performed at Diamond beamline I11, the same beamline used for the continuous flow microfluidic experiments (Section 2.4.1). The same detector and X-ray energy (15 keV) were employed for these millifluidic experiments, but some parameter changes were made to accommodate the different sizing of the KRAIC-D and account for the plug flow based on lessons learned from droplet microfluidic experiments (Section 2.2.4). A larger beam was utilized to irradiate a greater portion of each window (Table 7), where based on the length (~7 mm) and velocity of the solution plugs, it takes them approximately 280 ms to transit completely through an irradiated window section. X-ray scans were conducted with detector frame rates of 10 Hz for total exposure times of 10 seconds, where this enables ~2.8 XRD patterns to be collected per passing plug. However, operation of the I11 detector at this higher frame rate required pixel binning, resulting in a quarter of the spatial resolution compared to standard operating mode: 2880 x 2881 (Table 7). Different analysis windows were accessed by raising and lower the analysis module of the KRAIC-D on the hutch goniometer (Fig. 104b).

Table 7: New Beam and Detector Parameters at Diamond Beamline I11

Beam size (H x W mm^2)	Flux at sample (ph/s)	Aspect Ratio (H x W)	Sample-to-Detector Distance (mm)
1.0 x 1.0	~1.70 x 10^{13}	1440 x 1441	324

An additional consideration that must be made for XRD analysis in millifluidic devices as compared to microfluidic devices is the uncertainty in 2θ caused by the thickness of the flow channel (Fig. 106). A crystal that passes through an analysis window close to the tube wall will be at a different effective S-to-D distance than a crystal passing through the middle of the tube. Assuming these crystals are identical, it is then possible that reflections of the same scattering angle coming from both of these crystals can strike a different pixel on the X-ray detector. Similarly, a single pixel can be struck by reflections of varying scattering angle if they come from crystals at different positions in the channel (Fig. 106). Therefore, there is a small uncertainty in the 2θ

value of a particular pixel. This can be determined by calculating the difference between the angle of a reflection coming from the middle of the channel vs. the walls of the channel as a function of scattering angle, where the uncertainty increases from zero to a finite value from 0° to 45° then again approaches zero from 45° to 90°. The uncertainty for XRD patterns collected from the KRAIC-D based on the current tube size and S-to-D distance can be found in Figure 107. The maximum uncertainty at 45° is approximately ±0.14°, however, at 15 keV the range of interest for UBA peaks is within 5° to 20°, meaning the uncertainty of all relevant peak positions is less than ±0.1°.

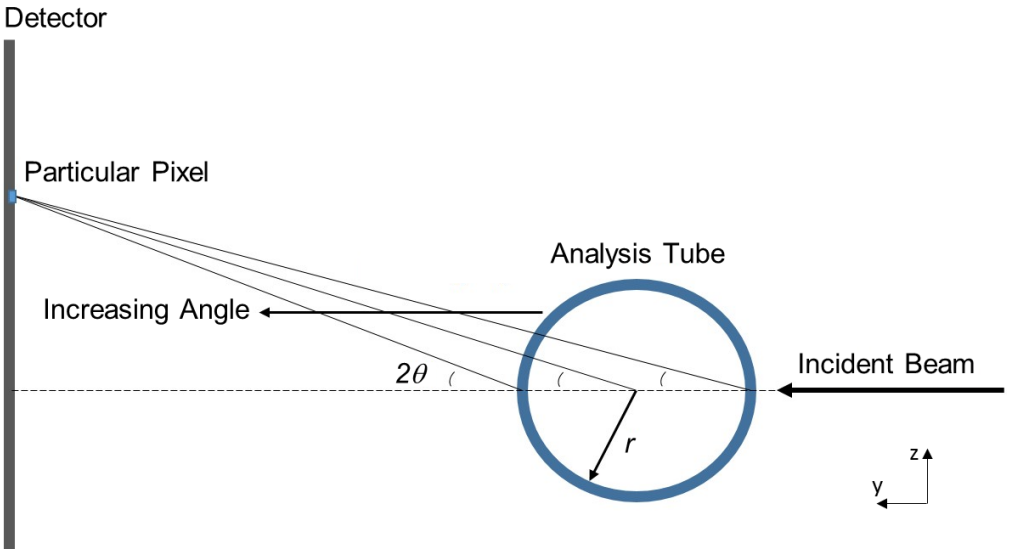

Figure 106: Diagram illustrating the uncertainty in the 2θ value of a particular pixel due to the radius, *r*, of the Kapton analysis tube. Flow is in the x-direction into the page.

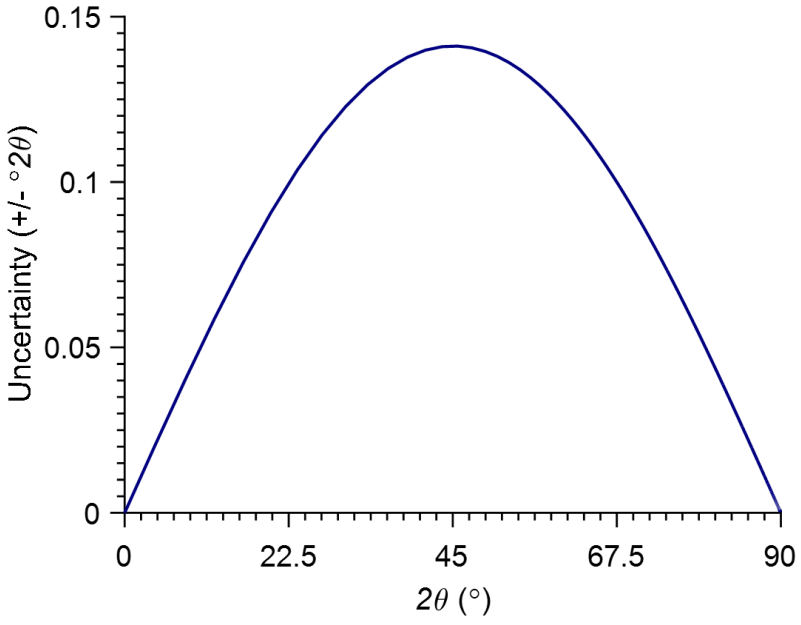

Figure 107: Uncertainty in angle as a function of 2θ with 324 mm S-to-D distance and 1.6 mm tube radius.

Powder XRD Results

The results from a representative UBA experimental run are presented here. Little diffraction was observed at the first or second window, so results are only presented for windows 3-5 since the slow z travel speed of the I11 goniometer made it difficult to repeatedly access more than three windows per experiment. Data were processed using the same MATLAB script as employed for DMC-XRD data using an α value of 2 (Equation 11) and a threshold of 20 a.u. (Section 2.3.2). Due to the triphasic nature of the flow and the large size of the beam – which allows multiple components to be irradiated at once – the scattering background was much more complex than the binary background of the water-in-oil microfluidics data. Additionally, the scattering difference between the methanol and Galden oil was not as clear as that between the water and FC-40 oil used in microfluidics experiments. For these reasons, oil frames were not excluded from KRAIC-D data. However, selecting a suitable background frame containing some methanol and oil scattering and applying the above processing parameters enabled sufficient background subtraction and the isolation of crystalline diffraction.

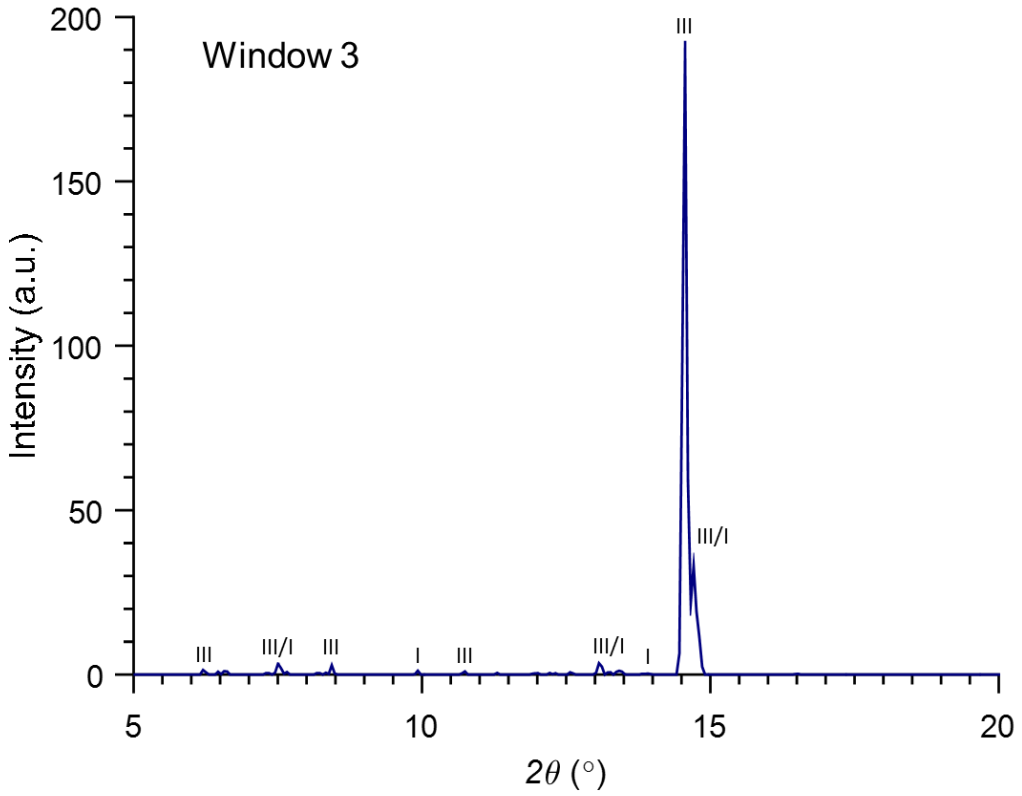

Figure 108: Combined XRD pattern from Window 3. Labelled peaks correspond to UBA Form I and Form III (CSD: EFOZAB and EFOZAB02). Peaks that could correspond to both are designated with a slash.

XRD patterns from Windows 3, 4, and 5 are presented in Figure 108 to Figure 110. Each pattern was produced by combining diffraction from four separate scans,

and thus represents 40 sec of flow exposure in total. Form III was the first polymorph observed at Window 3 (3.85 min residence time; Figure 108). A few small peaks which could belong to Form I were also observed, but since the highest intensity Form I peak was missing, it could be that these were just residual noise. A similar result was obtained at Window 4, where the main peak corresponded to Form III, and the highest intensity Form I peak was missing (5.41 min residence time; Figure 109). Subsequently, at Window 5 the presence of Form I in solution could be clearly seen, as evidenced by the emergence of its main Bragg reflection at ~15.5° (6.97 min residence time; Figure 110). These results suggest that Form III could be converting to Form I in solution, where this implies Form I may be the more stable phase.

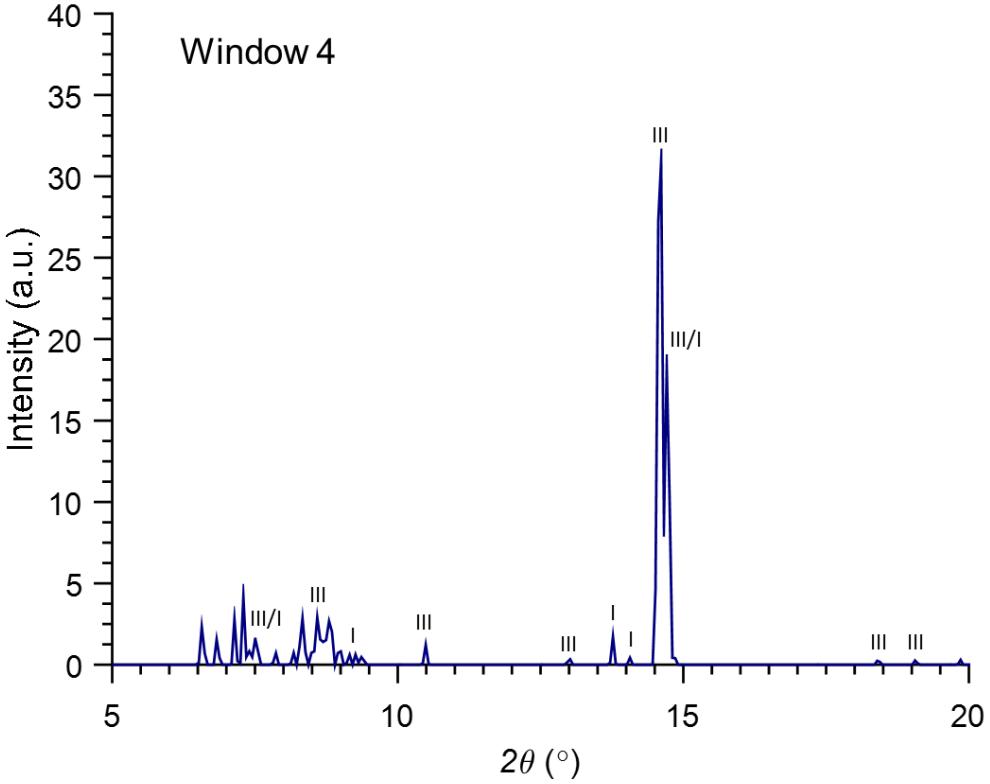

Figure 109: Combined XRD pattern from Window 4. Labelled peaks correspond to UBA Form I and Form III. Peaks that could correspond to both are designated with a slash.

Integration of the four diffraction patterns collected at each window reveals the increase in diffraction signal with time and also the statistical spread of the data (Fig. 111). While the median integrated intensity of Window 4 was actually slightly lower than that of Window 3, it is apparent that Window 3 data were skewed by an outlier scan. Through comparison with the crystallization of calcite (Chapters 2 and 3), there were far fewer UBA crystals per plug than calcite crystals per droplet in microfluidics experiments, therefore more frames must be collected to achieve similar scattering statistics, where it is expected that data will become more accurate as more scans are

incorporated per window. Nevertheless, this work confirms that serial powder diffraction analysis similar to DMC-XRD is possible at millifluidic length scales.

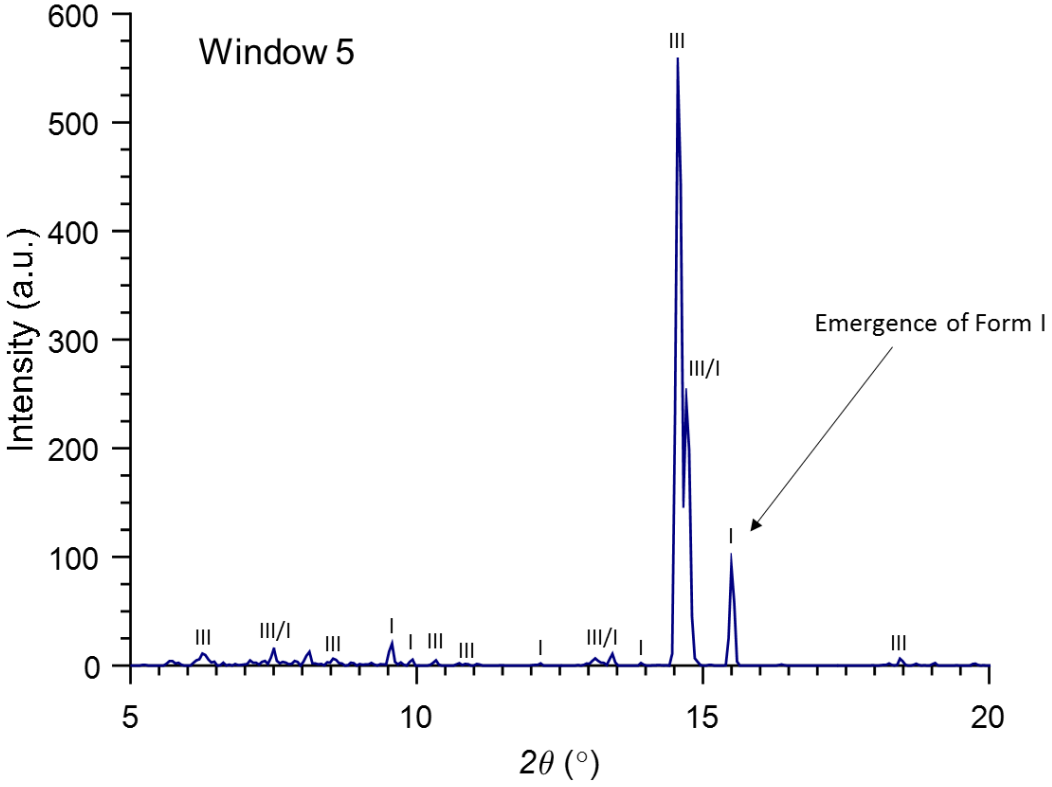

Figure 110: Combined XRD pattern from Window 5. Labelled peaks correspond to UBA Form I and Form III. Peaks that could correspond to both are designated with a slash.

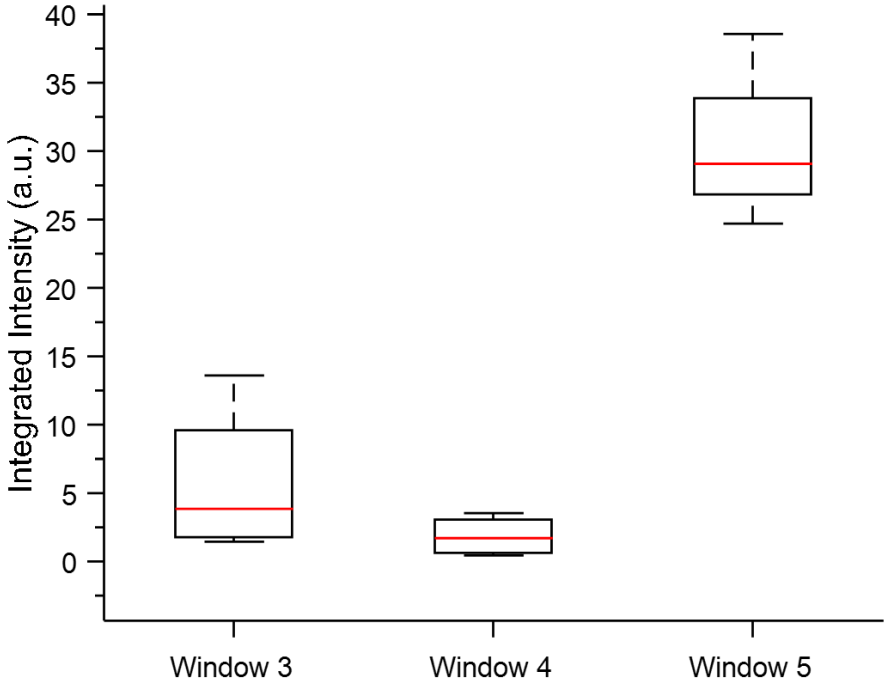

Figure 111: Box plots of the integrated intensity values of the four XRD patterns obtained at each window. The red lines represent the median values and the bottom and top of the box are the first and third quartiles, respectively. The upper and lower whiskers indicate the maximum and minimum values calculated, respectively.

4.2 The fReactor: A Continuous Stirred Tank Reactor (CSTR)

4.2.1 Background

All of the X-ray sample environments utilized thus far, especially in segmented flow mode, operate under a similar working principle; fluid elements mix as they travel downstream, there is no back flow, and there is only minimal mixing between elements along the direction of flow – as opposed to perpendicular to the flow direction. Chemical reactors that operate in this way are referred to as plug flow reactors.[315] However, there is great diversity in flow reactor designs used in chemical synthesis. Another important category of flow reactor is the mixed flow or continuous stirred tank reactor (CSTR).[315, 316] These types of reactors are similar to a conventional batch reactor, except that there is a continuous in- and out-flow (Fig. 112).

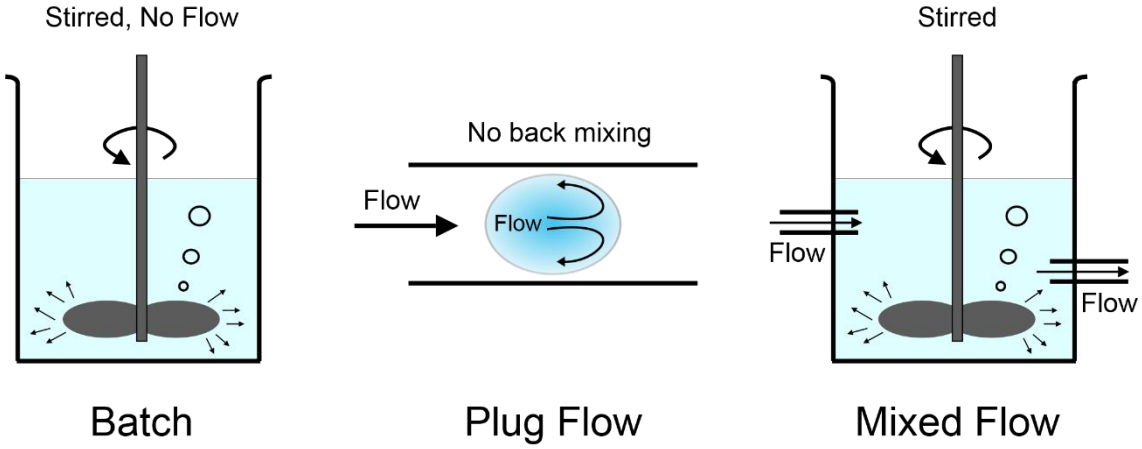

Figure 112: Comparison of some major types of chemical reactors. (a) Single-batch reactor with no in- or out-flow. (a) Plug flow reactor with no mixing parallel to the flow direction. (c) Hybrid mixed flow or continuous stirred tank reactor with in- and out-flows.

Inspired by developments in microfluidics over the past two decades, there has been recent interest in miniaturizing CSTRs and other types of flow reactors.[316-320] One of the pioneering groups in CSTR miniaturization is the Institute of Process Research & Development (iPRD) at the University of Leeds, who have developed a millifluidic-scale CSTR called the “fReactor” (free-to-access reactor; Figure 113a and b).[321] These fReactors are easily assembled into “cascades” of two or more individual reactor modules (Fig. 113c). Importantly, increasing the number of reactor modules (*N*) provides greater uniformity in the overall solution residence time distribution (RTD) than can be achieved by increasing the size of one reactor to match the total volume of *N* reactors.[321] As an added benefit, the size and scale of fReactors also makes them suitable for time-resolved analysis, where product samples or measurements can be taken at or between each reactor module. Consequently, a second collaboration was

undertaken with iPRD and a fellow PhD student, Carlos González Niño, to adapt a fReactor CSTR cascade for synchrotron X-ray analysis.

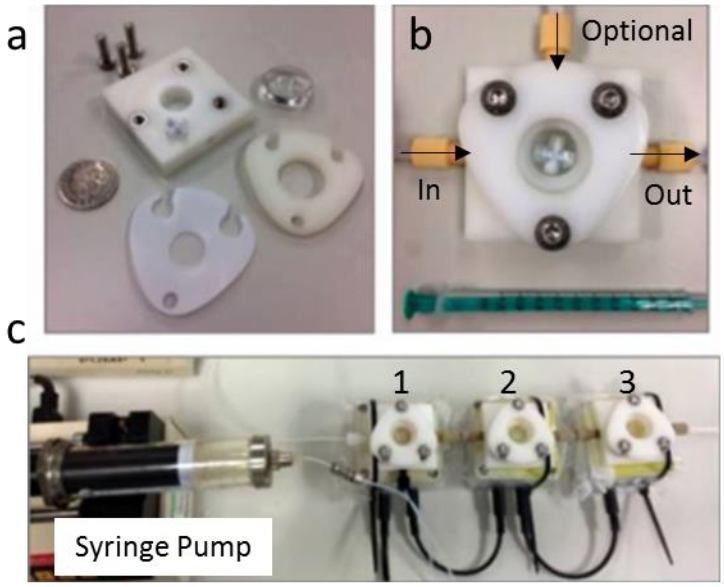

Figure 113: The "fReactor". (a) Components of an individual reactor module including the base, a gasket, optical window, bracket, magnetic stirrer bar, and three M5 bolts. (b) Assembled single fReactor module with labelled inlet, outlet, and optional extra port for probe, heater, additional inlet/outlet, etc. (c) Three-module fReactor cascade connected to syringe pumps. Adapted from ref.[321]

4.2.2 Device Characterization

Synchrotron experiments were conducted with a five-reactor cascade comprising 10 mL of total fluid volume (2 mL reactor volume x 5 reactors). Mixing within each reactor was facilitated by a cross-shaped magnetic stirrer bar rotating at 1000 rpm. Velocities near the stirrer can reach up to 0.6 m/s (Fig. 114a), which is more than two orders of magnitude faster than the average velocity of fluid entering and exiting each reactor due to the applied flow rate of 0.7 mL/min (~0.0015 m/s). While this ensures that there should be thorough mixing within every reactor, there is evidently a residence time distribution (RTD) due to fluid elements persisting in each reactor for differing amounts of time. It is important to quantify the RTD of the cascade since it dictates the amount of time reactants and material products remain within each reactor module, affecting the time-resolution of *in situ* experiments. The average fluid residence time (RT_{mean}) in a single reactor is given by the equation:

$$\mathbf{RT_{mean}} = \frac{\boldsymbol{V}}{\boldsymbol{Q_{total}}} = \frac{\mathbf{2}\ \mathrm{mL}}{\mathbf{0.7}\ \mathrm{mL\ min^{-1}}} \approx \mathbf{2.86\ min} \qquad \textbf{(12)}$$

where V is the volume of the reactor and Q_{total} is the total volumetric flow rate.[315] However, due to the circulatory flow, some fluid may enter and immediately exit a

reactor, other elements may reside within a reactor closer to RT_{mean}, and some may remain for even longer times.

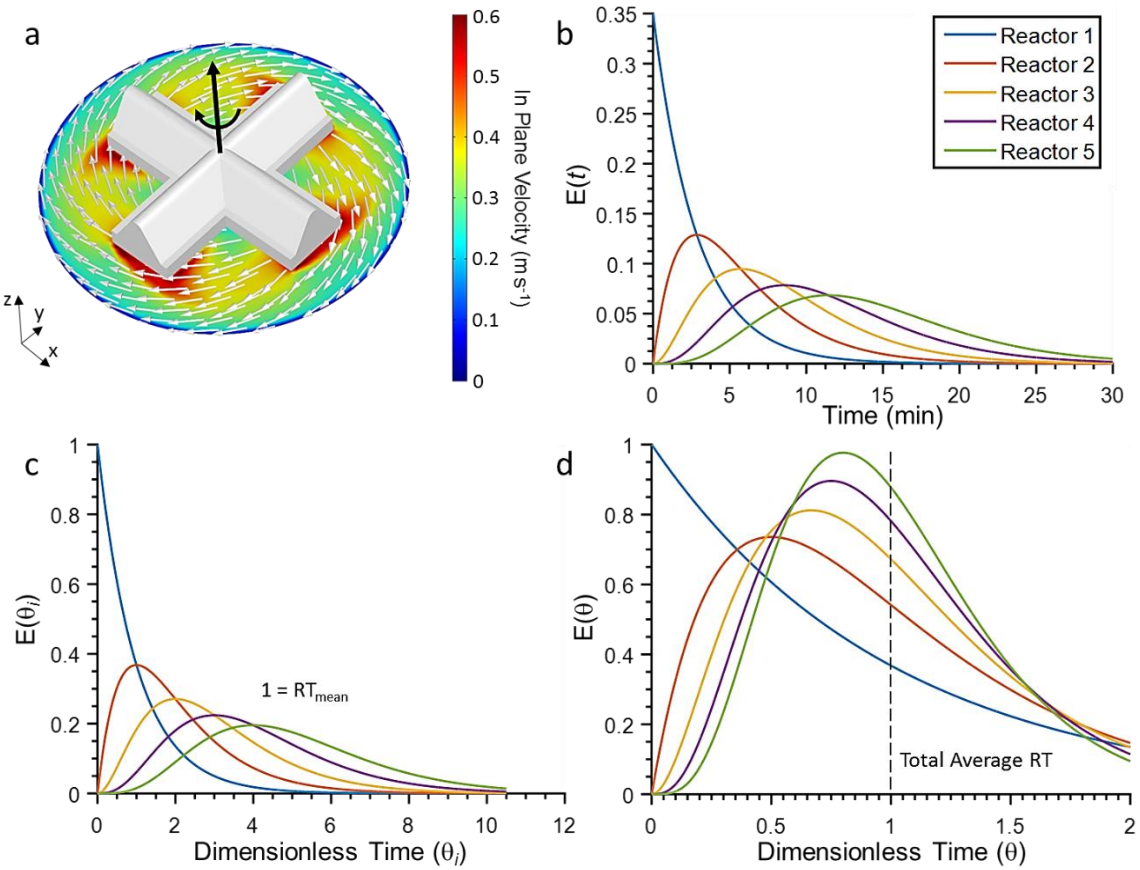

Figure 114: Characterization of five-fReactor cascade with total flow rate of 0.7 mL min^{-1} and stirrer speed of 1000 rpm. (a) CFD model of fluid mixing in a single fReactor module. Courtesy of Carlos González Niño. (b) Theoretical RTD function, E(*t*), of each reactor module with time. (c) Theoretical $E(\theta_i)$ function displaying the RTD normalized by RT_{mean}. (d) Theoretical $E(\theta)$ function displaying the RTD normalized by the total average RT of the entire cascade.

The theoretical framework for describing RTDs in mixed flow reactors was first developed in the 1930s,[322] and correlates well with experimentally measured distributions.[316] The theory imagines that a tracer species (e.g. a fluorescent dye) in a finite fluid volume is injected into a reactor at time (*t*) = 0. The tracer is diluted based on the RTD within each reactor, resulting in a change in the measured fluorescent intensity of fluid exiting the reactor with time. This distribution of material exiting a reactor is predicted by the equation:

$$\mathbf{E}(\boldsymbol{t}) = \frac{\boldsymbol{t}^{\boldsymbol{N-1}}}{(\boldsymbol{N-1})!(\mathbf{RT_{mean}})^{\boldsymbol{N}}}\boldsymbol{e}^{-\boldsymbol{t}/\mathbf{RT_{mean}}} \qquad \textbf{(13)}$$

where E(*t*) is the intensity response in inverse units of time.[315] The E(*t*) curves for the five reactors utilized here are shown in Figure 114b, where the area under each curve is equal to one (i.e. the total amount of tracer that entered the device). The RTD of each reactor compounds over the course of the cascade, resulting in a larger

distribution of material across each reactor. Here, most fluid is predicted to travel through the five reactors over 5 to 25 min of residence time, with an average residence time of 5 x 2.86 min (5 reactors x RT_{mean}).

Another helpful way of representing these RTDs is by normalizing them with respect to RT_{mean} (θ_i) and total RT_{mean} (θ). These allow easy visualization of the number of residence times it takes fluid elements to travel through each reactor (Fig. 114c) and the overall homogeneity in residence time across the entire cascade (Fig. 114d), respectively. Almost all fluid is predicted to pass through the cascade within 10 average residence times, however there is a great deal of overlap between modules, where it is possible for a small proportion of fluid to completely exit the device before other fluid elements leave the first module (Fig. 114b and c). Yet, the plot of $E(\theta)$ clearly demonstrates that as the number of reactors (*N*) is increased, the total RTD begins to converge on the average total residence time (Fig. 114d).

4.2.3 Iron Triazole (FeTrz): A Case Study

The Iron Triazole Coordination Polymer System

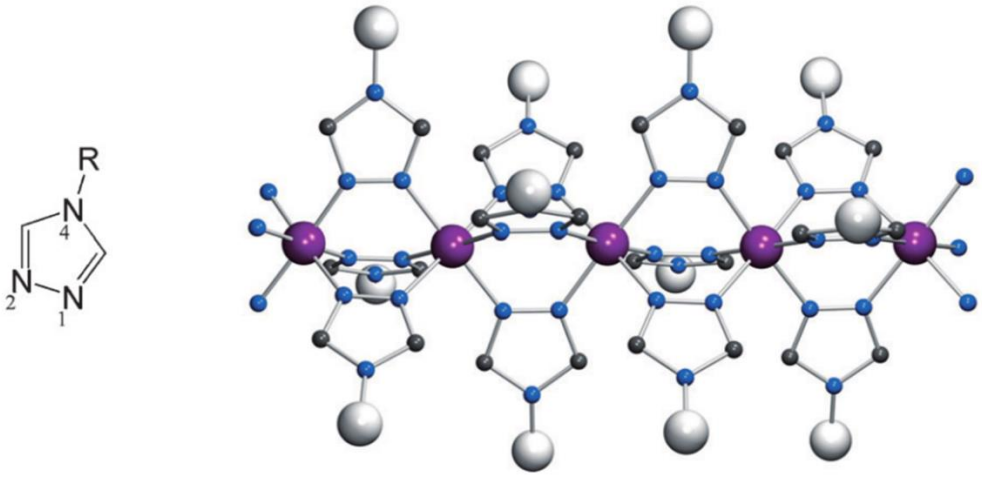

Figure 115: Molecular structure of $[Fe(trz)_3]R$ coordination polymers, where Fe is purple, N is blue, C is dark grey, and the anionic substituent (R) is white. Here, R corresponds to BF_4. Reproduced from ref.[323]

Synchrotron X-ray analysis of materials synthesis in a fReactor cascade was trialed using the production of iron(II) triazole-based (FeTrz) nanoparticles. The specific nanoparticles produced here, $Fe(Htrz)_2(trz)BF_4$, are coordination polymers consisting of chains of Fe(II) centers each bound to six 1,2,4-triazole ligands (Fig. 115). These nanoparticles have become a model system for near-room temperature spin-crossover (SCO) materials, which have potential for use in optical displays and magnetic storage.[323, 324] SCO materials can undergo a transition from a low-spin (LS) ground state to a high-spin (HS) excited state in response to stimuli such as light, temperature,

or pressure.[325] These different spin states have unique crystal structures, and thus can have differing optical and magnetic properties.[326] For $Fe(Htrz)_2(trz)BF_4$ – referred to as simply FeTrz in the remainder of the section – the LS state appears pink and the HS state appears white.[324] Interestingly, the white state has been shown to form first during synthesis, where it subsequently transforms *in situ*, turning the solution bright pink.[327] This provides an additional motivation for performing time-resolved analyses of FeTrz synthesis.

Experimental Setup at Diamond Beamline I22

The fReactor cascade was modified for X-ray analysis by exchanging the standard FEP tubing between reactors for Kapton tubing (Fig. 116). This is the same tubing as utilized for the analysis windows of the KRAIC-D (ID: 3.188 mm; wall thickness: 0.095 mm). After connections between modules were made, the entire cascade was placed on a five-position digital magnetic hotplate stirrer (RT 5, IKA) and mounted on the translational goniometer at Diamond beamline I22 using standard optomechanical components (Thorlabs; Figure 116). All beam parameters at beamline I22 were the same as those utilized for microfluidics experiments (Chapter 2.2, Table 1 and Table 2), with the exception of the S-to-D distance, which was approximately 218 mm.

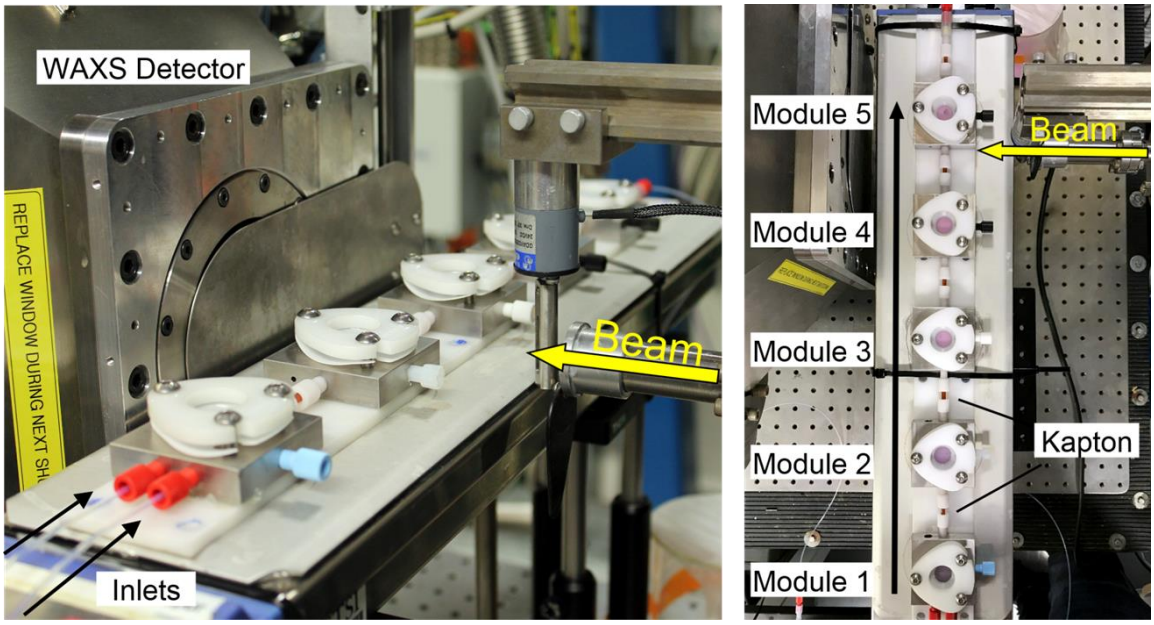

Figure 116: Photographs of fReactor setup at Diamond beamline I22. The top view (right) shows the Kapton analysis tubes after each reactor module. This image was taken during the synthesis of FeTrz, where the pink reaction product can be seen in each reactor window.

FeTrz synthesis was conducted through direct mixing of aqueous solutions of 50 mg/mL iron(II) tetrafluoroborate hexahydrate ($Fe(BF_4)_2{\cdot}6H_2O$) and 104 mg/mL 1,2,4-triazole ($C_2H_3N_3$) at room temperature in the first reactor module (final concentrations of 25 mg/mL and 52 mg/mL, respectively). The reagents were loaded into 60 mL plastic

syringes (BD Plastipak) and dosed into the fReactors with a twin syringe driver (Pump 33, Harvard Apparatus). The entire reactor cascade was prefilled with DI water before the injection of reagents to enable a slower and more uniform ramp up of the supersaturation across the five reactors. Analysis was facilitated at the Kapton sections after each module, providing five points which could be accessed by the beam. Due to the length of the fReactor cascade and the limited travel distance of the goniometer, only three analysis positions could be accessed per experiment. Therefore, the results presented below are the combination of two identical experiments, the first looking at the first three positions (Reactors 1-3), and the second looking at the last three positions (Reactors 3-5).

Powder XRD (WAXS) Results

Powder XRD patterns were initially collected using scans of 10 consecutive frames each of 1 sec duration (10 frames x 1 sec = 10 sec). However, utilizing 1 sec exposures at later experiment times and channel positions, i.e. once more material had formed, resulted in the overloading of the SAXS detector (N.B. SAXS and WAXS data were collected simultaneously, but SAXS data is not included here). For this reason, scan settings were changed to acquire 10 frames of 0.5 sec exposure, and once these parameters also caused overloading, to 15 frames of 0.3 sec exposure per scan. All frames from each scan were combined to form a single composite diffraction pattern, where skipping frames was not required since there was no second fluid phase. Before combination of frames, each frame was processed using the MATLAB script developed for DMC-XRD, with an α value of 1 ± 0.02 and a threshold between 20 and 40 a.u. (Equation 11, Section 2.3.2). The low contrast of broad diffraction rings arising from poorly crystalline nanoparticles also required additional Gaussian and median image filters to be implemented in MATLAB to process this data. After processing, composite patterns were exported to Diamond's free DAWN Scientific software[328] for integration, since detector tilt corrections not accounted for in MATLAB integration needed to be applied. The intensity of all data shown here was normalized to the 10 sec total exposure time provided by the original scan settings to enable fair comparison of integrated intensities at different analysis positions and experiment times.

XRD data were first collected after approximately 1.5-2 total residence times (~25-30 min) to allow the fReactors time to equilibrate. The integrated intensities of diffraction patterns collected from the same positions over ~30 min of operation show that diffraction intensity increases slightly with time, especially at Reactors 4 and 5 (Fig. 117). However, the overall intensity values remain very stable, especially at Reactors 1 and 3, indicating near steady-state operation across these experiment times. These data also demonstrate the expected trend of increasing diffraction intensity with

subsequent reactors. The small amount of crossover observed between Reactors 1 and 2, and between Reactors 3 and 4 are likely due to batch to batch variation or uncertainty in time between the two experimental runs. Crossover could also be caused by differences in residual background scattering between scans contributing to the calculated integrated intensity values.

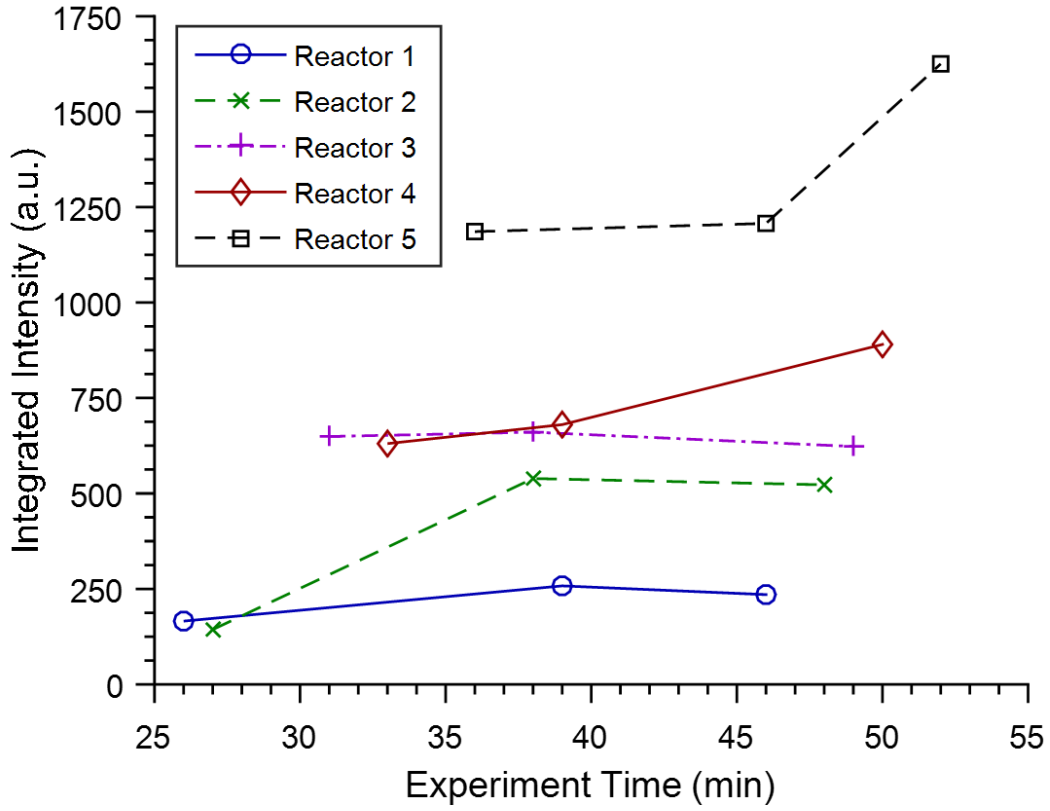

Figure 117: Integrated intensities of diffraction patterns obtained from each reactor with time, where time = 0 is when reagents are first injected into Reactor 1.

The final diffraction patterns collected at each position are presented in Figure 118. These correspond to the last integrated intensities values given for each reactor in Figure 117. Patterns corresponding to the pink LS phase could be observed from Reactor 1, where clear growth in diffraction signal was seen over the length of the cascade. All reflections observed throughout the fReactor cascade matched the LS state (labelled peaks, Figure 118). The HS phase was not detected, even within the first reactor, where it would be expected to appear. This could be due to its low abundance, which put it below the limit of detection, or simply due to the fact that all of the initial HS particles had converted to LS ones by the time diffraction patterns were collected (after ~25 min). The latter explanation is likely, since the RTD essentially seeds Reactor 1 with the LS phase, so that fresh reagents entering the reactor result in the growth of these particles rather than the primary nucleation of the HS phase.

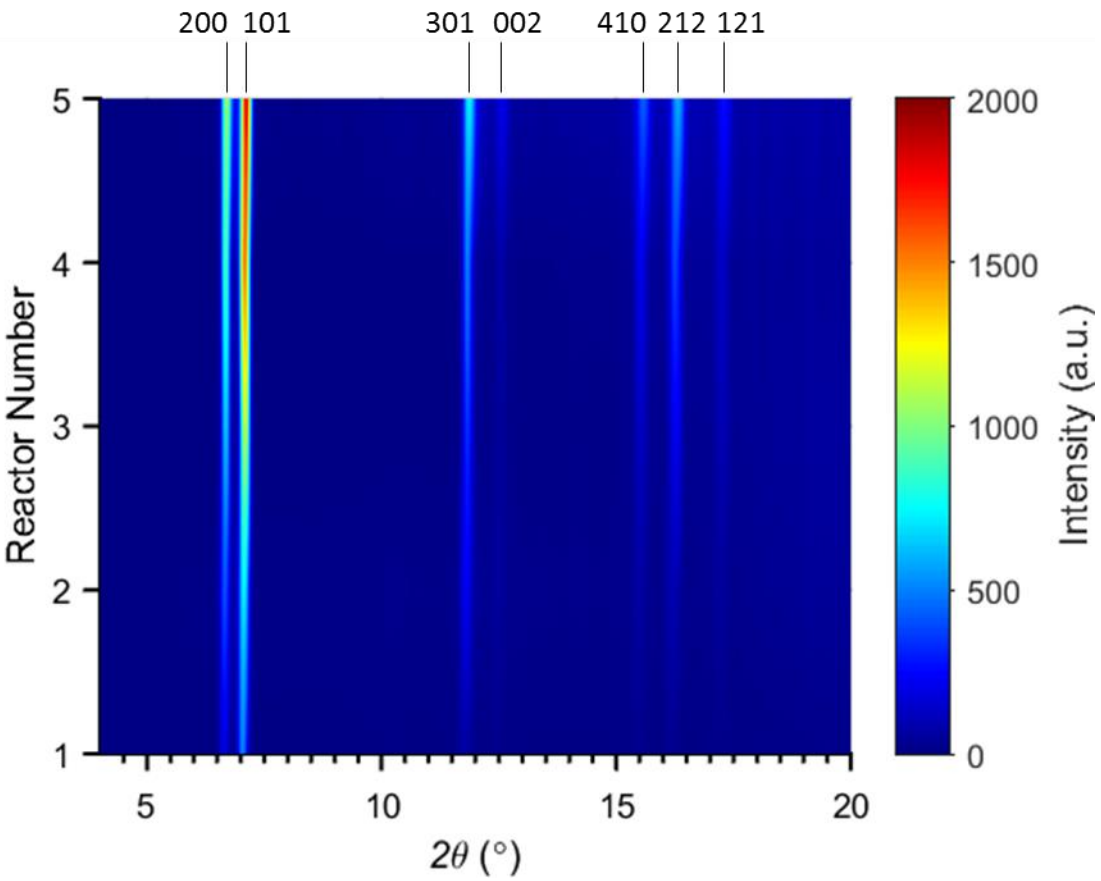

Figure 118: Spatially-resolved PXRD patterns collected from the fReactor cascade. All seven major FeTrz LS state reflections can be observed, and these are labelled with the corresponding lattice plane (CSD: FIBCEA01).

Identical experiments were also conducted at Leeds, so that solid products collected from the fReactors could be analyzed *ex situ*. Samples were collected from the fReactor outlet at various experiment times, vacuum filtered with water and ethanol, and allowed to dry in an oven at 60 °C for 1 day. SEM analysis of samples collected at 33 min and 51 min (in the same time range as the PXRD data) revealed very consistent particle morphology and sizing (Fig. 119). The large nanoparticles appeared tablet-shaped, being about twice as long as they were wide. Particles collected at 33 min had an average length of 579.0 nm with a standard deviation of 128.6 nm and particles collected at 51 min had an average length of 578.7 nm with a standard deviation of 129.0 nm. When particle length data collected from each sample was plotted as a Gaussian distribution, the curves were strikingly similar (Fig. 119b and d, black curves). These are in agreement with the integrated intensity data (Fig. 117), which also supports the assertion that fReactor operation was near steady-state over this time interval. However, while the size distributions were almost identical, the median size of the sample at 55 min was 585 nm – versus 550 nm at 31 min (Fig. 119b

and d) – where this could explain why diffraction intensity in Reactor 5 moderately increased with time.

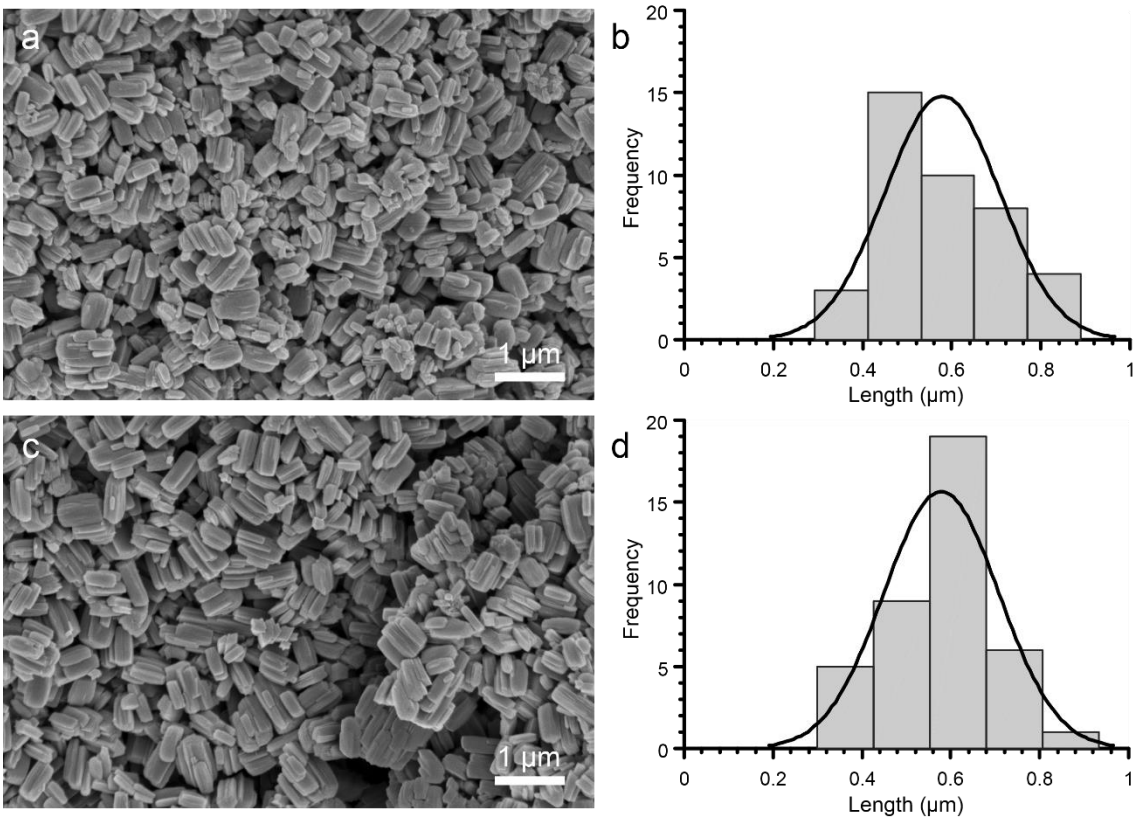

Figure 119: SEM analysis of FeTrz product collected from the five-reactor cascade at (a and b) 33 min and (c and d) 51 min experiment time. (b and d) Size histograms were made by measuring the length of 40 particles per image using ImageJ software. The black curves represent a normal distribution of the histogram data.

4.3 Discussion

These series of experiments with the KRAIC-D and an X-ray-enabled fReactor cascade illustrate the enormous potential of both microfluidic and millifluidic sample environments for X-ray analysis of crystallization and material synthesis. The successful utilization of the KRAIC-D for time-resolved serial powder diffraction demonstrates that DMC-XRD-type analysis can be conducted at an order of magnitude larger length scale. Further, the identification of UBA forms I and III in solution and the possible transition between the two provides an exemplary case for why *in situ* XRD analysis should be coupled to flow reactors. Likewise, experiments with the fReactor cascade show that it is possible to couple X-ray analysis to very different types of flow systems.

In many ways, the fReactor setup is less demanding of beamline hardware than either DMC-XRD or the KRAIC-D, since exposure times do not have to be selected to isolate data from fast moving droplets. It is also potentially less demanding of processing software, since frame sorting/selection is not required and diffraction

patterns should be of higher contrast due to the ability to introduce much more target material into the beam path. While extra image processing functions (i.e. filters) were required to increase the contrast of the relatively broad and low intensity FeTrz nanoparticle reflections against the strong solvent background scattering, more than satisfactory diffraction patterns could still be obtained. Conversely, analysis of FeTrz synthesis was actually first attempted in the KRAIC-D, but no diffraction peaks could be resolved. The need for short exposure times coupled with the dynamic oil/water background of segmented flow made it impossible to extract any crystalline diffraction from the plugs using Diamond beamline I11 instrumentation and current processing capabilities. This suggests that for challenging systems that scatter weakly (e.g. ultra-low concentration, nanocrystallites), single phase sample environments, such as CSTRs, may be preferred for *in situ* X-ray analysis.

As more options for flow sample environments become available, it will become necessary to select the best type of reactor for the project requirements. For instance, the large RTD of the fReactor cascade prevented isolation of HS and LS phases, making it difficult to obtain diffraction from the HS state. In order to capture this phase in the future, it may be possible to modify flow rates or solution conditions in the fReactor, or it could require a completely different flow system. Such aspects must be considered based on the goal of a particular study. If the primary aim of an experiment is monitoring a process, e.g. for quality control or optimization in industry, then perhaps such considerations are not important. In this case, the process should be studied as it is, and not manipulated for sake of the technique. However, if the primary aim of an experiment is to critically analyze a crystallization/synthesis pathway or study a particular step of a reaction, e.g. a transient or poorly scattering phase, then the process and the sample environment must be tuned to enable this. Here, two different techniques (four if including the continuous and segmented flow microfluidic experiments) have already been utilized to study three very different materials: calcite (a low solubility inorganic material), UBA (an organic co-crystal), and FeTrz (a nanoparticulate coordination polymer). Therefore, this work goes some ways towards providing a range of options for analyzing different assembly and crystallization processes with *in situ* X-ray scattering techniques.

Chapter 5:
Laboratory-Based Flow Diffraction and Scattering

Where the previous chapter investigated using different types of flow systems at the synchrotron, this chapter explores coupling flow systems to laboratory X-ray diffractometers. As mentioned in Chapter 2, it is difficult to gain access to synchrotron facilities since they employ a competitive proposal-based access model and are often oversubscribed. Even scientists who are fortunate enough to secure beamtime in this way typically do not have very much time (e.g. a week per year) and also find themselves in an unfamiliar laboratory, which may not have all of the necessary consumables or secondary equipment they need for an experiment. This latter obstacle requires a great deal of extra planning and logistics on the part of a researcher, where items must be shipped between the university and synchrotron and experimental apparatus must be set-up and taken down for each beamtime. Thus, limited time and resources make it extremely difficult to perform *in situ* experiments with complex sample environments away from the "home" laboratory. For instance, it took seven official beamtimes, not to mention extra commissioning beamtime, pre-beamtime visits, and set-up/set-down days, to obtain all of the data presented in Chapters 2-4 – more than one month of time at synchrotron radiation facilities in total! Therefore, it is evident why it would be beneficial to be able to perform these experiments in the home laboratory with effectively unlimited time and no set-up or shipping required.

5.1 State-of-the-Art Laboratory X-ray Systems

New generations of X-ray diffractometers with brighter X-ray sources and more sensitive detectors are bringing this goal within reach. Although not nearly as powerful as third-generation synchrotrons like Diamond and the ESRF, commercial diffractometers with modern sealed-tube or rotating anode microfocus X-ray sources perform just as well as second-generation synchrotrons (e.g. Synchrotron Radiation Source Daresbury).[329] Two such diffractometers were utilized here in order to investigate the suitability of state-of-the-art commercial systems for flow-based X-ray analysis in the home laboratory. A brief description as well as some important characteristics of each are given below.

5.1.1 The Xeuss 2.0 by Xenocs

The first laboratory diffractometer investigated was the Xenocs Xeuss 2.0 SAXS/WAXS "Laboratory Beamline" housed at the Soft Matter AnalyticaL Laboratory (SMALL) of the University of Sheffield. As its name suggests, this system

can perform both SAXS and WAXS analysis simultaneously using its two detectors. The primary SAXS detector is a laboratory variant of the hybrid photon counting Pilatus detectors (Dectris) utilized at many synchrotron beamlines including, Diamond I22. The smaller WAXS detector, located close to the sample and just below the beam path, is another hybrid photon counting detector custom-made by Dectris for Xenocs (Fig. 120). More information on both detectors can be found in Table 8, later in the section.

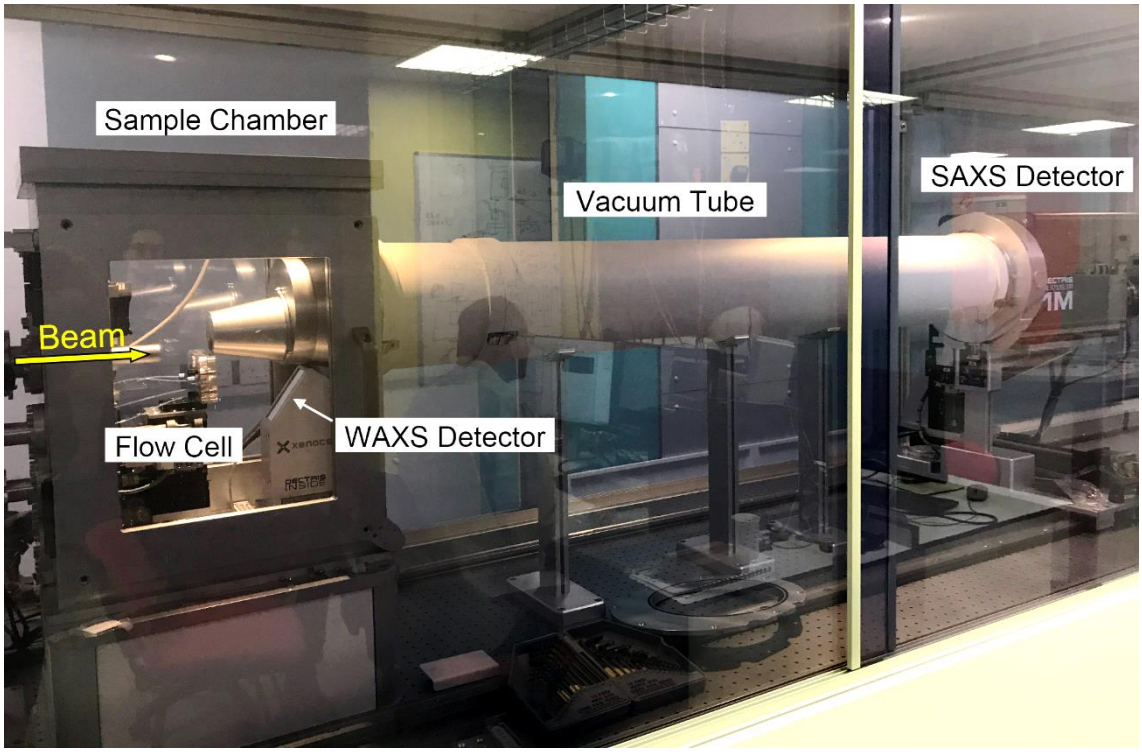

Figure 120: Photograph of the radiation enclosure of the Xeuss SAXS/WAXS system. The insert-based microfluidic device can be seen mounted on the translational goniometer in the sample chamber before being raised into the beam path.

In common with a beamline, the Xeuss system is housed in a large radiation shielded enclosure, which provides ample room for sample environments and movement of the SAXS detector. The vacuum tube between the sample and the SAXS detector minimizes air scattering and lowers the background noise of collected SAXS data. This tube can be removed to use the SAXS detector for WAXS or elongated to access even smaller angles. A second chamber within the main enclosure houses the standard WAXS detector and the translational sample stage. Microfluidics experiments conducted with the Xeuss demonstrated that the insert-based device (Chapter 2) could be mounted on this stage in the same way as at the synchrotron (Fig. 120).

Finally, the Xeuss 2.0 comprises an Excillium MetalJet D2+ X-ray source (Table 9). Rather than focusing an electron beam on a solid anode material to generate X-rays like most conventional X-ray sources, the MetalJet makes use of a continuously circulating jet of liquid gallium (Ga) metal as an anode.[330] This enables the use of high

current and power densities without the fear of damaging a solid anode and provides what many consider to be the highest possible flux with a lab X-ray source.[329]

5.1.2 The XtaLAB Synergy-R by Rigaku Oxford Diffraction

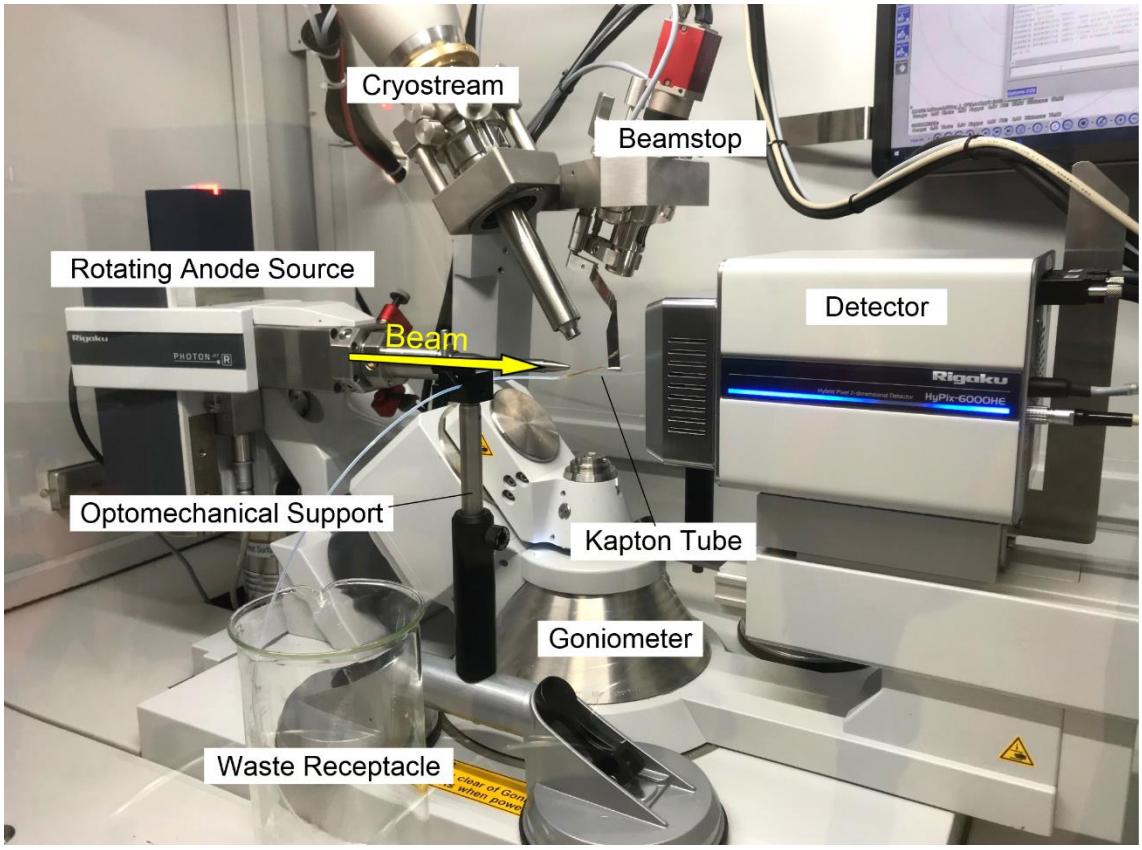

Figure 121: Photograph of the main enclosure of the XtaLAB Synergy-R diffractometer. Pictured is the experimental setup implemented for millifluidic experiments, where a Kapton tube connected to inlet and outlet tubing was mounted between optomechanical posts.

Flow trials were also conducted with an XtaLAB Synergy-R diffractometer after being invited by Rigaku Oxford Diffraction to perform some experiments at their application center in Wrocław, Poland. The Synergy-R has a more traditional layout for a lab diffractometer, where an X-ray source, goniometer, and detector all fit within a table-sized radiation enclosure (Fig. 121). The setup was originally designed for single crystal diffraction experiments, and thus has a 4-circle “Kappa”-type goniometer for orienting single crystals and not a translational XYZ stage like most synchrotron beamlines. The presence of the large Kappa goniometer and the smaller space available make mounting flow systems more challenging than with the Xeuss, although removal of the Kappa goniometer or fitting it with an add-on for XYZ capability (e.g. the XtalCheck-S) is possible. Additionally, the cryostream, which helps mitigate radiation damage in protein crystals (pictured, Figure 121), is not necessary for flow experiments and can be removed to free up more space.

The Synergy-R has its own hybrid photon counting detector designed in-house by Rigaku (Table 8). The HyPix-6000HE detector has a small pixel size and high maximum frame rate when compared to many other lab diffractometers, which provides good angular and temporal resolution. The Synergy-R also comprises a powerful rotating anode X-ray source (PhotonJet-R) and microfocus optics which give it a higher flux density than the Xeuss in situations requiring a small beam size size (discussed in more detail in Section 5.4). However, the goal of these experiments was not to compare the two diffractometers, but rather to explore the type and quality of data that could be obtained from both microfluidic and millifluidic segmented-flow systems. The following two sections present preliminary flow data collected from both diffractometers, possibly the *first of its kind* to be obtained from a laboratory source. Microfluidics experiments were conducted with the Xeuss 2.0, and millifluidics experiments were conducted with the Synergy-R.

Table 8: Laboratory Detector Characteristics

Diffractometer	Detector	Pixel Size (µm)	Aspect Ratio (H x W)	Max Frame Rate (Hz)	Sample-to-Detector Distance (mm)
Xeuss 2.0	SAXS: Pilatus3 R 1M	172	981 x 1043	5	1400
	WAXS: SWAXS module	172	487 x 195	20	160
Synergy-R	HyPix-6000HE	100	775 x 800	100	45

5.2 Microfluidics Experiments

5.2.1 Experimental Setup

The insert-based microfluidic device (Section 2.1.1) was mounted on the translational goniometer of the Xeuss 2.0 SAXS/WAXS system using the same optical rail carriage as in previous synchrotron experiments (Fig. 120). Three different flow experiments were conducted using this setup. The first was a simple water-in-FC-40 oil flow, to determine if droplets could be distinguished from the continuous phase (10:4 µL/min oil:water flow rate ratio). The second experiment was an imitation of the nucleant experiments of Chapter 3, which utilized a flow of aqueous droplets containing a final concentration of 50 mM Ca^{2+}/CO_3^{2-} and 0.0017 wt% porous bioactive glass (20:2:8:2 µL/min oil:$CaCl_2$:water:Na_2CO_3flow rate ratio). The final experiment was designed to test the SAXS capability of the laboratory setup, and utilized aqueous droplets of a well-characterized suspension of 10 wt% spherical silica nanoparticles (NPs; Bindzil colloidal silica CC401, AkzoNobel) in FC-40 oil (10:4 µL/min

oil:suspension flow rate ratio).[331] As before, fluid flow in each experiment was motivated with Cetoni neMESYS low-pressure dosing modules, where syringes containing the solutions were connected to the device using standard high performance liquid chromatography (HPLC) fittings. Simultaneous SAXS/WAXS data were obtained from the device with exposure times of 0.5 or 1 sec for 10 to 20 frames with 1 sec delay between each frame.

5.2.2 Wide Angle X-ray Scattering (WAXS)

In the first experiment, all frames collected from the WAXS and SAXS detectors appeared almost identical and contained very low counts (most pixel values between 0 and 2 a.u.). Thus, it was impossible to distinguish between water and FC-40 oil even with exposure times of 1 sec (Fig. 122). Since the droplets flow by the beam at approximately 1 Hz at the total flow rate utilized, this represents the maximum exposure length at which droplets can still be isolated from the oil phase. However, oil and water scattering are diffuse, so it could still be possible to detect higher contrast crystalline diffraction. This proved to be the case in the second experiment with 50 mM $CaCO_3$ and porous bioactive glass, where a few low contrast reflections possibly corresponding to calcite could be observed in some frames (Fig. 123). Unfortunately, these reflections were of such low contrast with respect to the background that any attempts to process (even with filters) or combine frames into a composite pattern using the standard MATLAB processing routine were unsuccessful. For these reasons, flow-based WAXS analysis with the Xeuss 2.0 using the current iteration of the insert-based device and processing software does not appear to be feasible.

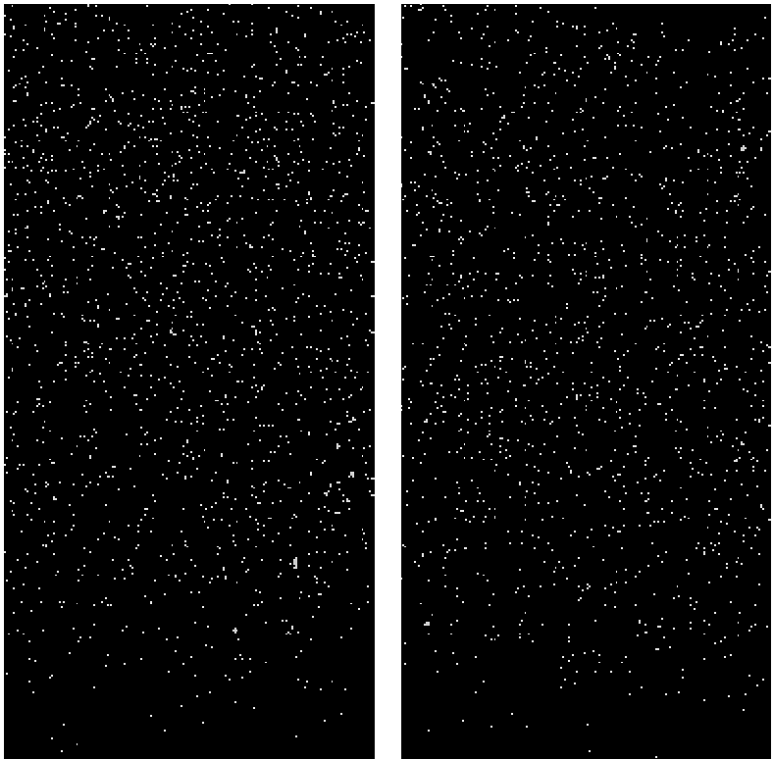

Figure 122: Two representative 1 sec WAXS frames of a water-in-oil droplet flow. It is unclear which frames correspond to water and which correspond to oil since the flux is so low.

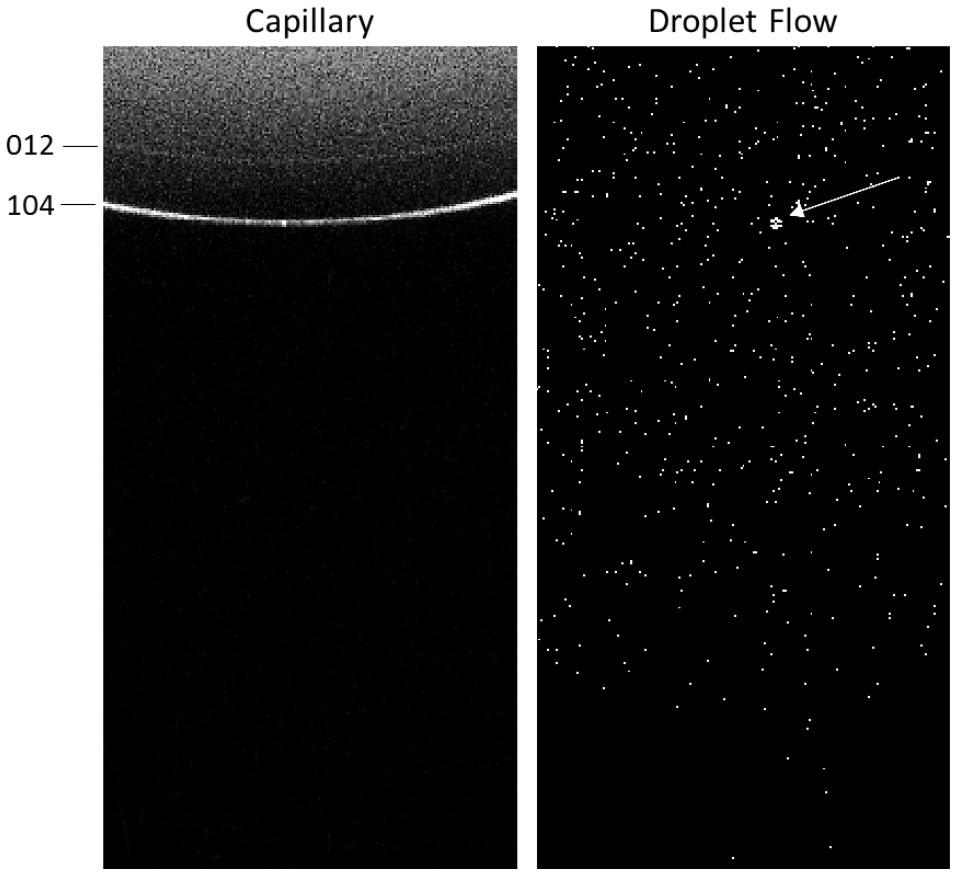

Figure 123: WAXS frames of (left) ACC and calcite in a glass capillary from a 300 sec exposure and (right) a droplet of 50 mM $CaCO_3$ and porous bioactive glass from a 0.5 sec exposure, where a single (104) calcite reflection is visible (white arrow).

5.2.3 Small Angle X-ray Scattering (SAXS)

Microfluidic SAXS analysis with the Xeuss was more promising. When droplets were filled with a homogeneous suspension of silica NPs, a clear difference between dispersed and continuous phase scattering could be observed. Frames corresponding to the continuous phase displayed almost no counts (Fig. 124a), whereas frames corresponding to the droplets contained noticeable scattering from the silica (Fig. 124b). When 40 frames totaling 30 seconds of exposure time were combined, they produced the high contrast image displayed in Figure 125a. Further, this image was of sufficient quality to be integrated and obtain the SAXS pattern shown in Figure 125b.

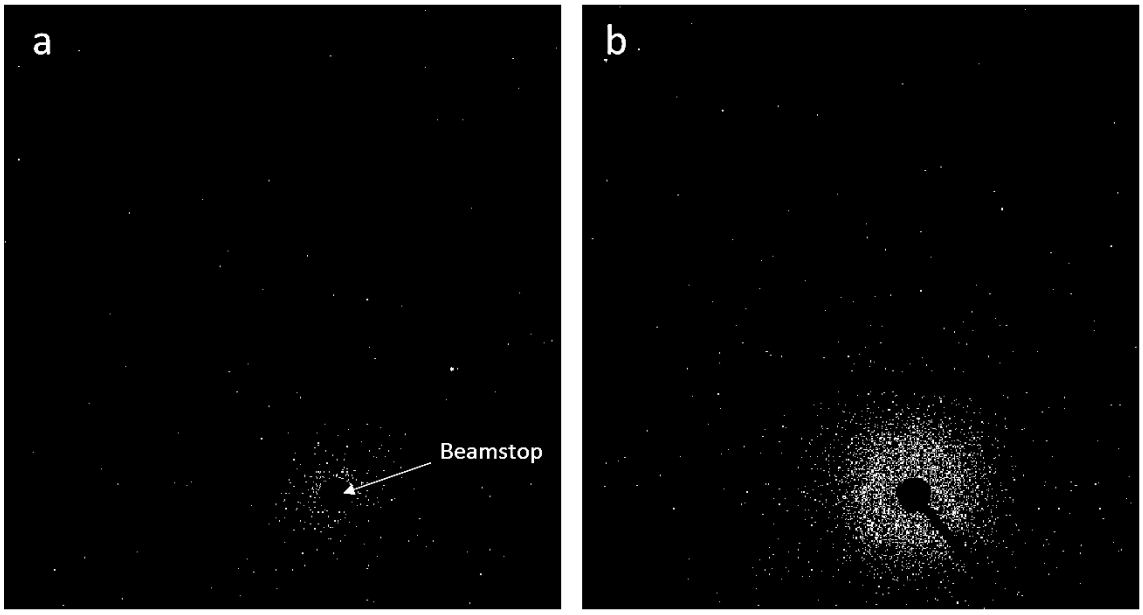

Figure 124: Single SAXS frames of 0.5 sec exposure coming from mainly (a) FC-40 oil and (a) droplets of 10 wt% silica nanoparticles.

To confirm the accuracy of this SAXS pattern, the data were fitted in DAWN Scientific using the Guinier approximation in order to estimate the size of the NPs.[182] A plot of the Guinier region of the data (~0.3-0.5 *q*) is displayed in Figure 126. The slope (*m*) of a linear fit to this so-called "Guinier Plot" (ln(Intensity) vs. q^2) can be used to obtain the radius of gyration (R_g) of a sample population using the equation:

$$\boldsymbol{R_g = \sqrt{-3m}} \qquad \textbf{(14)}$$

where the R_g of a sphere is equal to the square root of 3/5 its radius.[183, 332, 333] From this fitting procedure, the R_g of the silica NPs was determined to be 6.65 nm, corresponding to a physical radius of ~8.6 nm. This is in excellent agreement (>93%) with an earlier synchrotron SAXS study of the same sample at beamline ID02 of the ESRF, which reported the average particle radius to be ~9.2 nm.[331]

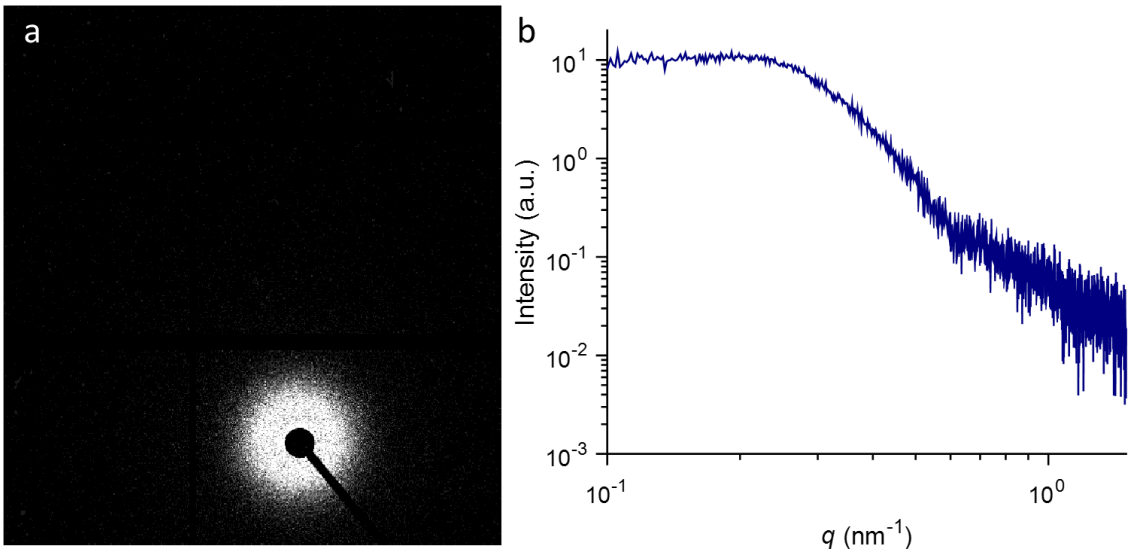

Figure 125: Composite (a) 2D and (b) 1D SAXS patterns obtained from 30 sec of total exposure of a flow of droplets containing 10 wt% silica nanoparticles.

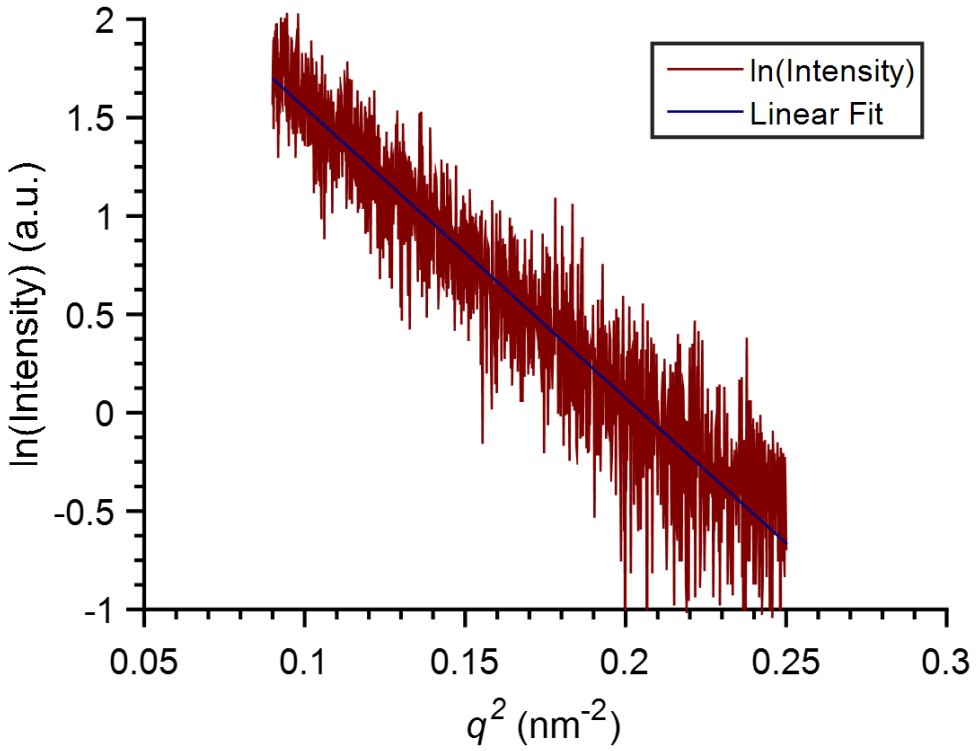

Figure 126: Guinier Plot of the SAXS pattern data from 0.3 to 0.5 q used to determine R_g.

5.3 Millifluidics Experiments

5.2.1 Experimental Setup

Due to space constraints, a simple millifluidic setup was used with the Rigaku Synergy-R diffractometer. A single Kapton tube (ID: 1.0 mm; wall thickness: 50 µm; Cole Parmer) was used as the flow channel with the Kapton allowing transmission of the X-rays. This tube was connected to FEP tubing (ID: 0.8 mm; OD: 1.6 mm; Cole Parmer) at both ends using flexible silicone rubber tubing (ID: 0.9 mm) as an adaptor that provided an interference fit with the ODs of both the FEP and Kapton tubing. The FEP tubing on both sides of the Kapton window was supported by optical post-mounted V-clamps (Thorlabs) bolted to double suction cup grippers for stability (Fig. 121). Inlet FEP tubing was fed through a port in the back of the Synergy-R radiation enclosure, and the outlet FEP tubing was directed into a waste glass beaker inside of the enclosure (Fig. 121).

Flow experiments were conducted with a water-in-oil (Galden SV110) plug flow containing either calcium carbonate powder (calcite, 98% <50 µm size, Sigma Aldrich) or paracetamol (PCM) Form I or II powder supplied by collaborators at the University of Bath. The Galden oil was pumped using neMESYS syringe pumps and the crystal suspensions were pumped from a stirred beaker using a variable speed peristaltic pump (V-3, VapourTec). These two fluids were combined at a Y-mixer piece to create the segmented flow. The exact weight percentages of the crystal powders in the aqueous plugs are uncertain due to the variable uptake and dosing of the slurries by the V-3 pumps and also due to the aggregation and settling of the powders in the Y-mixer. Based on subsequent quantification of the dosing of PCM Form I by the V-3 pump, it is likely that the actual concentration of plugs exposed to the X-ray beam was on the order of 0.5-1 wt%.

The high flux density and fast detector of the Synergy-R enabled the use of comparable scan settings to those used for microfluidics synchrotron experiments. Successive frame-by-frame exposures of 0.025-0.05 sec for between 45 and 90 sec were employed to capture the motion of the droplets through the Kapton tube and isolate diffraction from the crystals. The collected data were then sorted and processed using the same MATLAB code described in Section 2.3.2. Similar to synchrotron microfluidic experiments, it was possible to distinguish between oil and water frames by their characteristic scattering profiles (Fig. 127). However, while the images look very different by eye, individual pixel values inside and outside of the oil scattering band are within a similar range (~1-5 a.u.). For this reason, rather than using single test pixels to determine the presence of water or oil, a larger 37 x 45 pixel region of interest (ROI)

over the oil scattering band was utilized. This enabled more consistent identification of the two phases, where frames with an ROI pixel sum over 3000 a.u. were designated as oil and discarded. After sorting, selected frames were background subtracted with an α value of 1 (Equation 11, Section 2.3.2), passed through a median filter, thresholded with a value of 4 a.u., and finally combined into composite 2D diffraction patterns to be integrated and indexed.

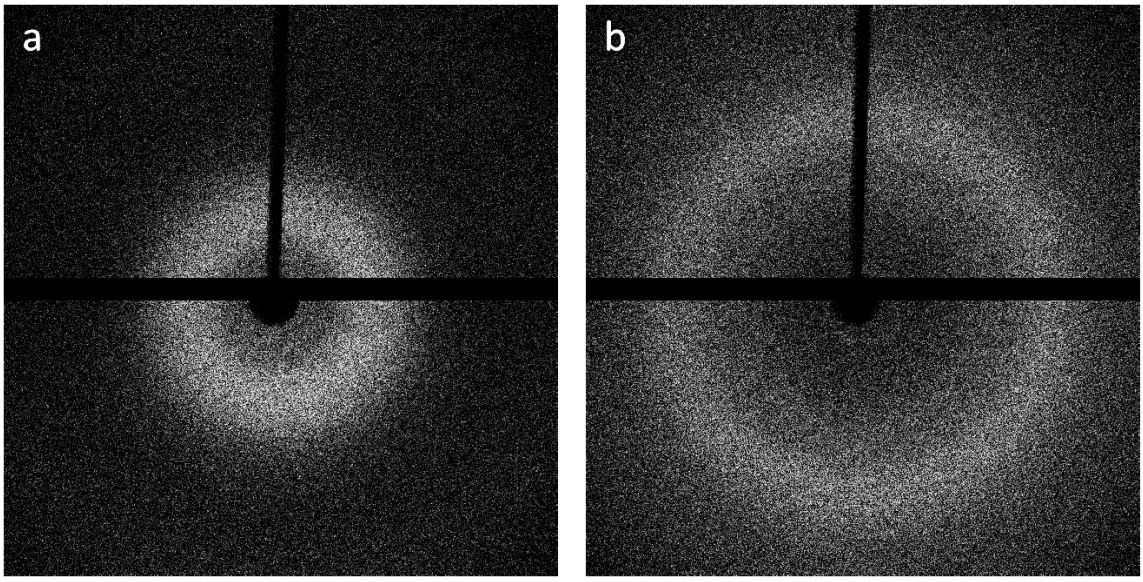

Figure 127: PXRD patterns of (a) oil and (b) water scattering from 0.025 sec exposures with the Synergy-R.

5.3.2 Calcium Carbonate

Plugs containing $CaCO_3$ powder were introduced into the beam using a solution flow rate of 730 µL/min and oil flow rate of 400 µL/min. The PXRD results from a single scan of the flow are presented in Figure 128. At least five Debye-Scherrer rings corresponding to calcite are visible in the 2D pattern (Fig. 128a). However, upon integration it is clear that the (104) reflection had much higher contrast against the background than the (012), (110), (113), or (202) peaks (Fig. 128b). This suggests that the intensity of these peaks in each individual frame was comparable to that of the background, causing some of their intensity to be removed during processing. However, this result still clearly demonstrates the ability of the Synergy-R to perform millifluidic experiments comparable to previous DMC-XRD experiments with $CaCO_3$, where further optimization of experimental and processing parameters is expected to improve relative peak intensities.

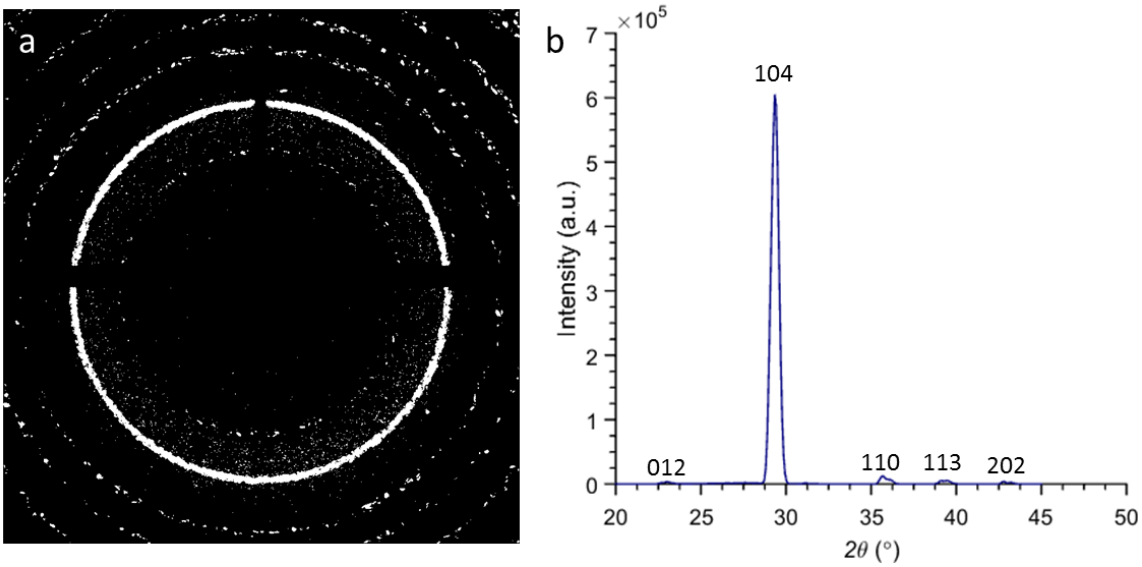

Figure 128: (a) 2D and (b) 1D PXRD pattern obtained from calcite powder in water plugs using a scan of 90 sec comprising consecutive 0.025 sec exposures (3600 frames in total). (b) Labelled peaks correspond to calcite lattice planes.

5.3.3 Paracetamol

Plugs containing powders of PCM Form I and II were introduced into the beam using an aqueous flow rate of 610 µL/min and oil flow rate of 800 µL/min. PXRD results from a single scan of the flow of PCM Form I are presented in Figure 129, where they exhibit higher contrast than the diffraction patterns obtained from calcite experiments. This is likely due to the larger size of these organic crystals, as indicated by the more speckled nature of the pattern in Figure 129a as compared to the more powder-like rings observed in Figure 128a. Diffraction spots produced by large single crystals typically have a higher contrast than rings produced by fine isotropic crystalline powders, and are thus easier to resolve. However, it is worth noting that some of the main lower angle reflections of PCM I, including the $(20\bar{1})$, (001), and $(2\bar{1}\bar{1})$, are underrepresented, where this could indicate some preferred orientation or be a product of less efficient background subtraction at lower angles.

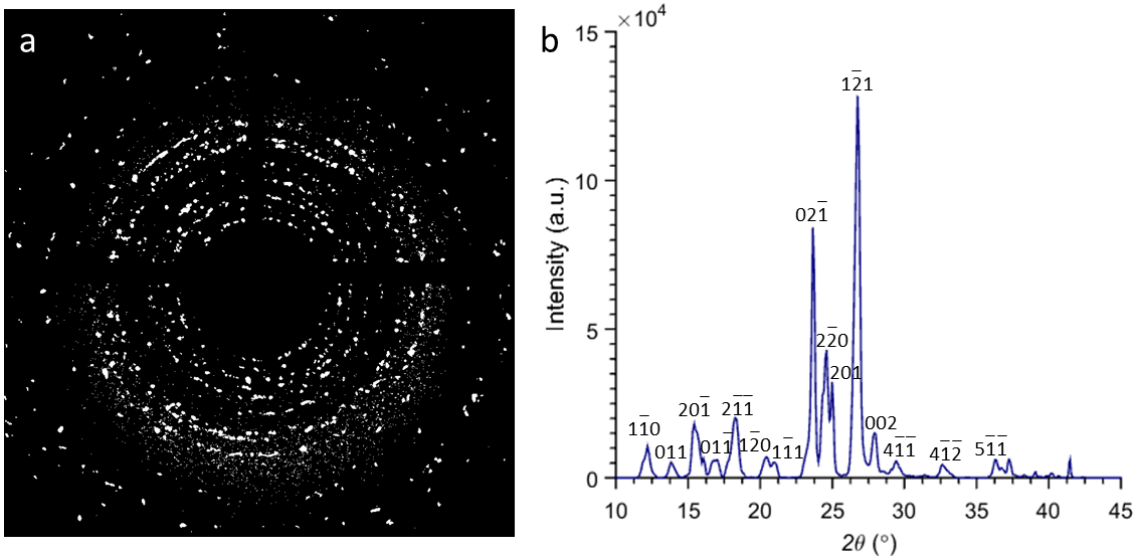

Figure 129: (a) 2D and (b) 1D PXRD pattern obtained from paracetamol Form I powder in water plugs using a scan of 90 sec comprising consecutive 0.025 sec exposures (3600 frames in total). (b) Labelled peaks correspond to PCM Form I lattice planes (CSD: HXACAN26).

PXRD results from a single scan of PCM Form II are presented in Figure 130. Even better scattering statistics were obtained than with Form I, and relative peak intensities appeared to align well with reference data.[334] Another scan of the Form II flow was collected using exposures of 0.05 sec duration rather than 0.025 sec (Fig. 131). Interestingly, the background subtraction routine did not work as well with these scan settings. More peaks could be distinguished in the integrated pattern (Fig. 131b), but there was also a great deal more noise remaining from diffuse solution scattering, highlighting the importance of optimizing scan and processing parameters for each experiment.

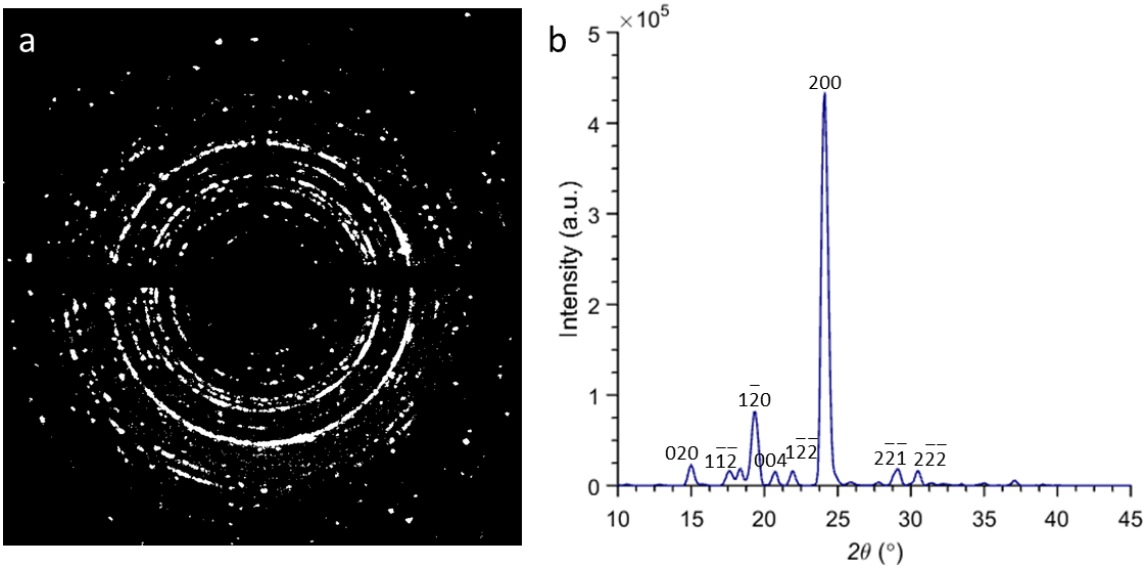

Figure 130: (a) 2D and (b) 1D PXRD pattern obtained from paracetamol Form II powder in water plugs using a scan of 90 sec comprising consecutive 0.025 sec exposures (3600 frames in total). (b) Labelled peaks correspond to PCM Form II lattice planes (CSD: HXACAN23).

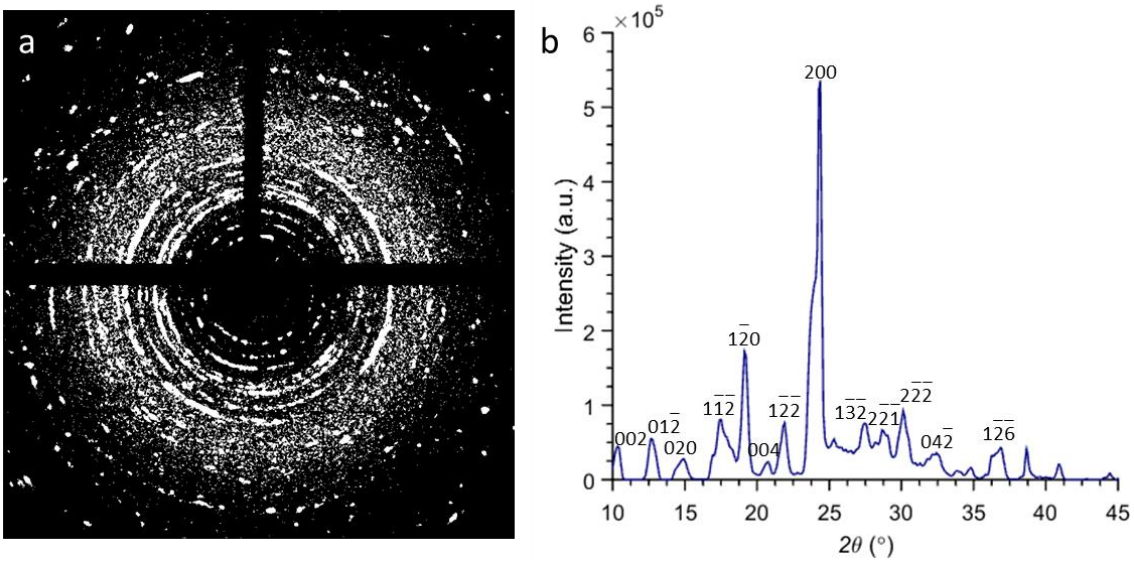

Figure 131: (a) 2D and (b) 1D PXRD pattern obtained from paracetamol Form II powder in water plugs using a scan of 180 sec comprising consecutive 0.05 sec exposures (3600 frames in total). (b) Labelled peaks correspond to PCM Form II lattice planes

5.4 Flux Comparison

The enormous difference in the intensity, contrast, and quality of the PXRD patterns obtained from millifluidic experiments with the Synergy-R when compared with the WAXS patterns obtained from the microfluidic experiments with the Xeuss 2.0 was unexpected and unlikely to be caused by differences in the length scale of the flow systems alone. This comparison led to a deeper investigation into the effective photon flux and flux density of experiments with both systems, where it is important to note that these values are dependent on the source operating voltage and the post-source X-ray optics and are rarely published. After contacting the manufacturer of both the liquid Ga metal X-ray source (Excillum) and the Xeuss 2.0 system (Xenocs), a representative from Xenocs provided a nominal flux value for the MetalJet D2+ source fitted on the Xeuss at the SMALL Laboratory.[335] This value was comparable with the flux value obtained for the microfocus source of the Synergy-R diffractometer provided by a representative from Rigaku Oxford Diffraction (Table 9).[336]

However, the flux value reported for the Xeuss was from a more standard beam size of 0.8 x 0.8 mm^2, which was much larger than the beam utilized during microfluidics experiments at the SMALL lab (0.25 x 0.25 mm^2). Subsequently, a more precise flux value was obtained from the SMALL laboratory manager,[337] where this showed that with the beam size utilized during the above microfluidic experiments, the effective flux density at the sample was almost four orders of magnitude lower than the flux density of the microfocused Synergy-R beam utilized for millifluidics experiments (Table 9). Thus, while liquid metal jet X-ray sources provide very high flux,[329] it is evident that microfocusing optics are required to fully exploit the benefits of liquid metal

sources when a small beam size is required. This large difference in flux density also explains the huge difference in the quality of PXRD/WAXS patterns obtained from both diffractometers.

Table 9: Laboratory X-ray Source Characteristics

Diffractometer	Source	Energy (keV)	Beam size (H x W μm^2)	Flux at sample (ph/s)††	Flux Density (ph/s/μm^2)
Xeuss 2.0	MetalJet D2+ (Ga)	9.24	250 x 250	~3.7 x 10^6	~59.2
Synergy-R	PhotonJet-R (Cu)	8.05	140 x 140	~5.68 x 10^9	~2.90 x 10^5

5.5 Discussion

The range of experiments conducted with the Xeuss 2.0 and XtaLAB Synergy-R provide valuable insight into the current capabilities of state-of-the-art laboratory diffractometers for performing flow-based materials characterization. Microfluidic experiments with the Xeuss demonstrate the difficulty of producing WAXS data comparable to that obtained at the synchrotron, where the photon flux at the sample over 0.5 and even 1 sec exposures was too low to distinguish between different fluid phases or to capture significant levels of crystalline diffraction. However, SAXS data obtained under these same conditions was of much higher quality, where droplets containing silica nanoparticles could be distinguished from the continuous phase and this data could even be fitted to extract an accurate particle size value. Therefore, while current Xeuss flux/optics make microfluidic WAXS analysis improbable, laboratory-based microfluidic SAXS analysis appears to be a promising area for future research.

Since the original assumption was that the two diffractometers were equivalent (or that the Xeuss actually provided higher flux), it was decided that millifluidic rather than microfluidic flow systems would be employed in subsequent experiments with the Synergy-R for better chance of success. These millifluidic experiments were indeed a success, and demonstrate that flow-based serial powder diffraction of inorganic and organic crystals is possible with a commercially available X-ray diffractometer. Notably, high quality diffraction data could be obtained with detector settings comparable to those used at the synchrotron (at 0.025 sec exposure; 40 Hz frame rate), suggesting that the PXRD or WAXS capability of current lab diffractometers was better than

†† Flux values were obtained from SMALL Laboratory Manager, Dr. Oleksandr Mykhaylyk, and Rigaku Oxford Diffraction Sales Manager, Dr. Marcus Winter, respectively.

previously thought. Subsequent investigation into the overall flux of the micrometer-sized beams provided in experiments with the Synergy-R and Xeuss showed that the Synergy-R actually produced four orders of magnitude larger flux densities (Table 9). This suggests that similar millifluidic WAXS analysis should be possible with the Xeuss if its source optics are tuned to produce a smaller beam, and even leaves open the possibility of performing microfluidic WAXS analysis with the Synergy-R or with a microfocus-optimized Xeuss.

In order to take full advantage of such capabilities, additional work in optimizing scan settings and subsequent data processing routines is required. Some progress in this area has already been made since the beginning of the synchrotron portion of project. For example, implementation of ROIs rather than individual test pixels was demonstrated to enable accurate identification of oil and water scattering in lower contrast scenarios, and frames of 0.025 sec duration were shown to produce lower noise than frames of 0.05 sec duration using identical processing parameters. These two examples illustrate the effect that seemingly small changes can have on the quality of data that can be extracted from flow experiments. In the future, continued optimization of experimental parameters such as flux density combined with optimized background subtraction procedures should enable better and better data to be obtained from laboratory- and also synchrotron-based experiments.

Chapter 6:
Conclusions and Outlook

6.1 Summary and Significance

Micro- and milli-fluidic flow platforms are well suited for the study of crystallization processes, and recent developments in flow-based sample environments for X-ray scattering analysis highlight the enormous potential for time-resolved studies of crystal nucleation and growth pathways. However, a problem with many previous flow platforms for X-ray scattering analysis is that they have been largely for proof-of-concept studies, and therefore, limited in the amount and type of data they can be used to capture. This thesis introduced a new robust microfluidic platform to address many of these issues. The insert-based microfluidic device enables reproducible fluidic connection and interfacing with beamline hardware, investigation of continuous and segmented flow and non-ambient conditions, and importantly, allows long residence times to be probed at >30 individual time points in a single experiment. Additionally, the modular nature of the device permits different window materials and channel designs to be interchanged for accommodating different analytical techniques and samples.

Notably, this thesis demonstrated several important technical and scientific achievements. Firstly, it demonstrated that well-engineered flow-cells can go beyond conventional microfluidic devices made from PDMS in terms of robustness, reproducibility, ease of operation, and even functionality. The insert-based device facilitated serial powder X-ray diffraction within a lab-on-a-chip device, going beyond previous studies with free-flowing microjets[246, 247] and enabling the acquisition of multiple time points per experiment using Droplet Microfluidics-Coupled X-ray Diffraction (DMC-XRD). Segmented flow was shown to be essential to this new data collection strategy, where it was required to minimize or eliminate parasitic crystal growth on the channel walls. Subsequently, after optimizing the flow configuration, DMC-XRD was utilized to study the nucleant-mediated growth of $CaCO_3$, where it demonstrated the ability to identify and quantify the nucleating efficiency of bioactive glass and NX illite powders – a topic rarely investigated in inorganic materials research.

Secondly, this thesis demonstrated that not only are equivalent segmented flow powder diffraction experiments possible at the millifluidic-scale, but also that it is possible to perform inline X-ray scattering analysis with very different types of flow reactors, i.e. laboratory-scale CSTRs, and very different types of samples, i.e. organic crystals and coordination polymers. Finally, this thesis proved that it is also now possible to couple such micro- and milli-fluidic flow systems to the latest generation of

laboratory X-ray diffractometers. Complementary experiments with two different diffractometers showed that comparable quality data to those recorded at synchrotron facilities can be obtained if the X-ray source flux, focusing optics, and detector specifications are optimized to provide microbeams and short consecutive exposures. Importantly, this last demonstration should make flow-based *in situ* X-ray scattering analysis accessible to a greater number of research groups and enable more complex experiments to be run without the time constraints of synchrotron beamtime.

6.2 Directions for Future Work

This research opens up a variety of new experimental possibilities and provides a range of opportunities for future work, some of which will be highlighted here. There are three main areas for further development: *(1)* device hardware, *(2)* beamline and laboratory hardware, and *(3)* software, where there is certainly a great deal of overlap between the three areas.

6.2.1 Device Hardware Development

Possible improvements in device hardware entail updating flow-cells for more efficient data collection, data collection from a wider range of systems, and data collection with additional techniques. For example, incorporating thinner and thinner analysis windows and materials such as silicon nitride (Si_3N_4) will allow collection of scattering data with the lowest possible background signal.[338] In turn, this higher quality data can be used by processing software to extract richer and more precise information (discussed below). Also, different flow rates and channel designs can be utilized with the insert-based device to accommodate different solution residence times. Depending on the kinetics of a particular process, it may be desirable to observe some systems over a few seconds with millisecond or greater time resolution, in contrast to the longer time-scales investigated in Chapters 2 and 3. Finally, specific window materials can be selected to enable different types of analysis, such as polyethylenimine (PEI) for SAXS as noted in Chapter 2 (Fig. 40) or calcium fluoride for synchrotron FTIR.[339] In particular, combined SAXS/WAXS and total scattering analysis seem to be the best candidates for future scattering studies, where they can provide a range of additional information even from dilute systems. There is also enormous potential for adapting flow-cells for non-scattering based X-ray analysis, for instance X-ray absorption spectroscopy (XAS), which would provide complementary chemical information about crystallization pathways.

6.2.2 Beamline and Laboratory Hardware Development

Based on lessons learned from many microfluidics (Section 2.2) and millifluidics (Section 4.1 and 4.2) beamtimes, there are also improvements that could be made to beamline hardware which would better facilitate flow-based sample environments and enhance data collection. A significant advantage would be providing inline microscopes that not only allow visualization of flow channels during device start-up, but also allow visualization during X-ray exposure. This would remove any uncertainty in the stability of the flow during a particular scan and also enable fouled devices to be immediately stopped and exchanged for a fresh flow-cell. Beyond experimental monitoring, incorporating optical microscopy and even other techniques (e.g. Raman, fluorescence) with simultaneous X-ray exposure could be useful for a variety of more comprehensive time-resolved studies of a wider range of systems. Another hardware problem, especially with millifluidic experiments, is the short travel distance and slow speed of goniometers, which limits the number of independent analysis windows that can be accessed. Of course, flow systems can be redesigned to have windows closer together, but also increasing the speed and range of motion of sample stages would provide even greater versatility.

As demand for these types of experiments grows, it would also be beneficial to build specific experimental hutches or even entire beamlines dedicated to flow experiments. Interest in such a capability is increasing, and as a part of the Extremely Brilliant Source (EBS) upgrade of the ESRF, the microfocus macromolecular crystallography beamline, ID29 is being rebuilt with a focus on time-resolved serial crystallography.[340] The new ID29 beamline will open in 2021/2022 and have a hutch dedicated to injector-based experiments. Further, beamline staff and users are interested in also exploring the application of microfluidic sample environments.‡‡ Hopefully this upgrade will spark the development of similar beamlines at other synchrotrons around the world, and that such instruments will not only be confined to macromolecular crystallography end-stations.

In addition to conducting analysis at synchrotron facilities, the previous chapter also highlighted the possibility of performing these experiments in the home laboratory. Since that work was only preliminary, a great deal of further development will be required on the part of universities and equipment manufacturers to optimize laboratory X-ray diffractometers for flow analysis. Through this project, a relationship between the

‡‡ The author gave an invited talk on this work at the microsymposium, “ID29: Tunable past and time-resolved future”, of the ESRF User Meeting on 6 February 2019 and discussed possible experiments with ID29 scientist-in-charge, Daniele de Sanctis, and other members of the ID29 user community.

Kapur/Meldrum Groups and Rigaku Oxford Diffraction was formed, and Rigaku has expressed interest in helping the groups develop both hardware and software for performing flow-based experiments on their Synergy-R diffractometer. Correspondingly, there is now a push to develop a dedicated national flow diffraction facility at the University of Leeds, and at the time of writing, a grant proposal to fund the creation of this facility is under review by the UK Engineering and Physical Sciences Research Council (EPSRC). If this facility is funded, it will represent a huge step forward for flow-based X-ray scattering analysis. However, even if this particular project is not supported, it is only a matter of time before university laboratories begin to acquire this kind of functionality.

6.2.3 Data Collection and Analysis Software Development

The final area for development is in data collection, processing, and analysis software, which will support both synchrotron- and laboratory-based flow analysis. One major problem that still needs to be addressed for data collection at high-resolution, time-resolved facilities is long-term data storage. Depending on the number of frames collected and the number of pixels per frame, each flow beamtime from this project produced anywhere from 1 to 20 TB of data. Importantly, many if not most of these frames will simply be eliminated during frame sorting since they will not contain crystal hits – meaning that much of the space storing this data is wasted. Furthermore, this is a problem that will only continue to worsen as techniques become even higher resolution and more researchers use them. For instance, at a dedicated university-based flow-diffraction facility, like the one proposed at Leeds, there could be a beamtime every week of the year.

One solution to this data problem would be to minimize the amount of collected data in the first place through “on-the-fly” processing (OTFP).[341] In this method, frame sorting/hit finding algorithms would be implemented in real-time, and only frames containing crystal hits would be downloaded from the detector – reducing the size of datasets by at least a factor of two, if not much more. Importantly, implementing such an OTFP strategy would require advances in data processing algorithms in order to guarantee that discarded frames do not contain any potentially useable data. This is exactly where processing software improvements such as region of interest (ROI) frame sorting and more intuitive and advanced background subtraction routines will find use. Moreover, raw data will become easier to sort and process with device hardware developments that result in lower noise data.

6.2.4 Broad Outlook

Ultimately, whether or not they are implemented for on-the-fly processing, higher quality raw data and better selection and processing algorithms offer the potential to produce much richer datasets and provide additional experimental control. For instance, if high enough quality diffraction patterns can be obtained, they can be used to perform Rietveld or similar types of peak shape analysis, where crystal size, strain, and lattice parameters can be refined at each step of the growth pathway of a material. Further, if this type of analysis could be done in real-time and the flow reactor itself was coupled to the data processing computer, it could even be possible to provide instantaneous feedback that optimizes reactor flow rates and temperatures to produce crystals with desired structures or properties. While such functionality seems futuristic, combined improvements in sample environments, diffractometers, and processing routines and teamwork between engineers, materials scientists, and crystallographers could make it a reality. In fact, it is exactly these types of developments in flow-cell manufacturing, detector technology, and X-ray generation and this type of collaboration between engineers and scientists that have enabled the progress reported here. As long as these partnerships continue, the future of flow-based X-ray scattering analysis appears to be very bright indeed.

Appendix I:

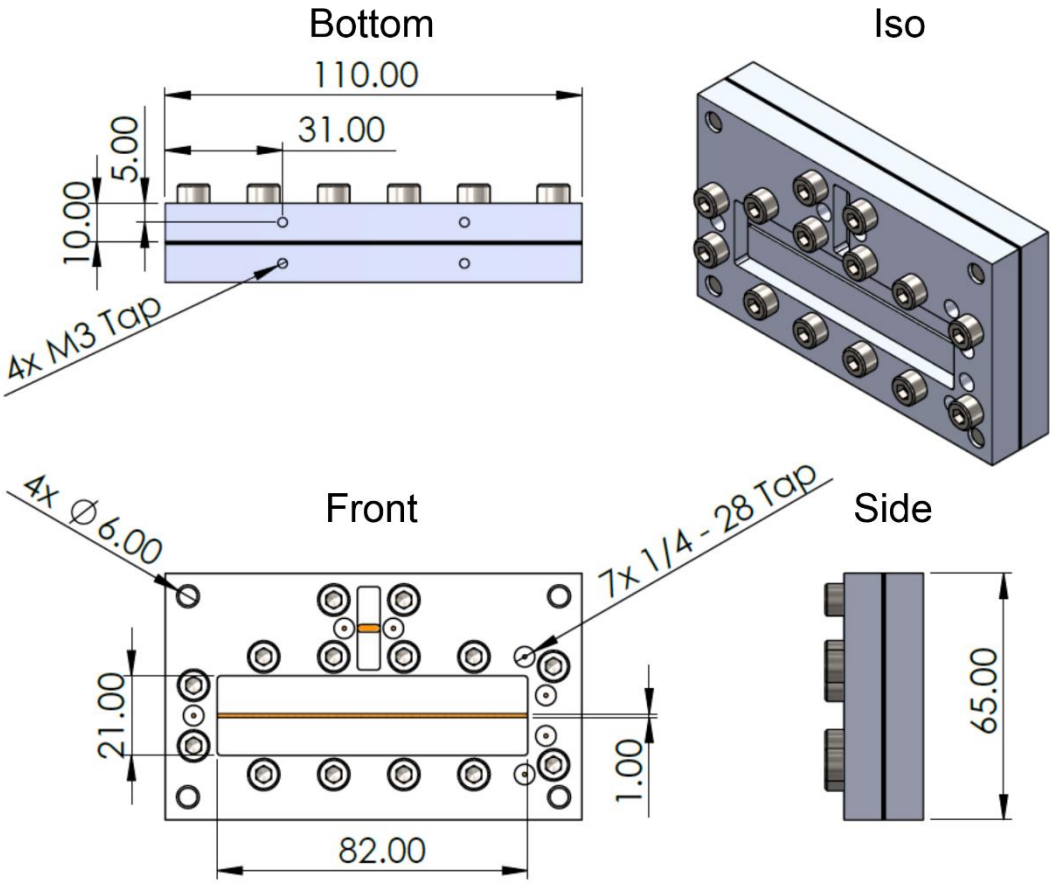

Figure AI-1: CAD drawing of assembled insert-based device made using SolidWorks. All dimensions in mm

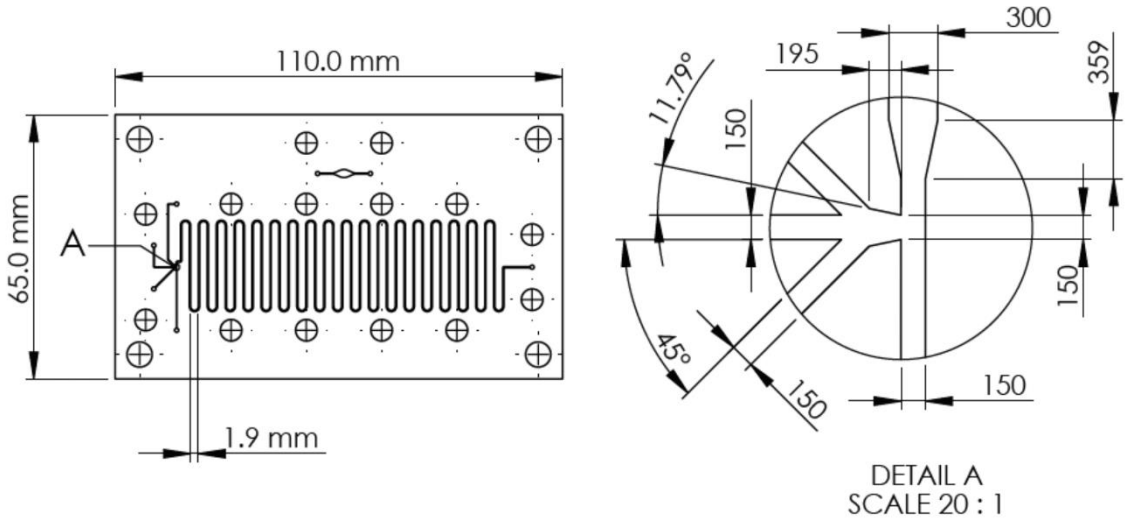

Figure AI-2: CAD drawing of the central channel insert made using SolidWorks. Detail A shows the “buffer channel” T-junction geometry. This drawing is mirrored from the one in Figure AI-1, as the central insert is flipped over during assembly. All dimensions are in microns unless noted otherwise.

Appendix II:

```
%% For reading HDF5 Files from ESRF Beamline ID13
% Written in 2017 by Mark A. Levenstein
% with some original code from Britta Weinhausen, Michael Sztucki, and
% Matlab Newsgroup User, David (clieberm@rochester.rr.com)

%% Display .h5 file info

h5disp('file_name');

%% Read Single Frame

myData = h5read('file_name','data_location_in_file',[500 450
201],[1571 1718 1]);

% Reset hot pixels to zero
for i = 1:1571
    for j = 1:1718
        if myData(i,j,1) > 100000
            myData(i,j,1) = 0;
        end
    end
end

%% Display single diffraction frame

image90 = rot90(myData);  % rotate image matrix 90 deg
diffpattern = flip(image90); % flip image over x axis
imshow(diffpattern, [0 250]); % display image (with intensity scaling)

%% Set Background Frame

background_raw =
h5read('backgound_file_name','data_location_in_background_file',[500
450 14],[1571 1718 1]);


% Reset dead pixels to zero
    for i = 1:1571
        for j = 1:1718
            if background_raw(i,j,1) > 100000
                background_raw(i,j,1) = 0;
            end
        end
    end

back_90 = rot90(background_raw);  % rotate image matrix 90 deg
background = flip(back_90); % flip image over x axis



%% Show background subtracted pattern

pattern_process = diffpattern - background;

imshow(pattern_process, [0 100]);
```

```
%% Make composite image from hit frames

composite_image = zeros(1718,1571);
composite_image = uint32(composite_image);

modifier = 2; % to vary background subtraction intensity

for k = 1:502 % 1:number of frames in scan

    myData = h5read('file_name','data_location_in_file',[500 450
k],[1571 1718 1]);

    % Reset dead pixels to zero
    for i = 1:1571
        for j = 1:1718
            if myData(i,j,1) > 100000
                myData(i,j,1) = 0;
            end
        end
    end

    image90 = rot90(myData);  % rotate image matrix 90 deg
    diffpattern = flip(image90); % flip image over x axis

    if diffpattern(817,1137) > 35   % identify and skip oil patterns
%(determine value for each experiment)
            continue
    end

    if diffpattern(811,1136) > 35   % identify and skip oil patterns
%(determine value for each experiment)
            continue
    end


    pattern_process = diffpattern - modifier*background; % background
%subtraction

    if max(pattern_process) < 100 % exclude frames without peaks
        continue
    end

    % Optional processing steps (use with caution)
    % pattern_process = medfilt2(pattern_process, [3 3]); % median
%filter for smoothing
    % pattern_process = imgaussfilt(pattern_process); % Gaussian
%filter if low contrast

    % Threshold
    for i = 1:1718
        for j = 1:1571
            if pattern_process(i,j,1) < 30 % determine value for each
%experiment
                pattern_process(i,j,1) = 0;
            end
        end
    end

    composite_image = composite_image + pattern_process;
```

```
end

figure
imshow(composite_image, [0 100]); % smaller scale to see all rings

%% Integrate 2D pattern and plot 2D and 1D patterns


img = double(composite_image); % load data
integration_radius = 1200; % radius
center = [822.5 853]; % center of X-ray beam on pattern


f=figure;
pos = get(f,'position');
set(f,'position',[(pos(1)-pos(4)/2) pos(2) 2*pos(3) pos(4)]); %Resize
subplot(121);
imagesc(img,[0 100]);
colormap(gray);
axis square; hold on;


% Create the meshgrid to be used in resampling
[X,Y] = meshgrid(1:1571,1:1718);

% Integrate
for radius = 1:round(integration_radius)

    % To avoid redundancy, sample at roughly 1 px distances
    num_pxls = 2*pi*radius;
    theta = 0:1/num_pxls:2*pi;

    x = center(1) + radius*cos(theta);
    y = center(2) + radius*sin(theta);


    sampled_radial_slice = interp2(X,Y,img,x,y); % obtains pixel
%values at the defined radius
    sampled_radial_slice(isnan(sampled_radial_slice))=[]; % removes
%NaN values when radius is larger than img size
    radial_average(radius) = sum(sampled_radial_slice); % sums pixel
%values around defined radius

    subplot(121);
    if(radius>1)
        delete(p);
    end
    p=plot(x,y,'y.',x(1),y(1),'r*'); % Starts at green spot and goes
%counter clockwise


end

title('2D Pattern');
set(gca, ...
  'XTickLabel'   , []        , ...
  'YTickLabel'   , []        , ...
  'FontSize'     , 12        , ...
```

```
  'LineWidth'    , 1          );



subplot(122)

r = 1:round(integration_radius);

% pixel size
det.pixel_size = 75E-6; % m     % 75E-6 for all data except non-porous
%bioglass from beamline I22 which is 172E-6

% detector distance
det.distance = 0.115927; % m    % 0.115927 for all data except non-
%porous bioglass from beamline I22 which is 0.1643438

twotheta = atand(det.pixel_size .* r ./ det.distance);
counts = radial_average;

pattern = line(twotheta, counts);
title('1D Pattern');
hXLabel = xlabel('\it{2}\rm\theta (\circ)'); hYLabel =
ylabel('Intensity (a.u.)');
set(pattern, 'Color', [0 0 0.5], 'LineWidth', 1);

set(gca, ...
  'Box'         , 'off'     , ...
  'TickDir'     , 'out'     , ...
  'TickLength'  , [.02 .02] , ...
  'XMinorTick'  , 'on'      , ...
  'YMinorTick'  , 'on'      , ...
  'YGrid'       , 'off'      , ...
  'XColor'      , [0 0 0], ...
  'YColor'      , [0 0 0], ...
  'FontSize'    , 12        , ...
  'LineWidth'   , 1         );

hold off;

intensity_integrated = trapz(twotheta, counts); % area under
%diffraction pattern curve

%% Save data to excel file

file_dir = 'file_location\';
file_pre = 'file_name';
file_name = [file_dir, file_pre,'.xlsx'];

xlswrite(file_name, [twotheta' counts']); % write to file
```

References

1. J. J. De Yoreo, P. U. P. A. Gilbert, N. A. J. M. Sommerdijk, R. L. Penn, S. Whitelam, D. Joester, H. Zhang, J. D. Rimer, A. Navrotsky, J. F. Banfield, A. F. Wallace, F. M. Michel, F. C. Meldrum, H. Cölfen and P. M. Dove, *Science*, 2015, **349**.
2. S. Mann, *Biomineralization: principles and concepts in bioinorganic materials chemistry*, Oxford University Press, 2001.
3. I. Rodriguez-Ruiz, S. Veesler, J. Gomez-Morales, J. M. Delgado-Lopez, O. Grauby, Z. Hammadi, N. Candoni and J. M. Garcia-Ruiz, *Crystal Growth & Design*, 2014, **14**, 792-802.
4. C. N. Nanev, in *The Handbook of Crystal Growth, Fundamentals: Thermodynamics and Kinetics*, ed. T. Nishinaga, Elsevier, Boston, 2nd edn., 2015, vol. IA, ch. 7, pp. 315-358.
5. H. K. Christenson, *Crystengcomm*, 2013, **15**, 2030-2039.
6. J. Aizenberg, A. J. Black and G. M. Whitesides, *Nature*, 1999, **398**, 495-498.
7. T. F. Whale, M. A. Holden, A. N. Kulak, Y. Y. Kim, F. C. Meldrum, H. K. Christenson and B. J. Murray, *Physical Chemistry Chemical Physics*, 2017, **19**, 31186-31193.
8. N. E. Chayen, E. Saridakis and R. P. Sear, *Proceedings of the National Academy of Sciences of the United States of America*, 2006, **103**, 597-601.
9. G. Falini, S. Albeck, S. Weiner and L. Addadi, *Science*, 1996, **271**, 67-69.
10. R. P. Sear, *International Materials Reviews*, 2012, **57**, 328-356.
11. R. P. Sear, *Nature Materials*, 2011, **10**, 809-810.
12. Y. Diao, T. Harada, A. S. Myerson, T. A. Hatton and B. L. Trout, *Nature Materials*, 2011, **10**, 867-871.
13. A. van Blaaderen, R. Ruel and P. Wiltzius, *Nature*, 1997, **385**, 321-324.
14. J. A. van Meel, R. P. Sear and D. Frenkel, *Physical Review Letters*, 2010, **105**, 4.
15. R. T. Bruintjes, *Bulletin of the American Meteorological Society*, 1999, **80**, 805-820.
16. A. Zipori, D. Rosenfeld, J. Shpund, D. M. Steinberg and Y. Erel, *Atmospheric Research*, 2012, **114**, 119-130.
17. J. D. Atkinson, B. J. Murray, M. T. Woodhouse, T. F. Whale, K. J. Baustian, K. S. Carslaw, S. Dobbie, D. O'Sullivan and T. L. Malkin, *Nature*, 2013, **498**, 355-358.
18. D. O'Sullivan, B. J. Murray, J. F. Ross, T. F. Whale, H. C. Price, J. D. Atkinson, N. S. Umo and M. E. Webb, *Scientific Reports*, 2015, **5**, 7.
19. J. Vergara-Temprado, A. K. Miltenberger, K. Furtado, D. P. Grosvenor, B. J. Shipway, A. A. Hill, J. M. Wilkinson, P. R. Field, B. J. Murray and K. S. Carslaw, *Proceedings of the National Academy of Sciences of the United States of America*, 2018, **115**, 2687-2692.
20. B. Vonnegut, *Journal of Applied Physics*, 1947, **18**, 593-595.
21. P. Conrad, G. E. Ewing, R. L. Karlinsey and V. Sadtchenko, *J. Chem. Phys.*, 2005, **122**, 11.
22. A. Kiselev, F. Bachmann, P. Pedevilla, S. J. Cox, A. Michaelides, D. Gerthsen and T. Leisner, *Science*, 2017, **355**, 367-371.
23. E. Saridakis and N. E. Chayen, *Trends in Biotechnology*, 2009, **27**, 99-106.

24. N. E. Chayen, E. Saridakis, R. El-Bahar and Y. Nemirovsky, *Journal of Molecular Biology*, 2001, **312**, 591-595.
25. P. Asanithi, E. Saridakis, L. Govada, I. Jurewicz, E. W. Brunner, R. Ponnusamy, J. A. S. Cleaver, A. B. Dalton, N. E. Chayen and R. P. Sear, *ACS Appl. Mater. Interfaces*, 2009, **1**, 1203-1210.
26. F. Kertis, S. Khurshid, O. Okman, J. W. Kysar, L. Govada, N. Chayen and J. Erlebacher, *Journal of Materials Chemistry*, 2012, **22**, 21928-21934.
27. S. Khurshid, E. Saridakis, L. Govada and N. E. Chayen, *Nature Protocols*, 2014, **9**, 1621-1633.
28. N. E. Chayen and E. Saridakis, *J. Cryst. Growth*, 2001, **232**, 262-264.
29. A. J. Page and R. P. Sear, *Physical Review Letters*, 2006, **97**, 4.
30. Y. Diao, M. E. Helgeson, A. S. Myerson, T. A. Hatton, P. S. Doyle and B. L. Trout, *Journal of the American Chemical Society*, 2011, **133**, 3756-3759.
31. L. O. Hedges and S. Whitelam, *Soft Matter*, 2013, **9**, 9763-9766.
32. K. Henzler, E. O. Fetisov, M. Galib, M. D. Baer, B. A. Legg, C. Borca, J. M. Xto, S. Pin, J. L. Fulton, G. K. Schenter, N. Govind, J. I. Siepmann, C. J. Mundy, T. Huthwelker and J. J. De Yoreo, *Science Advances*, 2018, **4**, 11.
33. R. Lacmann, A. Herden and C. Mayer, *Chemical Engineering & Technology*, 1999, **22**, 279-289.
34. W. K. Burton, N. Cabrera and F. C. Frank, *Phil. Trans. R. Soc. Lond. A*, 1951, **243**, 299-358.
35. D. P. Woodruff, *Philosophical Transactions of the Royal Society A - Mathematical Physical and Engineering Sciences*, 2015, **373**, 11.
36. H. H. Teng, P. M. Dove and J. J. De Yoreo, *Geochimica Et Cosmochimica Acta*, 2000, **64**, 2255-2266.
37. Y. Y. Kim, C. L. Freeman, X. Q. Gong, M. A. Levenstein, Y. W. Wang, A. Kulak, C. Anduix-Canto, P. A. Lee, S. B. Li, L. Chen, H. K. Christenson and F. C. Meldrum, *Angewandte Chemie-International Edition*, 2017, **56**, 11885-11890.
38. B. D. Hamilton, J. M. Ha, M. A. Hillmyer and M. D. Ward, *Accounts of Chemical Research*, 2012, **45**, 414-423.
39. W. Ostwald, *Zeitschrift für Physikalische Chemie*, 1897, **22**, 289-330.
40. F. C. Meldrum and H. Colfen, *Chemical Reviews*, 2008, **108**, 4332-4432.
41. M. A. Levenstein, M.Sc. (Eng) by Research, University of Leeds, 2015.
42. Y. W. Wang, Y. Y. Kim, H. K. Christenson and F. C. Meldrum, *Chemical Communications*, 2012, **48**, 504-506.
43. A. Gal, W. Habraken, D. Gur, P. Fratzl, S. Weiner and L. Addadi, *Angewandte Chemie-International Edition*, 2013, **52**, 4867-4870.
44. D. Erdemir, A. Y. Lee and A. S. Myerson, *Accounts of Chemical Research*, 2009, **42**, 621-629.
45. L. B. Gower, *Chemical Reviews*, 2008, **108**, 4551-4627.
46. P. J. M. Smeets, A. R. Finney, W. Habraken, F. Nudelman, H. Friedrich, J. Laven, J. J. De Yoreo, P. M. Rodger and N. Sommerdijk, *Proceedings of the National Academy of Sciences of the United States of America*, 2017, **114**, E7882-E7890.
47. S. Mann, *Nature*, 1993, **365**, 499-505.
48. F. C. Meldrum, *International Materials Reviews*, 2003, **48**, 187-224.

49. W. J. Cai, Y. N. Ma, B. M. Hopkinson, A. G. Grottoli, M. E. Warner, Q. Ding, X. P. Hu, X. C. Yuan, V. Schoepf, H. Xu, C. H. Han, T. F. Melman, K. D. Hoadley, D. T. Pettay, Y. Matsui, J. H. Baumann, S. Levas, Y. Ying and Y. C. Wang, *Nature Communications*, 2016, **7**, 8.
50. A. Mucci and J. W. Morse, *Geochimica Et Cosmochimica Acta*, 1983, **47**, 217-233.
51. A. M. Belcher, X. H. Wu, R. J. Christensen, P. K. Hansma, G. D. Stucky and D. E. Morse, *Nature*, 1996, **381**, 56-58.
52. L. Addadi, J. Moradian, E. Shay, N. G. Maroudas and S. Weiner, *Proceedings of the National Academy of Sciences of the United States of America*, 1987, **84**, 2732-2736.
53. F. Nudelman, K. Pieterse, A. George, P. H. H. Bomans, H. Friedrich, L. J. Brylka, P. A. J. Hilbers, G. de With and N. Sommerdijk, *Nature Materials*, 2010, **9**, 1004-1009.
54. D. Faivre and D. Schuler, *Chemical Reviews*, 2008, **108**, 4875-4898.
55. D. Kim, B. Lee, S. Thomopoulos and Y. S. Jun, *Nature Communications*, 2018, **9**, 9.
56. S. Mann, D. D. Archibald, J. M. Didymus, T. Douglas, B. R. Heywood, F. C. Meldrum and N. J. Reeves, *Science*, 1993, **261**, 1286-1292.
57. S. Mann, J. P. Hannington and R. J. P. Williams, *Nature*, 1986, **324**, 565-567.
58. C. C. Tester, C. H. Wu, S. Weigand and D. Joester, *Faraday Discussions*, 2012, **159**, 345-356.
59. E. Beniash, *Wiley Interdiscip. Rev.-Nanomed. Nanobiotechnol.*, 2011, **3**, 47-69.
60. M. L. Zeng, Y. Y. Kim, C. Anduix-Canto, C. Frontera, D. Laundy, N. Kapur, H. K. Christenson and F. C. Meldrum, *Proceedings of the National Academy of Sciences of the United States of America*, 2018, **115**, 7670-7675.
61. E. Loste and F. C. Meldrum, *Chemical Communications*, 2001, DOI: 10.1039/b101563j, 901-902.
62. E. Loste, R. J. Park, J. Warren and F. C. Meldrum, *Advanced Functional Materials*, 2004, **14**, 1211-1220.
63. Y. Y. Kim, N. B. J. Hetherington, E. H. Noel, R. Kroger, J. M. Charnock, H. K. Christenson and F. C. Meldrum, *Angewandte Chemie-International Edition*, 2011, **50**, 12572-12577.
64. J. W. McCauley and R. Roy, *Am. Miner.*, 1974, **59**, 947-963.
65. H. Y. Li and L. A. Estroff, *Journal of the American Chemical Society*, 2007, **129**, 5480-5483.
66. L. A. Estroff, L. Addadi, S. Weiner and A. D. Hamilton, *Organic & Biomolecular Chemistry*, 2004, **2**, 137-141.
67. H. Y. Li, H. L. Xin, D. A. Muller and L. A. Estroff, *Science*, 2009, **326**, 1244-1247.
68. C. Anduix-Canto, Y. Y. Kim, Y. W. Wang, A. Kulak, F. C. Meldrum and H. K. Christenson, *Crystal Growth & Design*, 2016, **16**, 5403-5411.
69. C. J. Stephens, S. F. Ladden, F. C. Meldrum and H. K. Christenson, *Advanced Functional Materials*, 2010, **20**, 2108-2115.
70. Y. W. Wang, H. K. Christenson and F. C. Meldrum, *Advanced Functional Materials*, 2013, **23**, 5615-5623.

71. C. J. Stephens, Y. Y. Kim, S. D. Evans, F. C. Meldrum and H. K. Christenson, *Journal of the American Chemical Society*, 2011, **133**, 5210-5213.
72. S. E. Wolf, J. Leiterer, M. Kappl, F. Emmerling and W. Tremel, *Journal of the American Chemical Society*, 2008, **130**, 12342-12347.
73. R. Grossier and S. Veesler, *Crystal Growth & Design*, 2009, **9**, 1917-1922.
74. A. Arakaki, K. Shimizu, M. Oda, T. Sakamoto, T. Nishimura and T. Kato, *Organic & Biomolecular Chemistry*, 2015, **13**, 974-989.
75. N. Sommerdijk and G. de With, *Chemical Reviews*, 2008, **108**, 4499-4550.
76. R. Q. Song and H. Colfen, *Crystengcomm*, 2011, **13**, 1249-1276.
77. G. Binnig, C. F. Quate and C. Gerber, *Physical Review Letters*, 1986, **56**, 930-933.
78. P. E. Hillner, A. J. Gratz, S. Manne and P. K. Hansma, *Geology*, 1992, **20**, 359-362.
79. J. H. Tao, M. H. Nielsen and J. J. De Yoreo, *Current Opinion in Colloid & Interface Science*, 2018, **34**, 74-88.
80. T. Ando, *Nanotechnology*, 2012, **23**, 27.
81. J. J. De Yoreo, T. A. Land and B. Dair, *Physical Review Letters*, 1994, **73**, 838-841.
82. L. M. Hamm, A. J. Giuffre, N. Han, J. H. Tao, D. B. Wang, J. J. De Yoreo and P. M. Dove, *Proceedings of the National Academy of Sciences of the United States of America*, 2014, **111**, 1304-1309.
83. W. Habraken, J. H. Tao, L. J. Brylka, H. Friedrich, L. Bertinetti, A. S. Schenk, A. Verch, V. Dmitrovic, P. H. H. Bomans, P. M. Frederik, J. Laven, P. van der Schoot, B. Aichmayer, G. de With, J. J. DeYoreo and N. Sommerdijk, *Nature Communications*, 2013, **4**, 12.
84. J. J. De Yoreo, S. Chung and R. W. Friddle, *Advanced Functional Materials*, 2013, **23**, 2525-2538.
85. J. J. De Yoreo and N. A. J. M. Sommerdijk, *Nature Reviews Materials*, 2016, **1**, 18.
86. R. Garcia and A. San Paulo, *Physical Review B*, 2000, **61**, 13381-13384.
87. M. J. Williamson, R. M. Tromp, P. M. Vereecken, R. Hull and F. M. Ross, *Nature Materials*, 2003, **2**, 532-536.
88. M. H. Nielsen, S. Aloni and J. J. De Yoreo, *Science*, 2014, **345**, 1158-1162.
89. N. M. Schneider, M. M. Norton, B. J. Mendel, J. M. Grogan, F. M. Ross and H. H. Bau, *Journal of Physical Chemistry C*, 2014, **118**, 22373-22382.
90. T. H. Moser, H. Mehta, C. Park, R. T. Kelly, T. Shokuhfar and J. E. Evans, *Science Advances*, 2018, **4**, 8.
91. B. P. Pichon, P. H. H. Bomans, P. M. Frederik and N. Sommerdijk, *Journal of the American Chemical Society*, 2008, **130**, 4034-4040.
92. E. M. Pouget, P. H. H. Bomans, J. Goos, P. M. Frederik, G. de With and N. Sommerdijk, *Science*, 2009, **323**, 1455-1458.
93. A. E. S. Van Driessche, N. Van Gerven, P. H. H. Bomans, R. R. M. Joosten, H. Friedrich, D. Gil-Carton, N. Sommerdijk and M. Sleutel, *Nature*, 2018, **556**, 89-94.
94. J. H. Chung, I. Granja, M. G. Taylor, G. Mpourmpakis, J. R. Asplin and J. D. Rimer, *Nature*, 2016, **536**, 446-450.

95. Y. F. Xu, K. C. H. Tijssen, P. H. H. Bomans, A. Akiva, H. Friedrich, A. P. M. Kentgens and N. Sommerdijk, *Nature Communications*, 2018, **9**, 12.
96. J. J. De Yoreo, L. A. Zepeda-Ruiz, R. W. Friddle, S. R. Qiu, L. E. Wasylenki, A. A. Chernov, G. H. Gilmer and P. M. Dove, *Crystal Growth & Design*, 2009, **9**, 5135-5144.
97. W. Shockley, J. Bardeen and W. H. Brattain, *Science*, 1948, **108**, 678-679.
98. G. E. Moore, 1975.
99. G. M. Whitesides, *Nature*, 2006, **442**, 368-373.
100. M. L. Kovarik, P. C. Gach, D. M. Ornoff, Y. L. Wang, J. Balowski, L. Farrag and N. L. Allbritton, *Analytical Chemistry*, 2012, **84**, 516-540.
101. D. J. Harrison, K. Fluri, K. Seiler, Z. H. Fan, C. S. Effenhauser and A. Manz, *Science*, 1993, **261**, 895-897.
102. G. H. W. Sanders and A. Manz, *TrAC Trends in Analytical Chemistry*, 2000, **19**, 364-378.
103. D. R. Reyes, D. Iossifidis, P. A. Auroux and A. Manz, *Analytical Chemistry*, 2002, **74**, 2623-2636.
104. D. C. Duffy, J. C. McDonald, O. J. A. Schueller and G. M. Whitesides, *Analytical Chemistry*, 1998, **70**, 4974-4984.
105. J. C. McDonald and G. M. Whitesides, *Accounts of Chemical Research*, 2002, **35**, 491-499.
106. K. Dhouib, C. K. Malek, W. Pfleging, B. Gauthier-Manuel, R. Duffait, G. Thuillier, R. Ferrigno, L. Jacquamet, J. Ohana, J. L. Ferrer, A. Theobald-Dietrich, R. Giege, B. Lorber and C. Sauter, *Lab on a Chip*, 2009, **9**, 1412-1421.
107. X. Casadevall i Solvas and A. deMello, *Chemical Communications*, 2011, **47**, 1936-1942.
108. H. Song, D. L. Chen and R. F. Ismagilov, *Angewandte Chemie-International Edition*, 2006, **45**, 7336-7356.
109. S. B. Li, X. Q. Gong, C. S. Mc Nally, M. L. Zeng, T. Gaule, C. Anduix-Canto, A. N. Kulak, L. A. Bawazer, M. J. McPherson and F. C. Meldrum, *RSC Advances*, 2016, **6**, 25927-25933.
110. J. N. Lee, C. Park and G. M. Whitesides, *Analytical Chemistry*, 2003, **75**, 6544-6554.
111. M. A. Levenstein, L. A. Bawazer, C. S. Mc Nally, W. J. Marchant, X. Gong, F. C. Meldrum and N. Kapur, *Microfluidics and Nanofluidics*, 2016, **20**, 143.
112. A. Liga, J. A. S. Morton and M. Kersaudy-Kerhoas, *Microfluidics and Nanofluidics*, 2016, **20:164**, 12.
113. Y. Temiz, R. D. Lovchik, G. V. Kaigala and E. Delamarche, *Microelectronic Engineering*, 2015, **132**, 156-175.
114. M. Briceno, J. L. Salager and J. Bertrand, *Chemical Engineering Research & Design*, 2001, **79**, 943-948.
115. R. V. Bell, L. A. Rochford, R. T. M. de Rosales, M. Stevens, J. V. M. Weaver and S. A. F. Bon, *J. Mat. Chem. B*, 2015, **3**, 5544-5552.
116. A. Schuch, P. Deiters, J. Henne, K. Koehler and H. P. Schuchmann, *Journal of Colloid and Interface Science*, 2013, **402**, 157-164.
117. S. Y. Teh, R. Lin, L. H. Hung and A. P. Lee, *Lab on a Chip*, 2008, **8**, 198-220.
118. L. Mazutis, J. Gilbert, W. L. Ung, D. A. Weitz, A. D. Griffiths and J. A. Heyman, *Nature Protocols*, 2013, **8**, 870-891.

119. J.-u. Shim, R. T. Ranasinghe, C. A. Smith, S. M. Ibrahim, F. Hollfelder, W. T. S. Huck, D. Klenerman and C. Abell, *ACS Nano*, 2013, **7**, 5955-5964.
120. W. Stephenson, L. T. Donlin, A. Butler, C. Rozo, B. Bracken, A. Rashidfarrokhi, S. M. Goodman, L. B. Ivashkiv, V. P. Bykerk, D. E. Orange, R. B. Darnell, H. P. Swerdlow and R. Satija, *Nature Communications*, 2018, **9**, 10.
121. J. J. Agresti, E. Antipov, A. R. Abate, K. Ahn, A. C. Rowat, J. C. Baret, M. Marquez, A. M. Klibanov, A. D. Griffiths and D. A. Weitz, *Proceedings of the National Academy of Sciences of the United States of America*, 2010, **107**, 4004-4009.
122. A. R. Abate, J. J. Agresti and D. A. Weitz, *Applied Physics Letters*, 2010, **96**, 3.
123. H. D. Xi, H. Zheng, W. Guo, A. M. Ganan-Calvo, Y. Ai, C. W. Tsao, J. Zhou, W. H. Li, Y. Y. Huang, N. T. Nguyen and S. H. Tan, *Lab on a Chip*, 2017, **17**, 751-771.
124. R. A. L. Leon, W. Y. Wan, A. M. Badruddoza, T. A. Hatton and S. A. Khan, *Crystal Growth & Design*, 2014, **14**, 140-146.
125. A. M. Nightingale, T. W. Phillips, J. H. Bannock and J. C. de Mello, *Nature Communications*, 2014, **5**.
126. I. Lignos, L. Protesescu, S. Stavrakis, L. Piveteau, M. J. Speirs, M. A. Loi, M. V. Kovalenko and A. J. deMello, *Chemistry of Materials*, 2014, **26**, 2975-2982.
127. A. Schuch, K. Koehler and H. P. Schuchmann, *Journal of Thermal Analysis and Calorimetry*, 2013, **111**, 1881-1890.
128. L.-Y. Chu, A. S. Utada, R. K. Shah, J.-W. Kim and D. A. Weitz, *Angewandte Chemie-International Edition*, 2007, **46**, 8970-8974.
129. T. Thorsen, R. W. Roberts, F. H. Arnold and S. R. Quake, *Physical Review Letters*, 2001, **86**, 4163-4166.
130. P. Garstecki, M. J. Fuerstman, H. A. Stone and G. M. Whitesides, *Lab on a Chip*, 2006, **6**, 437-446.
131. S. L. Anna, N. Bontoux and H. A. Stone, *Applied Physics Letters*, 2003, **82**, 364-366.
132. S. Okushima, T. Nisisako, T. Torii and T. Higuchi, *Langmuir*, 2004, **20**, 9905-9908.
133. A. S. Utada, E. Lorenceau, D. R. Link, P. D. Kaplan, H. A. Stone and D. A. Weitz, *Science*, 2005, **308**, 537-541.
134. G. M. Whitesides, *Lab on a Chip*, 2013, **13**, 11-13.
135. G. Whitesides, *Lab on a Chip*, 2014, **14**, 3125-3126.
136. D. T. Chiu, A. J. deMello, D. Di Carlo, P. S. Doyle, C. Hansen, R. M. Maceiczyk and R. C. R. Wootton, *Chem*, 2017, **2**, 201-223.
137. P. J. Pritchard, *Fox and McDonald's Introduction to Fluid Mechanics*, John Wiley & Sons, New Jersey, 8th edn., 2011.
138. T. M. Squires and S. R. Quake, *Reviews of Modern Physics*, 2005, **77**, 977-1026.
139. H. A. Stone, A. D. Stroock and A. Ajdari, *Annual Review of Fluid Mechanics*, 2004, **36**, 381-411.
140. A. Gunther and K. F. Jensen, *Lab on a Chip*, 2006, **6**, 1487-1503.
141. H. Song, J. D. Tice and R. F. Ismagilov, *Angewandte Chemie-International Edition*, 2003, **42**, 768-772.
142. A. J. deMello, *Nature*, 2006, **442**, 394-402.

143. F. Courtois, L. F. Olguin, G. Whyte, A. B. Theberge, W. T. S. Huck, F. Hollfelder and C. Abell, *Analytical Chemistry*, 2009, **81**, 3008-3016.
144. P. Atkins and J. de Paula, *Atkin's Physical Chemistry*, Oxford University Press, Oxford, 7th edn., 2002.
145. J. D. Tice, H. Song, A. D. Lyon and R. F. Ismagilov, *Langmuir*, 2003, **19**, 9127-9133.
146. H. Song, M. R. Bringer, J. D. Tice, C. J. Gerdts and R. F. Ismagilov, *Applied Physics Letters*, 2003, **83**, 4664-4666.
147. D. Turnbull, *J. Chem. Phys.*, 1952, **20**, 411-424.
148. B. Zheng, L. S. Roach and R. F. Ismagilov, *Journal of the American Chemical Society*, 2003, **125**, 11170-11171.
149. P. Laval, N. Lisai, J. B. Salmon and M. Joanicot, *Lab on a Chip*, 2007, **7**, 829-834.
150. P. Laval, C. Giroux, J. Leng and J. B. Salmon, *J. Cryst. Growth*, 2008, **310**, 3121-3124.
151. M. Ildefonso, N. Candoni and S. Veesler, *Crystal Growth & Design*, 2011, **11**, 1527-1530.
152. M. Ildefonso, E. Revalor, P. Punniam, J. B. Salmon, N. Candoni and S. Veesler, *J. Cryst. Growth*, 2012, **342**, 9-12.
153. M. Ildefonso, N. Candoni and S. Veesler, *Crystal Growth & Design*, 2013, **13**, 2107-2110.
154. Z. Hammadi, N. Candoni, R. Grossier, M. Ildefonso, R. Morin and S. Veesler, *C. R. Phys.*, 2013, **14**, 192-198.
155. Z. Hammadi, R. Grossier, A. Ikni, N. Candoni, R. Morin and S. Veesler, *Faraday Discussions*, 2015, DOI: 10.1039/C4FD00274A.
156. A. Yashina, F. Meldrum and A. deMello, *Biomicrofluidics*, 2012, **6**, 22001-2200110.
157. J. Leng and J. B. Salmon, *Lab on a Chip*, 2009, **9**, 24-34.
158. H. H. Shi, Y. Xiao, S. Ferguson, X. Huang, N. Wang and H. X. Hao, *Lab on a Chip*, 2017, **17**, 2167-2185.
159. T. W. Phillips, I. G. Lignos, R. M. Maceiczyk, A. J. deMello and J. C. deMello, *Lab on a Chip*, 2014, **14**, 3172-3180.
160. A. Abou-Hassan, O. Sandre and V. Cabuil, *Angewandte Chemie-International Edition*, 2010, **49**, 6268-6286.
161. R. W. Epps, K. C. Felton, C. W. Coley and M. Abolhasani, *Lab on a Chip*, 2017, **17**, 4040-4047.
162. E. D. Greaves and A. Manz, *Lab on a Chip*, 2005, **5**, 382-391.
163. W. C. Röntgen, *Nature*, 1896, **53**, 274.
164. B. D. Cullity and S. R. Stock, *Elements of X-Ray Diffraction*, Prentice Hall, New Jersey, 3rd edn., 2001.
165. V. K. Pecharsky and P. Y. Zavalij, *Fundamentals of powder diffraction and structural characterization of materials*, Springer, 2009.
166. W. L. Bragg, *Science*, 1960, **131**, 1870-1874.
167. W. H. Bragg and W. L. Bragg, *Proc. R. soc. Lond. Ser. A-Contain. Pap. Math. Phys. Character*, 1913, **88**, 428-438.
168. S. A. Markgraf and R. J. Reeder, *Am. Miner.*, 1985, **70**, 590-600.
169. J. C. Kendrew, G. Bodo, H. M. Dintzis, R. G. Parrish, H. Wyckoff and D. C. Phillips, *Nature*, 1958, **181**, 662-666.
170. J. D. Watson and F. H. C. Crick, *Nature*, 1953, **171**, 737-738.

171. C.-J. Chen, J. P. Rose, M. G. Newton, Z.-J. Liu and B.-C. Wang, in *Modern protein chemistry: practical aspects*, eds. G. C. Howard and W. E. Brown, CRC Press, Boca Raton, 2001.
172. A. Ilari and C. Savino, in *Bioinformatics: Data, Sequence Analysis and Evolution*, ed. J. M. Keith, Humana Press, Totowa, NJ, 2008, DOI: 10.1007/978-1-60327-159-2_3, pp. 63-87.
173. P. Barnes, S. Jacques and M. Vickers, Powder Diffraction, http://pd.chem.ucl.ac.uk/pdnn/diff2/kinemat2.htm, (accessed March 13, 2019).
174. P. Debye and P. Scherrer, *Nachrichten von der Gesellschaft der Wissenschaften zu Göttingen, Mathematisch-Physikalische Klasse*, 1916, 1-15.
175. H. M. Rietveld, *Journal of Applied Crystallography*, 1969, **2**, 65-&.
176. *Structure Determination from Powder Diffraction Data*, Oxford University Press, New York, 2002.
177. I. Margiolaki and J. P. Wright, *Acta Crystallographica Section A*, 2008, **64**, 169-180.
178. I. Margiolaki, J. P. Wright, A. N. Fitch, G. C. Fox and R. B. von Dreele, *Acta Crystallographica Section D-Structural Biology*, 2005, **61**, 423-432.
179. S. Shian and K. H. Sandhage, *Rev. Sci. Instrum.*, 2009, **80**, 7.
180. A. Zeilinger, J. Todt, C. Krywka, M. Muller, W. Ecker, B. Sartory, M. Meindlhumer, M. Stefenelli, R. Daniel, C. Mitterer and J. Keckes, *Scientific Reports*, 2016, **6**, 14.
181. C. A. Murray, J. Potter, S. J. Day, A. R. Baker, S. P. Thompson, J. Kelly, C. G. Morris, S. H. Yang and C. C. Tang, *Journal of Applied Crystallography*, 2017, **50**, 172-183.
182. A. Guinier and G. Fournet, *Small Angle Scattering of X-rays*, John Wiley & Sons, New York, 1955.
183. L. Boldon, F. Laliberte and L. Liu, *Nano Reviews & Experiments*, 2015, **6**, 21.
184. B. R. Pauw, *Journal of Physics-Condensed Matter*, 2013, **25**, 24.
185. M. L. Whittaker, P. J. M. Smeets, H. Asayesh-Ardakani, R. Shahbazian-Yassar and D. Joester, *Angewandte Chemie-International Edition*, 2017, **56**, 16028-16031.
186. A. Ghazal, J. P. Lafleur, K. Mortensen, J. P. Kutter, L. Arleth and G. V. Jensen, *Lab on a Chip*, 2016, **16**, 4263-4295
187. J. Bolze, B. Peng, N. Dingenouts, P. Panine, T. Narayanan and M. Ballauff, *Langmuir*, 2002, **18**, 8364-8369.
188. T. Egami and S. J. Billinge, *Underneath the Bragg Peaks: Structural Analysis of Complex Materials*, Elsevier, Oxford, 2003.
189. S. J. L. Billinge, *Zeitschrift Fur Kristallographie*, 2007, 17-26.
190. M. W. Terban, M. Johnson, M. Di Michiel and S. J. L. Billinge, *Nanoscale*, 2015, **7**, 5480-5487.
191. S. J. L. Billinge and M. G. Kanatzidis, *Chemical Communications*, 2004, DOI: 10.1039/b309577k, 749-760.
192. V. Petkov, Y. Maswadeh, Y. G. Zhao, A. L. Lu, H. Cronk, F. F. Chang, S. Y. Shan, H. Kareem, J. Luo, C. J. Zhong, S. Shastri and P. Kenesei, *Nano Energy*, 2018, **49**, 209-220.
193. M. Levantino, B. A. Yorke, D. C. F. Monteiro, M. Cammarata and A. R. Pearson, *Current Opinion in Structural Biology*, 2015, **35**, 41-48.

194. B. C. Larson and J. Z. Tischler, in *Time-resolved Diffraction*, eds. J. R. Helliwell and P. M. Rentzepis, Oxford University Press, Oxford, 1997, ch. 5, pp. 137-160.
195. W. Clegg, *Journal of the Chemical Society-Dalton Transactions*, 2000, DOI: 10.1039/b004136j, 3223-3232.
196. J. C. Phillips, A. Wlodawer, M. M. Yevitz and K. O. Hodgson, *Proceedings of the National Academy of Sciences of the United States of America*, 1976, **73**, 128-132.
197. J. R. Helliwell, *Acta Crystallographica Section A*, 1998, **54**, 738-749.
198. H. Toyokawa, C. Broennimann, E. F. Eikenberry, B. Henrich, M. Kawase, M. Kobas, P. Kraft, M. Sato, B. Schmitt, M. Suzuki, H. Tanida and T. Uruga, *Nucl. Instrum. Methods Phys. Res. Sect. A-Accel. Spectrom. Dect. Assoc. Equip.*, 2010, **623**, 204-206.
199. C. Riekel, M. Burghammer and R. Davies, *IOP Conference Series: Materials Science and Engineering*, 2010, **14**.
200. S. P. Thompson, J. E. Parker, J. Potter, T. P. Hill, A. Birt, T. M. Cobb, F. Yuan and C. C. Tang, *Rev. Sci. Instrum.*, 2009, **80**, 9.
201. A. Merlin, J. Angly, L. Daubersies, C. Madeira, S. Schoder, J. Leng and J. B. Salmon, *European Physical Journal E*, 2011, **34**.
202. S. Guha, S. L. Perry, A. S. Pawate and P. J. A. Kenis, *Sensors and Actuators B-Chemical*, 2012, **174**, 1-9.
203. K. N. Toft, B. Vestergaard, S. S. Nielsen, D. Snakenborg, M. G. Jeppesen, J. K. Jacobsen, L. Arleth and J. P. Kutter, *Analytical Chemistry*, 2008, **80**, 3648-3654.
204. J. P. Lafleur, D. Snakenborg, S. S. Nielsen, M. Moller, K. N. Toft, A. Menzel, J. K. Jacobsen, B. Vestergaard, L. Arleth and J. P. Kutter, *Journal of Applied Crystallography*, 2011, **44**, 1090-1099.
205. B. Weinhausen and S. Köster, *Lab on a Chip*, 2013, **13**, 212-215.
206. J. Kehres, T. Pedersen, F. Masini, J. W. Andreasen, M. M. Nielsen, A. Diaz, J. H. Nielsen, O. Hansen and I. Chorkendorff, *Journal of Synchrotron Radiation*, 2016, **23**, 455-463.
207. T. Beuvier, E. A. C. Panduro, P. Kwasniewski, S. Marre, C. Lecoutre, Y. Garrabos, C. Aymonier, B. Calvignac and A. Gibaud, *Lab on a Chip*, 2015, **15**, 2002-2008.
208. S. Sui, Y. X. Wang, K. W. Kolewe, V. Srajer, R. Henning, J. D. Schiffman, C. Dimitrakopoulos and S. L. Perry, *Lab on a Chip*, 2016, **16**, 3082-3096.
209. R. Barrett, M. Faucon, J. Lopez, G. Cristobal, F. Destremaut, A. Dodge, P. Guillot, P. Laval, C. Masselon and J. B. Salmon, *Lab on a Chip*, 2006, **6**, 494-499.
210. R. Dootz, H. Evans, S. Köster and T. Pfohl, *Small*, 2007, **3**, 96-100.
211. P. Wassell, A. Okamura, N. W. G. Young, G. Bonwick, C. Smith, K. Sato and S. Ueno, *Langmuir*, 2012, **28**, 5539-5547.
212. S. Köster and T. Pfohl, *Modern Physics Letters B*, 2012, **26**.
213. P. Wägli, A. Homsy and N. F. de Rooij, *Sensors and Actuators B: Chemical*, 2011, **156**, 994-1001.
214. M. E. Brennich, J. F. Nolting, C. Dammann, B. Noding, S. Bauch, H. Herrmann, T. Pfohl and S. Köster, *Lab on a Chip*, 2011, **11**, 708-716.
215. P. Panine, S. Finet, T. M. Weiss and T. Narayanan, *Advances in Colloid and Interface Science*, 2006, **127**, 9-18.

216. I. Grillo, *Current Opinion in Colloid & Interface Science*, 2009, **14**, 402-408.
217. B. Abécassis, F. Testard, O. Spalla and P. Barboux, *Nano Letters*, 2007, **7**, 1723-1727.
218. T. M. Stawski, A. E. S. van Driessche, M. Ossorio, J. Diego Rodriguez-Blanco, R. Besselink and L. G. Benning, *Nature Communications*, 2016, **7**.
219. J. Cravillon, C. A. Schroder, R. Nayuk, J. Gummel, K. Huber and M. Wiebcke, *Angewandte Chemie-International Edition*, 2011, **50**, 8067-8071.
220. B. Zheng, J. D. Tice, L. S. Roach and R. F. Ismagilov, *Angewandte Chemie-International Edition*, 2004, **43**, 2508-2511.
221. F. Schwemmer, C. E. Blanchet, A. Spilotros, D. Kosse, S. Zehnle, H. D. T. Mertens, M. A. Graewert, M. Rossle, N. Paust, D. I. Svergun, F. von Stetten, R. Zengerle and D. Mark, *Lab on a Chip*, 2016, **16**, 1161-1170.
222. S. L. Perry, S. Guha, A. S. Pawate, A. Bhaskarla, V. Agarwal, S. K. Nair and P. J. A. Kenis, *Lab on a Chip*, 2013, **13**, 3183-3187.
223. C. L. Hansen, E. Skordalakes, J. M. Berger and S. R. Quake, *Proceedings of the National Academy of Sciences of the United States of America*, 2002, **99**, 16531-16536.
224. S. L. Perry, G. W. Roberts, J. D. Tice, R. B. Gennis and P. J. A. Kenis, *Crystal Growth & Design*, 2009, **9**, 2566-2569.
225. S. Sui and S. L. Perry, *Structural Dynamics*, 2017, **4**, 29.
226. Z. Ren, M. Ayhan, S. Bandara, K. Bowatte, I. Kumarapperuma, S. Gunawardana, H. Shin, C. Wang, X. T. Zeng and X. J. Yang, *Lab on a Chip*, 2018, **18**, 2246-2256.
227. M. Heymann, A. Opthalage, J. L. Wierman, S. Akella, D. M. E. Szebenyi, S. M. Gruner and S. Fraden, *IUCRrJ*, 2014, **1**, 349-360.
228. L. Pollack, M. W. Tate, N. C. Darnton, J. B. Knight, S. M. Gruner, W. A. Eaton and R. H. Austin, *Proceedings of the National Academy of Sciences of the United States of America*, 1999, **96**, 10115-10117.
229. A. Otten, S. Köster, B. Struth, A. Snigirev and T. Pfohl, *Journal of Synchrotron Radiation*, 2005, **12**, 745-750.
230. A. Martel, M. Burghammer, R. J. Davies, E. Di Cola, C. Vendrely and C. Riekel, *Journal of the American Chemical Society*, 2008, **130**, 17070-17074.
231. R. Graceffa, R. P. Nobrega, R. A. Barrea, S. V. Kathuria, S. Chakravarthy, O. Bilsel and T. C. Irving, *Journal of Synchrotron Radiation*, 2013, **20**, 820-825.
232. A. S. Poulos, M. Nania, P. Lapham, R. M. Miller, A. J. Smith, H. Tantawy, J. Caragay, J. Gummel, O. Ces, E. S. J. Robles and J. T. Cabral, *Langmuir*, 2016, **32**, 5852-5861.
233. O. Saldanha, M. E. Brennich, M. Burghammer, H. Herrmann and S. Köster, *Biomicrofluidics*, 2016, **10**, 024108.
234. B. F. B. Silva, *Physical Chemistry Chemical Physics*, 2017, **19**, 23690-23703.
235. N. Pham, D. Radajewski, A. Round, M. Brennich, P. Pernot, B. Biscans, F. Bonnete and S. Teychene, *Analytical Chemistry*, 2017, **89**, 2282-2287.
236. O. Saldanha, R. Graceffa, C. Hemonnot, C. Ranke, G. Brehm, M. Liebi, B. Marmiroli, B. Weinhausen, M. Burghammer and S. Köster, *ChemPhysChem*, 2017, **18**, 1220.

237. C. G. Lopez, T. Watanabe, M. Adamo, A. Martel, L. Porcar and J. T. Cabral, *Journal of Applied Crystallography*, 2018, **51**, 570-583.
238. C. G. Lopez, T. Watanabe, A. Martel, L. Porcar and J. T. Cabral, *Scientific Reports*, 2015, **5**, 7.
239. M. Adamo, A. S. Poulos, C. G. Lopez, A. Martel, L. Porcar and J. O. T. Cabral, *Soft Matter*, 2018, **14**, 1759-1770.
240. T. Chen, A. Neville, K. Sorbie and Z. Zhong, *Faraday Discussions*, 2007, **136**, 355-365.
241. T. Chen, A. Neville, K. Sorbie and Z. Zhong, *Chemical Engineering Science*, 2009, **64**, 912-918.
242. D. Burkle, R. De Motte, W. Taleb, A. Kleppe, T. Comyn, S. M. Vargas, A. Neville and R. Barker, *Rev. Sci. Instrum.*, 2016, **87**, 7.
243. M. Zobel, A. Windmuller, E. M. Schmidt, K. Gotz, T. Milek, D. Zahn, S. A. J. Kimber, J. M. Hudspeth and R. B. Neder, *CrystEngComm*, 2016, **18**, 2163-2172.
244. M. W. Terban, D. Banerjee, S. Ghose, B. Medasani, A. Shukla, B. A. Legg, Y. Zhou, Z. Zhu, M. L. Sushko, J. J. De Yoreo, J. Liu, P. K. Thallapally and S. J. L. Billinge, *Nanoscale*, 2018, DOI: 10.1039/C7NR07949D.
245. R. Stehle, G. Goerigk, D. Wallacher, M. Ballauff and S. Seiffert, *Lab on a Chip*, 2013, **13**, 1529-1537.
246. D. A. Shapiro, H. N. Chapman, D. DePonte, R. B. Doak, P. Fromme, G. Hembree, M. Hunter, S. Marchesini, K. Schmidt, J. Spence, D. Starodub and U. Weierstall, *Journal of Synchrotron Radiation*, 2008, **15**, 593-599.
247. M. S. Hunter, D. P. DePonte, D. A. Shapiro, R. A. Kirian, X. Wang, D. Starodub, S. Marchesini, U. Weierstall, R. B. Doak, J. C. H. Spence and P. Fromme, *Biophysical Journal*, 2011, **100**, 198-206.
248. A. Meents, M. O. Wiedorn, V. Srajer, R. Henning, I. Sarrou, J. Bergtholdt, M. Barthelmess, P. Y. A. Reinke, D. Dierksmeyer, A. Tolstikova, S. Schaible, M. Messerschmidt, C. M. Ogata, D. J. Kissick, M. H. Taft, D. J. Manstein, J. Lieske, D. Oberthuer, R. F. Fischetti and H. N. Chapman, *Nature Communications*, 2017, **8**, 12.
249. H. N. Chapman, P. Fromme, A. Barty, T. A. White, R. A. Kirian, A. Aquila, M. S. Hunter, J. Schulz, D. P. DePonte, U. Weierstall, R. B. Doak, F. Maia, A. V. Martin, I. Schlichting, L. Lomb, N. Coppola, R. L. Shoeman, S. W. Epp, R. Hartmann, D. Rolles, A. Rudenko, L. Foucar, N. Kimmel, G. Weidenspointner, P. Holl, M. N. Liang, M. Barthelmess, C. Caleman, S. Boutet, M. J. Bogan, J. Krzywinski, C. Bostedt, S. Bajt, L. Gumprecht, B. Rudek, B. Erk, C. Schmidt, A. Homke, C. Reich, D. Pietschner, L. Struder, G. Hauser, H. Gorke, J. Ullrich, S. Herrmann, G. Schaller, F. Schopper, H. Soltau, K. U. Kuhnel, M. Messerschmidt, J. D. Bozek, S. P. Hau-Riege, M. Frank, C. Y. Hampton, R. G. Sierra, D. Starodub, G. J. Williams, J. Hajdu, N. Timneanu, M. M. Seibert, J. Andreasson, A. Rocker, O. Jonsson, M. Svenda, S. Stern, K. Nass, R. Andritschke, C. D. Schroter, F. Krasniqi, M. Bott, K. E. Schmidt, X. Y. Wang, I. Grotjohann, J. M. Holton, T. R. M. Barends, R. Neutze, S. Marchesini, R. Fromme, S. Schorb, D. Rupp, M. Adolph, T. Gorkhover, I. Andersson, H. Hirsemann, G. Potdevin, H. Graafsma, B. Nilsson and J. C. H. Spence, *Nature*, 2011, **470**, 73-U81.
250. J. Tenboer, S. Basu, N. Zatsepin, K. Pande, D. Milathianaki, M. Frank, M. Hunter, S. Boutet, G. J. Williams, J. E. Koglin, D. Oberthuer, M.

Heymann, C. Kupitz, C. Conrad, J. Coe, S. Roy-Chowdhury, U. Weierstall, D. James, D. J. Wang, T. Grant, A. Barty, O. Yefanov, J. Scales, C. Gati, C. Seuring, V. Srajer, R. Henning, P. Schwander, R. Fromme, A. Ourmazd, K. Moffat, J. J. Van Thor, J. C. H. Spence, P. Fromme, H. N. Chapman and M. Schmidt, *Science*, 2014, **346**, 1242-1246.

251. C. Gati, D. Oberthuer, O. Yefanov, R. D. Bunker, F. Stellato, E. Chiu, S. M. Yeh, A. Aquila, S. Basu, R. Bean, K. R. Beyerlein, S. Botha, S. Boutetg, D. P. DePonte, R. B. Doak, R. Fromme, L. Galli, I. Grotjohann, D. R. James, C. Kupitz, L. Lomb, M. Messerschmidt, K. Nass, K. Rendek, R. L. Shoeman, D. J. Wang, U. Weierstall, T. A. White, G. J. Williams, N. A. Zatsepin, P. Fromme, J. C. H. Spence, K. N. Goldie, J. A. Jehle, P. Metcalf, A. Barty and H. N. Chapman, *Proceedings of the National Academy of Sciences of the United States of America*, 2017, **114**, 2247-2252.
252. M. O. Wiedorn, D. Oberthur, R. Bean, R. Schubert, N. Werner, B. Abbey, M. Aepfelbacher, L. Adriano, A. Allahgholi, N. Al-Qudami, J. Andreasson, S. Aplin, S. Awel, K. Ayyer, S. Bajt, I. Barak, S. Bari, J. Bielecki, S. Botha, D. Boukhelef, W. Brehm, S. Brockhauser, I. Cheviakov, M. A. Coleman, F. Cruz-Mazo, C. Danilevski, C. Darmanin, R. B. Doak, M. Domaracky, K. Dorner, Y. Du, H. Fangohr, H. Fleckenstein, M. Frank, P. Fromme, A. M. Ganan-Calvo, Y. Gevorkov, K. Giewekemeyer, H. M. Ginn, H. Graafsma, R. Graceffa, D. Greiffenberg, L. Gumprecht, P. Gottlicher, J. Hajdu, S. Hauf, M. Heymann, S. Holmes, D. A. Horke, M. S. Hunter, S. Imlau, A. Kaukher, Y. Kim, A. Klyuev, J. Knoska, B. Kobe, M. Kuhn, C. Kupitz, J. Kuper, J. M. Lahey-Rudolph, T. Laurus, K. Le Cong, R. Letrun, P. L. Xavier, L. Maia, F. Maia, V. Mariani, M. Messerschmidt, M. Metz, D. Mezza, T. Michelat, G. Mills, D. C. F. Monteiro, A. Morgan, K. Muhlig, A. Munke, A. Munnich, J. Nette, K. A. Nugent, T. Nuguid, A. M. Orville, S. Pandey, G. Pena, P. Villanueva-Perez, J. Poehlsen, G. Previtali, L. Redecke, W. M. Riekehr, H. Rohde, A. Round, T. Safenreiter, I. Sarrou, T. Sato, M. Schmidt, B. Schmitt, R. Schonherr, J. Schulz, J. A. Sellberg, M. M. Seibert, C. Seuring, M. L. Shelby, R. L. Shoeman, M. Sikorski, A. Silenzi, C. A. Stan, X. T. Shi, S. Stern, J. Sztuk-Dambietz, J. Szuba, A. Tolstikova, M. Trebbin, U. Trunk, P. Vagovic, T. Ve, B. Weinhausen, T. A. White, K. Wrona, C. Xu, O. Yefanov, N. Zatsepin, J. G. Zhang, M. Perbandt, A. P. Mancuso, C. Betzel, H. Chapman and A. Barty, *Nature Communications*, 2018, **9**, 11.
253. V. Panneels, W. T. Wu, C. J. Tsai, P. Nogly, J. Rheinberger, K. Jaeger, G. Cicchetti, C. Gati, L. M. Kick, L. Sala, G. Capitani, C. Milne, C. Padeste, B. Pedrini, X. D. Li, J. Standfuss, R. Abela and G. Schertler, *Structural Dynamics*, 2015, **2**, 8.
254. J. J. van Thor and A. Madsen, *Structural Dynamics*, 2015, **2**, 21.
255. M. Schmidt, *Advances in Condensed Matter Physics*, 2013, DOI: 10.1155/2013/167276, 10.
256. J. R. Stagno, Y. Liu, Y. R. Bhandari, C. E. Conrad, S. Panja, M. Swain, L. Fan, G. Nelson, C. Li, D. R. Wendel, T. A. White, J. D. Coe, M. O. Wiedorn, J. Knoska, D. Oberthuer, R. A. Tuckey, P. Yu, M. Dyba, S. G. Tarasov, U. Weierstall, T. D. Grant, C. D. Schwieters, J. Zhang, A. R. Ferre-D'Amare, P. Fromme, D. E. Draper, M. Liang, M. S. Hunter, S. Boutet, K. Tan, X. Zuo, X. Ji, A. Barty, N. A. Zatsepin, H. N. Chapman, J.

C. H. Spence, S. A. Woodson and Y. X. Wang, *Nature*, 2017, **541**, 242-+.
257. C. David, P. Karvinen, M. Sikorski, S. Song, I. Vartiainen, C. J. Milne, A. Mozzanica, Y. Kayser, A. Diaz, I. Mohacsi, G. A. Carini, S. Herrmann, E. Farm, M. Ritala, D. M. Fritz and A. Robert, *Scientific Reports*, 2015, **5**, 6.
258. J. Titus, *Test & Measurement World*, Nov. 2007, 41-46.
259. R. Dinapoli, A. Bergamaschi, B. Henrich, R. Horisberger, I. Johnson, A. Mozzanica, E. Schmid, B. Schmitt, A. Schreiber, X. T. Shi and G. Theidel, *Nucl. Instrum. Methods Phys. Res. Sect. A-Accel. Spectrom. Dect. Assoc. Equip.*, 2011, **650**, 79-83.
260. I. Johnson, A. Bergamaschi, H. Billich, S. Cartier, R. Dinapoli, D. Greiffenberg, M. Guizar-Sicairos, B. Henrich, J. Jungmann, D. Mezza, A. Mozzanica, B. Schmitt, X. Shi and G. Tinti, *Journal of Instrumentation*, 2014, **9**, 9.
261. B. Henrich, A. Bergamaschi, C. Broennimann, R. Dinapoli, E. F. Eikenberry, I. Johnson, M. Kobas, P. Kraft, A. Mozzanica and B. Schmitt, *Nucl. Instrum. Methods Phys. Res. Sect. A-Accel. Spectrom. Dect. Assoc. Equip.*, 2009, **607**, 247-249.
262. P. Fromme and J. C. H. Spence, *Current Opinion in Structural Biology*, 2011, **21**, 509-516.
263. J. Vlassenbroeck, V. Cnudde, B. Masschaele, M. Dierick, L. Van Hoorebeke and P. Jacobs, in *Building Stone Decay: From Diagnosis to Conservation*, eds. R. Prikryl and B. J. Smith, Geological Soc Publishing House, Bath, 2007, vol. 271, pp. 277-+.
264. R. Henderson, *Proceedings of the Royal Society of London. Series B: Biological Sciences*, 1990, **241**, 6-8.
265. L. Mandel, *Proceedings of the Physical Society of London*, 1959, **74**, 233-243.
266. H.-S. Kim, D.-S. Suhr, G.-H. Kim and D.-W. Kum, *Metals and Materials*, 1996, **2**, 15-21.
267. J. A. Newman, P. D. Schmitt, S. J. Toth, F. Y. Deng, S. J. Zhang and G. J. Simpson, *Analytical Chemistry*, 2015, **87**, 10950-10955.
268. E. M. Smith, M. G. Kopylova, L. Dubrovinsky, O. Navon, J. Ryder and E. L. Tomlinson, *Mineralogical Magazine*, 2011, **75**, 2657-2675.
269. C. Nunes, A. Mahendrasingam and R. Suryanarayanan, *Pharmaceutical Research*, 2005, **22**, 1942-1953.
270. L. Dupont, F. Portemer and M. Figlarz, *Journal of Materials Chemistry*, 1997, **7**, 797-800.
271. D. C. Green, J. Ihli, P. D. Thornton, M. A. Holden, B. Marzec, Y. Y. Kim, A. N. Kulak, M. A. Levenstein, C. Tang, C. Lynch, S. E. D. Webb, C. J. Tynan and F. C. Meldrum, *Nature Communications*, 2016, **7**, 13.
272. L. Addadi, S. Raz and S. Weiner, *Advanced Materials*, 2003, **15**, 959-970.
273. L. Brecevic and A. E. Nielsen, *J. Cryst. Growth*, 1989, **98**, 504-510.
274. L. N. Plummer and E. Busenberg, *Geochimica et Cosmochimica Acta*, 1982, **46**, 1011-1040.
275. M. Faatz, F. Grohn and G. Wegner, *Advanced Materials*, 2004, **16**, 996-1000.
276. J. D. Rodriguez-Blanco, S. Shaw and L. G. Benning, *Mineralogical Magazine*, 2008, **72**, 283-286.

277. C. Holtze, A. C. Rowat, J. J. Agresti, J. B. Hutchison, F. E. Angile, C. H. J. Schmitz, S. Köster, H. Duan, K. J. Humphry, R. A. Scanga, J. S. Johnson, D. Pisignano and D. A. Weitz, *Lab on a Chip*, 2008, **8**, 1632-1639.
278. R. W. Liefferink, A. Naillon, D. Bonn, M. Prat and N. Shahidzadeh, *Lab on a Chip*, 2018, **18**, 1094-1104.
279. Y. A. Alzahid, P. Mostaghimi, A. Gerami, A. Singh, K. Privat, T. Amirian and R. T. Armstrong, *Scientific Reports*, 2018, **8**, 15.
280. L. Addadi and S. Weiner, *Proceedings of the National Academy of Sciences of the United States of America*, 1985, **82**, 4110-4114.
281. S. Von Euw, Q. H. Zhang, V. Manichev, N. Murali, J. Gross, L. C. Feldman, T. Gustafsson, C. Flach, R. Mendelsohn and P. G. Falkowski, *Science*, 2017, **356**, 933-+.
282. J. R. Jones, *Acta Biomaterialia*, 2013, **9**, 4457-4486.
283. Z. Abbasi, M. Bahrololoom, M. Shariat and R. Bagheri, *Journal of Dental Biomaterials*, 2015, **2**, 1-9.
284. S. Le Caer, F. Brunet, C. Chatelain, D. Durand, V. Dauvois, T. Charpentier and J. P. Renault, *Journal of Physical Chemistry C*, 2012, **116**, 4748-4759.
285. D. D. Archibald, S. B. Qadri and B. P. Gaber, *Langmuir*, 1996, **12**, 538-546.
286. P. Sepulveda, J. R. Jones and L. L. Hench, *Journal of Biomedical Materials Research*, 2001, **58**, 734-740.
287. S. L. Broadley, B. J. Murray, R. J. Herbert, J. D. Atkinson, S. Dobbie, T. L. Malkin, E. Condliffe and L. Neve, *Atmospheric Chemistry and Physics*, 2012, **12**, 287-307.
288. Y. W. Wang, Y. Y. Kim, C. J. Stephens, F. C. Meldrum and H. K. Christenson, *Crystal Growth & Design*, 2012, **12**, 1212-1217.
289. B. J. Murray, D. O'Sullivan, J. D. Atkinson and M. E. Webb, *Chemical Society Reviews*, 2012, **41**, 6519-6554.
290. T. Kokubo and H. Takadama, *Biomaterials*, 2006, **27**, 2907-2915.
291. A. L. B. Macon, T. B. Kim, E. M. Valliant, K. Goetschius, R. K. Brow, D. E. Day, A. Hoppe, A. R. Boccaccini, I. Y. Kim, C. Ohtsuki, T. Kokubo, A. Osaka, M. Vallet-Regi, D. Arcos, L. Fraile, A. J. Salinas, A. V. Teixeira, Y. Vueva, R. M. Almeida, M. Miola, C. Vitale-Brovarone, E. Verne, W. Holand and J. R. Jones, *Journal of Materials Science-Materials in Medicine*, 2015, **26**, 10.
292. M. R. Filgueiras, G. Latorre and L. L. Hench, *Journal of Biomedical Materials Research*, 1993, **27**, 445-453.
293. P. Sepulveda, J. R. Jones and L. L. Hench, *Journal of Biomedical Materials Research*, 2002, **61**, 301-311.
294. L. Rybarikova, J. Had and I. Holubova, *Ceramics-Silikaty*, 1995, **39**, 34-39.
295. J. R. Jones, P. Sepulveda and L. L. Hench, *Journal of Biomedical Materials Research*, 2001, **58**, 720-726.
296. D. Lukito, J. M. Xue and J. Wang, *Materials Letters*, 2005, **59**, 3267-3271.
297. M. Bohner and J. Lemaitre, *Biomaterials*, 2009, **30**, 2175-2179.
298. A. Oyane, K. Onuma, A. Ito, H. M. Kim, T. Kokubo and T. Nakamura, *Journal of Biomedical Materials Research Part A*, 2003, **64A**, 339-348.

299. G. S. Lazaro, S. C. Santos, L. E. Almeida, L. S. Barreto and E. Araujo dos Santos, *Key Engineering Materials*, 2012, **493-494**, 102-107.
300. G. Poologasundarampillai, M. Boix Alberich, D. Clarke, A. Smith, R. Martin, P. D. Lee and J. R. Jones, *Frontiers in Bioengineering and Biotechnology*, 2016, DOI: 10.3389/conf.FBIOE.2016.01.02877.
301. M. Mackovic, A. Hoppe, R. Detsch, D. Mohn, W. J. Stark, E. Spiecker and A. R. Boccaccini, *Journal of Nanoparticle Research*, 2012, **14**, 22.
302. N. Hiranuma, S. Augustin-Bauditz, H. Bingemer, C. Budke, J. Curtius, A. Danielczok, K. Diehl, K. Dreischmeier, M. Ebert, F. Frank, N. Hoffmann, K. Kandler, A. Kiselev, T. Koop, T. Leisner, O. Mohler, B. Nillius, A. Peckhaus, D. Rose, S. Weinbruch, H. Wex, Y. Boose, P. J. DeMott, J. D. Hader, T. C. J. Hill, Z. A. Kanji, G. Kulkarni, E. J. T. Levin, C. S. McCluskey, M. Murakami, B. J. Murray, D. Niedermeier, M. D. Petters, D. O'Sullivan, A. Saito, G. P. Schill, T. Tajiri, M. A. Tolbert, A. Welti, T. F. Whale, T. P. Wright and K. Yamashita, *Atmospheric Chemistry and Physics*, 2015, **15**, 2489-2518.
303. *CRC Handbook of Chemistry and Physics*, CRC Press, Boca Raton, 93rd edn., 2012.
304. W. H. Sun, S. Jayaraman, W. Chen, K. A. Persson and G. Ceder, *Proceedings of the National Academy of Sciences of the United States of America*, 2015, **112**, 3199-3204.
305. M. Inoue and I. Hirasawa, *J. Cryst. Growth*, 2013, **380**, 169-175.
306. D. Kralj and N. Vdovic, *Water Res.*, 2000, **34**, 179-184.
307. M. G. Lioliou, C. A. Paraskeva, P. G. Koutsoukos and A. C. Payatakes, *Journal of Colloid and Interface Science*, 2007, **308**, 421-428.
308. J. M. Campbell, F. C. Meldrum and H. K. Christenson, *Proceedings of the National Academy of Sciences of the United States of America*, 2017, **114**, 810-815.
309. M. A. Holden, T. F. Whale, M. D. Tarn, D. O'Sullivan, R. D. Walshaw, B. J. Murray, F. C. Meldrum and H. K. Christenson, *Science Advances*, 2019, **5**, eaav4316.
310. A. L. B. Macon, T. B. Kim, E. M. Valliant, K. Goetschius, R. K. Brow, D. E. Day, A. Hoppe, A. R. Boccaccini, I. Y. Kim, C. Ohtsuki, T. Kokubo, A. Osaka, M. Vallet-Regi, D. Arcos, L. Fraile, A. J. Salinas, A. V. Teixeira, Y. Vueva, R. M. Almeida, M. Miola, C. Vitale-Brovarone, E. Verne, W. Holand and J. R. Jones, *Journal of Materials Science-Materials in Medicine*, 2015, **26**, 115.
311. K. Robertson, P. B. Flandrin, A. R. Klapwijk and C. C. Wilson, *Crystal Growth & Design*, 2016, **16**, 4759-4764.
312. K. A. Powell, G. Bartolini, K. E. Wittering, A. N. Saleemi, C. C. Wilson, C. D. Rielly and Z. K. Nagy, *Crystal Growth & Design*, 2015, **15**, 4821-4836.
313. X. Y. Zhang, J. S. Yang, Y. Y. Wu and X. G. Zhou, *J. Cryst. Growth*, 2018, **502**, 45-53.
314. M. Gryl, A. Krawczuk and K. Stadnicka, *Acta Crystallographica Section B-Structural Science*, 2008, **64**, 623-632.
315. O. Levenspiel, *Chemical Reaction Engineering*, John Wiley & Sons, New York, 3rd edn., 1999.
316. Y. M. Mo and K. F. Jensen, *Reaction Chemistry & Engineering*, 2016, **1**, 501-507.
317. D. L. Browne, B. J. Deadman, R. Ashe, I. R. Baxendale and S. V. Ley, *Organic Process Research & Development*, 2011, **15**, 693-697.

318. C. J. Richmond, H. N. Miras, A. R. de la Oliva, H. Y. Zang, V. Sans, L. Paramonov, C. Makatsoris, R. Inglis, E. K. Brechin, D. L. Long and L. Cronin, *Nature Chemistry*, 2012, **4**, 1038-1044.
319. S. Falss, G. Tomaiuolo, A. Perazzo, P. Hodgson, P. Yaseneva, J. Zakrzewski, S. Guido, A. Lapkin, R. Woodward and R. E. Meadows, *Organic Process Research & Development*, 2016, **20**, 558-567.
320. F. J. Weiberth, M. R. Powers, C. Gallin and D. McDonald, *Organic Process Research & Development*, 2018, **22**, 512-519.
321. M. R. Chapman, M. H. T. Kwan, G. King, K. E. Jolley, M. Hussain, S. Hussain, I. E. Salama, C. G. Nino, L. A. Thompson, M. E. Bayana, A. D. Clayton, B. N. Nguyen, N. J. Turner, N. Kapur and A. J. Blacker, *Organic Process Research & Development*, 2017, **21**, 1294-1301.
322. R. B. Macmullin and M. Weber, *Transactions of the American Institute of Chemical Engineers*, 1935, **31**, 409-458.
323. O. Roubeau, *Chemistry - A European Journal*, 2012, **18**, 15230-15244.
324. E. Coronado, J. R. Galan-Mascaros, M. Monrabal-Capilla, J. Garcia-Martinez and P. Pardo-Ibanez, *Advanced Materials*, 2007, **19**, 1359-+.
325. C. Bartual-Murgui, E. Natividad and O. Roubeau, *Journal of Materials Chemistry C*, 2015, **3**, 7916-7924.
326. A. Michalowicz, J. Moscovici, B. Ducourant, D. Cracco and O. Kahn, *Chemistry of Materials*, 1995, **7**, 1833-1842.
327. K. Robertson, P. B. Flandrin, H. J. Shepherd and C. C. Wilson, *Chimica Oggi-Chemistry Today*, 2017, **35**, 19-22.
328. M. Basham, J. Filik, M. T. Wharmby, P. C. Y. Chang, B. El Kassaby, M. Gerring, J. Aishima, K. Levik, B. C. A. Pulford, I. Sikharulidze, D. Sneddon, M. Webber, S. S. Dhesi, F. Maccherozzi, O. Svensson, S. Brockhauser, G. Naray and A. W. Ashton, *Journal of Synchrotron Radiation*, 2015, **22**, 853-858.
329. T. Skarzynski, *Acta Crystallographica Section D-Biological Crystallography*, 2013, **69**, 1283-1288.
330. O. Hemberg, M. Otendal and H. M. Hertz, *Applied Physics Letters*, 2003, **83**, 1483-1485.
331. C. J. Mable, M. J. Derry, K. L. Thompson, L. A. Fielding, O. O. Mykhaylyk and S. P. Armes, *Macromolecules*, 2017, **50**, 4465-4473.
332. H. Schnablegger and Y. Singh, *The SAXS Guide: Getting acquainted with the princliples*, Anton Paar GmbH, Austria, 3rd edn., 2013.
333. O. Gang, Small Angle X-Ray Scattering (SAXS) from Bulks and Surfaces, https://www.bnl.gov/ps/userguide/lectures/Lecture-7-Gang.pdf, (accessed March 8, 2019).
334. T. N. Drebushchak and E. V. Boldyreva, *Zeitschrift Fur Kristallographie*, 2004, **219**, 506-512.
335. M. Fernandez Martinez, personal communication.
336. M. Winter, personal communication.
337. O. O. Mykhaylyk, personal communication.
338. P. T. Torma, H. J. Sipila, M. Mattila, P. Kostamo, J. Kostamo, E. Kostamo, H. Lipsanen, N. Nelms, B. Shortt, M. Bavdaz and C. Laubis, *IEEE Transactions on Nuclear Science*, 2013, **60**, 1311-1314.
339. S. B. Li, J. Ihli, W. J. Marchant, M. L. Zeng, L. Chen, K. Wehbe, G. Cinque, O. Cespedes, N. Kapur and F. C. Meldrum, *Lab on a Chip*, 2017, **17**, 1616-1624.

340. R. Dimper, H. Reichert, P. Raimondi, L. Sánchez Ortiz, F. Sette and J. Susini, *ESRF Upgrade Programme Phase II (2015-2022) - Technical Design Study ("The Orange Book")*, The European Synchrotron Radiation Facility.
341. R. Vitale, A. Zhyrova, J. F. Fortuna, O. E. de Noord, A. Ferrer and H. Martens, *Chemometrics and Intelligent Laboratory Systems*, 2017, **161**, 118-129.